

AD-A263 926



DTIC
S **ELECTE** **D**
C
AUG 31 1993

AEOSR-TR- 93 0652

2

**HIGH RESOLUTION GEOLOGICAL SITE CHARACTERIZATION
UTILIZING GROUND MOTION DATA**

Approved for public release;
distribution unlimited.

FINAL REPORT
GRANT AFOSR-89-0176
01 NOV 88 - 31 JAN 93

PI: BRIAN W STUMP
DEPARTMENT OF GEOLOGICAL SCIENCES
SOUTHERN METHODIST UNIVERSITY
DALLAS, TEXAS 75275-0395

9 JULY 93

93-20274



93 0652

REPORT DOCUMENTATION PAGE

1a. REPORT SECURITY CLASSIFICATION Unclassified			1b. RESTRICTIVE MARKINGS		
2a. SECURITY CLASSIFICATION AUTHORITY			3. DISTRIBUTION / AVAILABILITY OF REPORT Approved for public release; distribution unlimited.		
2b. DECLASSIFICATION / DOWNGRADING SCHEDULE					
4. PERFORMING ORGANIZATION REPORT NUMBER(S) SMU G-11			5. MONITORING ORGANIZATION REPORT NUMBER(S)		
6a. NAME OF PERFORMING ORGANIZATION Southern Methodist Univ.		6b. OFFICE SYMBOL (if applicable)		7a. NAME OF MONITORING ORGANIZATION AFOSR/NL	
6c. ADDRESS (City, State, and ZIP Code) Southern Methodist University Department of Geological Sciences Dallas, Texas 75275-0395			7b. ADDRESS (City, State, and ZIP Code) AFOSR/NL Dr. Stanley K. Dickinson Building 410 Bolling AFB, DC 20332-6448		
8a. NAME OF FUNDING / SPONSORING ORGANIZATION AFOSR/NL		8b. OFFICE SYMBOL (if applicable) NL		9. PROCUREMENT INSTRUMENT IDENTIFICATION NUMBER AFOSR-89-0176	
8c. ADDRESS (City, State, and ZIP Code) AFOSR/NL Dr. Stanley K. Dickinson Building 410 Bolling AFB, DC 20332-6448			10. SOURCE OF FUNDING NUMBERS		
			PROGRAM ELEMENT NO. 61102F	PROJECT NO. 2309	TASK NO. 172
11. TITLE (Include Security Classification) HIGH RESOLUTION GEOLOGICAL SITE CHARACTERIZATION UTILIZING GROUND MOTION DATA, AFOSR-89-0176					
12. PERSONAL AUTHOR(S) Mike Craven, Brian Stump					
13a. TYPE OF REPORT Final		13b. TIME COVERED FROM 01 Nov 88 TO 31 Jan 93		14. DATE OF REPORT (Year, Month, Day) 93 07 09	
15. PAGE COUNT					
16. SUPPLEMENTARY NOTATION					
17. COSATI CODES			18. SUBJECT TERMS (Continue on reverse if necessary and identify by block number)		
FIELD	GROUP	SUB-GROUP	seismology, geological site characterization, shear waves, surface waves, Rayleigh Waves, Love Waves, dispersion analysis, velocity inversion		
19. ABSTRACT (Continue on reverse if necessary and identify by block number) Experimentally produced surface waves at high frequencies (5-50 Hz) and short source-receiver distances (5-100 m) are utilized in the determination of shallow shear structures in geological materials. This procedure is shown to provide a high resolution picture of these shallow materials which may be of interest to the engineering and environmental community. Love waves are generated by the Sh source, SWIG, developed under this contract. Rayleigh waves are produced by the commercially available Betsy Seisgun. Group velocity determination includes multiple filter analysis with the application of narrow band Gaussian filters to the data and determination of the peaks in the resulting amplitude envelopes. Phase velocities are determined from the array data using the p-omega technique. Dispersion data is inverted to refine the velocity estimates and produce an attenuation model.					
20. DISTRIBUTION / AVAILABILITY OF ABSTRACT <input checked="" type="checkbox"/> UNCLASSIFIED/UNLIMITED <input type="checkbox"/> SAME AS RPT. <input type="checkbox"/> DTIC USERS			21. ABSTRACT SECURITY CLASSIFICATION		
22a. NAME OF RESPONSIBLE INDIVIDUAL Dr. Stanley K. Dickinson			22b. TELEPHONE (Include Area Code) (202) 762-5021		22c. OFFICE SYMBOL NL

23 JUL 1993

Compressional and shear wave velocities were found to vary laterally across the test bed. Love waves generated by the SWIG source produce the most stable results. Surface waves provide velocity constraints to depth of 10 m. Deeper structure determination requires additional low frequency information below the natural frequency of the geophones (10 Hz) used in this investigation.

SHEAR WAVE VELOCITY DETERMINATION
USING SURFACE WAVE DISPERSION

A Thesis Presented to the Graduate Faculty of
Dedman College
of
Southern Methodist University
in
Partial Fulfillment of the Requirements
for the Degree of
Master of Science
with a
Major in Geophysics
by

Mike E. Craven
(B.A., Rice University, 1977)

December 19, 1992

DTIC QUALITY INSPECTED 3

Accession For	
NTIS CRA&I	<input checked="checked" type="checkbox"/>
DTIC TAB	<input type="checkbox"/>
Unannounced	<input type="checkbox"/>
Justification	
By	
Distribution /	
Availability Codes	
Dist	Avail and/or Special
A-1	

Craven, Mike Eric

B.A., Rice University, 1977

Shear Wave Velocity Determination
Using Surface Wave Dispersion

Advisor: Dr. Brian W. Stump

Master of Science degree conferred December 19, 1992

Thesis completed November 18, 1992

Shear wave velocity structure was determined through the use of phase and group velocity dispersion of surface waves. The project consisted of three stages, data acquisition, dispersion analysis and inversion for shear velocity structure.

Two sources were used, the SWIG which generated SH waves and subsequent Love surface waves, and the Betsy source which generated a P wavefield and subsequent Rayleigh surface waves. The data were acquired with a receiver array at ranges from 5 to 94.5 meters. The phones were oriented vertically to respond to Rayleigh and oriented transversely to acquire Love waves.

Group velocity dispersion analysis included the multiple filter analysis technique which involves taking narrow Gaussian filters of the data and picking the peaks of the instantaneous amplitude for velocity determination. The Barker extension of this technique used here provides average dispersion over an array of data. The phase matched filter technique was used to fine tune single phone estimates, as well as to remove surface waves for individual analysis. The p-omega technique provided phase velocity information for the inversion techniques.

Standard refraction techniques were applied to both the P and the SH data sets to provide a starting model for the inversion. The data was then inverted for shear velocity and shear Q structure. Synthetic surface waves were generated to test the inverted results. The compressional and shear waves were discovered to vary laterally as well as vertically. The final velocity model inverted from the surface waves consisted of average velocities over the interval imaged. The imaged interval for the phase velocity measurements was different than the imaged interval for the group velocity.

TABLE OF CONTENTS

LIST OF FIGURES	vii
LIST OF TABLES.....	xv
LIST OF SYMBOLS	xvi
LIST OF ABBREVIATIONS.....	xvii
ACKNOWLEDGEMENTS	xviii
CHAPTER	
1. INTRODUCTION.....	1
A. Fundamental Principles	3
1. Surface waves	3
2. Phase and group velocity	6
3. Dispersion analysis using paper records	8
4. Dispersion analysis using moving window technique	11
5. Inversion fundamentals.....	13
B. Previous Work	15
C. Test Site	17
D. Overview of the Thesis	18
2. FIELD DATA ACQUISITION.....	20
3. DATA PROCESSING FOR SURFACE WAVE DISPERSION	35
A. Pre-processing of Field Data	35
B. Multiple Filter Analysis	36
1. Experimental technique	36
2. Experimental results	50
C. Array Processing of Group Velocity.....	77
1. Experimental technique	77

CHAPTER	Page
2. Experimental results	79
D. Phase Matched Filter	104
1. Experimental technique	104
2. Experimental results	105
E. Array Processing for Phase Velocity.....	114
1. Experimental technique	114
2. Experimental results	123
4. INVERSION FOR VELOCITY STRUCTURE.....	135
A. Refraction Technique.....	135
1. Experimental technique	135
2. Experimental results	140
B. Inversion of Dispersion Data.....	140
1. Experimental technique	140
2. Experimental results	149
C. Forward Modeling.....	166
5. CONCLUSIONS	181
A. Acquisition Techniques.....	181
B. Dispersion Analysis	182
C. Inversion Technique	185
D. Recommendations for Future Work.....	187
APPENDIX: MULTIPLE FILTER ANALYSIS	190
BIBLIOGRAPHY	212

LIST OF FIGURES

Figure	Page
1. Geometric Analysis of Love Wave Generation.....	5
2. Rayleigh Wave Dispersion from Synthetic	9
3. Moving Window Analysis.....	12
4. Betsy Source	21
5. Side and End View of SWIG Source	23
6. SWIG Data at 5.0 Meters	24
7. Betsy Data at 5.0 Meters.....	25
8. Instrument Response of L-410 Geophones	26
9. Acquisition Geometry for SWIG and Betsy data.....	28
10. SWIG Data at 35.0 Meters	29
11. Betsy Data at 35.0 Meters.....	30
12. SWIG Data at 65.0 Meters	31
13. Betsy Data at 65.0 Meters.....	32
14. Spectral Response of Single Receiver SWIG Data 5 to 30 Meters	34
15. Comparison of Amplitude Spectrums of SWIG Data.....	37
16. SWIG Data After Instrument Correction at 5.0 Meters.	38
17. SWIG Data After Instrument Correction at 35.0 Meters.	39
18. SWIG Data After Instrument Correction at 65.0 Meters.	40

Figure		Page
19.	Betsy Data After Instrument Correction at 5.0 Meters.....	40
20.	Betsy Data After Instrument Correction at 35.0 Meters.....	42
21.	Betsy Data After Instrument Correction at 65.0 Meters.....	43
22.	Impulse Response in Time Domain of Bandpass Filters, $A_0 = 5$...	45
23.	Impulse Response in Time Domain of Bandpass Filters, $A_0 = 75$.	46
24.	Impulse Response in Frequency Domain at Center Frequency of 50 Hz for Various Values of A_0	48
25.	MFT Analysis at 5.0 Meters for SWIG Data	53
26.	MFT Analysis at 10.5 Meters for SWIG Data	54
27.	MFT Analysis at 15.0 Meters for SWIG Data	55
28.	MFT Analysis at 20.0 Meters for SWIG Data	56
29.	MFT Analysis at 25.0 Meters for SWIG Data	57
30.	MFT Analysis at 30.0 Meters for SWIG Data	58
31.	MFT Analysis at 34.5 Meters for SWIG Data	59
32.	MFT Analysis at 35.0 Meters for SWIG Data	60
33.	MFT Analysis at 40.5 Meters for SWIG Data	61
34.	MFT Analysis at 45.0 Meters for SWIG Data	62
35.	MFT Analysis at 50.0 Meters for SWIG Data	63
36.	MFT Analysis at 55.0 Meters for SWIG Data	64
37.	MFT Analysis at 60.0 Meters for SWIG Data	65
38.	MFT Analysis at 64.5 Meters for SWIG Data	66
39.	MFT Analysis at 65.0 Meters for SWIG Data	67
40.	MFT Analysis at 70.5 Meters for SWIG Data	68

Figure		Page
41.	MFT Analysis at 75.0 Meters for SWIG Data	69
42.	MFT Analysis at 80.0 Meters for SWIG Data	70
43.	MFT Analysis at 85.0 Meters for SWIG Data	71
44.	MFT Analysis at 90.0 Meters for SWIG Data	72
45.	MFT Analysis at 94.5 Meters for SWIG Data	73
46.	Interpreted Dispersion Curves for Love Wave Group Velocity from MFT at range of 5.0 to 34.5 Meters	74
47.	Interpreted Dispersion Curves for Love Wave Group Velocity from MFT at range of 35.0 to 64.5 Meters	75
48.	Interpreted Dispersion Curves for Love Wave Group Velocity from MFT at range of 65.0 to 94.5 Meters	76
49.	Barker Array Processing of 5 Meter SWIG Data	80
50.	Barker Array Processing of 35 Meter SWIG Data	81
51.	Barker Array Processing of 65 Meter SWIG Data	82
52.	Overlay of Barker Array Processing of 5, 35 & 65 Meter SWIG	83
53.	Overlay of 65 Meter Barker with 65 Meter MFT for SWIG	84
54.	Overlay of 65 Meter Barker with 70 Meter MFT for SWIG	85
55.	Overlay of 65 Meter Barker with 75 Meter MFT for SWIG	86
56.	Overlay of 65 Meter Barker with 80 Meter MFT for SWIG	87
57.	Overlay of 65 Meter Barker with 85 Meter MFT for SWIG	88
58.	Overlay of 65 Meter Barker with 90 Meter MFT for SWIG	89
59.	Overlay of 65 Meter Barker with 94.5 Meter MFT for SWIG	90
60.	Comparison of MFT and Array Techniques at 34.5 and 35 Meters	93
61.	Comparison of MFT and Array Techniques at 64.5 and 65 Meters	94

Figure		Page
62.	Attenuation Coefficients from Array Processing of SWIG	95
63.	Array Processing for Group Velocity of 5 Meter Betsy	97
64.	Array Processing for Group Velocity of 35 Meter Betsy	98
65.	Array Processing for Group Velocity of 65 Meter Betsy	99
66.	Overlay of the Interpreted Group Velocity of Rayleigh Fundamental	100
67.	Overlay of the Interpreted Group Velocity of Rayleigh higher mode	101
68.	Overlay of the Interpreted Attenuation of Rayleigh Fundamental ..	102
69.	Overlay of the Interpreted Attenuation of Rayleigh Higher mode...	103
70.	Comparison of Array Group Velocity with PMF at 65 Meters	106
71.	Comparison of Array Group Velocity with PMF at 70.5 Meters	107
72.	Comparison of Array Group Velocity with PMF at 75 Meters	108
73.	Comparison of Array Group Velocity with PMF at 80 Meters	109
74.	Comparison of Array Group Velocity with PMF at 85 Meters	110
75.	Comparison of Array Group Velocity with PMF at 90 Meters	111
76.	Comparison of Array Group Velocity with PMF at 94.5 Meters	112
77.	PMF Extracted Love Waves from 65m SWIG Data.....	115
78.	MFT Processing of PMF Extracted Love Waves at 65m	116
79.	MFT Processing of PMF Extracted Love Waves at 70.5m	117
80.	MFT Processing of PMF Extracted Love Waves at 75m	118
81.	MFT Processing of PMF Extracted Love Waves at 80m	119
82.	MFT Processing of PMF Extracted Love Waves at 85m	120
83.	MFT Processing of PMF Extracted Love Waves at 90m	121

Figure		Page
84.	MFT Processing of PMF Extracted Love Waves at 94.5m	122
85.	P-omega Stacking of 65 Meter SWIG Data(Nray=100).....	124
86.	P-omega Stacking of 65 Meter SWIG Data(Nray=40).....	125
87.	P-omega Stacking of 5 Meter SWIG Data.....	127
88.	P-omega Stacking of 35 Meter SWIG Data.....	128
89.	Interpreted Love Wave phase Velocity at 5, 35 and 65 Meters.....	129
90.	P-omega Stacking of 5 Meter Betsy Data	130
91.	P-omega Stacking of 35 Meter Betsy Data	131
92.	P-omega Stacking of 65 Meter Betsy Data	132
93.	Interpreted Rayleigh Wave Phase Velocity at 5, 35 and 65 Meters	134
94.	Raypaths for 2 Layer Model with Time-Distance Curves (Telford).	138
95.	Raypaths for 3 Layer Model with Time-Distance Curves (Telford).	139
96.	Instrument Corrected 5m Betsy with Refraction Analysis Marked..	141
97.	Instrument Corrected 35m Betsy with Refraction Analysis Marked	142
98.	Instrument Corrected 65m Betsy with Refraction Analysis Marked	143
99.	Instrument Corrected 5m SWIG with Refraction Analysis Marked .	144
100.	Instrument Corrected 35m SWIG with Refraction Analysis Marked	145
101.	Instrument Corrected 65m SWIG with Refraction Analysis Marked	146
102.	65m Betsy Inversion for Shear Velocity.....	151
103.	65m Betsy Inversion for Shear Q Inverse	152
104.	Comparison of Observed to Predicted Gamma for 65m Betsy Inversion.....	153
105.	Comparison of Observed to Predicted Group and Phase Velocities for 65m Betsy Inversion	156

Figure		Page
106.	65 Meter SWIG Data Phase Velocity/Gamma Inversion for Shear Velocity Structure	157
107.	65 Meter SWIG Data Phase Velocity/Gamma Inversion for Q Structure.....	158
108.	65 Meter SWIG Data Observed Versus Predicted Phase Velocity after Final Inversion.....	159
109.	65 Meter SWIG Data Observed Versus Predicted Attenuation Coefficients after Final Inversion	160
110.	65 Meter SWIG Data Group Velocity/Gamma Inversion for Shear Velocity Structure	161
111.	65 Meter SWIG Data Group Velocity/Gamma Inversion for Q Structure.....	162
112.	65 Meter SWIG Data Observed Versus Predicted Group Velocity After Second Inversion	163
113.	65 Meter SWIG Data Observed Versus Predicted Group Velocity After Third and Final Inversion	164
114.	65 Meter SWIG Data Observed Versus Predicted Attenuation Coefficients after Final Inversion	165
115.	65 Meter SWIG Data Combined Group and Phase Velocity/Gamma Inversion for Shear Velocity Structure.....	167
116.	65 Meter SWIG Data Combined Group and Phase Velocity/Gamma Inversion for Q Structure.....	168
117.	65 Meter SWIG Data Observed Versus Predicted Group and Phase Velocity after Final Inversion	169
118.	65 Meter SWIG Data Observed Versus Predicted Attenuation Coefficients after Final Inversion of Group Velocity, Phase Velocity and Gamma	170
119.	Unfiltered Love Wave Synthetic	174
120.	Love Wave Synthetic with Low Cut Filter at 10 Hz.....	175

Figure		Page
121.	Love Wave Synthetic with Low Cut Filter at 20 Hz (Triangular Source Width 40 msec)	176
122.	Love Wave Synthetic with Low Cut Filter at 20 Hz (Triangular Source Width 8 msec)	177
123.	Rayleigh Wave Synthetic of Fundamental Mode Only	178
124.	Rayleigh Wave Synthetic of First Higher Mode Only.....	179
125.	Rayleigh Wave Synthetic of Fundamental and First Higher Mode .	180
126.	MFT Analysis at 5.0 Meters for Betsy Data	191
127.	MFT Analysis at 10.0 Meters for Betsy Data.....	192
128.	MFT Analysis at 15.0 Meters for Betsy Data	193
129.	MFT Analysis at 20.0 Meters for Betsy Data	194
130.	MFT Analysis at 25.0 Meters for Betsy Data	195
131.	MFT Analysis at 30.0 Meters for Betsy Data	196
132.	MFT Analysis at 34.5 Meters for Betsy Data	197
133.	MFT Analysis at 35.0 Meters for Betsy Data	198
134.	MFT Analysis at 40.0 Meters for Betsy Data	199
135.	MFT Analysis at 45.0 Meters for Betsy Data	200
136.	MFT Analysis at 50.0 Meters for Betsy Data	201
137.	MFT Analysis at 55.0 Meters for Betsy Data	202
138.	MFT Analysis at 60.0 Meters for Betsy Data	203
139.	MFT Analysis at 64.5 Meters for Betsy Data	204
140.	MFT Analysis at 65.0 Meters for Betsy Data	205
141.	MFT Analysis at 70.0 Meters for Betsy Data	206
142.	MFT Analysis at 75.0 Meters for Betsy Data	207

Figure		Page
143.	MFT Analysis at 80.0 Meters for Betsy Data	208
144.	MFT Analysis at 85.0 Meters for Betsy Data	209
145.	MFT Analysis at 90.0 Meters for Betsy Data	210
146.	MFT Analysis at 94.5 Meters for Betsy Data	211

LIST OF TABLES

Table	Page
1. Previous McCormick Ranch Site Models	19
2. Acquisition Geometry of 6 Data Sets	33
3. Characteristics of Various Gaussian Filters	49
4. Betsy Data Refraction Analysis	147
5. Swig Data Refraction Analysis	147
6. Input Parameters for Synthetic Surface Wave Computations	171

LIST OF SYMBOLS

Symbol	Units	Notes
ρ	gm/cm ³	bulk density
α	m/sec	compressional velocity
β	m/sec	shear velocity
C	m/sec	phase velocity
U	m/sec	group velocity
λ	meters	wavelength
σ		Poisson's ratio
μ	dyne-cm/s ²	modulus of rigidity
K	dyne-cm/s ²	bulk modulus of elasticity
Q_{α}		compressional wave attenuation
Q_{β}		shear wave attenuation
ω	radians/s	angular frequency

LIST OF ABBREVIATIONS

DAS	Data acquisition subsystems
FFT	Fast fourier transform
MFA	Multiple filter analysis
PAF	Pseudo-autocorrelation function
PMF	Phase matched filter
SWIG	Shear Wave Impulsive Generator

ACKNOWLEDGEMENTS

I would like to express my appreciation to my advisor Professor Brian Stump who provided continuous guidance and support. Without his patience and persistence, I do not believe this thesis would have been completed. In addition, I would like to thank the other members of my committee, Gene Herrin, Bob Reinke, Tom Goforth and Dave Blackwell for their efforts in this study. Funding for this work was provided under Air Force Grant number AFOSR-84-0016 and AFOSR-89-0176.

I want to thank Bob Reinke for hosting Mark Bogaards, Brian Stump and myself in New Mexico for the original field data acquisition phase of this study. I appreciate the help of Bob Reinke, Kent Anderson, Robert Goerke and Mark Bogaards who all were instrumental in acquiring this first data set. I would also like to thank Craig Pearson, Karl Thomason and Brian Stump for providing me with the data sets that were used in the final processing for this project.

My thanks also go to Dr. Robert B. Herrmann of St. Louis University who provided the software and source code which were used to perform the processing used in this project.

Additionally, I would like to thank the staff and students for their friendship and support. It seems that any time I was bogged down, there was someone ready and willing to help, or provide some badly needed advice.

Lastly, I would like to thank my wife, Angela, for her patience during this time.

CHAPTER 1

INTRODUCTION

There has been increased interest in shear wave exploration in the past decade. A thorough knowledge of the weathered zone shear wave velocities can be used for static corrections in surface seismic applications (Mari, 1984). If the information on velocity structures extends deep enough, then the determined shear structure can be used directly in exploration. Shear and compressional velocities can be related to elastic parameters (Waters, 1981):

$$(1.1) \quad \begin{aligned} \beta &= \sqrt{\frac{\mu}{\rho}} = \text{shear velocity,} \\ \alpha &= \sqrt{\frac{K + 4/3\mu}{\rho}} = \text{compressional velocity,} \end{aligned}$$

where K is the bulk modulus of elasticity, ρ is the bulk density, and μ is the modulus of rigidity. Another common way of looking at material properties is through the use of Poisson's ratio which can be expressed in terms of shear and compressional velocities:

$$(1.2) \quad \sigma = \frac{\text{transverse strain}}{\text{longitudinal strain}} = \frac{\alpha^2 - 2\beta^2}{2\alpha^2 - 2\beta^2} = \text{Poisson's ratio.}$$

As a result, a knowledge of S-wave velocities can be used to determine elastic moduli of earth materials at shallow depths. This information has substantial engineering application (Kitsunczaki, 1980). For earthquake engineering, S-wave velocities are used for evaluation of transmission characteristics of the ground. This information in turn leads to knowledge of ground vibrations during earthquakes, which can be used to minimize earthquake damage. Elastic moduli determination through shear velocities is also used for site evaluation in civil engineering.

Modeling of shallow layers or the weathered zone has historically been accomplished with refraction surveys. Miller and Steeples (1990) have utilized reflection techniques to yield structure and compressional velocity as shallow as 30 meters. The refraction method works quite well for determining compressional wave velocities and layer thicknesses. Defining the S-wave velocity structure is not generally as easily accomplished. Since P-wave velocities are always faster than shear wave velocities, S-wave arrivals are always contaminated by compressional arrivals. An S-wave refraction technique could only work if a source generated shear waves without compressional waves or if the two wave-fields could be easily separated. It has historically been very difficult to generate shear waves without creating an interfering compressional disturbance. Picking the first arrival time on a shear wave thus very difficult because of this P-wave interference. Additional interference is caused by large amplitude surface waves or ground roll, which has a velocity similar to the shear velocity of the surface layer. This study will include data acquired with a new, clean SH energy source. Refraction processing of both P and SH data will be employed prior to an interpretation of the surface wave arrivals.

There is imaging information applicable to the near surface structure throughout the wavetrain of short array seismic data sets. The body wave portion includes reflection and refraction information. Most body wave techniques require the minimization of the surface wave portion of the wavetrain. The surface waves can be used separately to determine near surface material models. In this study, the body wave models will be compared to surface wave models. One technique that has been used successfully to determine shear velocity structures is the interpretation of surface wave dispersion curves. The technique involves measuring the surface wave velocity as a function of frequency or period. The measured surface wave dispersion is then related to shear velocity structure. A shear wave source is used to generate Love waves and a compressional source is used to generate Rayleigh waves. Both phase and group velocity dispersion curves from Love and Rayleigh waves will be analyzed. Relating dispersion curves to velocity structure is done with an iterative forward modeling technique or one of a number of inversion techniques. Both approaches will be utilized in this study.

A. Fundamental Principles

1. Surface Waves

Since the new aspect of this study is the interpretation of the surface wave portion of the wavefield, some fundamental concepts that deal with surface waves and surface wave propagation are introduced. Surface wave effects are confined closely to the free surface boundary. Rayleigh waves are a type of surface wave that are trapped near a free plane boundary. Rayleigh waves consist of a mixture of shear (SV) and compressional energy. For the theoretical case

of a half space, the velocity along the surface is independent of frequency and depends on the shear and compressional velocities or equivalently, Poisson's ratio. For a Poisson's ratio of 1/4, the speed of the Rayleigh wave is .9194 times the shear velocity. The particle motion at the surface is retrograde elliptical. The amplitude of motion decays away from the free surface as:

$$(1.3) \quad \text{Amp} = \exp(-r Z 2\pi/\lambda),$$

where r is a factor related to velocity and Z is depth. The amplitude decays more rapidly for small wavelengths or high frequencies. As a result, long wavelengths penetrate deeper below the boundary. In most normal weathered situations, velocities increase with depth. This velocity profile leads to the situation of normal dispersion in phase velocity, where long wavelengths have a greater phase velocity than short wavelengths.

Love waves are large amplitude trapped surface waves whose presence depends on near surface layering. Their presence makes the interpretation of shear wave (SH) reflection records difficult. A simple model for a Love wave can be illustrated by considering an SH wave propagating from a source, S , in a layer over a half space (Figure 1). The wave front velocity or phase propagation C_S , along the surface can be shown geometrically to be:

$$(1.4) \quad C_S = \beta_1 / \cos(\pi/2 - \theta),$$

where β_1 is the shear velocity in layer 1. The critical angle θ_c is:

$$(1.5) \quad \theta_c = \arcsin \beta_1/\beta_2.$$

where β_2 is the shear velocity in the halfspace. The larger the contrast for β , the smaller θ_c becomes. For any wave propagating with an angle equal to or greater than the critical angle, the wave will be trapped between the layer and the surface interfaces. No mode conversions will occur because only SH waves are considered. A phase shift dependent on the incident angle will occur at the layer interface, but there will be no phase change for SH at the free surface.

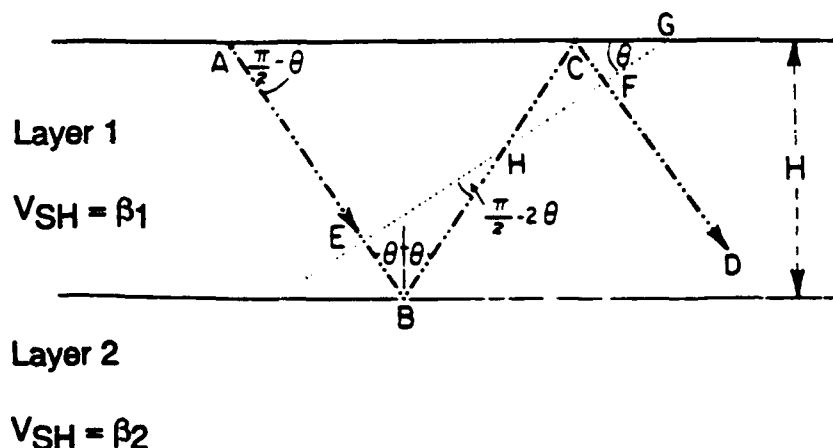


Figure 1. Geometric analysis of Love wave generation in layer over a half space (After Waters, 1981).

For waves of a constant frequency, there are points on the same wavefront, such as E and F (Figure 1), that constructively interfere if the distance EBCF is an integral multiple of the wavelength. If a constant phase change at the layer interface is assumed, it can be argued geometrically that the constructive modes will be dependent only on the wavelength and the angle of incidence.

As the wavelength or frequency changes, then θ must change to maintain constructive interference. Since equation (1.4) has already demonstrated that the phase velocity is dependent on θ , it follows that the phase velocity of this constructive interference changes with frequency. This frequency dependence of velocity, known as dispersion, causes the wave packet to spread out as it propagates. This dispersion is the reason that phase velocity and group velocity are not identical.

2. Phase and Group Velocity

The distinction between phase and group velocity is fundamental to the dispersion techniques utilized in this thesis. Velocity is simply the rate of propagation in a medium. Velocity, V , is proportional to the distance traveled D , divided by the time of travel Δt :

$$(1.6) \quad V = \frac{D}{\Delta t}.$$

Phase velocity is associated with the propagation velocity of a particular feature of the waveform, such as a peak or a trough (Waters, 1981). The term phase velocity refers to the effective velocity along the ground surface of a particular frequency. If observations are made at points sufficiently close together, the phase velocity C is simply the distance, ΔD , between observation points divided by the change in time of arrival of a particular phase, Δt :

$$(1.7) \quad C = \Delta D / \Delta t .$$

Phase velocity can also be thought of as the change in phase angle Θ , measured for the frequency f , over time, which would be proportional to angular frequency ω . This linear phase shift is proportional to a time delay:

$$(1.8) \quad \Delta t = \Theta(\omega) / \omega.$$

This results in:

$$(1.9) \quad C = D / \Delta t = \omega D / \Theta \approx 2 \pi f D / \Theta.$$

It has been previously shown that for some surface waves, the phase velocity is dependent upon frequency.

Group velocity can be defined as the velocity with which the energy associated with a narrow band of frequencies has traveled. Group velocity is a function of frequency, the velocity of the media, and the thickness of the layering. The group velocity U for a given period T , is related to the phase velocity, C :

$$(1.10) \quad U(T) = C + k \frac{dC}{dk},$$

where $k = \text{wave number} = 2\pi/CT$.

In its simplest form, group velocity is inversely proportional to the time for a delta function signal to travel from a source to a receiver. If there is no dispersion or variation in velocity with frequency or period, then the group and phase velocities are identical. Even with dispersion, the group velocity can be deter-

mined with only one seismometer, since the group velocities can be calculated by the simple equation:

$$(1.11) \quad U(T) = \frac{D}{\Delta t}.$$

Figure 2 displays group and phase velocities as a function of frequency for Rayleigh waves generated from a plane layered model. The model was derived from P and SH wave refraction analysis of data acquired for this study. The Q values utilized were those from the Grant (1988) model (Table 1). The top two curves are the first higher mode. The higher velocity curve in each pair is the phase velocity, while the lower curve is the group velocity. Since the group velocity is related by a derivative to the phase velocity (equation 1.10), the resulting group velocity curve is less smooth than the corresponding phase velocity curve.

3. Dispersion Analysis Using Paper Records

One of the earliest techniques for determining group velocity of dispersed surface waves was known as the peak and trough technique. Press (1956) documents how this procedure was employed. He would make use of the paper records of the Rayleigh wave primary mode arrival from one earthquake on a single seismic recording station. The individual cycles were measured to yield the period T, to be used with the known distance D and measured Δt or travel time from the epicenter. This process could be repeated for a series of periods to obtain the group velocity dispersion curve. This group velocity would be a function

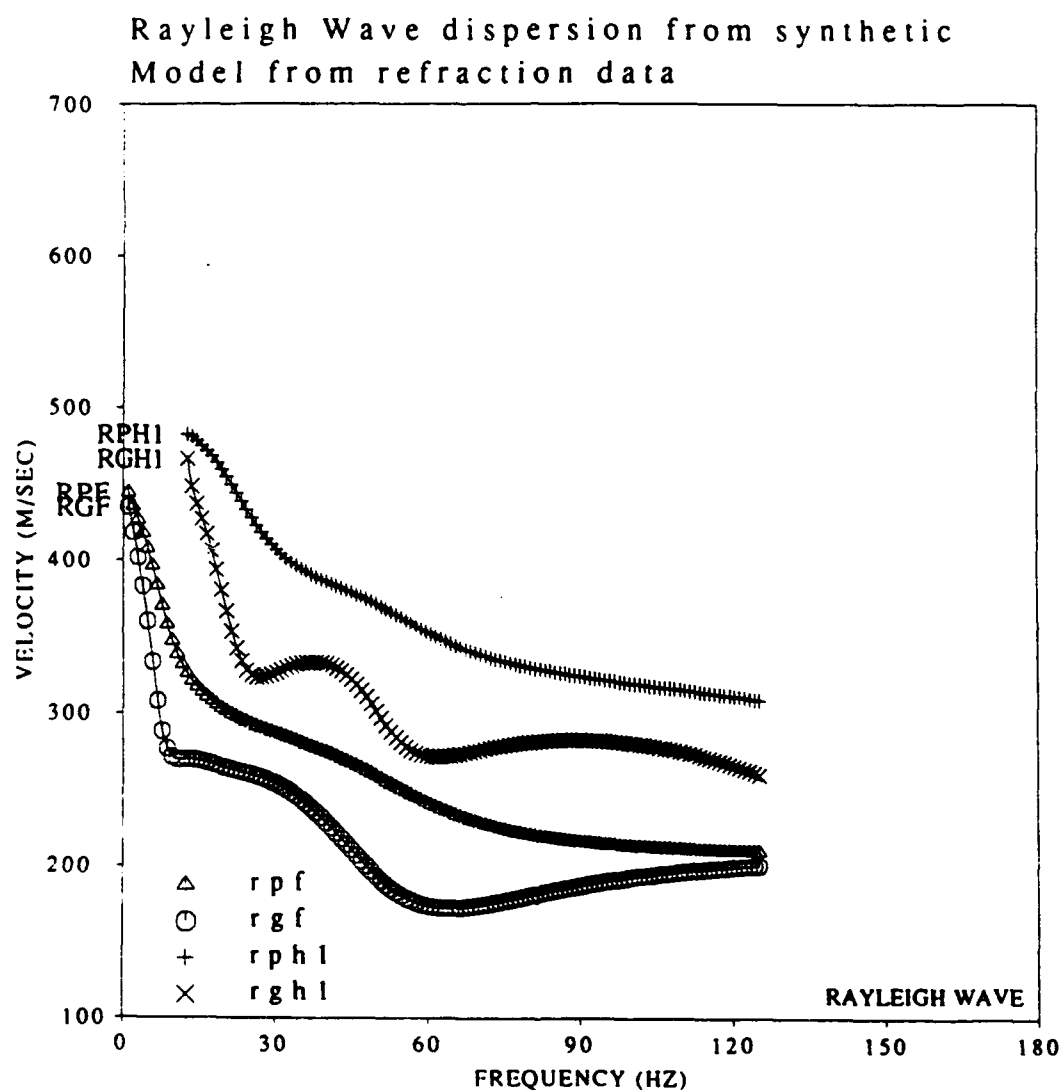


Figure 2. Rayleigh wave dispersion curves from a plane layered synthetic model. Curves from top to bottom are: RPH1, Rayleigh wave phase velocity, higher mode 1. RGH1, Rayleigh wave group velocity, higher mode 1. RPF, Rayleigh wave phase velocity, fundamental mode. RGF, Rayleigh wave group velocity, fundamental mode.

of the average velocities of the crust between the point of origin for the earthquake and the recording station. To determine local variations, it is necessary to use the phase velocity. At least two receivers must be utilized to calculate phase velocity. The peak and trough technique for phase velocity determination was also documented by Press (1956). This method can best be understood by using two recordings along a great circle path from the epicenter of an earthquake. If the two stations are within one wavelength of each other, the two seismograms of the Rayleigh wave portion can be aligned in time and then carefully compared. The peaks and troughs that are the same can be compared for time differences. The time difference is Δt and the distance D can be measured along the great circle path. The period T is measured as before, by the length of the cycle. The actual implementation, in practice, is slightly more complicated since the earthquakes and seismometers do not normally fall conveniently on a great circle path. Three stations and some simple geometry are used to make the actual phase velocity calculations. The final dispersion curve can be used as before to make inferences about the crustal structure, but the horizontal extent is much smaller than before.

The analysis of the dispersion results was done by computing theoretical phase velocity curves from measured group velocities using equation (1.10). These group velocities were interpreted to be the results of the average structure and average elastic constants over a long distance. The measured phase velocities were then compared to these predicted curves. Any differences were interpreted to be due to local variations in crustal thickness.

4. Dispersion Analysis Using Moving Window Technique

The previous technique was utilized before the widespread availability of digital computers and the advent of the FFT. The peak and trough technique would not work well under conditions of low signal to noise ratio or if the signal was otherwise obscured. Microseisms or long period drifts may obscure the signal. Additionally, several dispersive modes or several branches of the same mode may appear simultaneously at the recording site.

The moving window analysis (Landisman et al., 1969) can be used to measure group velocities in recordings of multi-mode propagation. The time and distance measured from the earthquake epicenter yield a group velocity for a point on the time series. A section of the time series centered around this point or group velocity is extracted by windowing with a boxcar in the time domain. The extracted data is then windowed again with a symmetrical weighting function such as \cos^2 in the time domain. Windowing the second time reduces the ringing or Gibb's phenomena in the frequency domain. The symmetrical nature of the weighting function emphasizes the center of the window which most closely corresponds to the current time or group velocity of interest. The next stage of moving window analysis involves the Fourier transformation of the windowed data and the presentation of instantaneous amplitude in dB versus period. This process is continued over time or group velocity. The window is of variable length in order to maintain the same frequency resolution at all periods. After complete analysis a plot is generated on which equal energy contours are drawn as shown in Figure 3. Figure 3 contains moving window analysis of fundamental mode Rayleigh wave data from a study by Simila (1982) in the same

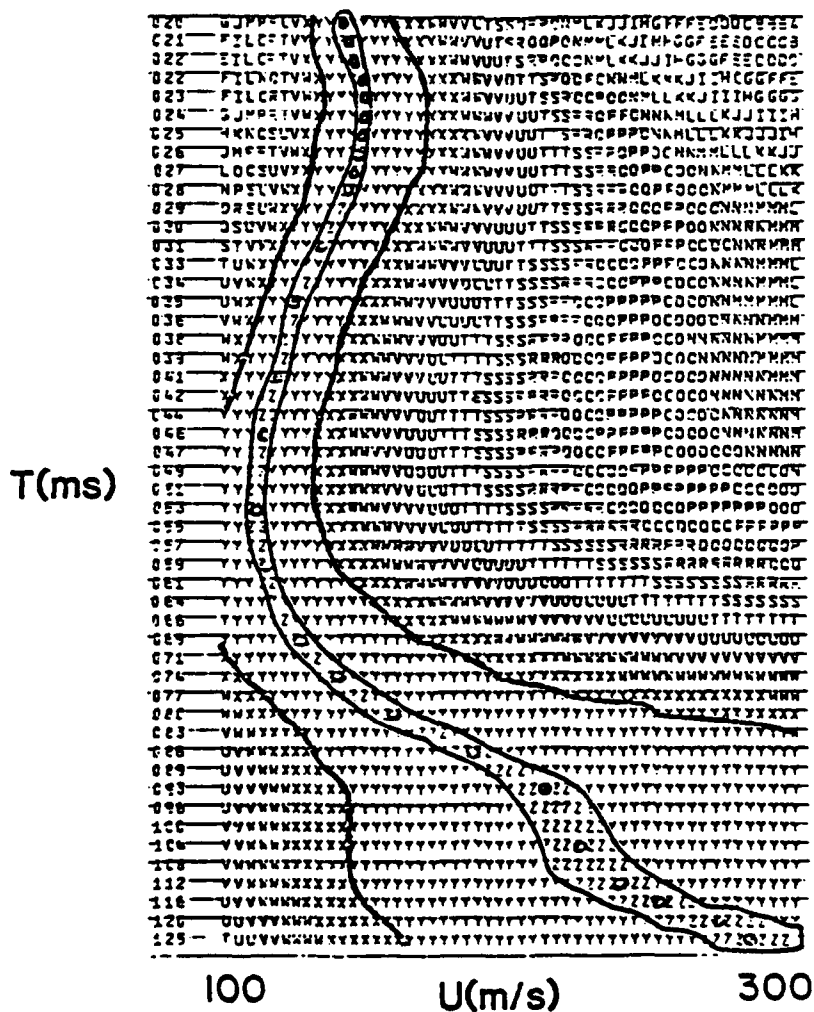


Figure 3. Moving window analysis (Simila, 1982). Group velocity analysis of Rayleigh wave data at McCormick Ranch. T is period in milliseconds, U is group velocity in m/s.

area as this thesis. The hand drawn circles through the maximum energy at each period and velocity define the group velocity or dispersion curve.

5. Inversion Fundamentals

Forward modeling is defined (Menke, 1989) as the process of predicting the results of measurements on the basis of some general principle or model and a set of specific conditions relevant to the problem at hand. Inverse theory tackles the reverse problem, starting with measured data and a general principle or model, it determines estimates of the model parameters. An example of inverse theory or inversion would be determining a velocity from a given set of time offset pairs. For a presumed constant velocity, the problem would be to fit a straight line through a series of points. With real data, in general, the points would not all fall exactly on a line. Part of inverse theory would involve deriving a best fit of a model to the data.

The physical properties that can be dealt with using inversion techniques fall into two general classes. The first category would be properties that can be described by discrete parameters and the second class would be those that are described by continuous functions. This paper will deal with discrete inverse theory or parameters that are truly discrete or that can be approximated as discrete. The parameters that are determined in this thesis are assumed to have a finite quantity of numerical values. The earth will be assumed to be composed of several discrete layers that can be represented by fundamental parameters, including velocity, density and Q or attenuation. The data used to determine these parameters will be the surface wave phase and group velocity dispersion curves introduced earlier.

One of the most easily understood forms of inverse problems is the linear equation:

$$(1.12) \quad G m = d,$$

where d is a vector of the data, m is a vector or matrix of the model parameters being estimated and G is the data kernel. This equation is at the heart of most discrete inverse theory. Inversion is generally an iterative technique where this equation can be worked backwards based on the estimated model parameters m^{est} to yield the predicted data $d^{pre} = G m^{est}$. The frequently used least squares solution is a technique to pick model parameters that force the predicted data to be as close as possible to the observed data. An error or misfit for each observation can be defined as:

$$(1.13) \quad e_i = d_i^{obs} - d_i^{pre}.$$

The best fit line is then the one with the smallest summed squared error E , defined as:

$$(1.14) \quad E = \sum_{i=1}^N e_i^2.$$

This technique is common for deriving a best fit line to a series of points. A non-linear problem can be solved by approximating it as a linear problem. The model can be slightly perturbed, and the comparison of the predicted data to that

observed can be checked. An estimate of the improved fit can be made as well as iterative changes to the model. As with most iterative schemes, large perturbations can lead to either overshoot or undershoot. The perturbation of the model can be done using a partial derivative approach, which is effectively the relationship between the changes of two parameters. The inversion techniques used in this thesis are based upon the principles documented in this section.

B. Previous Work

The basic technique of using surface wave dispersion to model shear velocity structures has been used by several groups. Mooney and Bolt (1966) calculated theoretical group and phase velocity dispersion curves for Rayleigh waves under varying conditions of shear velocity contrast for a layer over a half space. Included in their numerical exercise was a model for a shallow alluvium site that included the calculation of the fundamental as well as the first and second higher modes. The results indicated that periods of up to 2 seconds would be required to image 100 meters of alluvium or a 0.5 second period to image 25 meters.

Mari (1984) used Love wave phase velocity measurements to obtain static corrections. He generated Love waves with the Marthor source, which is a high energy shear impulsive source. This study utilized exploration seismology phones, as well as normal exploration seismology source and receiver spreads. The source-receiver spacings ranged from 250 to 490 meters. The results were generated using frequencies from 5 to 20 Hz to yield surface layer thicknesses of 6 to 10 meters and phase velocities of 140 to 210 m/s. This study built on the previous numerical analysis of Mooney and Bolt (1966). Mari assumed a layer

over a half space model, and interpreted his slowest velocity as the shear velocity for the layer and the fastest velocity as the velocity for the half space or substratum.

Cherry et al. (1979) used Rayleigh wave group velocities to create a shear model. This study used a weight drop source and a linear array with receivers spaced 500 meters apart over the interval 1 to 5.5 km. Surface wave velocities ranged from 400 to 700 m/s. Frequencies between 2 and 20 Hz were used to invert for shear structure to 500 meters. Mokhtar et al. (1988) used phase and group velocity dispersion to invert for shallow crustal structure. Rayleigh wave frequencies between 1 and 20 Hz were used to image the top 1 to 2 km of the crust. The source receiver spacings were 55 to 80 km and yielded phase velocities in the range of 2.8 to 3.4 km/s. Velocities were determined with linear inversion software developed by the authors. The same software is utilized in this thesis.

Surface wave investigations have been completed over a wide range of length and frequency scales. Press (1956) studied crustal structure with thicknesses from 15 to 50 km using Rayleigh wave phase velocity dispersion from periods of 10 to 40 seconds (wavelengths from 50 to 100 km). The Press (1956) study can be contrasted to the study of Stokoe and Nazarian (1984), who also used Rayleigh wave phase velocity dispersion. This work was to determine shear velocities in concrete runways approximately ten inches thick. This remarkable range of scale can be achieved by utilizing data of different wavelengths.

C. Test Site

This study will utilize seismic data acquired in a manner similar to a normal refraction survey. The test site is the McCormick Ranch area, which is south of Albuquerque, New Mexico. This area is a relatively flat region at the base of the Sandia Mountains. The subsurface geology consists of dry alluvium down to the water table at approximately 75 meters. Caliche is present in the test site and has been exposed during some high explosive test shots. The layers of alluvium are assumed to be horizontally stratified and laterally homogenous. Some of the previous work on this test site includes a study by Grant (1988), who performed a source characterization study in the area using small explosives sources which required some knowledge of the near surface structure. Additional studies performed in the area which characterized the shallow structure includes Stump and Reinke (1982) and Reinke and Stump (1988). Bogaards (1989) used model based spectral analysis techniques to generate dispersion curves for surface waves utilizing similar acquisition techniques to the current study. Two previous models for the McCormick ranch study area are summarized in Table 1.

Simila (1982) used Rayleigh wave group velocities to model velocity structures in shallow (less than 25 meters) structures at McCormick Ranch. He utilized explosive sources to generate the Rayleigh waves. The dispersion analysis incorporated single phone processing at distances ranging from 6.55 to 228.6 meters. The processing included the moving window analysis technique for frequencies from 5 to 25 Hz for the fundamental mode and 25 to 50 Hz for the first higher mode. This thesis will extend Simila's work. New processing schemes are available to analyze arrays of data for both group and phase velocity. New

equipment is now available that makes it more practical and economical to acquire an array of data, as opposed to the single phone acquisition used in the Simila study. A new shear source makes it possible to generate shear data and a resulting Love wave. The final extension of this work, as proposed by Simila, will be the use of inversion techniques, instead of relying on a trial and error forward modeling method.

D. Overview of the Thesis

The seismic data acquisition for this study will be discussed at length in Chapter 2. The processing techniques for deriving dispersion curves and analysis of the results are contained in Chapter 3. Chapter 4 covers inversion of the dispersion data and refraction data for velocity structures. Chapter 5 summarizes this work and includes recommendations for further study.

Table 1
PREVIOUS MCCORMICK RANCH SITE MODELS

Grant (1988) Model

	α (m/s)	β (m/s)	ρ (gm/cm ³)	Q_α	Q_β	Depth(m)
Layer 1	270	120	1.8	10	4	0.0
Layer 2	670	230	1.9	50	22	3.0
Half space	930	360	2.0	100	44	19.0

Stump-Reinke 1982 Model

	α (m/s)	β (m/s)	ρ (gm/cm ³)	Q_α	Q_β	Depth(m)
Layer 1	366	244	1.8			0.0
Layer 2	671	366	1.9			3.4
Layer 3	823	366	2.0			13.4
Half space	1128	610	2.1			24.0

Where: α = P-wave velocity in m/sec

β = S-wave velocity in m/sec

ρ = density in gm/cm³

Q_α = P-wave attenuation

Q_β = S-wave attenuation

CHAPTER 2

FIELD DATA ACQUISITION

The seismic data utilized in this study was acquired by Pearson and Stump of SMU. The acquisition hardware was fully documented by Stump et al. (1991). The intent for this study was to generate two types of surface waves, both Rayleigh and Love waves. The seismic data were acquired in two parts with a different source in each case. The P-SV data set was acquired utilizing a commercially available source, the Betsy Seisgun* (Figure 4). The Betsy is effectively a shotgun with the barrel pointing down at the ground. The source is an eight gauge shotgun shell with a single solid lead or iron slug. A tire at the base of the source is used to muffle airblast. There are a number of advantages to using the Betsy for this type of study. The source is relatively portable, simple and inexpensive to operate, and is capable of generating a repeatable signature. This source is relatively low energy, but is capable of generating sufficient energy for the 100 meters of maximum source-receiver offset acquired for this study. Frequency content of this source is in excess of 200 Hz, although the data acquired at McCormick Ranch had somewhat less bandwidth due to the highly attenuative nature of the media. The Betsy generates a good compressional wavefield, and for this study a significant Rayleigh wave.

*Note: Betsy Seisgun is a registered trademark of Betsy Seisgun, Inc.

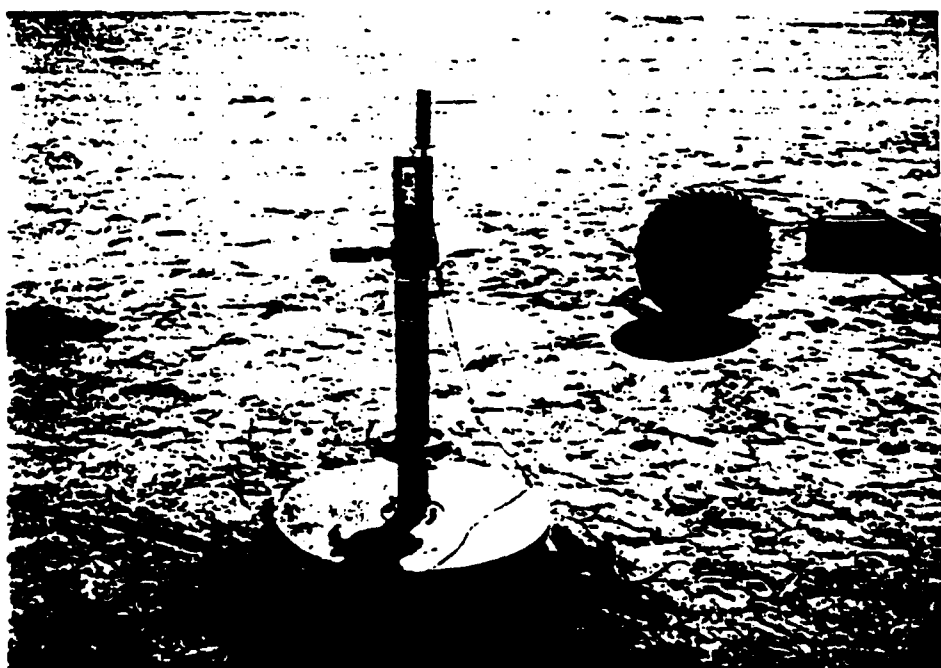


Figure 4. Betsy source (Stump et al., 1991)

The second source was the SMU fabricated SWIG, which stands for Shear Wave Impulsive Generator. The SWIG is a modification of a source described by Liu et al. (1988). The SWIG (Figure 5) is a pneumatic ram mounted between two channels that is weighed down by a pickup truck. The SWIG is oriented perpendicular to the source-receiver plane. One side of the piston is evacuated to the outside air and the high pressure side drives the mass horizontally until it impacts an anvil at the end of the SWIG. This impact produces a wavefield with particle motion perpendicular to the direction of propagation from the source to the geophones.

The SWIG provides a very clean SH wavefield. In the test site for this study, the source generated a very distinct Love wave along with the shear wavefield. Figures 6 and 7 show the SH and P first arrivals respectively. It can be seen that there is no arrival corresponding to the P first arrival from the Betsy source occurring on the SWIG data set. This uncontaminated shear wavefield will be used in refraction calculations to determine shear velocity structure as well as for Love wave dispersion analysis.

The data was acquired sixty channels at a time. The recording instruments were six channel Refraction Technology data acquisition subsystems (DAS), time synchronized through a radio telemetry system. In this study, 10 of the DAS were deployed. 1000 samples at 1 msec sample interval were recorded for all data sets. The DAS have a 16 bit analog to digital converter with an effective dynamic range of 90 dB. The system has 7 selectable gains from 1 to 8192. The geophones were Mark Products, Inc. L-410H's. The geophones have a corner frequency of 10 Hz and a damping of 0.6.(Figure 8). Sixty horizontal geophones were oriented transverse to the propagation path for the SWIG

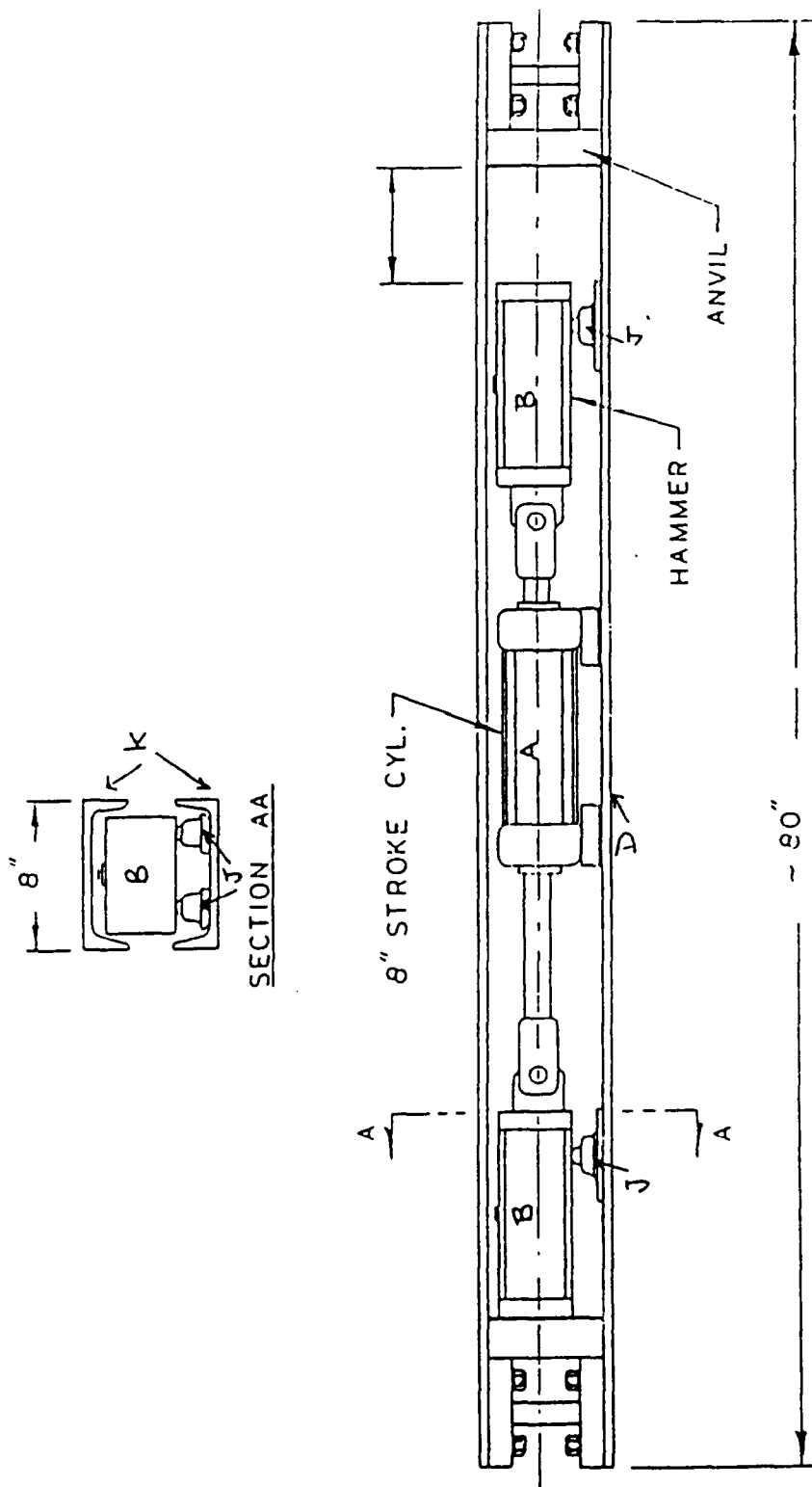


Figure 5. Side and end view of SWIG source (Stump, et al. 1991)

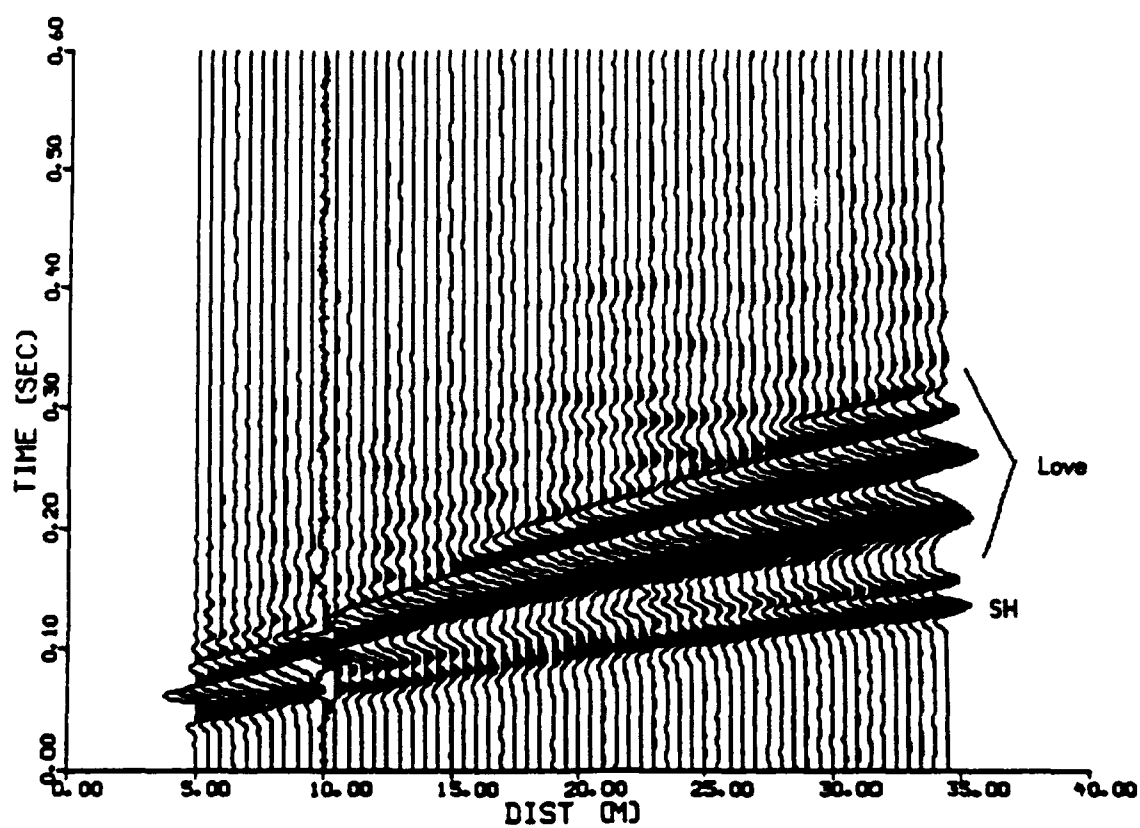


Figure 6. Swig data with source offset at 5.0 meters from the nearest receiver.

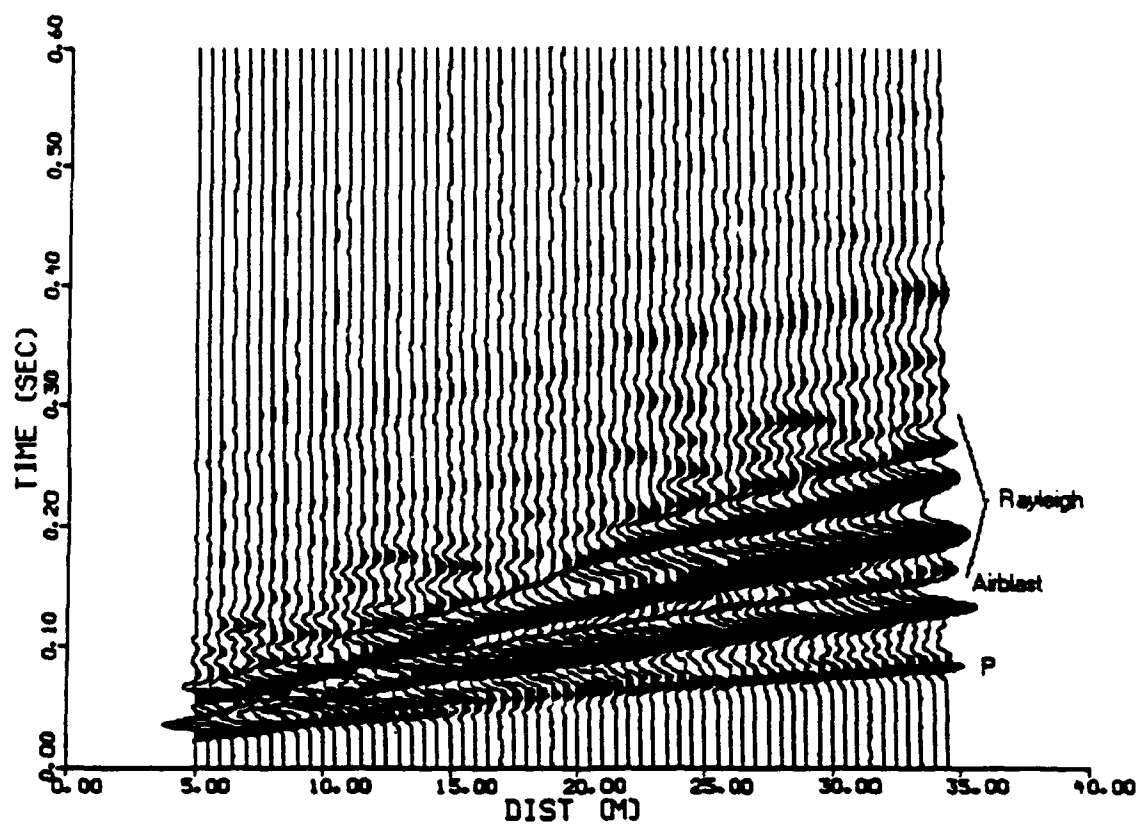


Figure 7. Betsy data with source offset at 5.0 meters from the nearest receiver.

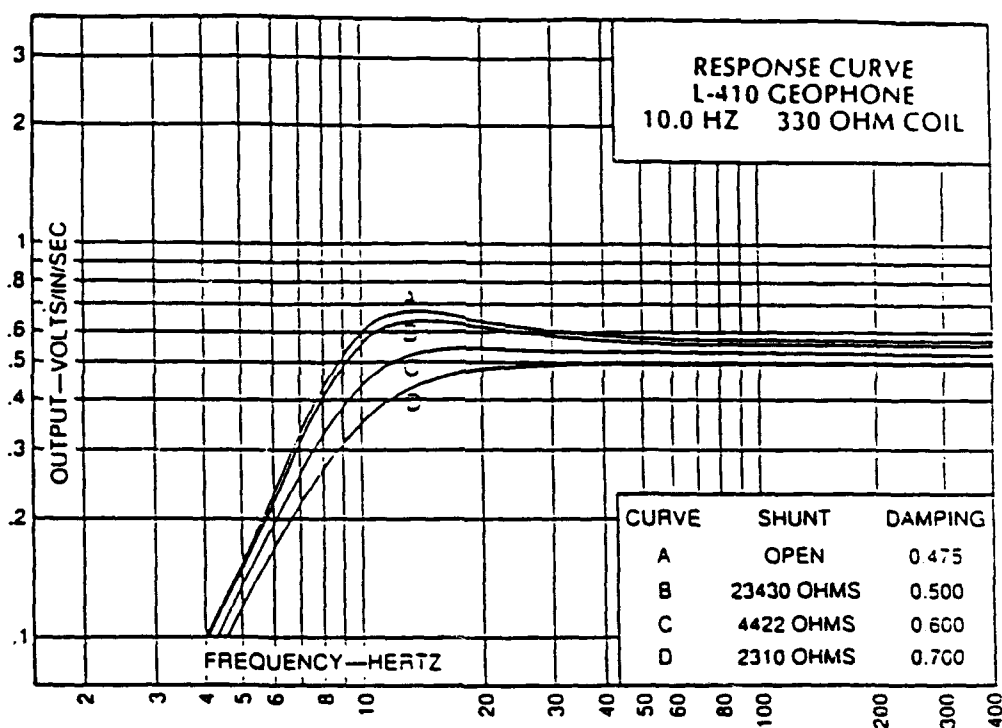


Figure 8. Instrument response of L-410 geophones used in this study.

source and sixty phones were oriented vertically for the Betsy source. Figure 9 illustrates the acquisition layout. Both the SWIG (Figure 6) and Betsy (Figure 7) data sets were acquired with the geophones spaced at one half meter increments and covering the range from 5 to 34.5 meters. The sources were moved by 30 meters so that source-receiver coverage was extended to 35-64.5 meters. This data is plotted as Figure 10 for the SWIG source and Figure 11 for the Betsy. The sources were moved one more time to extend the coverage from 65 to 94.5 meters. The final data sets are plotted in Figure 12 for the SWIG source and Figure 13 for the Betsy source. The acquisition geometry of the 6 data sets are summarized in Table 2. The different arrays of data acquired in this study are identified by the spacing between the source and the nearest receiver.

The spectral data at 5 meter increments for the SWIG source are reproduced in Figure 14. These spectra with a spectral peak near 25 Hz and data above the background noise to beyond 100 Hz demonstrate the broad band nature of the source. The low Q materials in the formations cause the higher frequencies to lose amplitude fairly rapidly. The observed spectra are not smooth, but show notches which are apparently a result of propagation path effects. The first hole in the spectra occurs at 68 Hz in the 5 meter data and then decreases to 57 Hz at 10.5 meters, 40 Hz at 15 meters and even lower with increasing range. The decreasing frequency of this interference hole with increasing range may represent an increasing time separation of two interfering signals with range.

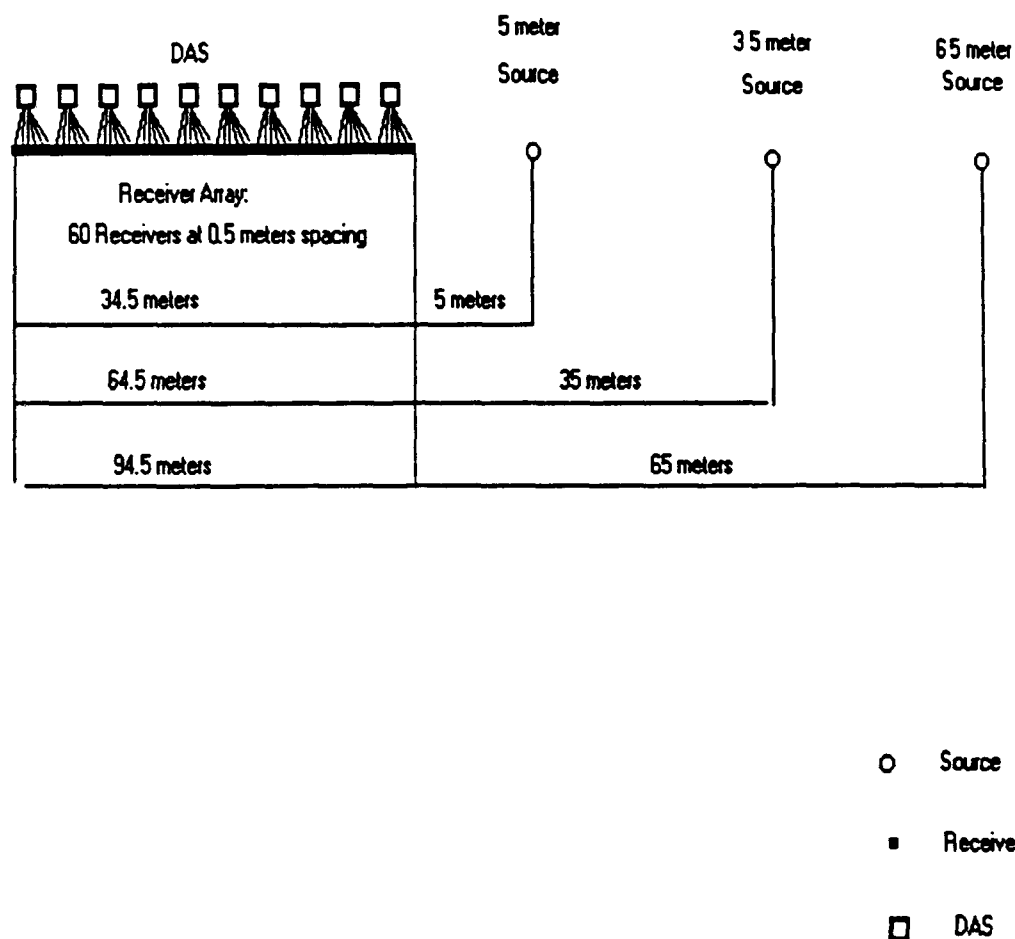


Figure 9. Acquisition geometry for both SWIG and Betsy data sets. Sources were located at 3 positions: 5, 35 and 65 meters from the near geophone. Note the distances from the far geophones. The far phone for the 5 meter data set is 34.5 meters, almost identical to near phone distance for next source at 35.0 meters although the geology sampled by the paths is quite different.

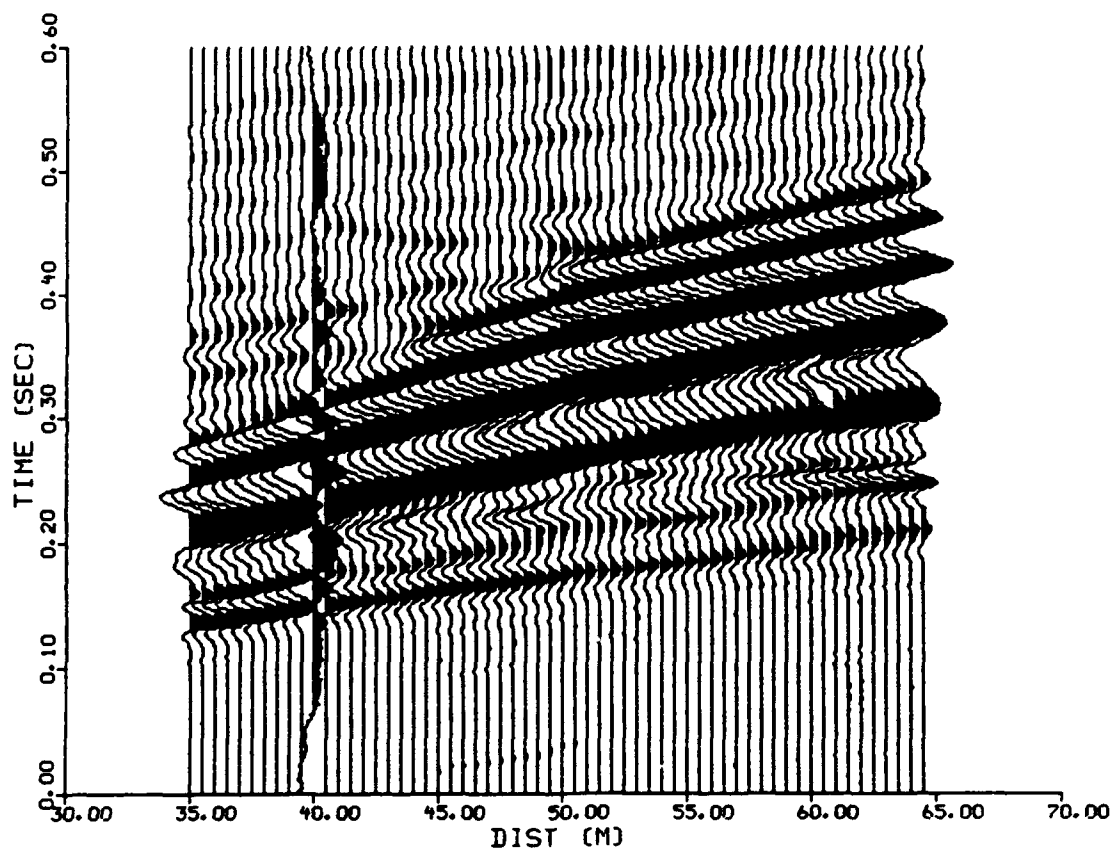


Figure 10. Swig data with source offset at 35.0 m from near receiver.

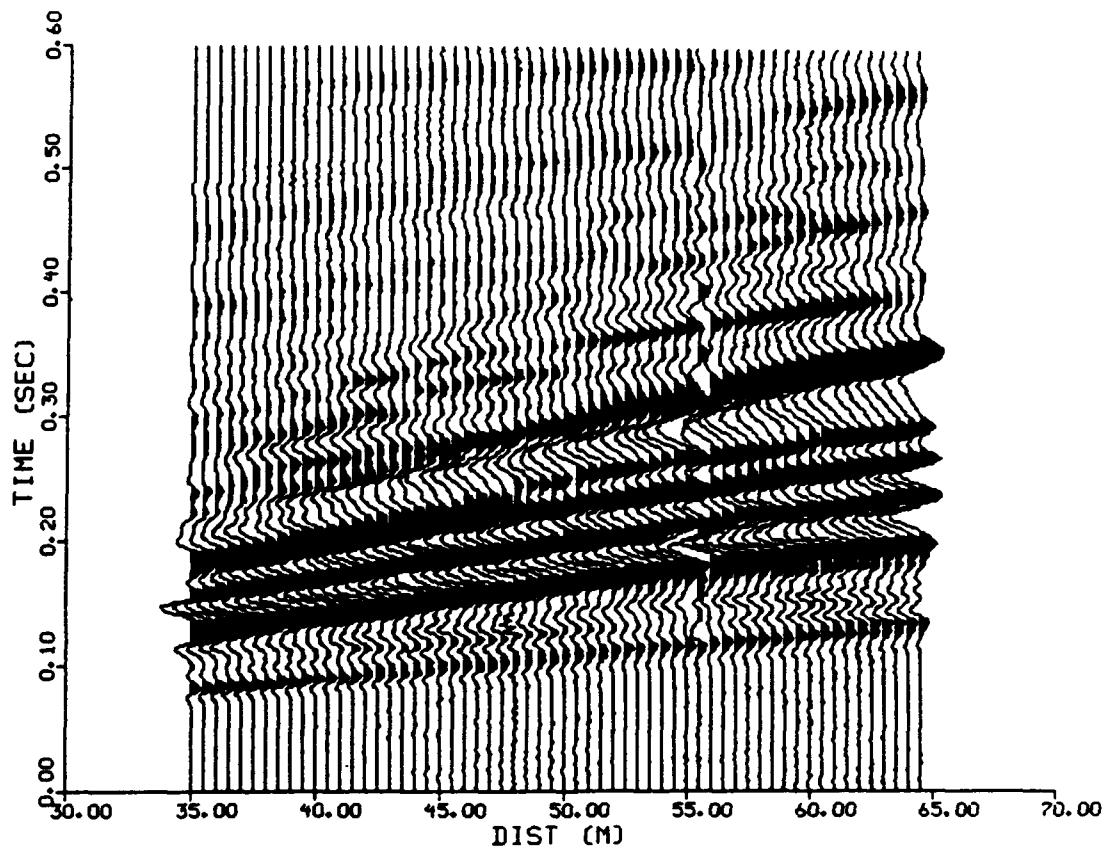


Figure 11. Betsy data with source offset at 35.0 m from near receiver.

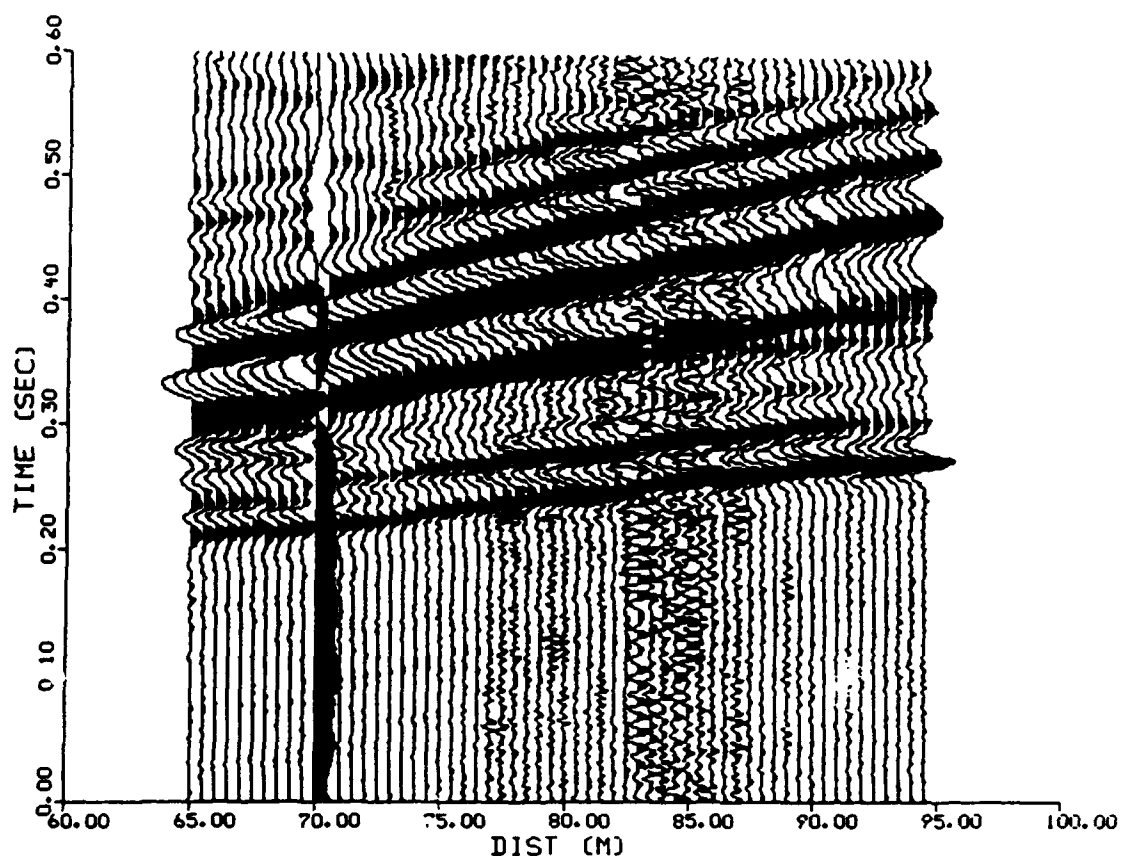


Figure 12. Swig data with source offset at 65.0 m from near receiver.

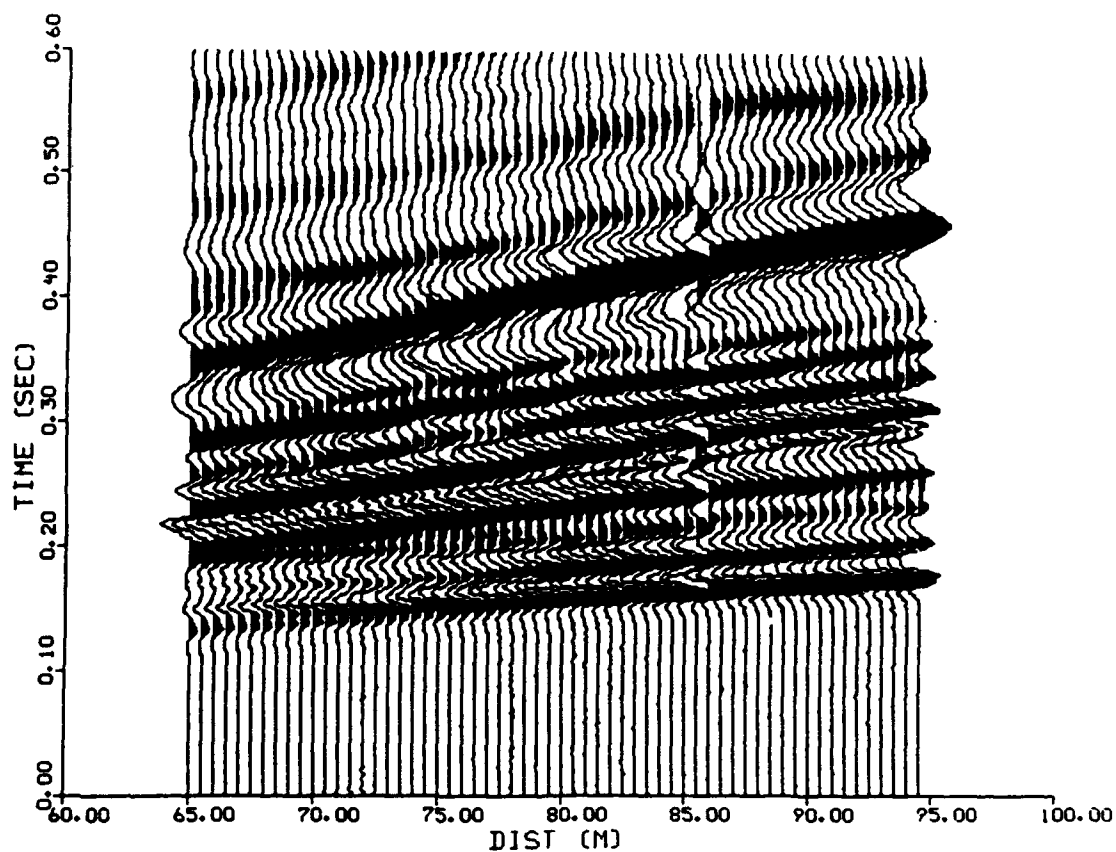


Figure 13. Betsy data with source offset at 65 m from near receiver.

Table 2

ACQUISITION GEOMETRY OF 6 DATA SETS

Data set name	Source	Receivers
5 meter SWIG	SWIG located 5 meters from nearest receiver	60 transverse oriented geophones in linear array spaced at 0.5 meter increments over interval 5.0 to 34.5 meters.
35 meter SWIG	SWIG located 35 meters from nearest receiver	60 transverse oriented geophones in linear array spaced at 0.5 meter increments over interval 35.0 to 64.5 meters.
65 meter SWIG	SWIG located 65 meters from nearest receiver	60 transverse oriented geophones in linear array spaced at 0.5 meter increments over interval 65.0 to 94.5 meters.
5 meter Betsy	Betsy located 5 meters from nearest receiver	60 vertical oriented geophones in linear array spaced at 0.5 meter increments over interval 5.0 to 34.5 meters.
35 meter Betsy	Betsy located 35 meters from nearest receiver	60 vertical oriented geophones in linear array spaced at 0.5 meter increments over interval 35.0 to 64.5 meters.
65 meter Betsy	Betsy located 65 meters from nearest receiver	60 vertical oriented geophones in linear array spaced at 0.5 meter increments over interval 65.0 to 94.5 meters.

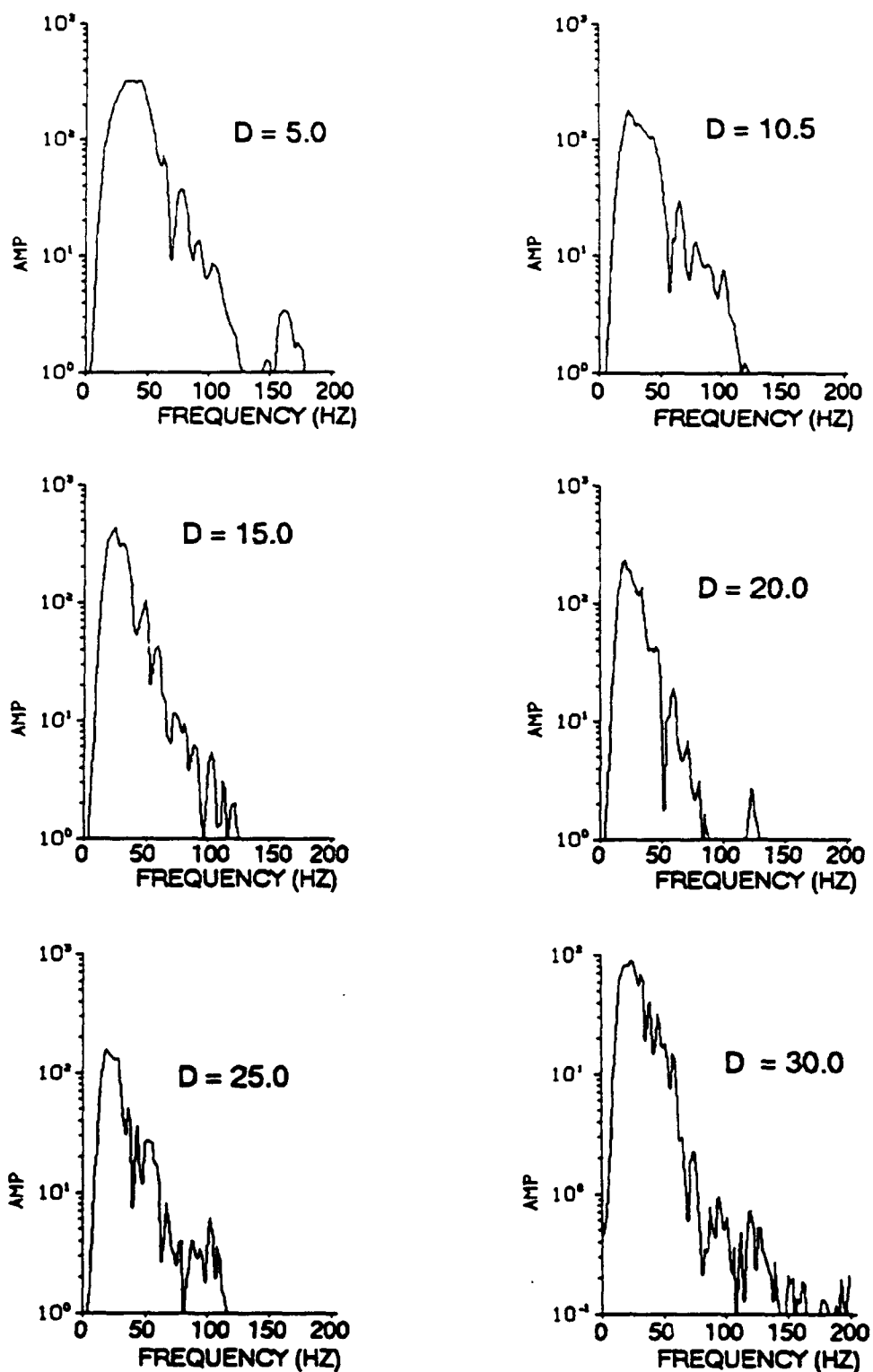


Figure 14. Spectral Response of single receiver SWIG data from 5 to 30 meters. Clockwise from upper left, 5 meters, 10 meters, 20 meters, 30 meters, 25 meters, 15 meters.

CHAPTER 3

DATA PROCESSING FOR SURFACE WAVE DISPERSION

The data processing was done on a Sun 3/60 workstation in the SMU geophysics lab. The processing primarily utilized a system of programs developed as an ongoing project by Robert Herrmann of St. Louis University. This package contains interrelated programs which allowed the output from one program to be used as input to another. The software descriptions throughout this section will describe the Herrmann implementations of the various techniques.

A. Pre-processing of field data

The field data was copied from IBM PC compatible disks to the Sun workstation as ASCII files. The software processes data starting from a frequency domain representation of the seismic traces. The data was converted to this format while simultaneously detrending , or removing the DC bias. The detrending was accomplished by taking the average value of the entire trace and subtracting that average value from every sample of the trace. The decision was made to process the seismic data as six separate data sets of sixty traces each. Each data set contained a separate source firing. It appeared that there were some slight differences between the data sets each time the source was moved. It also seemed reasonable that sixty traces were as many traces as would be needed for any array type processing. The previous section showed plots of the

data after detrending for the six data sets. One bad trace exists on each data set due to a connection problem during the acquisition.

The initial processing and previous results indicated that low frequency or long period data would provide the best resolution of the deep structure. Since the geophones used had a corner frequency of 10 Hz an instrument response correction was applied to the data in order to expand the usable bandwidth of the data. A comparison of the spectra at select distances before and after instrument correction (Figure 15) show that the only difference was a boosting of the amplitude below about 10 Hz. The instrument corrected data is reproduced in Figures 16 to 21. The seismic records after correction for instrument response were then processed to determine dispersion through various techniques. The most fundamental technique for determining group velocity dispersion utilized in this study was the multiple filter technique.

B. Multiple Filter Analysis

1. Experimental Technique

The Multiple Filter Analysis (MFA) technique used throughout this project to derive group velocity dispersion was first proposed by Dziewonski et. al. (1969). The group velocity is determined by performing a narrow band filter on the data and searching for the maximum amplitude of the envelope function. This procedure is repeated for each frequency over the band of interest. The group velocity can be related to the time for the peak of the envelope by equation (1.7). Some advantages of the MFA over the moving window analysis are documented by Dziewonski et al. (1969). These advantages include better frequency resolution, no intrinsic period shift and less computer processing time.

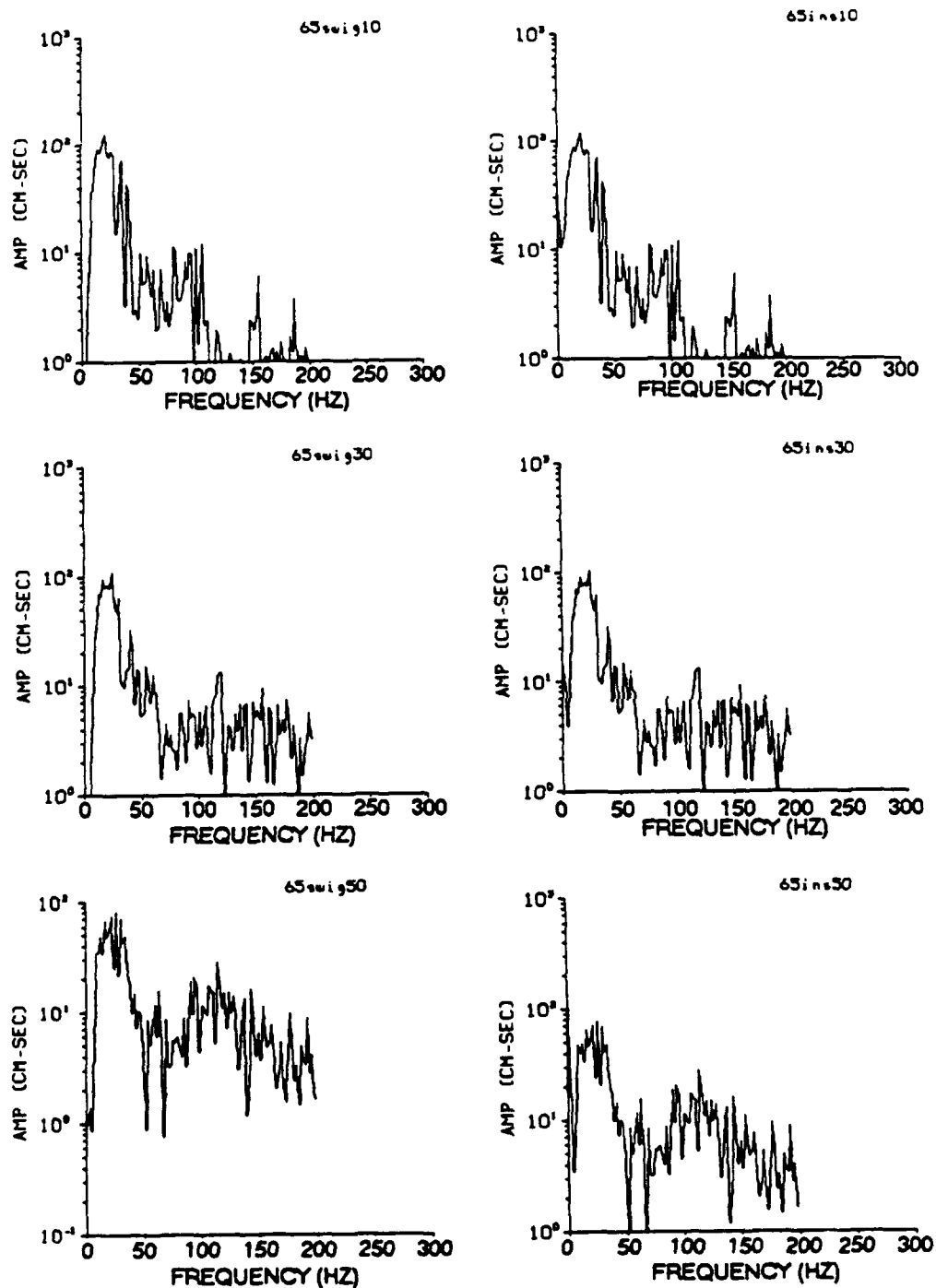


Figure 15. Comparison of amplitude spectrums of SWIG data. Data on the left is the original data. Data on the right is with instrument correction. From top to bottom, distance is 65 meters, 75 meters and 85 meters.

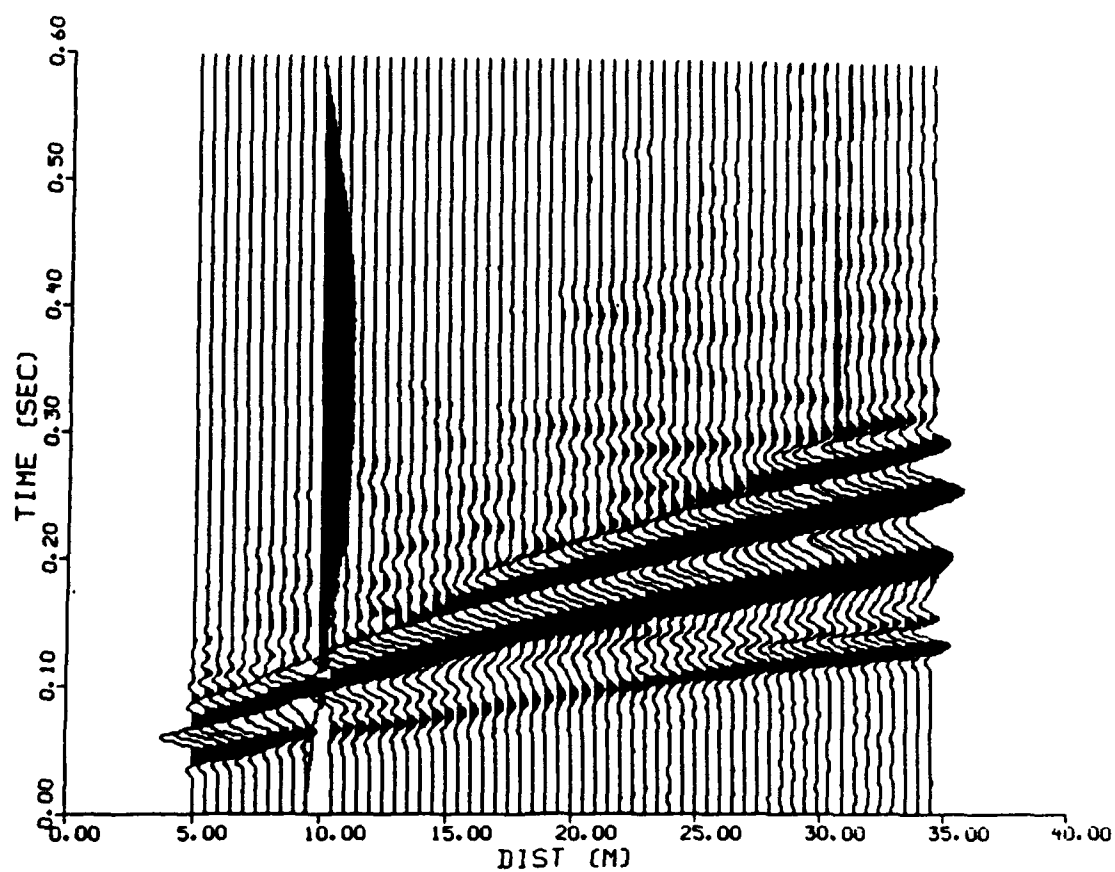


Figure 16. SWIG data after instrument response correction for source offset of 5 m from near receiver.

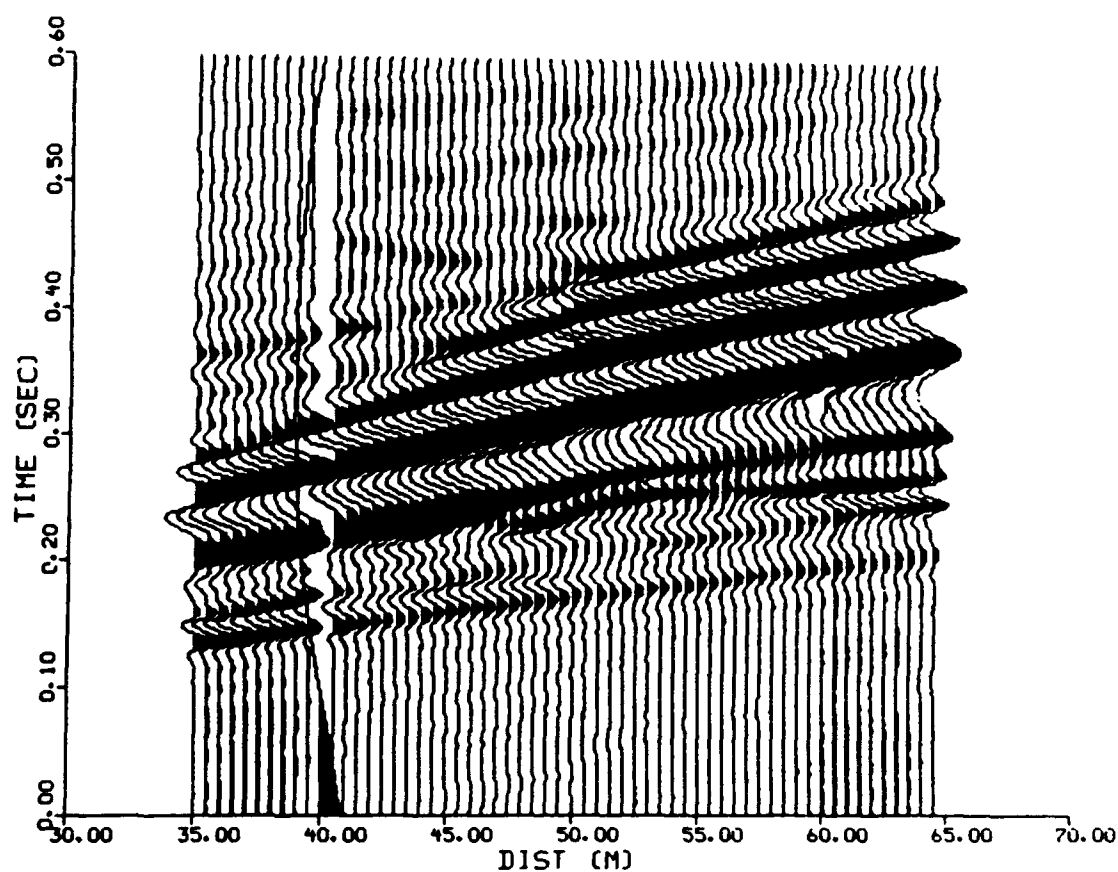


Figure 17. SWIG data after instrument response correction for source offset of 35 m from near receiver.

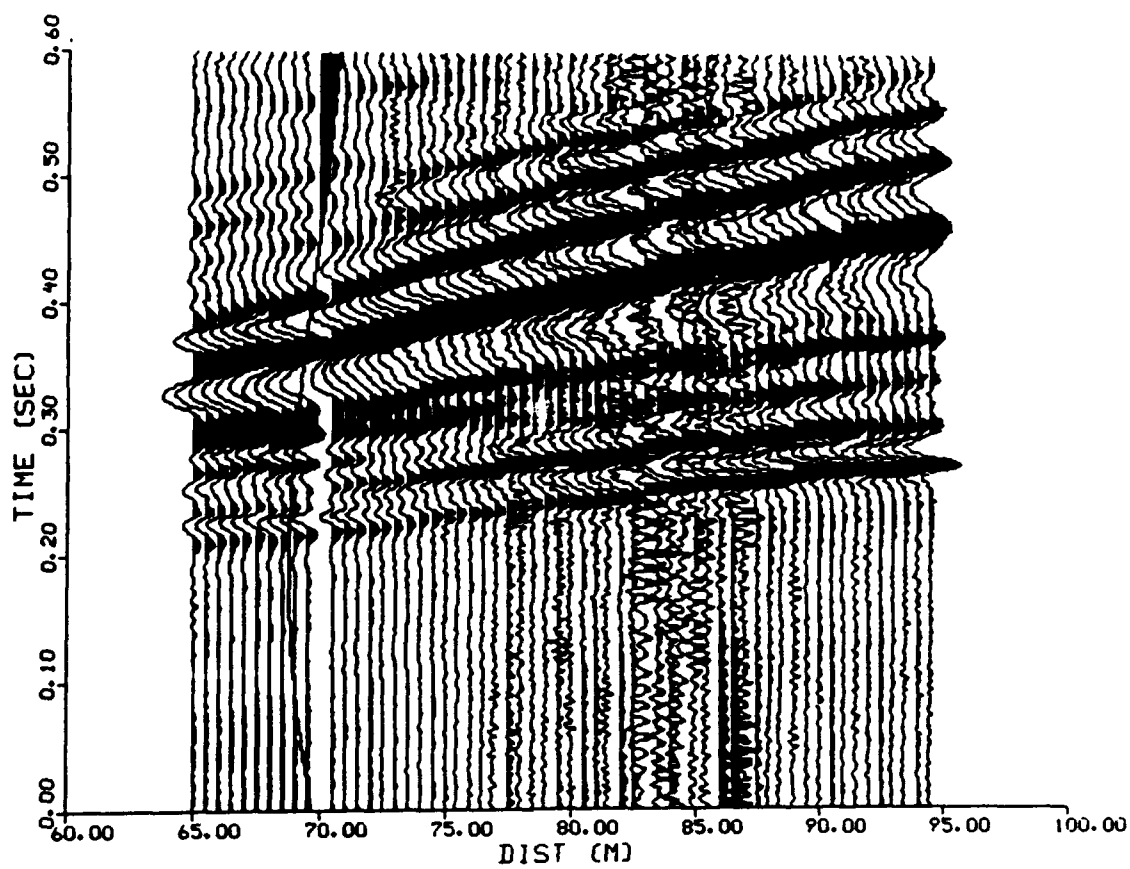


Figure 18. SWIG data after instrument response correction for source offset of 65 m from near receiver.

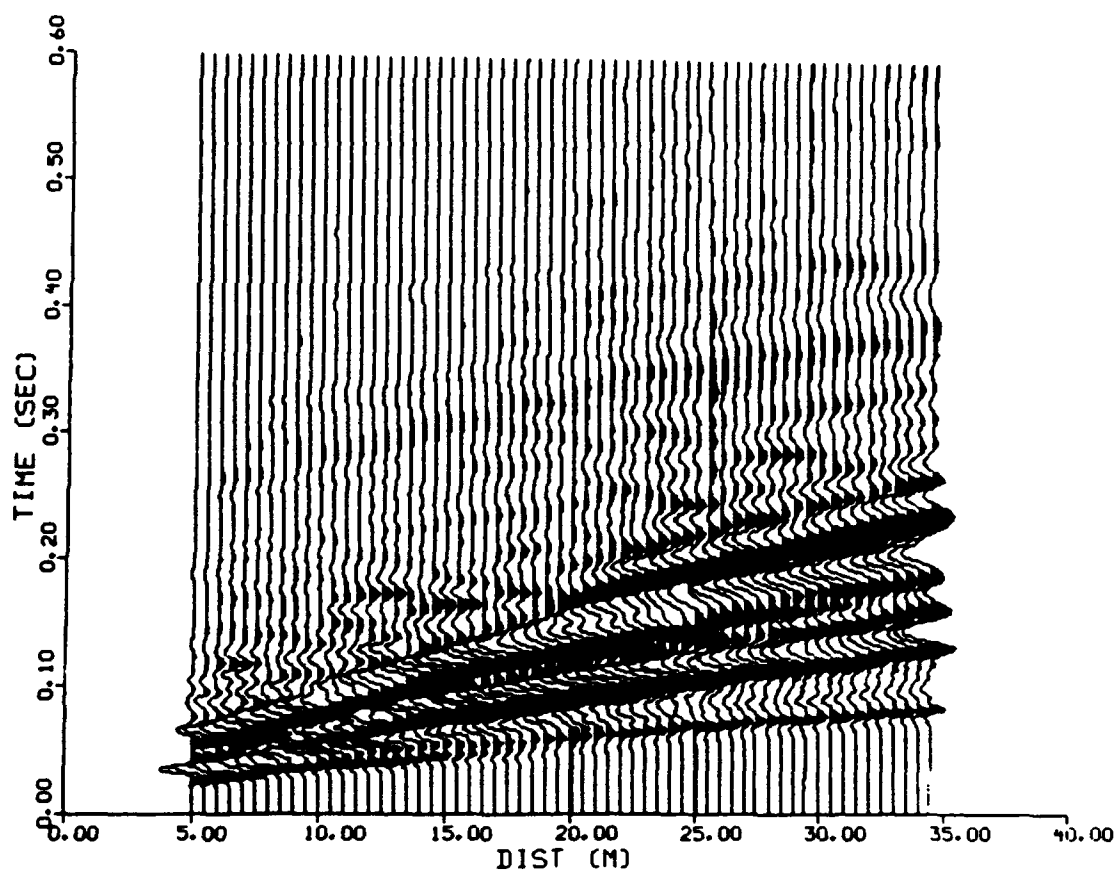


Figure 19. Betsy data after instrument response correction for source offset of 5 m from near receiver.

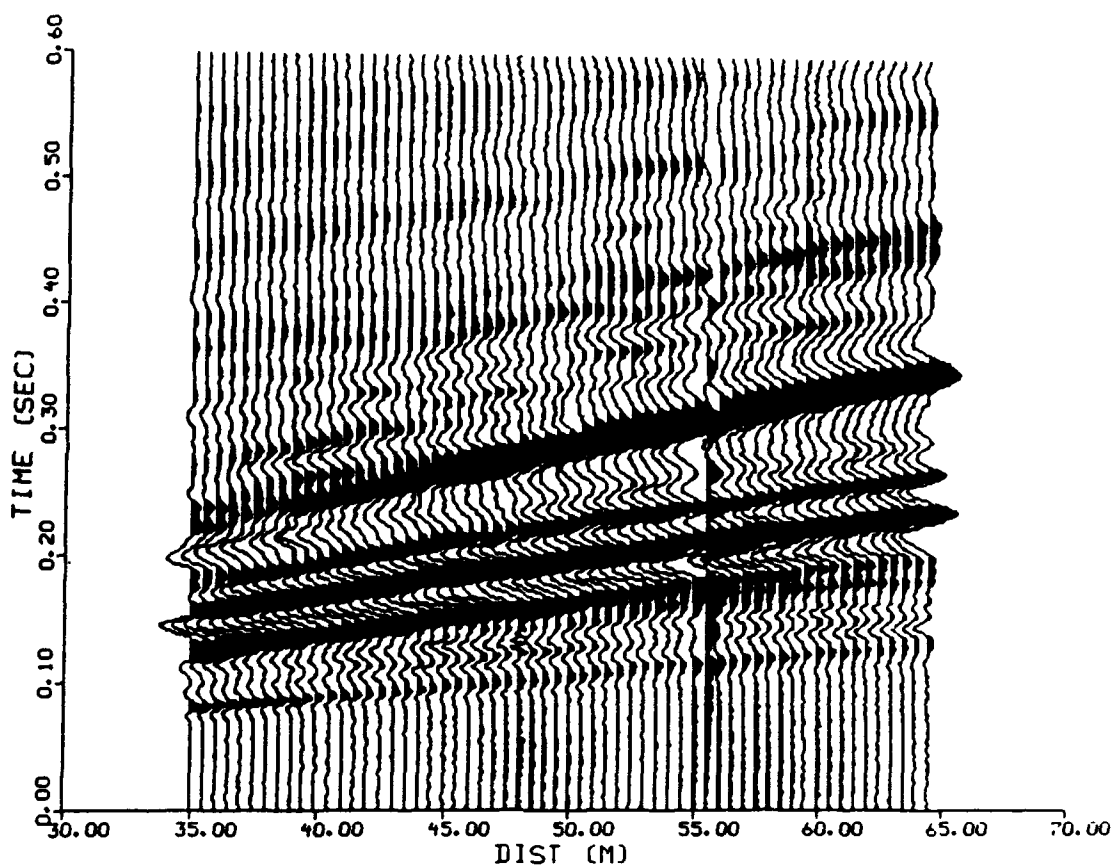


Figure 20. Betsy data after instrument response correction for source offset of 35 m from near receiver.

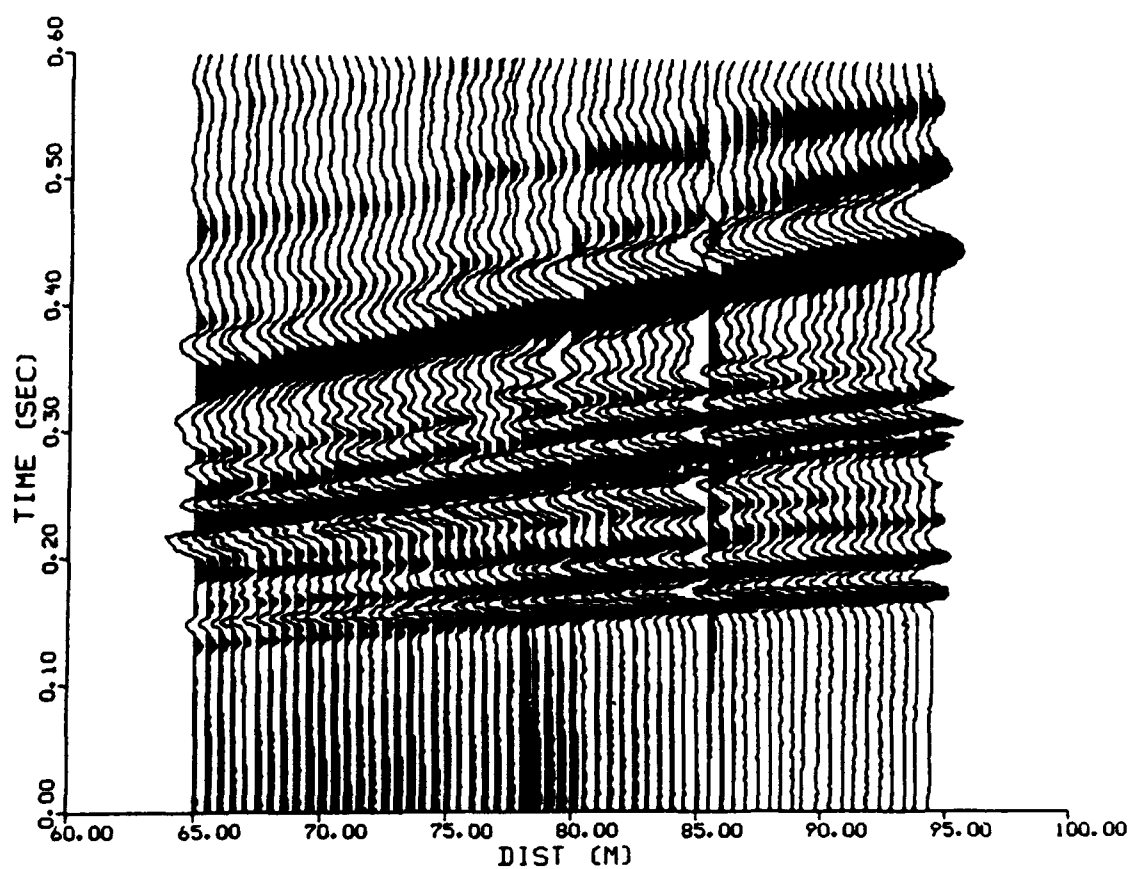


Figure 21. Betsy data after instrument response correction for source offset of 65 m from near receiver.

Filtering is accomplished with a Gaussian filter which is set to zero outside a given bandwidth and is tapered inside this bandwidth from the center frequency. The range of center frequencies are selected by the user with the bandwidth controlled by one parameter α (which will be used interchangeably with A0). The bandwidth is:

$$(3.1) \quad \text{BAND} = (\pi/\alpha)^{1/2}.$$

The default value for α is 50.27 which yields a value for BAND of 25%. This means that for a center frequency of 100 Hz, the non-zero frequency range would be 75 to 125 Hz. The selected value for α is a compromise between resolution in the frequency domain and resolution in the time domain. Some simple tests of impulse response were made to quantify this compromise. An impulse data set was created which contained one thousand samples at 1 msec sample rate. The value of all samples was set to zero except for one non-zero sample at 0.5 seconds. The trace was then filtered from 1 to 50 Hz using a Gaussian bandpass filter with various values of α . Figure 22. shows the impulse response in the time domain versus frequency for α equal to 5 or 79% bandwidth in the frequency domain. The trace at approximately 75 Hz is the input impulse trace. The corresponding envelope appears at the bottom of the page. Figure 23 contains the same plots for A0 set to 75 for comparison.

Time domain sidelobes from the bandwidth increase as frequency decreases or the period increases. Below 10 Hz the sidelobes become so large it is difficult to discriminate between closely spaced events in time. The envelope

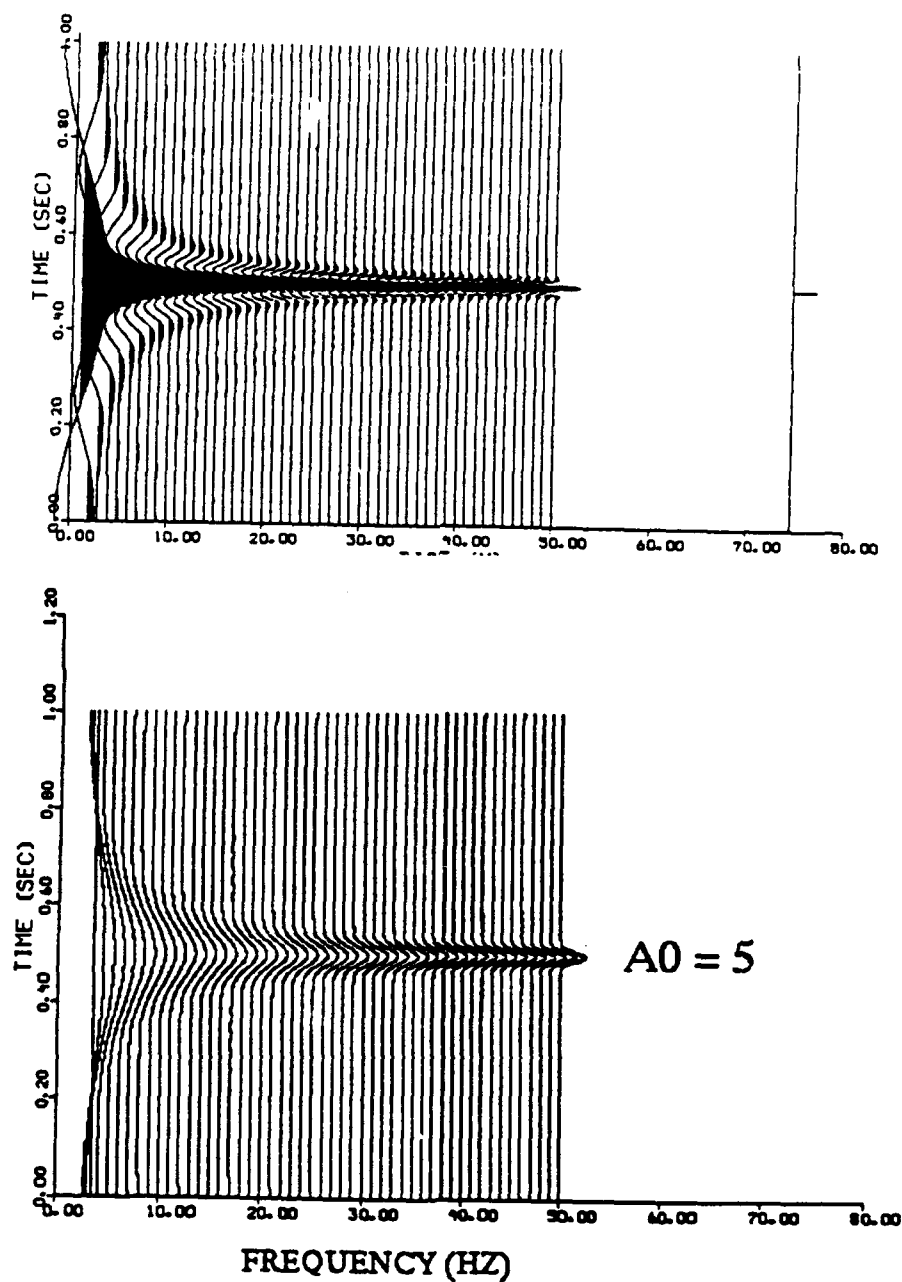


Figure 22. Impulse response in time domain of bandpass filters for different center frequencies. α or A_0 equals 5 in this case so bandwidth is 79%. Trace at approximately 75 Hz is input impulse trace. Bottom plot is envelope function of top plot.

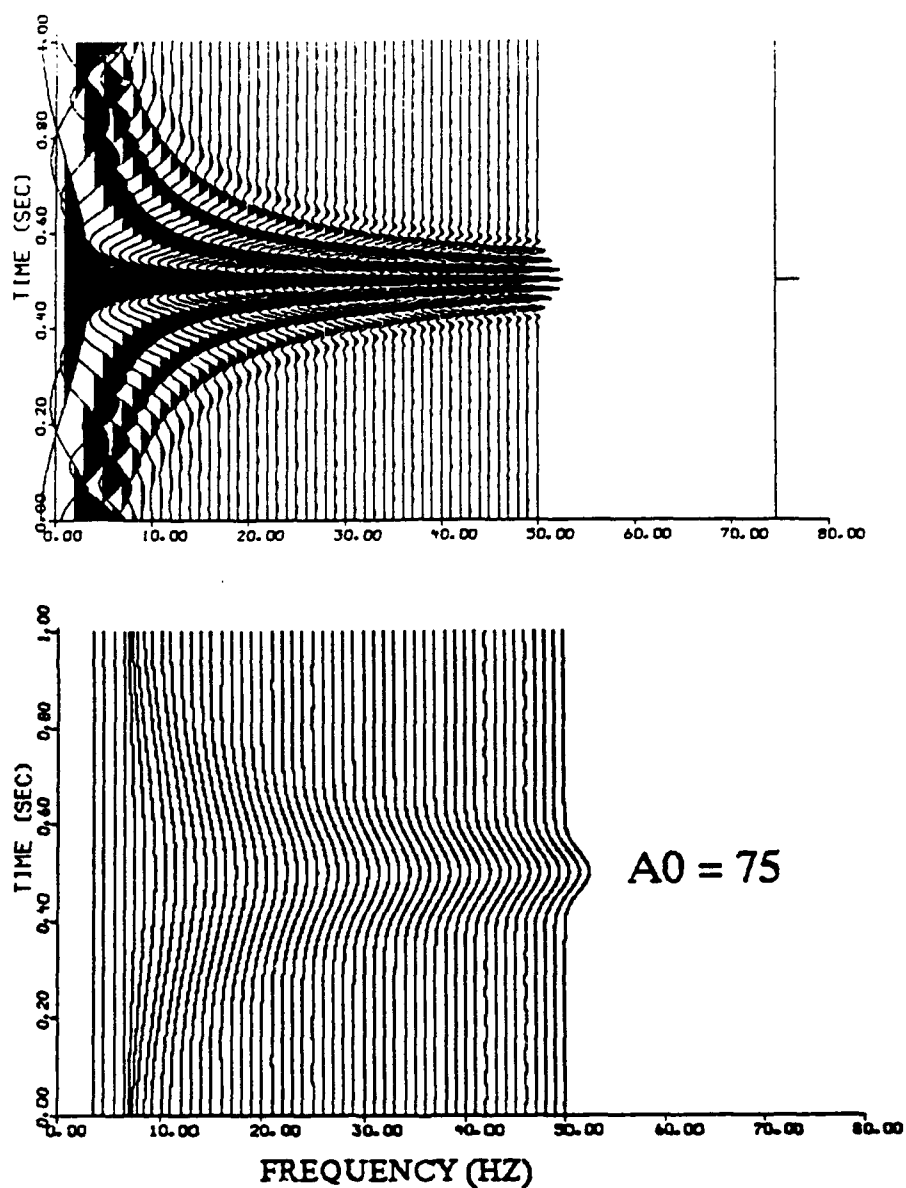


Figure 23. Impulse response in time domain of bandpass filters for different center frequencies. α or A_0 equals 75 in this case so bandwidth is 20%. Trace at approximately 75 Hz is input impulse trace. Bottom plot is envelope function of top plot.

function is a Gaussian shaped curve in the time domain, representing one smooth output event for one input event.

Figure 24 displays the frequency domain response of the Gaussian filter for various values of α for a center frequency of 50 Hz. For a value of α equal to 75 or a bandwidth of 20%, it can be seen that the filter is very tight in the frequency domain yielding a good frequency resolution. Unfortunately, the side-lobes are so large in the time domain that it becomes difficult to separate different velocity events, especially at low frequencies.

Resolution in the time domain or separation in time between two events is related to the bandwidth in the frequency domain and the period T (Herrmann, 1988):

$$(3.2) \quad \text{Time Resolution} = T/\text{Band.}$$

Table 3 summarizes the results of the impulse response tests, and demonstrates the tradeoff between frequency resolution and time domain resolution. This information, along with processing panels of data with various values of A_0 , was used to select A_0 for the rest of the project. A value of 25 was used for all of the data in this project. In theory this should only allow the determination of group velocity when interfering events are separated by 100 msec or more.

The bandwidth of the acquired data used in this study is approximately 10 to 30 Hz. Some effort was expended to recover quality data below 10 Hz, including correction for instrument response. It appears that this was not efficacious since the major events were separated by less than 200 msec at this distance. In order for this technique to work at these frequencies, it appears that

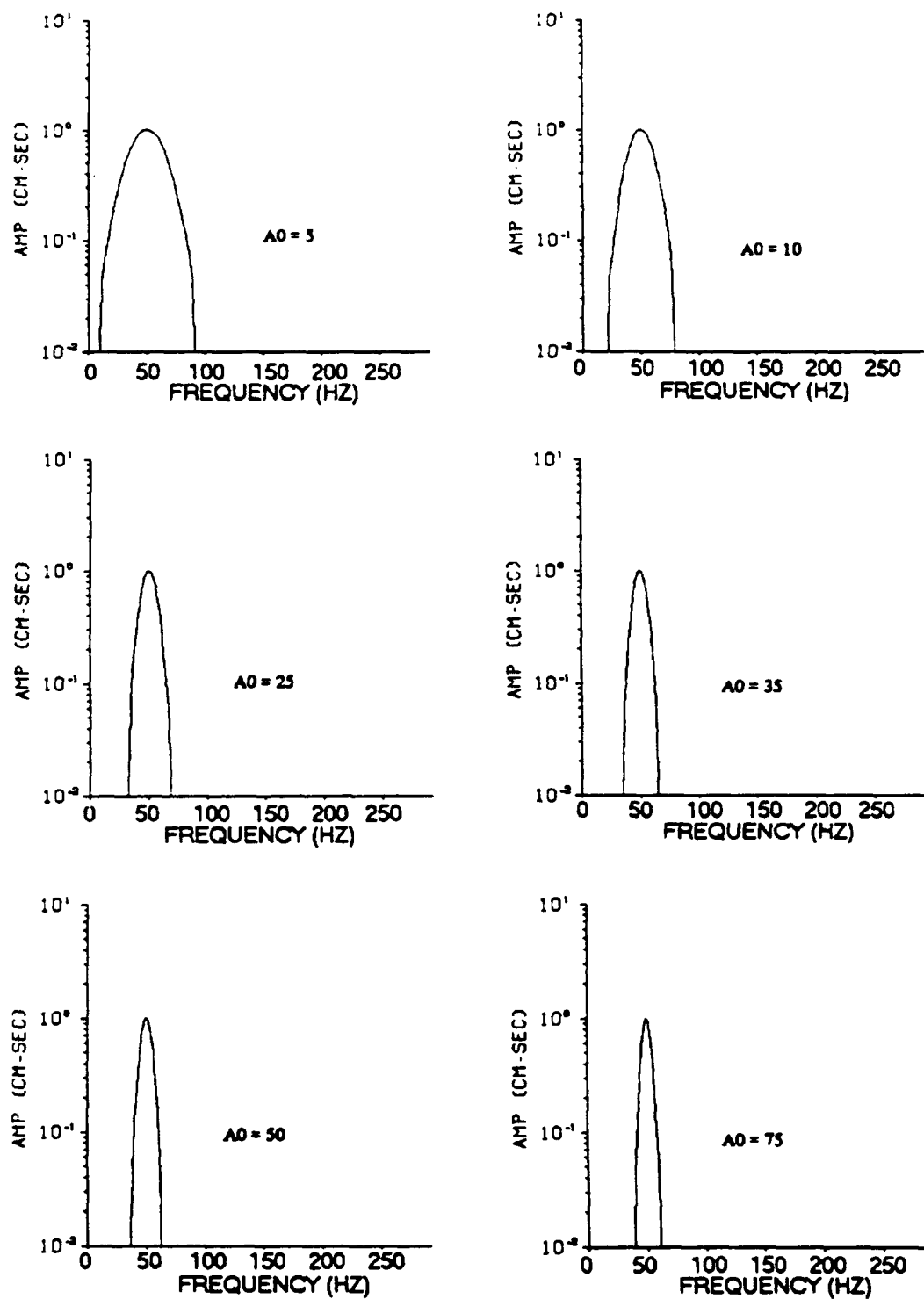


Figure 24. The impulse response in frequency domain at center frequency of 50 Hz for various values of A_0 . Clockwise from upper left, A_0 is 5, 10, 35, 75, 50 and 25.

Table 3

CHARACTERISTICS OF VARIOUS GAUSSIAN FILTERS

α or A0	Bandwidth	Frequency	Period	Time Resolution
75	.20	10	.100	0.500
75	.20	20	.050	0.250
75	.20	50	.020	0.100
50	.25	10	.100	0.400
50	.25	20	.050	0.200
50	.25	50	.020	0.080
35	.30	10	.100	0.333
35	.30	20	.050	0.167
35	.30	50	.020	0.067
25	.35	10	.100	0.285
25	.35	20	.050	0.143
25	.35	50	.020	0.057
10	.56	10	.100	0.179
10	.56	20	.050	0.089
10	.56	50	.020	0.036
5	.79	10	.100	0.127
5	.79	20	.050	0.063
5	.79	50	.020	0.025

data would have to be acquired at much further source-receiver offsets which would provide larger time separation between arrivals.

2. Experimental Results

The MFT was applied to all six data sets. Displays of the MFT analysis of the SWIG generated Love wave data at approximately 5 m intervals are presented in Figures 25 to 45. The bottom plot contains the amplitude contours across the various frequencies on the x-axis. The y-axis is time scaled by group velocity according to equation (1.7). The input trace is presented to the far right scaled in linear time and also in linear velocity for comparison to the contoured results. The four largest peaks of the envelope function at each frequency are noted and marked on the plot with the largest amplitude marked with a square, second largest with a circle, third with a triangle and the fourth peak with a plus sign. These amplitudes are scaled relatively and presented in the frequency domain in the top plot.

Some general things can be noted by studying figure 25. The trace at the far right shows that there is a small period of time in which most of the energy arrives. The second trace shows that the peak amplitude of the trace arrives with a velocity of approximately 90 m/s. A dispersion curve could be drawn connecting the squares from 3 Hz to 60 Hz. The dispersion does not match the classical shape we would expect of velocity decreasing with frequency. This difference is due in part to the fact that the body waves and surface waves have not had enough time to separate at this range. Another reason could be that the Love waves have not had sufficient time to stabilize. One other feature that can be seen in the spectral plot at the top is that the amplitude of the main event is

over an order of magnitude larger than the next largest event over a broad band. This implies that the data set contains information from 8-60 Hz.

Figure 26 shows the bandwidth dropping to 8-55 Hz at a source-receiver spacing of 10.5 m. There is no indication of dispersion with the main body of energy arriving at 100 m/s. At 20 ms (Figure 28) there is some indication of dispersion. Group velocity for the event of interest is about 150 m/s at 13 Hz and drops to about 100 m/s at 45 Hz. The spectral plot shows two strong events that cross at 60 Hz. This information can be used to help determine continuity of an event on the velocity plot. In this case, the main event would be a square. The dispersion curve would be drawn connecting squares from 8 Hz. to about 60 Hz. The dispersion curve would be drawn connecting circles from that point forward. This technique would be most useful if the velocities of two events converge for a small interval and then diverge.

At 30 m (Figure 30) the trace can be seen to clearly contain two events. The first event of velocities 180 to 300 m/s is clearly the direct and refracted shear body waves. The largest amplitude event on the trace arrives directly afterwards, corresponding to a velocities between 100 and 180 m/s. The event has several cycles with the longest period portion arriving earliest and is interpreted as a Love wave with normal dispersion. As the source-receiver spacing increases, the Love wave portion generally becomes more widely separated in time from the body waves or direct arrivals. The Love wave portion of the seismic trace also shows increased dispersion with offset.

The group velocity determined from the seismic trace is an average over the spatial interval between the source and receiver. This implies that for any given receiver, say at 80 m, the next receiver should have very similar results. It

can be seen from analyzing Figure 37 and 38 that the results at 80 and 85 m are very similar, in spite of a being relatively noisy. If the site were horizontally stratified and homogeneous, two receiver locations 0.5 m apart should be extremely similar.

There exist two portions of the data set that are at approximately the same source receiver spacing, but cover a different interval of ground. When the data was acquired, the source was moved back 30 m at a time with the receivers left in the same 60 locations. Figure 9 demonstrates that the source at 35 m from the near receiver and the source at 34.5 m from the far receiver cover a similar distance, although the travel path for these two stations overlaps by only 5 m. Figure 31 and 32 are analyzed at 34.5 and 35 m, and exhibit different Love wave dispersion as well as different amplitude levels for the entire seismic trace. Differences between these two traces is most pronounced at the higher frequencies. The two data sets at 64.5 and 65 m (Figures 38 and 39) demonstrate even larger differences. The data set at 64.5 m has almost 4 full cycles apparent on the raw trace of the Love wave. The Love wave in the trace at 65 m consists of only about two cycles. This alone is enough to indicate that the two intervals imaged by the Love wave are geologically different. The dispersion results are very similar between 10 and 30 Hz. The high frequency components show the most variability over the entire data set.

Figure 46 is a composite diagram of the group velocity dispersion for the Love wave on the 5 meter data set at 5 m increments. The velocity increases for each dispersion curve as the range increases from 5 to 34.5 m. This result is consistent with Mari's (1984) statement that it would take an offset distance of 4 to 6 times the deepest layer imaged for the Love wave to stabilize. The velocity

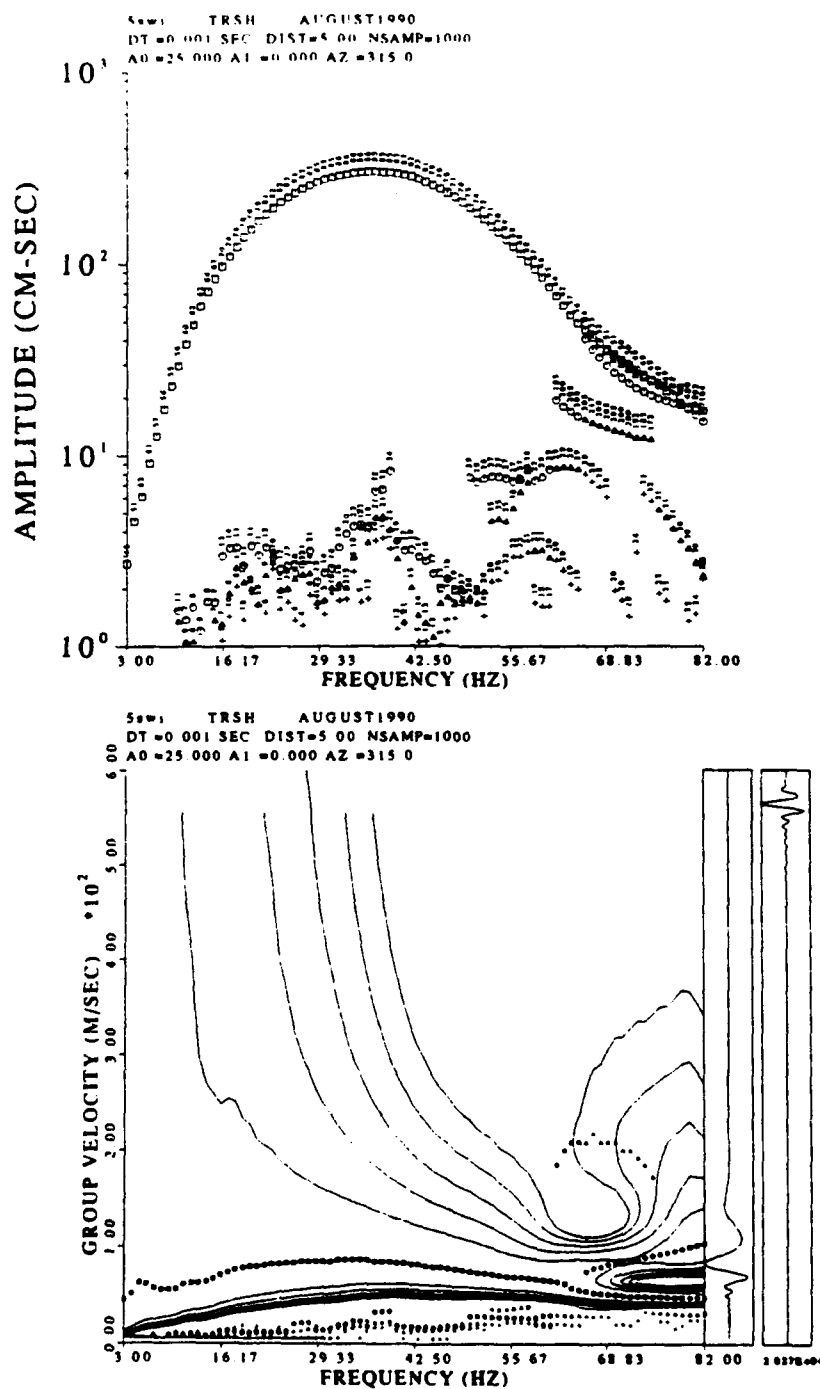


Figure 25. MFT analysis at 5.0 m for SWIG data

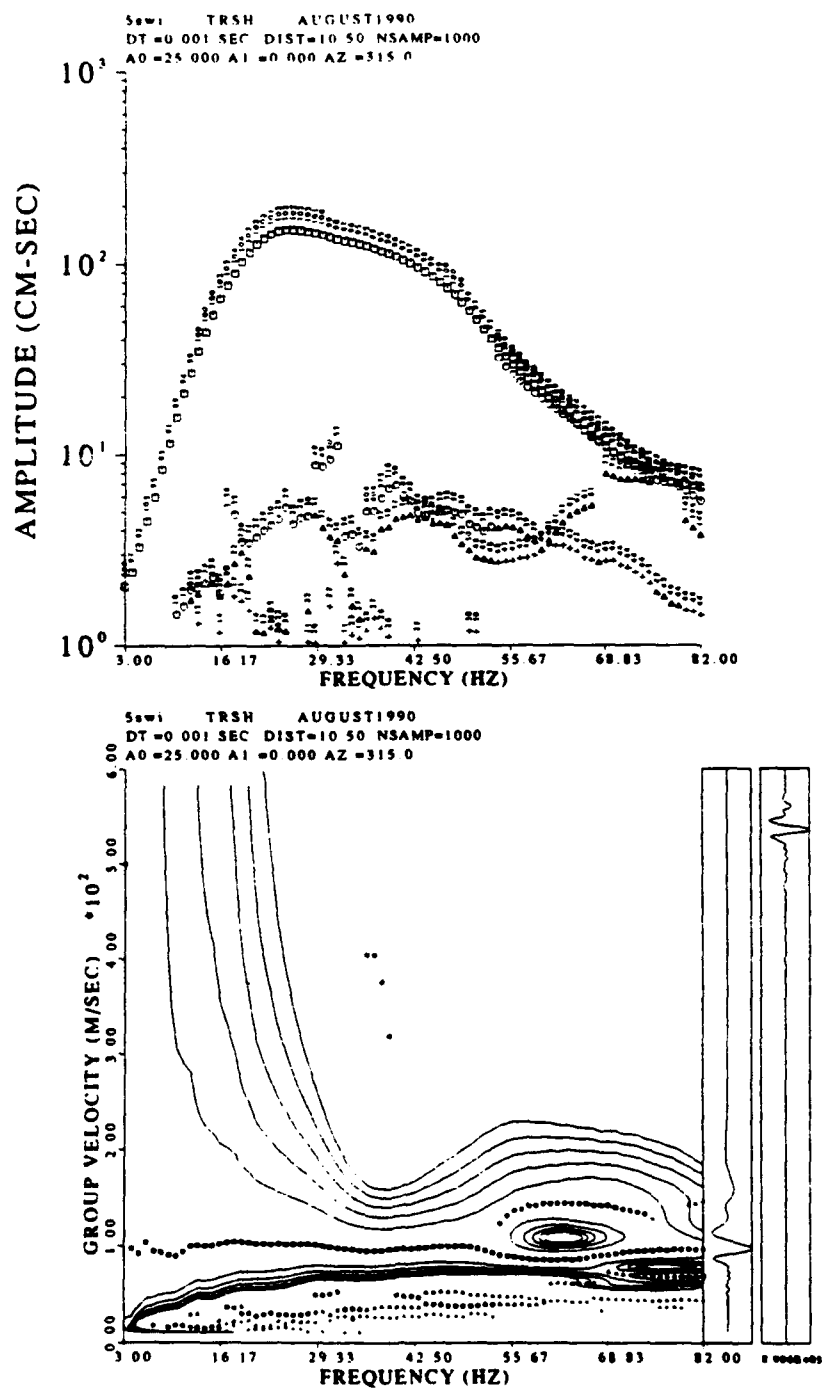


Figure 26. MFT analysis at 10.5 m for SWIG data

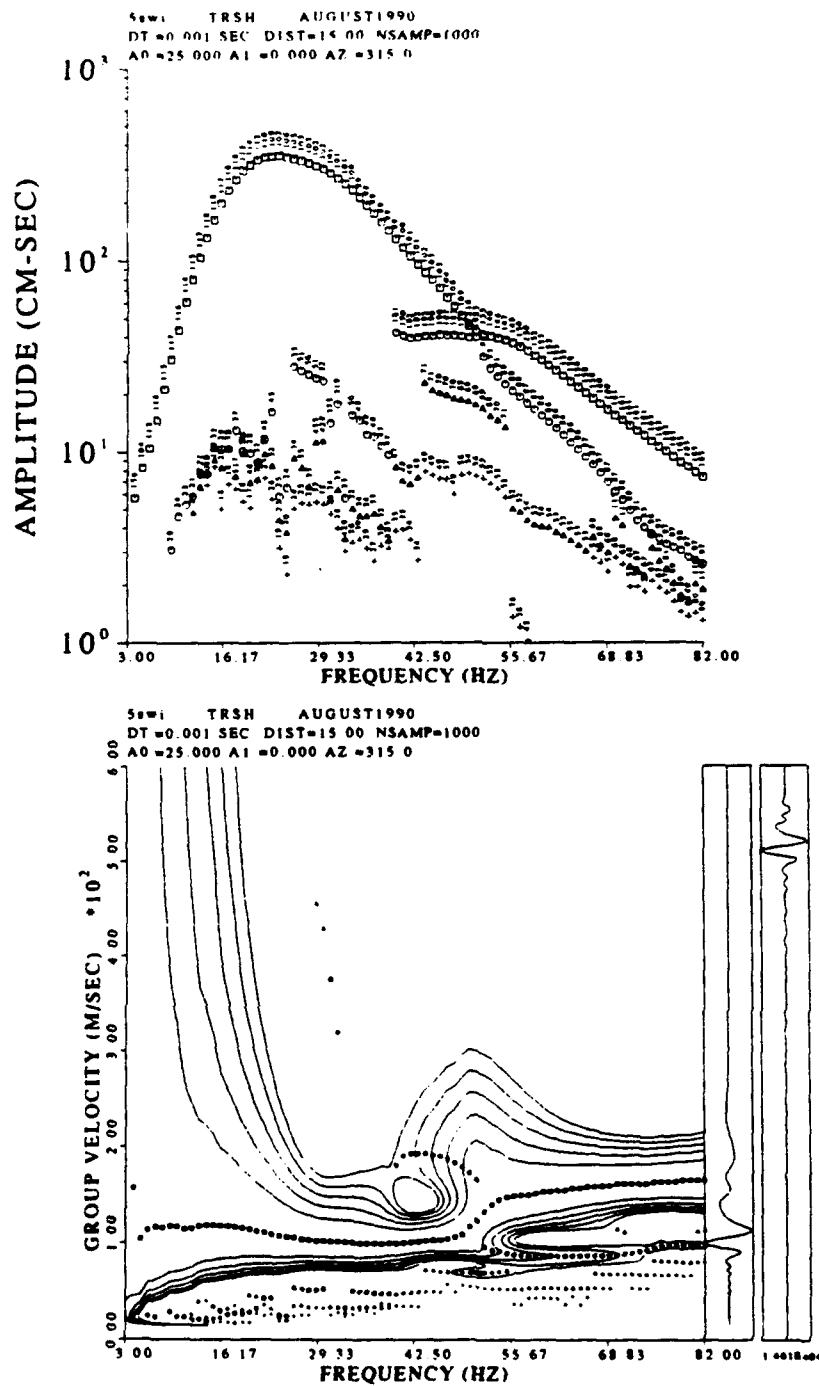


Figure 27. MFT analysis at 15.0 m for SWIG data

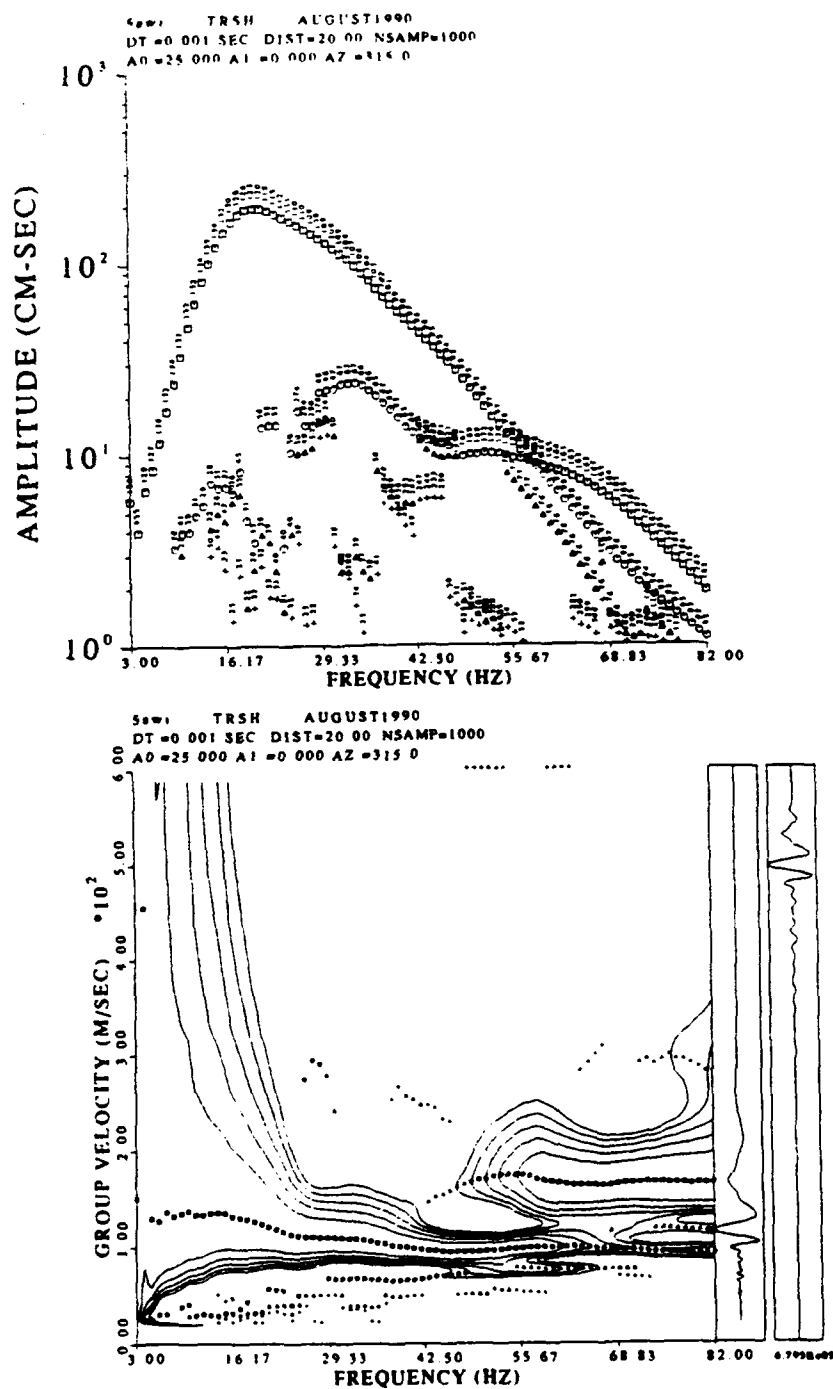


Figure 28. MFT analysis at 20.0 m for SWIG data

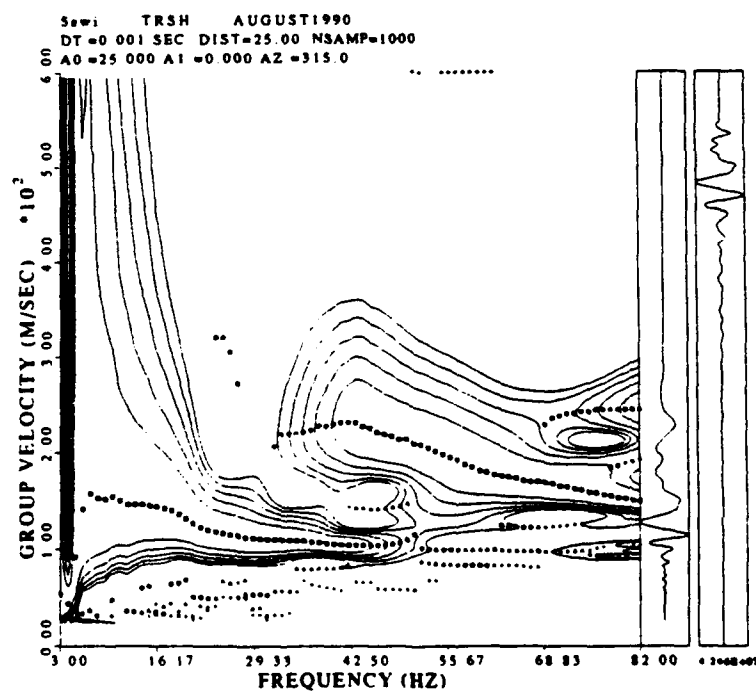
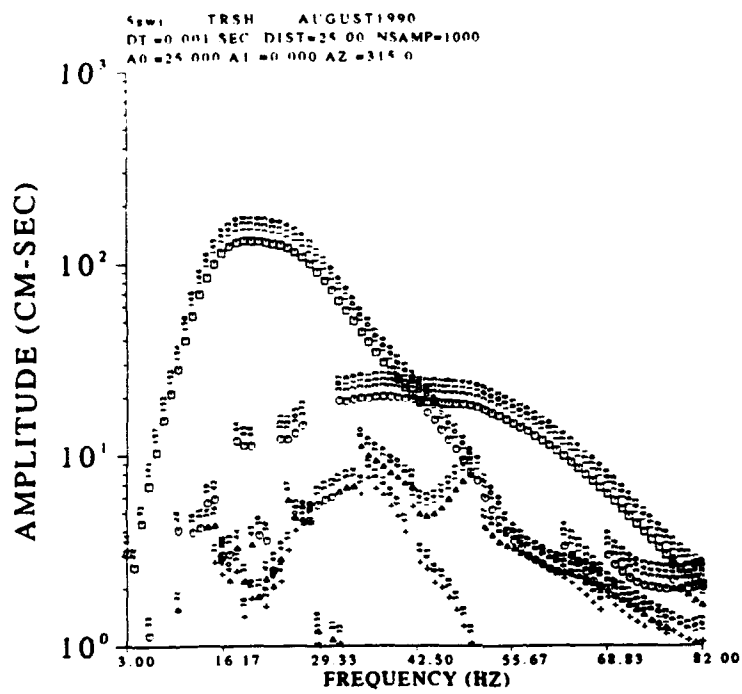


Figure 29. MFT analysis at 25.0 m for SWIG data

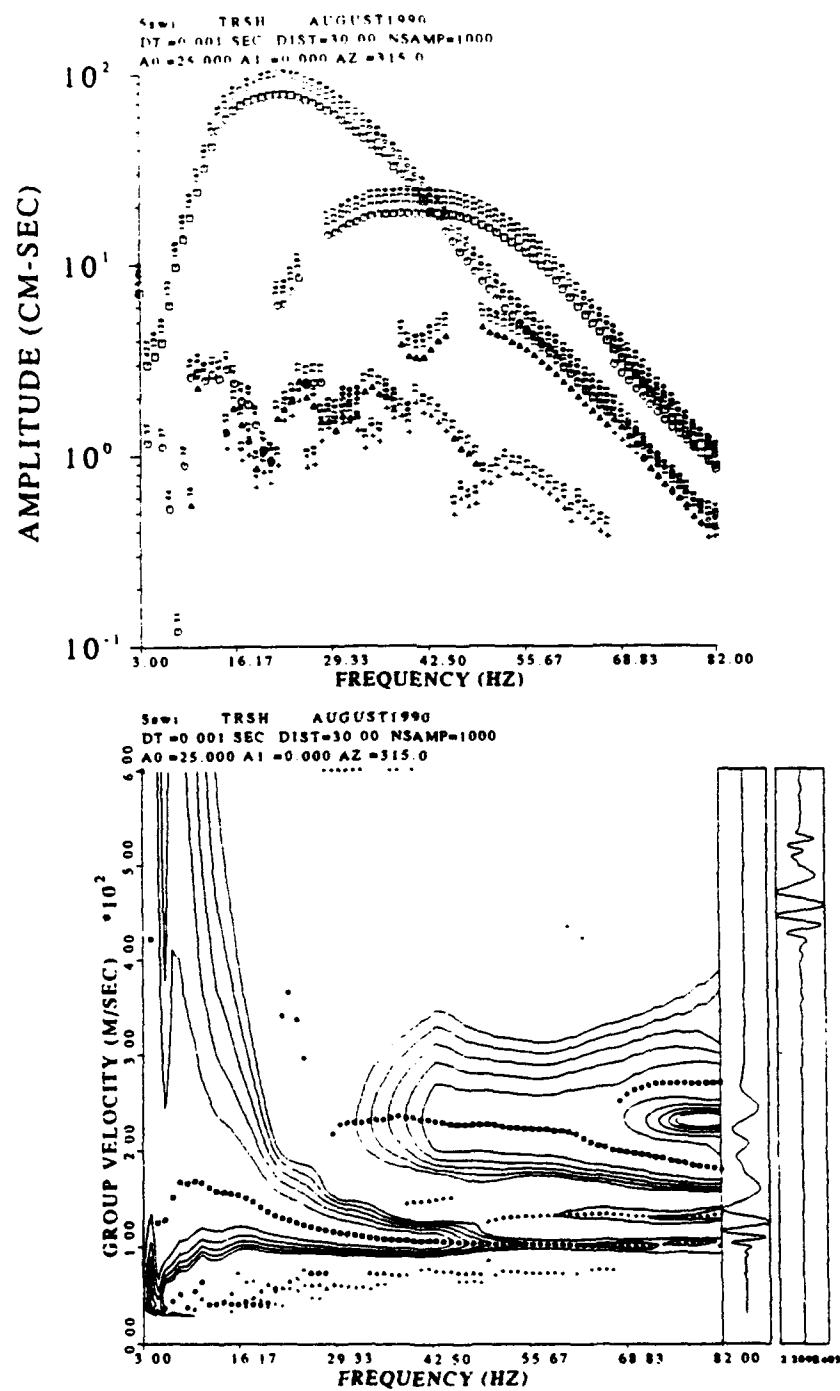


Figure 30. MFT analysis at 30.0 m for SWIG data

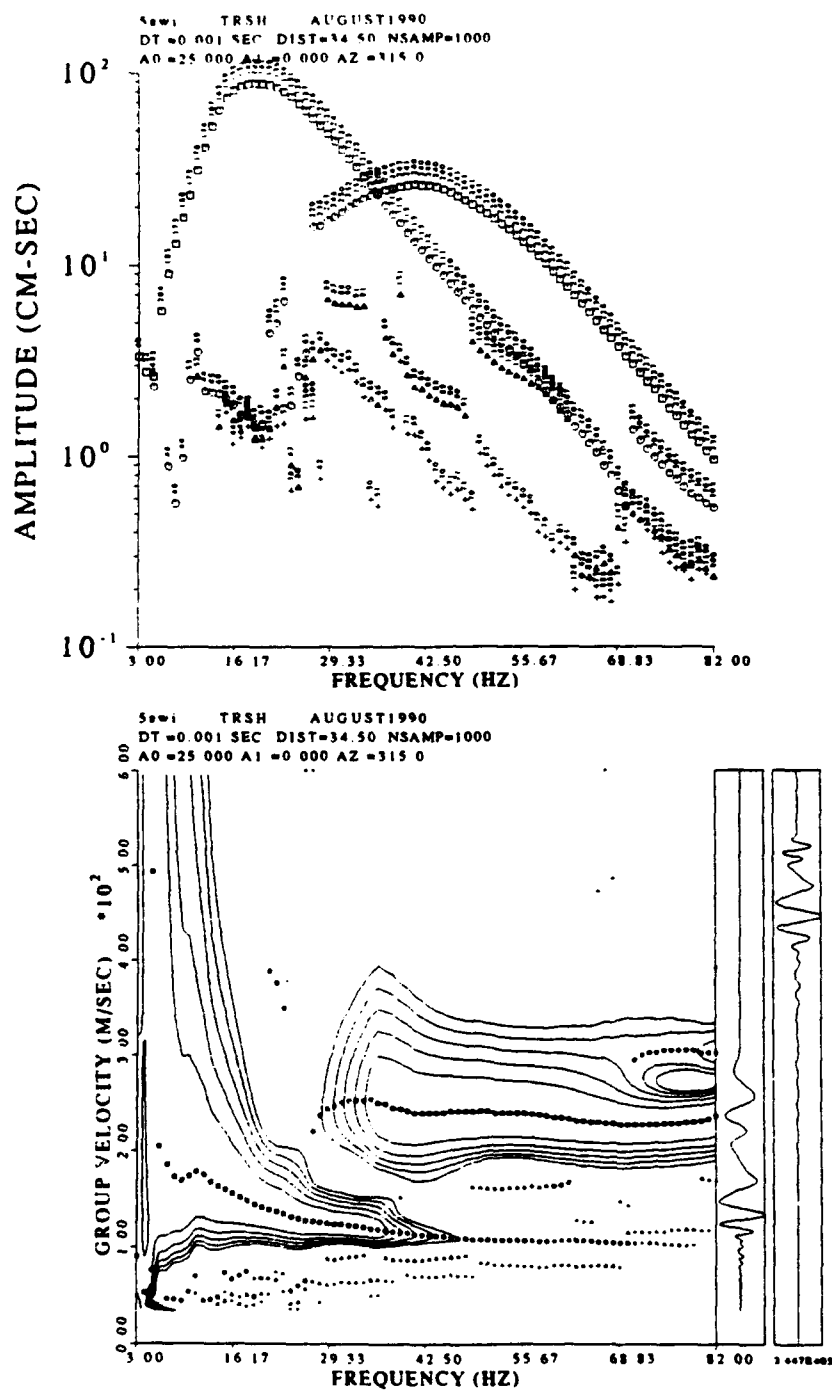


Figure 31. MFT analysis at 34.5 m for SWIG data

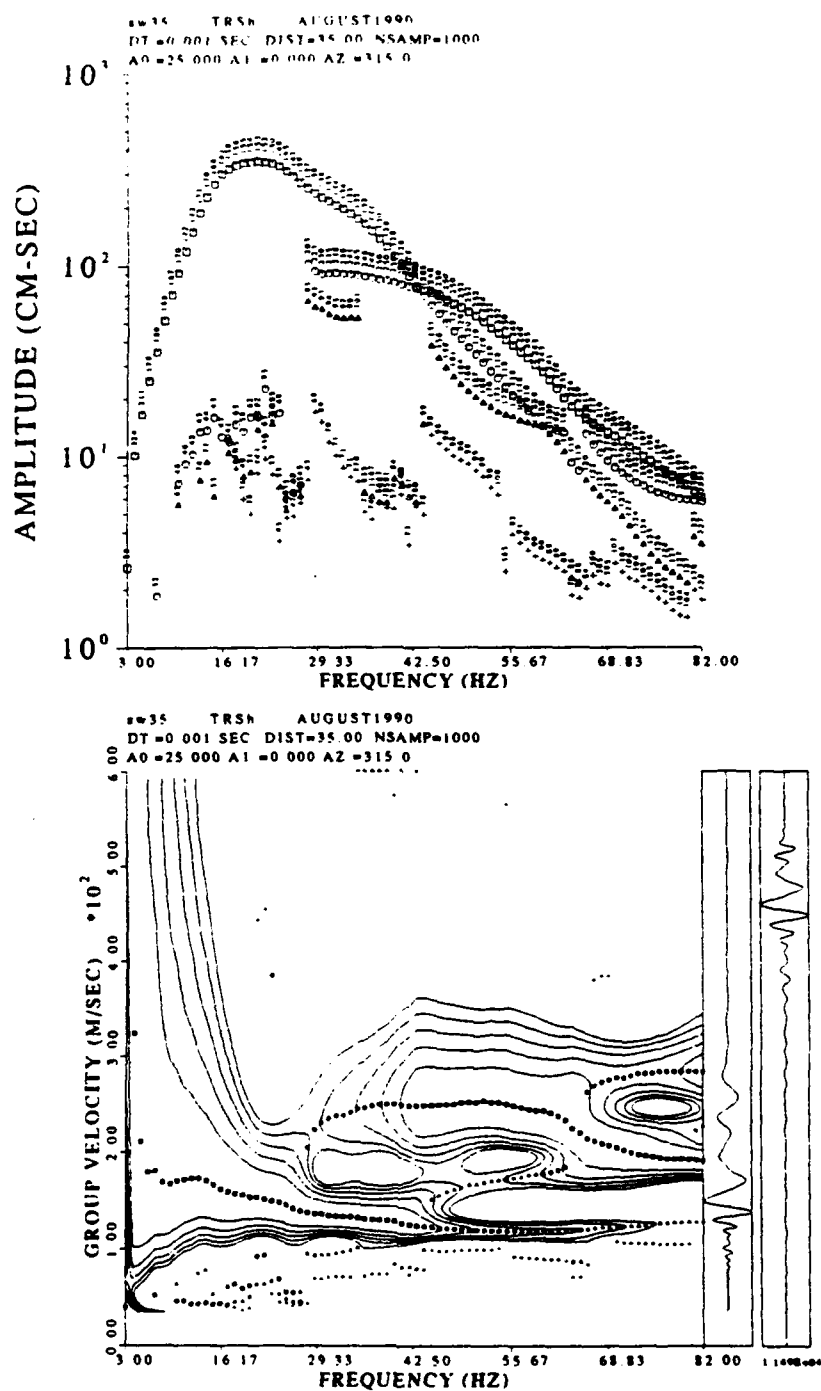


Figure 32. MFT analysis at 35.0 m for SWIG data

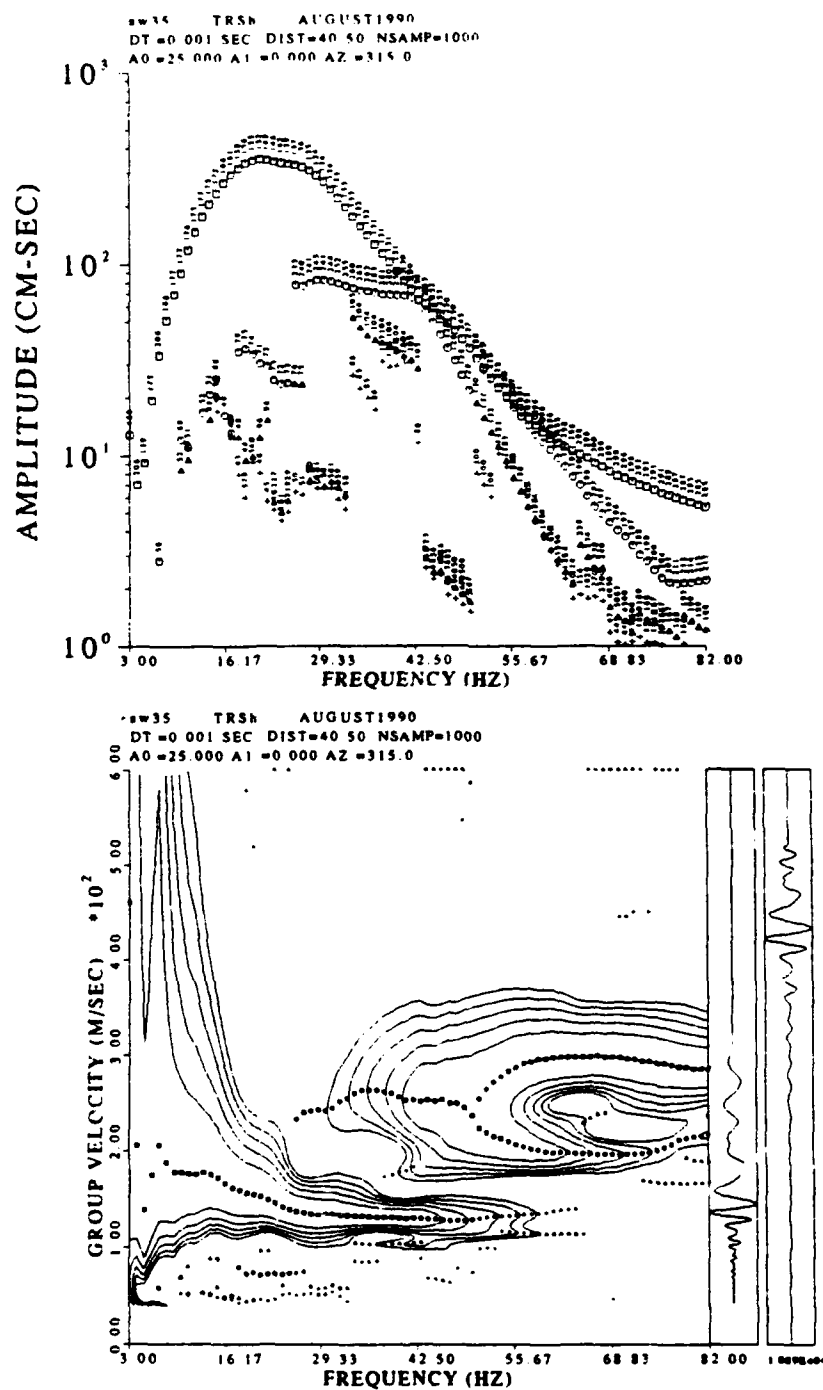


Figure 33. MFT analysis at 40.5 m for SWIG data

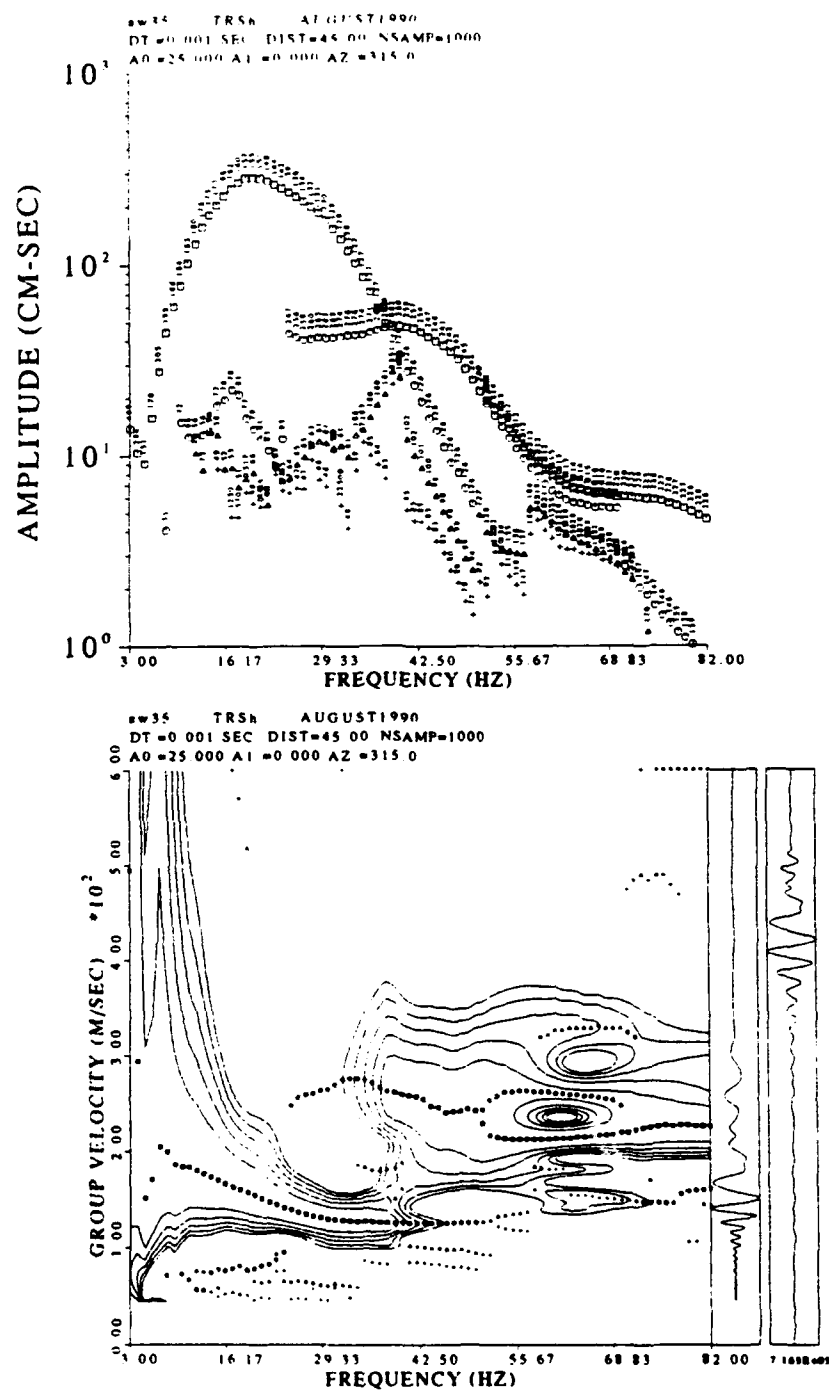


Figure 34. MFT analysis at 45.0 m for SWIG data

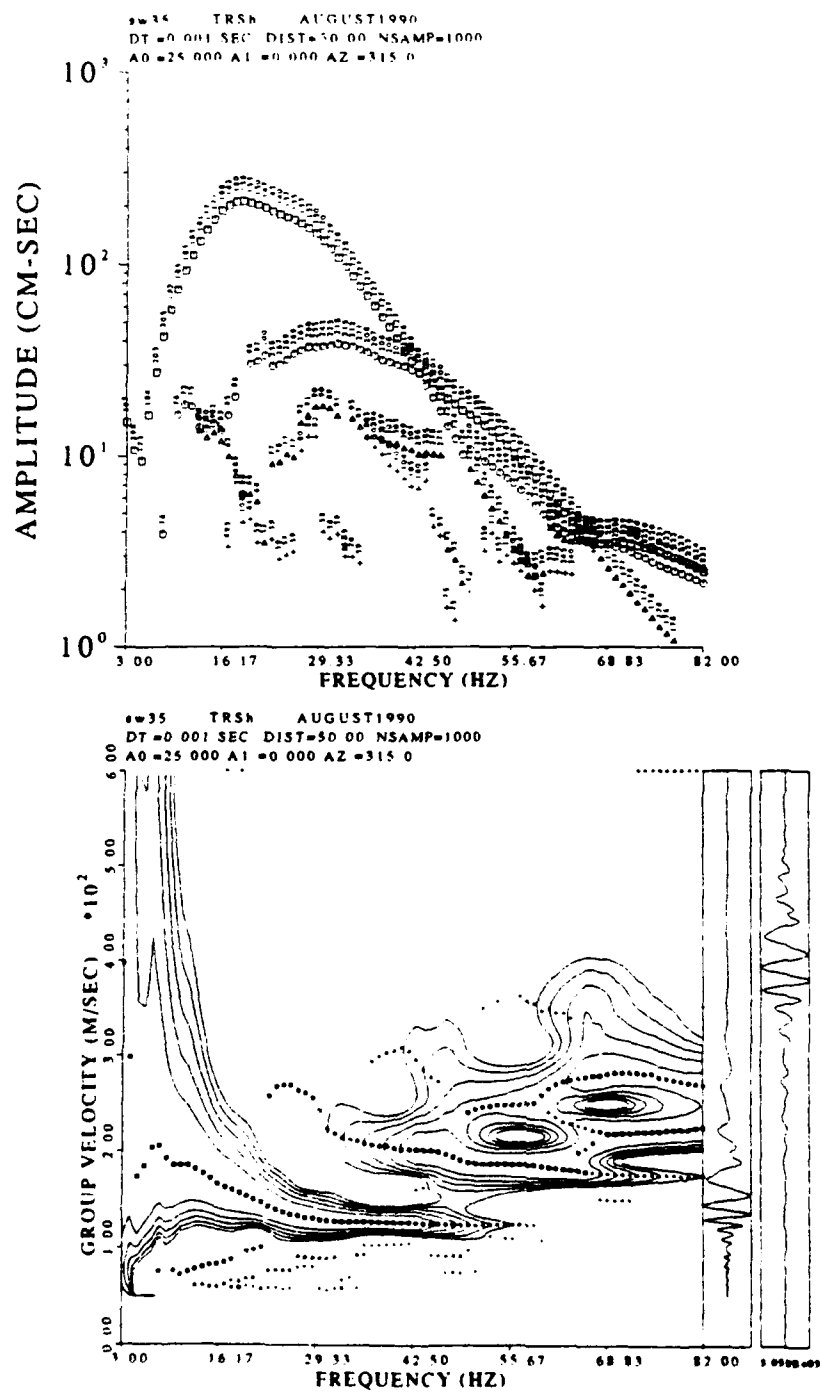


Figure 35. MFT analysis at 50.0 m for SWIG data

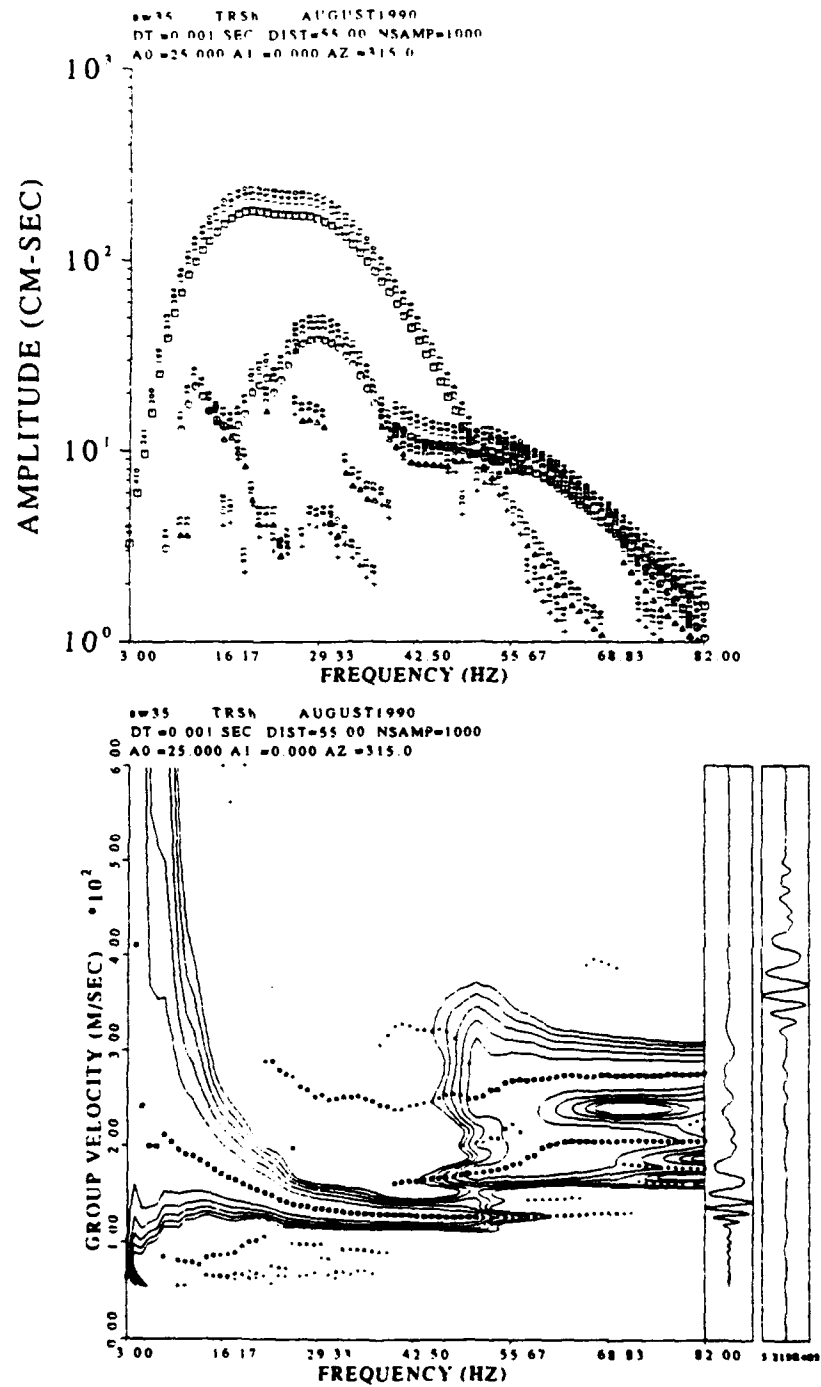


Figure 36. MFT analysis at 55.0 m for SWIG data

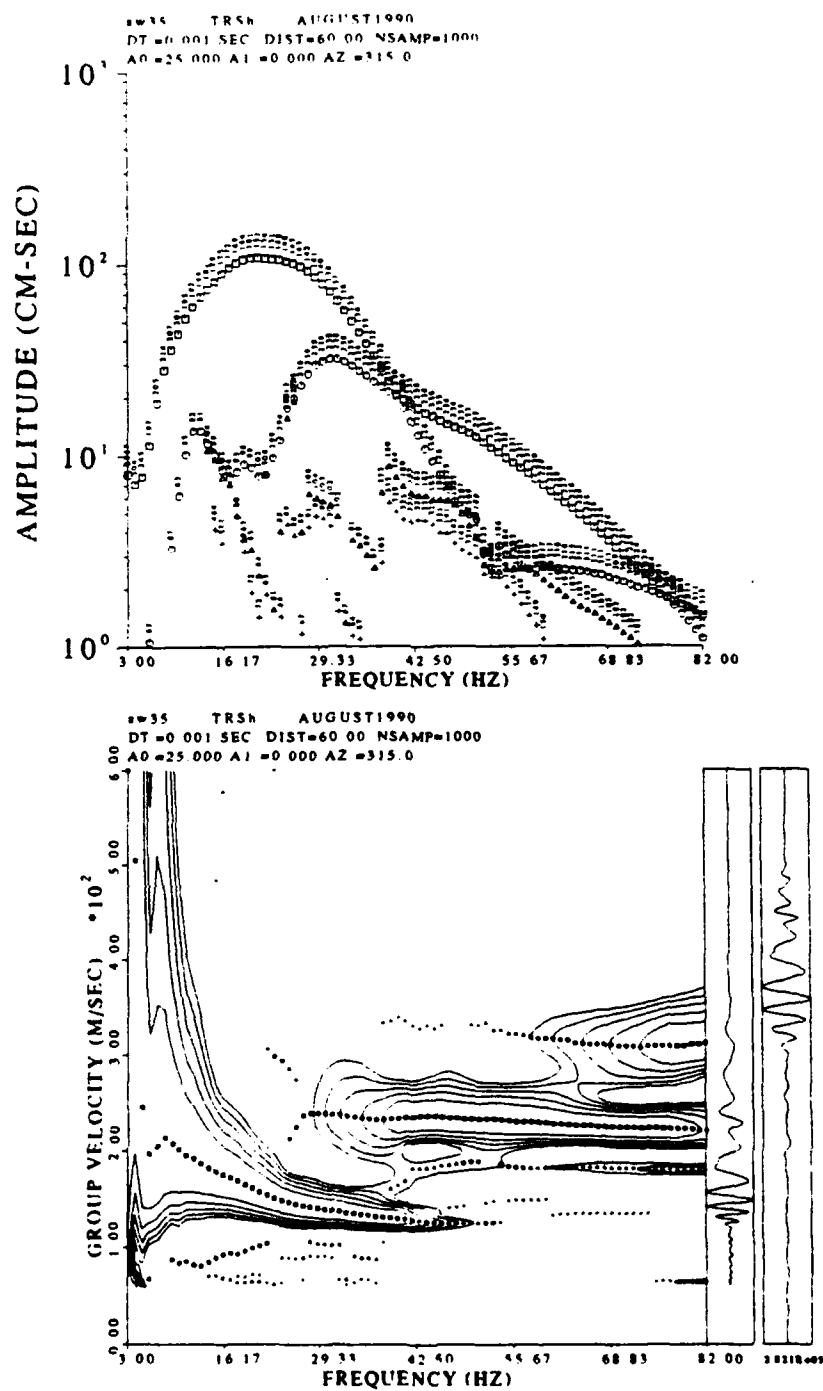


Figure 37. MFT analysis at 60.0 m for SWIG data

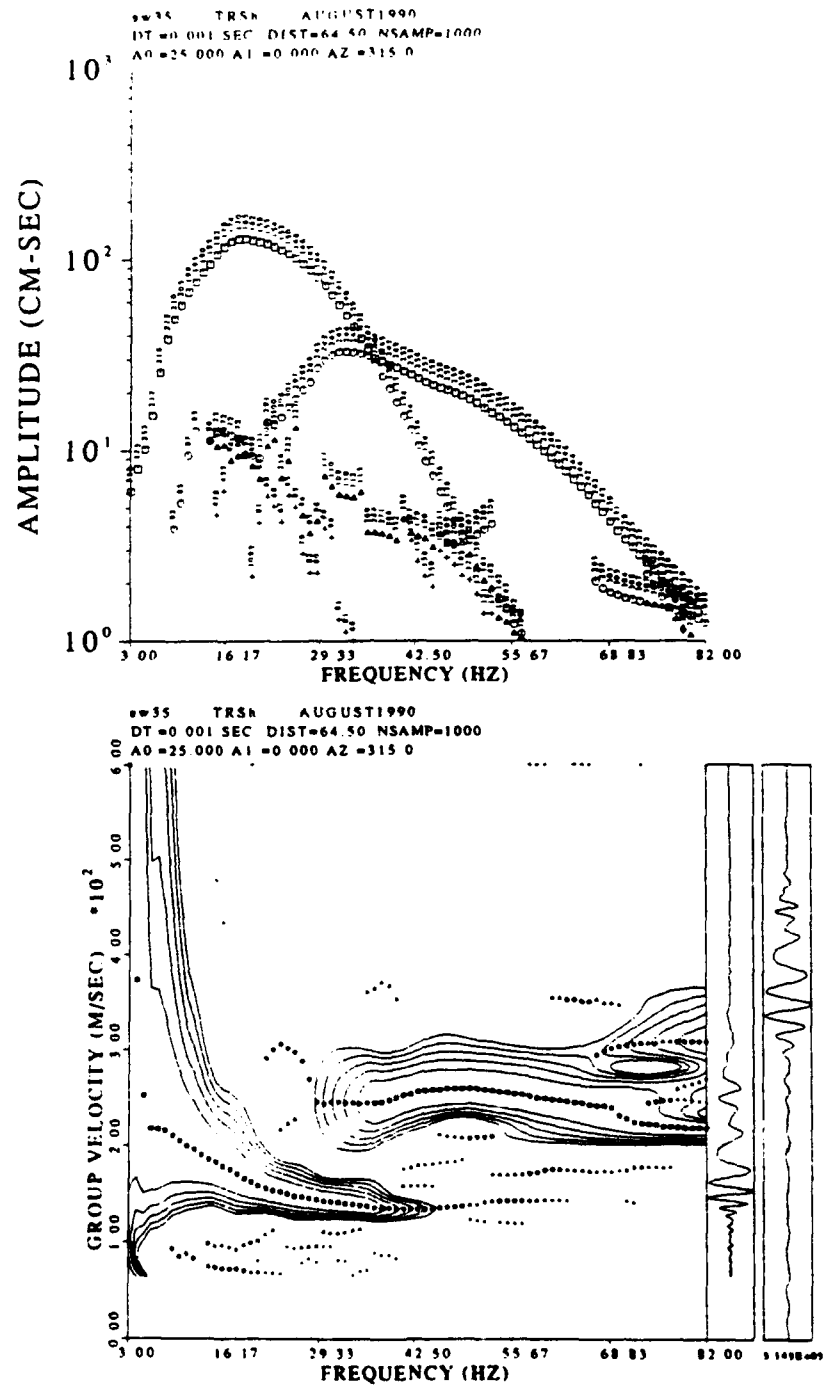


Figure 38. MFT analysis at 64.5 m for SWIG data

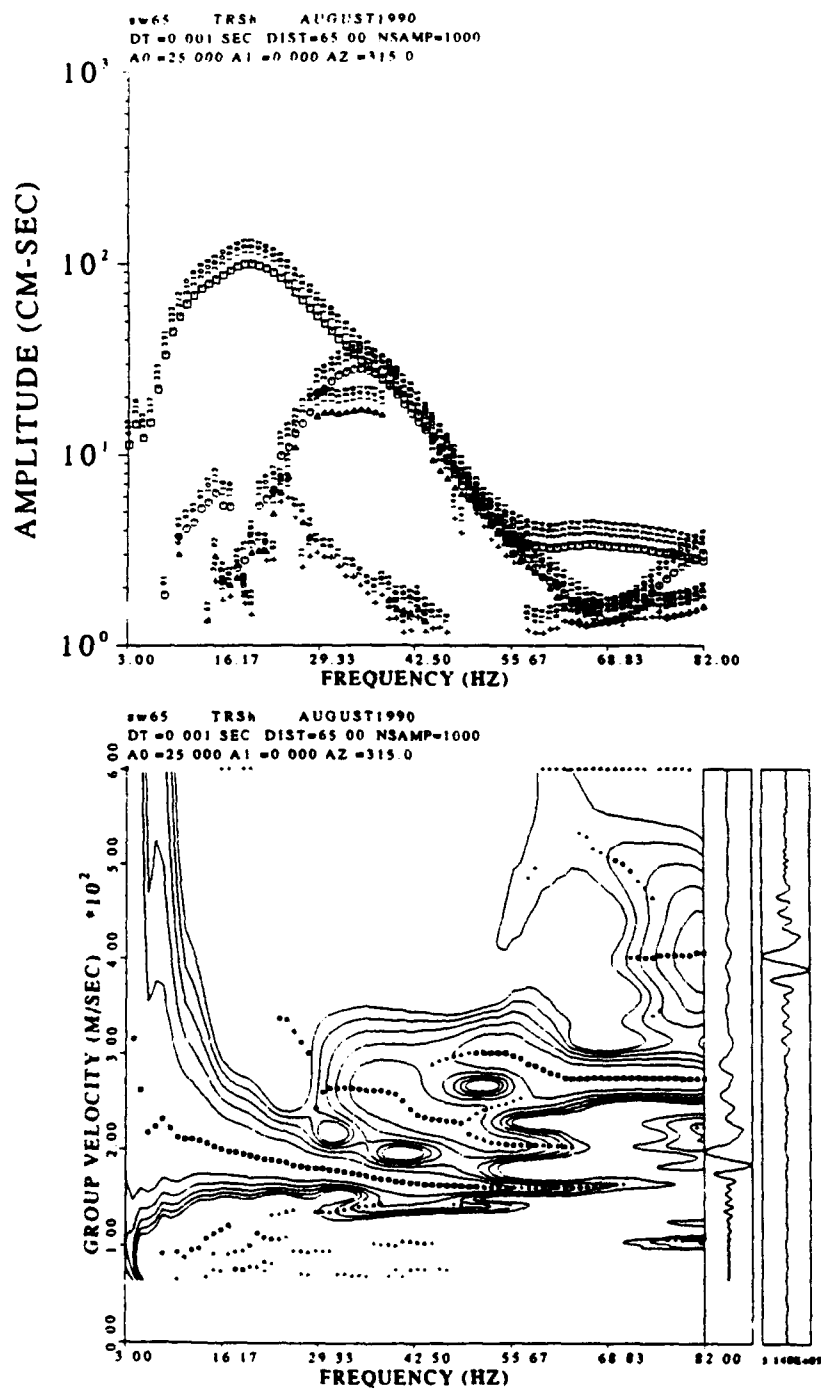


Figure 39. MFT analysis at 65.0 m for SWIG data

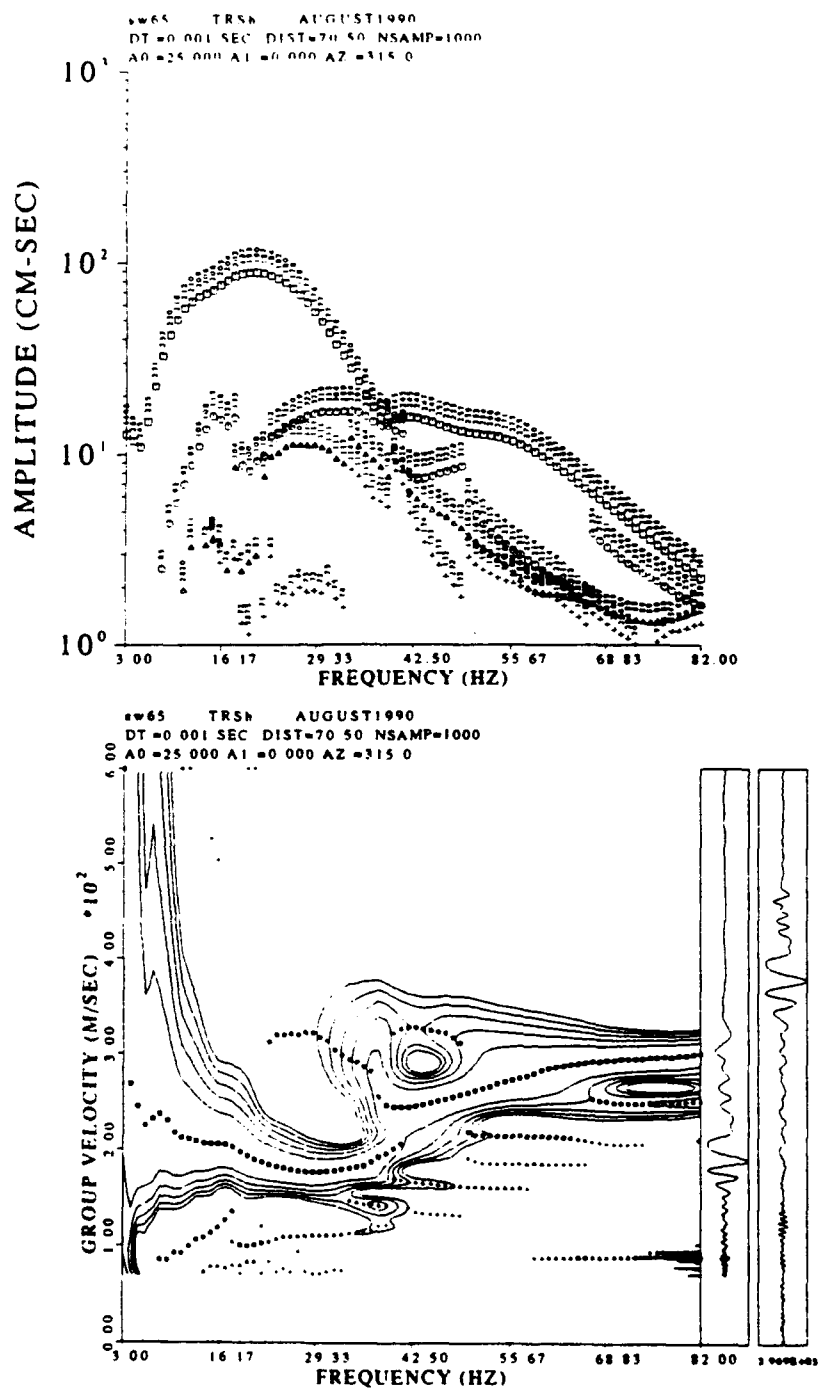


Figure 40. MFT analysis at 70.5 m for SWIG data

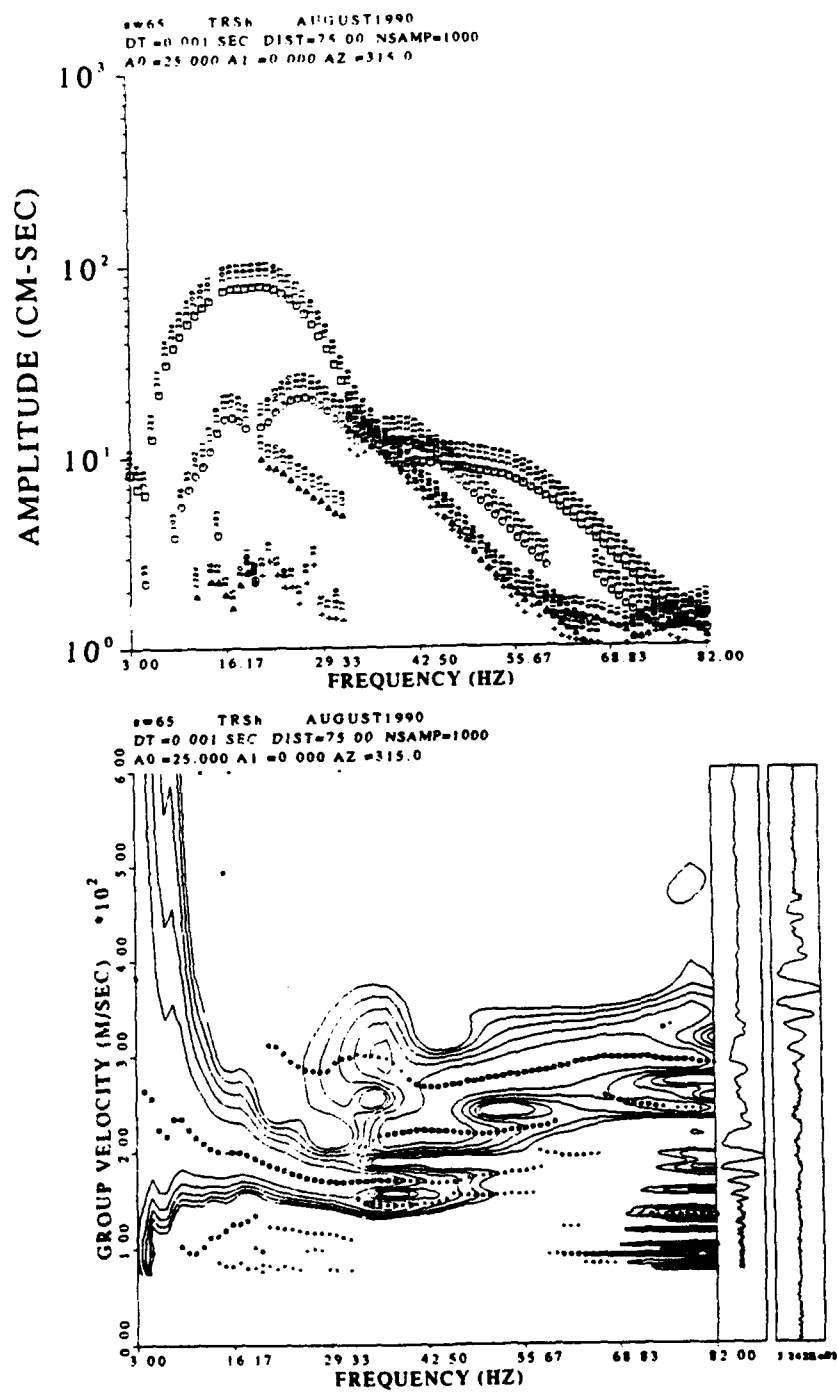


Figure 41. MFT analysis at 75.0 m for SWIG data

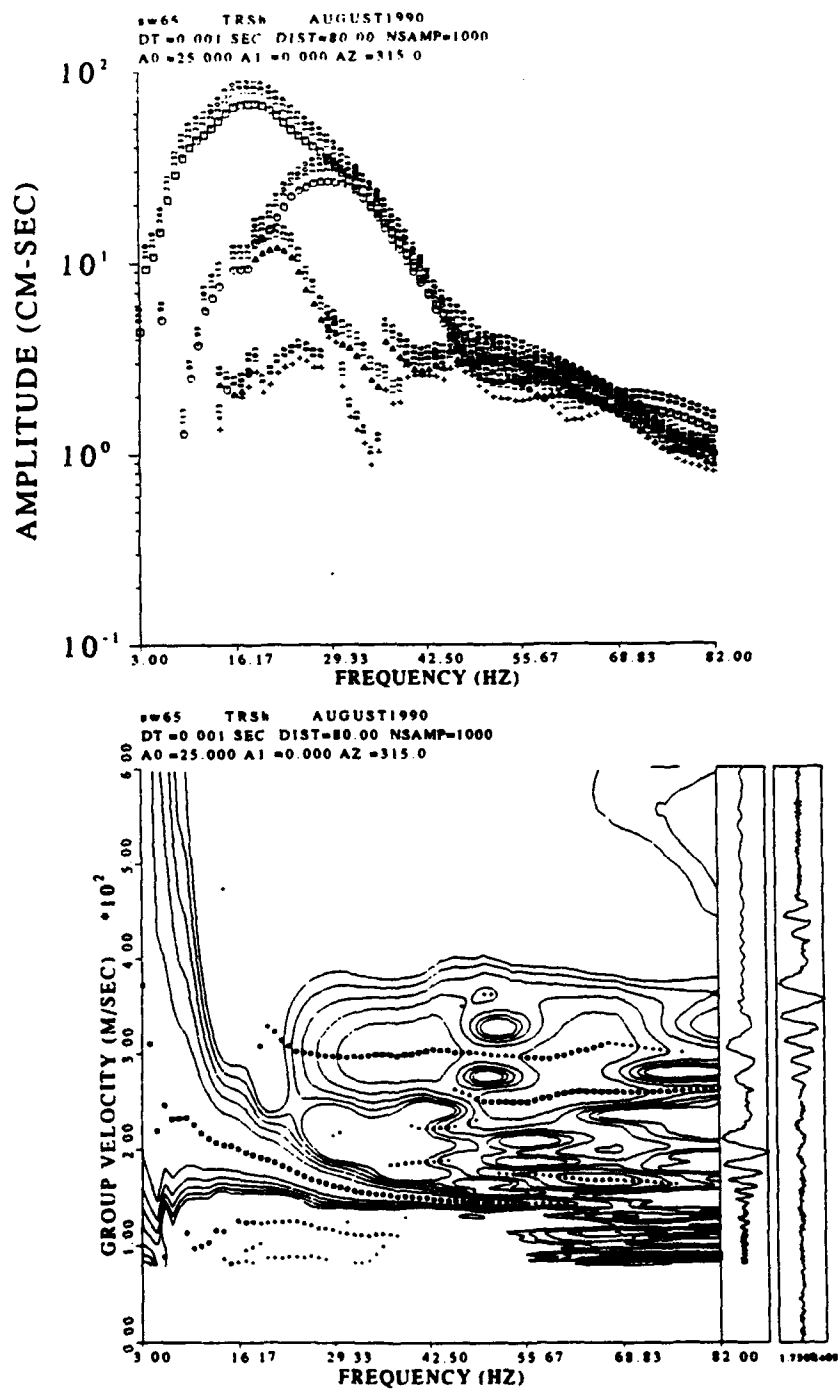


Figure 42. MFT analysis at 80.0 m for SWIG data

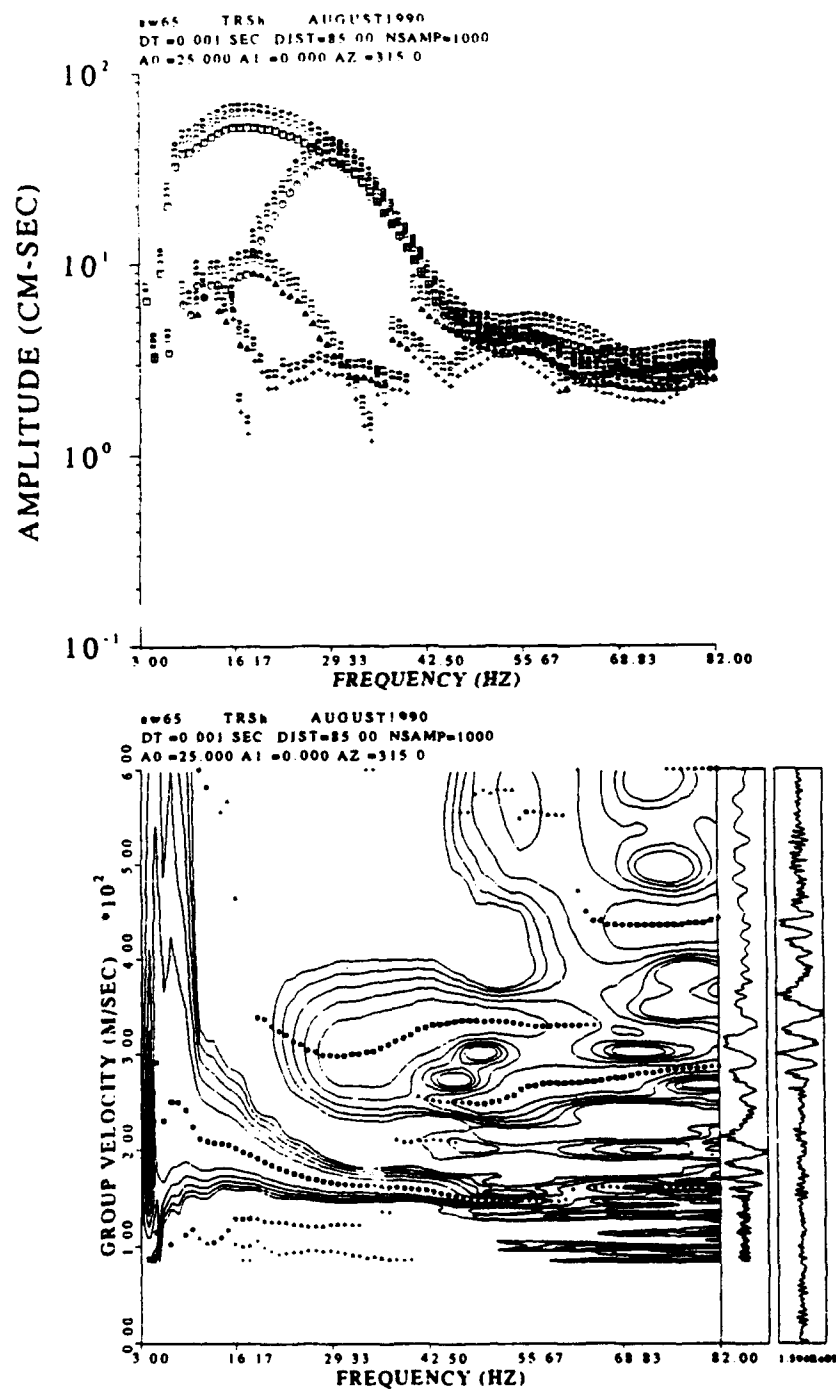


Figure 43. MFT analysis at 85.0 m for SWIG data

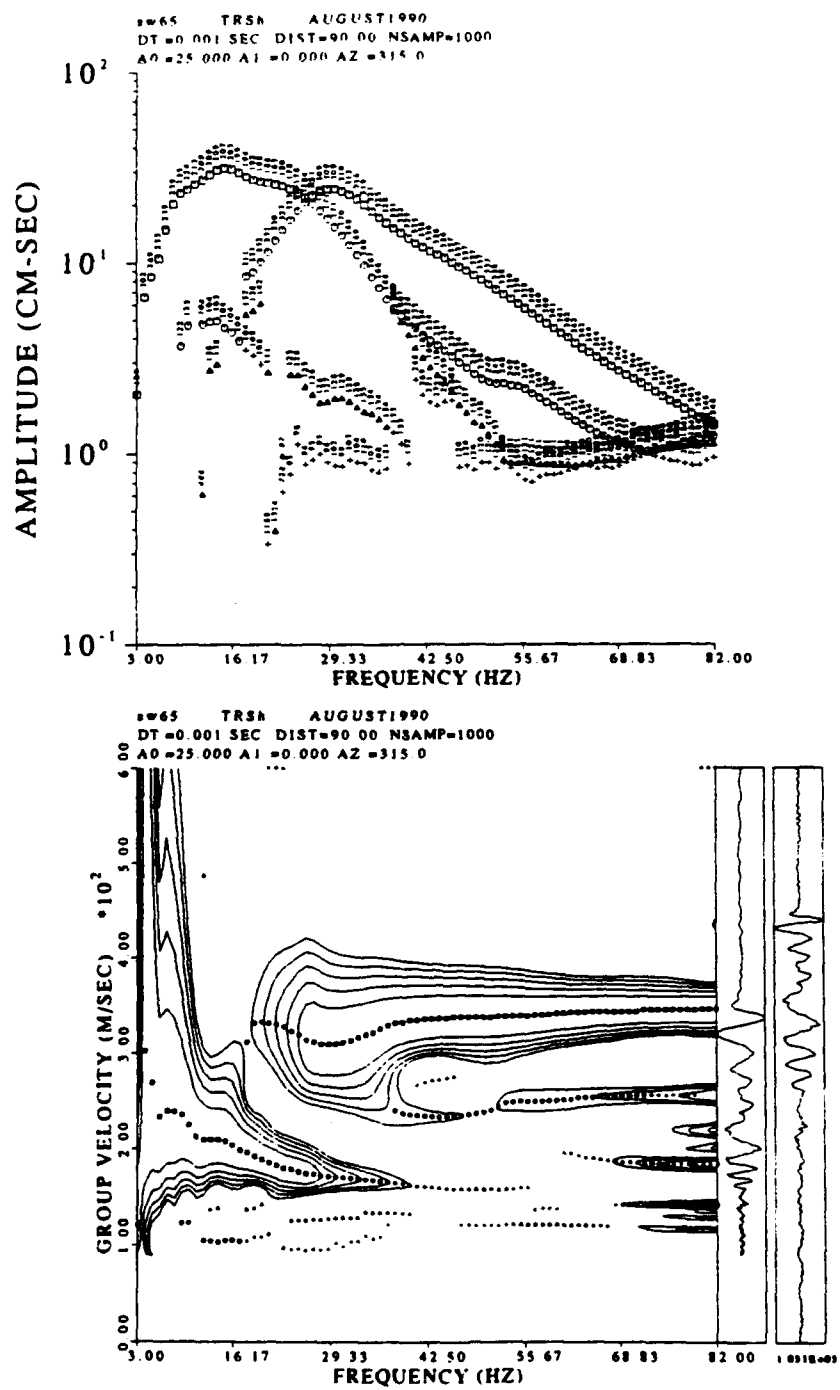


Figure 44. MFT analysis at 90.0 m for SWIG data

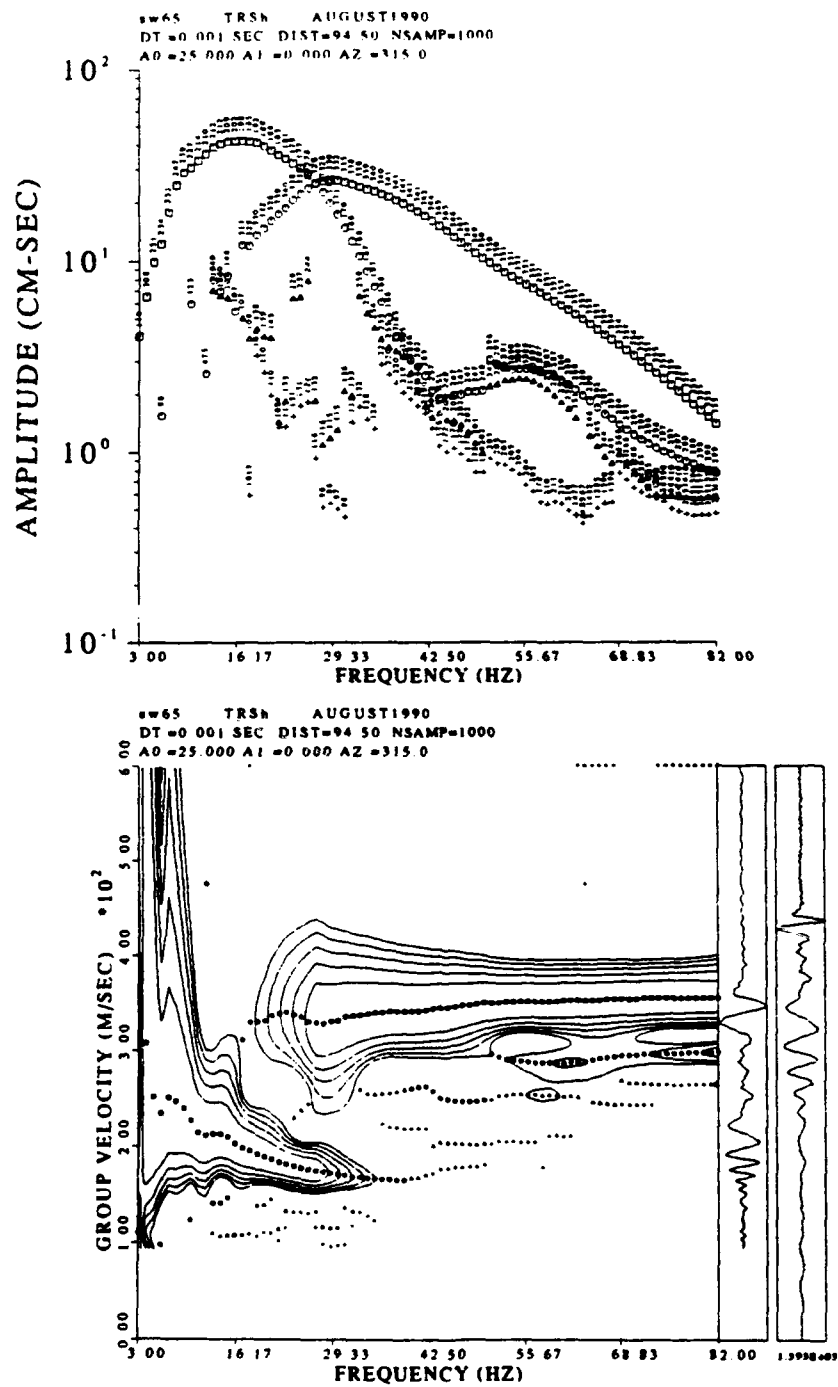


Figure 45. MFT analysis at 94.5 m for SWIG data

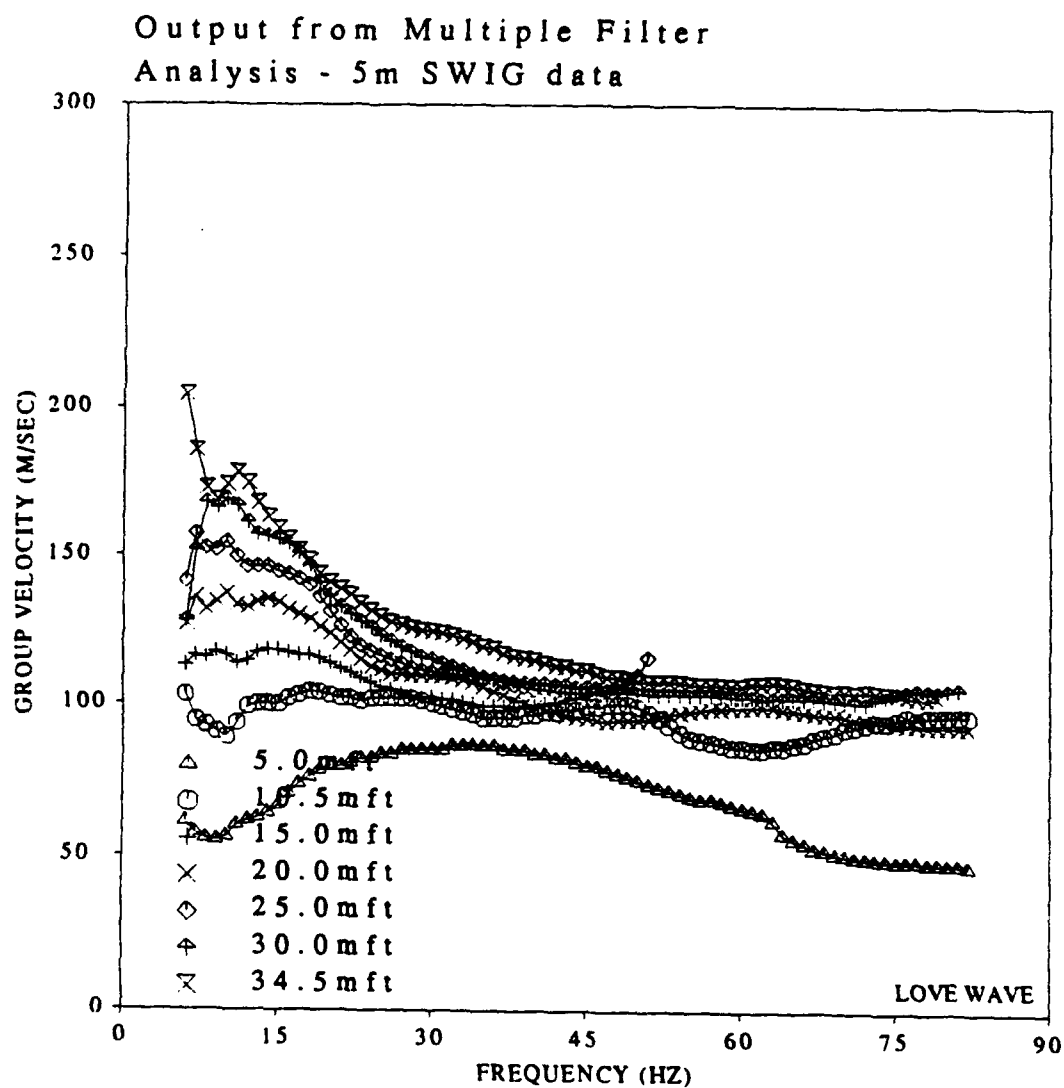


Figure 46. Interpreted dispersion curves for Love wave group velocity from multiple filter analysis at range of 5 to 34.5 m. Source at 5 m from near receiver.

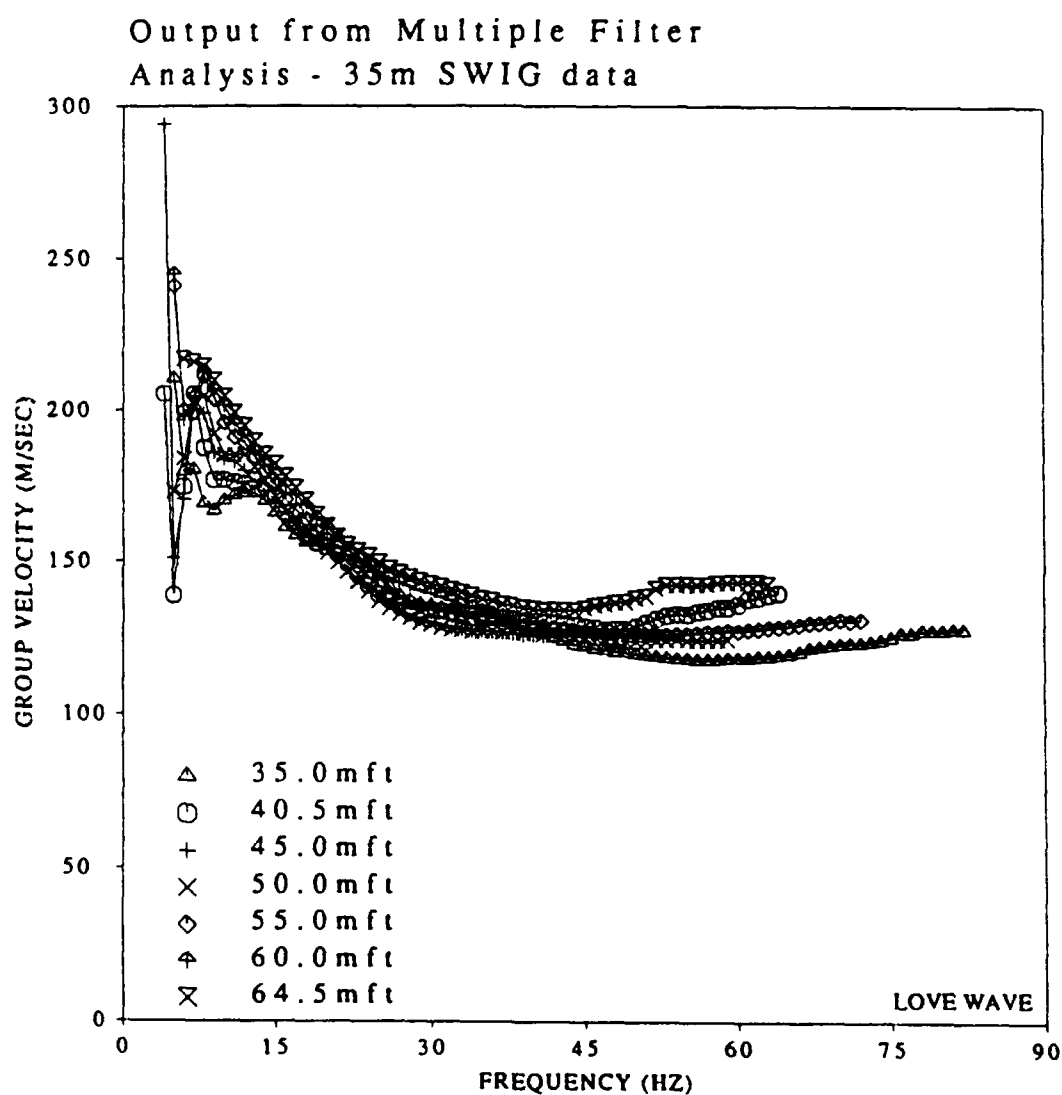


Figure 47. Interpreted dispersion curves for Love wave group velocity from multiple filter analysis at range of 35 to 64.5 m. Source at 35 m from near receiver.

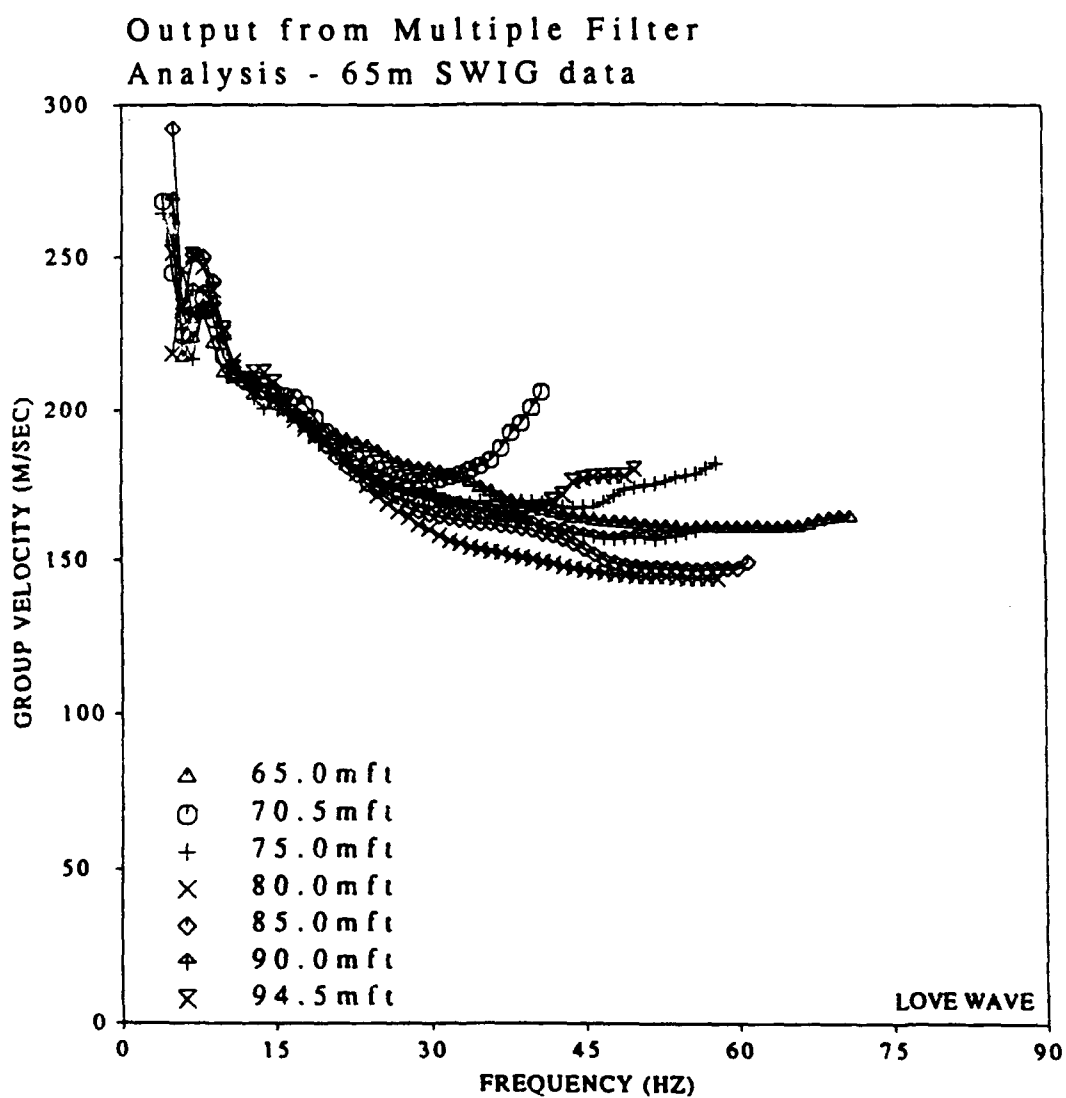


Figure 48. Interpreted dispersion curves for Love wave group velocity from multiple filter analysis at range of 65 to 94.5 m. Source at 65 m from near receiver.

still shows some increase over the interval from 35 to 64.5 m (Figure 47), but substantially less change than observed in the 5 to 34.5 m data set. This result implies that the Love wave is not fully stabilized by 35 m, but is nearly so at 65 m. The final composite plot, Figure 48, shows the MFA interpreted dispersion curves from 65 to 94.5 m. The values are almost coincident between 10 and 25 Hz. The Love wave appears stabilized and usable for making geological interpretations at these offsets.

The Betsy data sets covers the same intervals, but are slightly more complicated since they contains both a fundamental mode as well as the first higher mode Rayleigh wave. In addition, the temporal separation of the events is smaller, making analysis more difficult. The multiple filter processing of the Betsy data set is contained in the Appendix.

C. Array Processing of Group Velocity

1. Experimental Technique

The Herrmann (1987) software package used in this study implements a technique from Barker (1988) which makes use of an array of seismograms to determine group velocity. This technique uses the multiple filter algorithms previously documented. Each trace is bandpassed with a series of Gaussian filters. The envelope of each resulting bandpassed trace is then computed. The additional step involved in array processing is to stack the normalized envelopes along lines of constant velocities. As Herrmann notes, this step is not a slant stack, since only a single point results from stacking along each velocity. Up to four peaks of this stacked envelope function are selected to yield group velocities of up to four modes at a particular frequency. This processing is then fol-

lowed by a more detailed analysis, in which each original envelope trace is searched around each of the four average velocities to obtain the individual group velocities, which generally differ from the initial estimate. The individual velocities are used to compute a mean group velocity and standard error. These velocities represent an average response of the material being imaged by the different source receiver pairs. As with the multiple filter analysis, the different modes must be separated in time by:

$$(3.3) \quad T(A_0/\pi)^{1/2},$$

where T is the period of the current bandpass filter. If several modes occur too near one another, the results of this analysis would indicate only one mode present. The group velocities would thus be in error due to interference phenomena.

One additional feature of this array analysis is that it can be used to calculate the anelastic attenuation coefficient, γ . The peak amplitudes of the unnormalized envelopes are input into a regression analysis of logarithmic amplitude versus offset which assumes a model of the form:

$$(3.4) \quad \ln A(r, \omega) = \ln A_0 - \gamma R(\omega)r$$

The option exists for making a geometrical spreading correction before calculating the attenuation coefficients. The anelastic coefficients determined here can be used to invert for Q . This procedure will be used later in the study to limit the uncertainty in the inversion of the velocity dispersion.

2. Experimental Results

The Barker technique for group velocity determination was applied to the SWIG data in 3 groups. The value for A_0 used for this work was 25, corresponding to a bandwidth of 35%, the same value that was used for the multiple filter analysis. The eleventh trace on all three sections of the SWIG data set was noisy and was not included in the processing. One of the useful features of this type of processing is that the stacking is across equal velocities. Uneven spatial sampling can thus be accommodated.

The outputs of this processing on the three sections of the SWIG data (Figures 49 through 51) contain contours of the amplitude corresponding to 99%, 90%, 80%, 70%, 60% and 50% of the maximum amplitude of the envelopes. As with the MFT, the largest amplitude peak is marked by squares, second largest by circles, third largest by triangles and the fourth largest by plus signs. The largest event over the interval 10 to 30 Hz corresponds to the fundamental mode Love wave with its frequency content decreasing with distance. The near data set appears coherent from 6 Hz to 80 Hz with velocities ranging from about 95 to 150 m/s. The group velocity shows more dispersion and higher velocities with distance. This effect appears to be the result of some near field effects combined with the fact that it takes some time (or distance) for the surface waves to be set up, especially at the longer periods. The velocity dispersion of the 3 data sets (Figure 52) show no overlap even at the higher frequencies. This difference certainly implies that an offset greater than 65 m would be necessary for consistent results. Figures 53 to 59 are overlays of the single station MFT results with the array results for the data set from 65 to 94.5 m. The results are

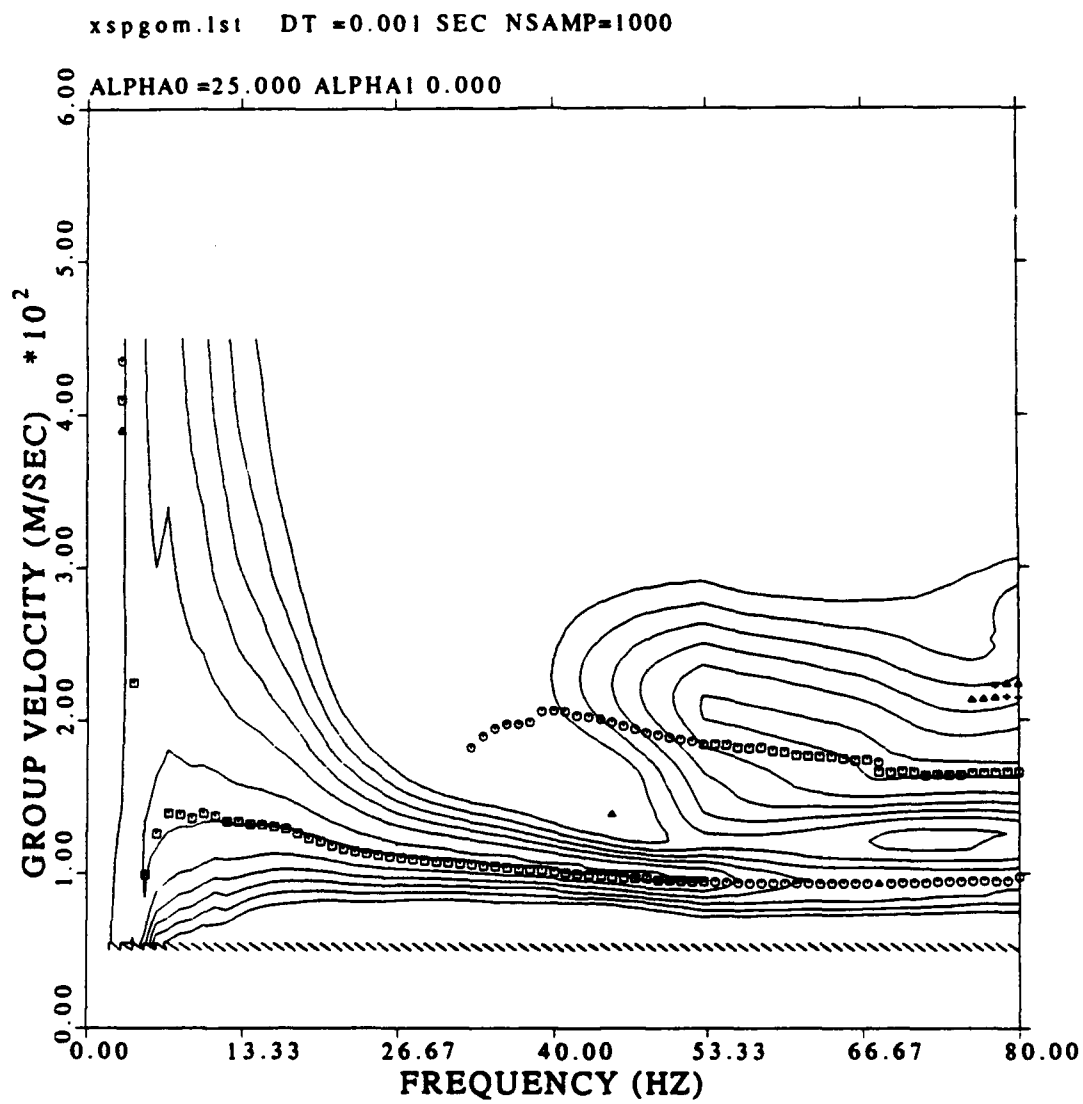


Figure 49. Barker technique array processing of the SWIG data set for group velocity over the interval from 5 to 34.5 m

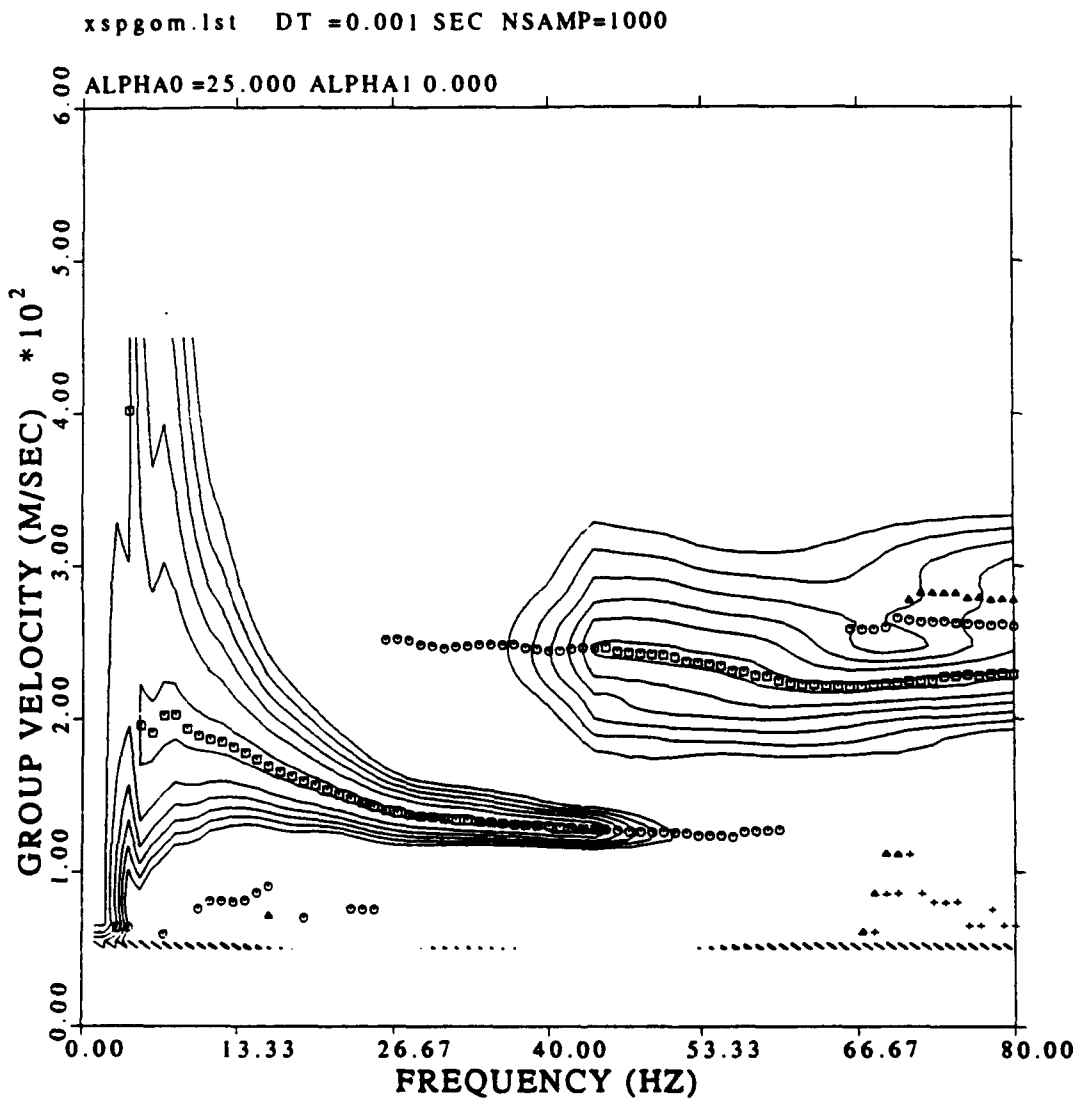


Figure 50. Barker technique array processing of the SWIG data set for group velocity over the interval from 35 to 64.5 m

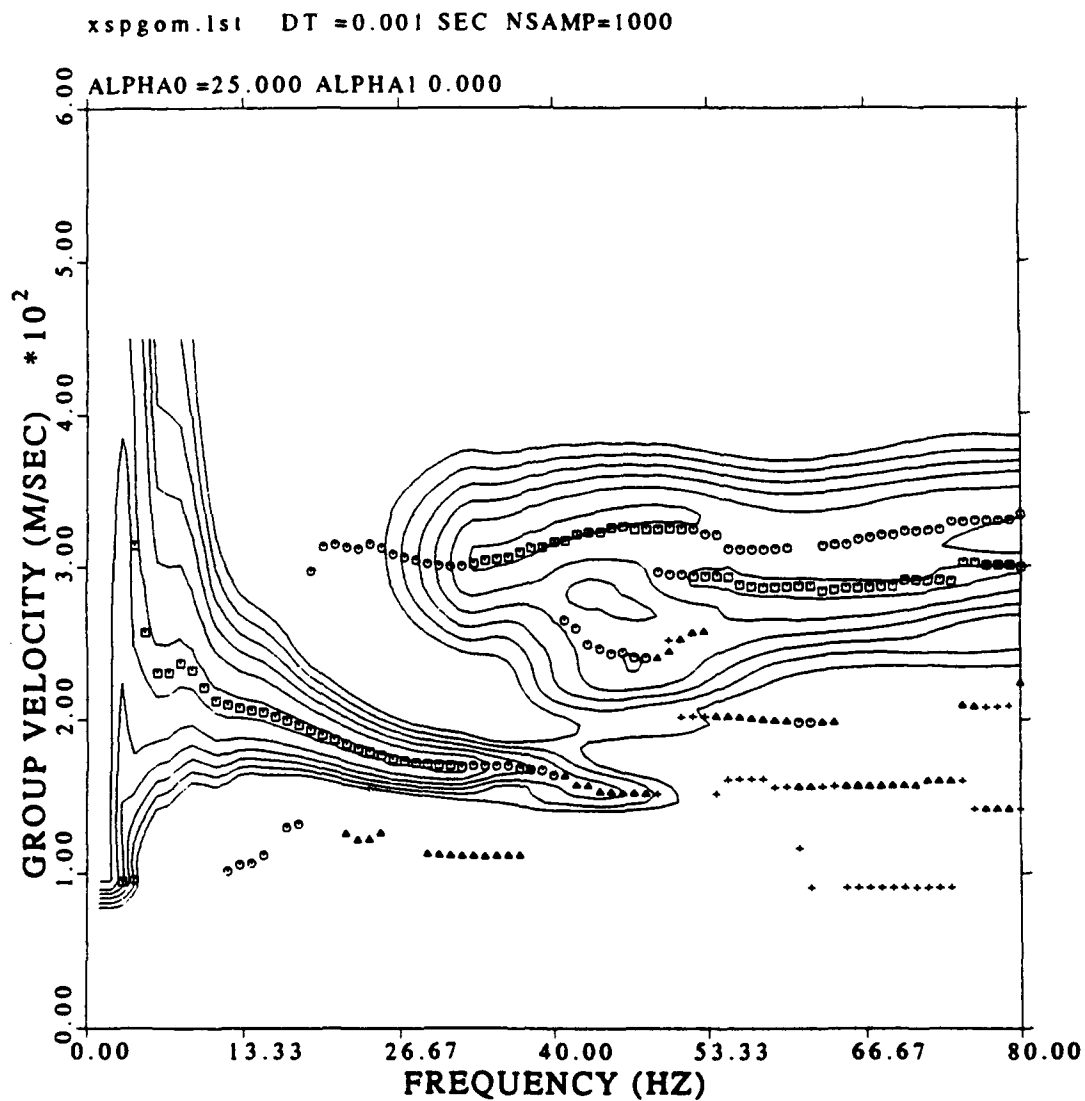


Figure 51. Barker technique array processing of the SWIG data set for group velocity over the interval from 65 to 94.5 m

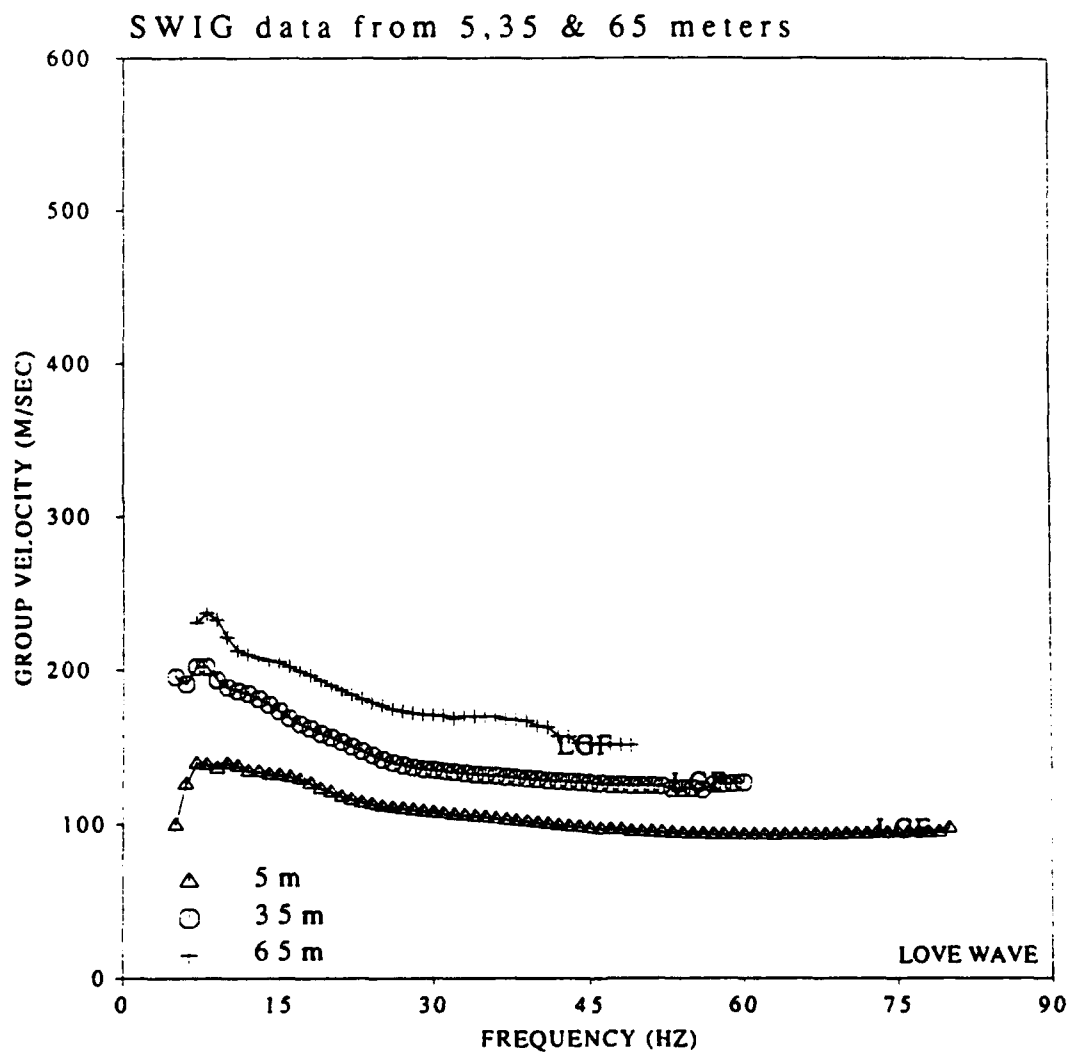


Figure 52. Overlay of the Barker technique group velocity dispersion from 5, 35 and 65 meter SWIG data sets

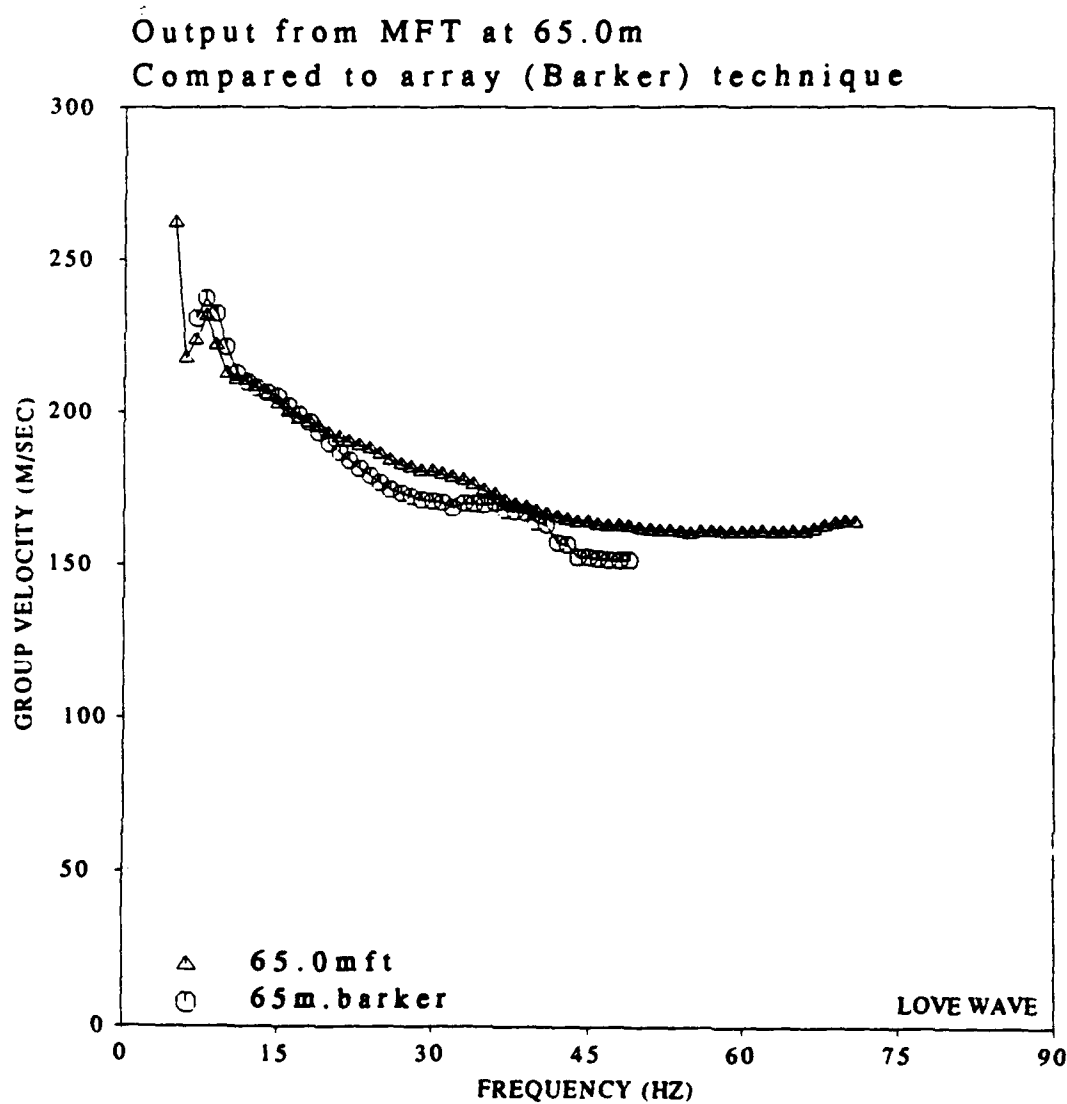


Figure 53. Single station processing at 65.0 m (triangles) versus array processing using Barker technique(circles) of 65 meter SWIG data

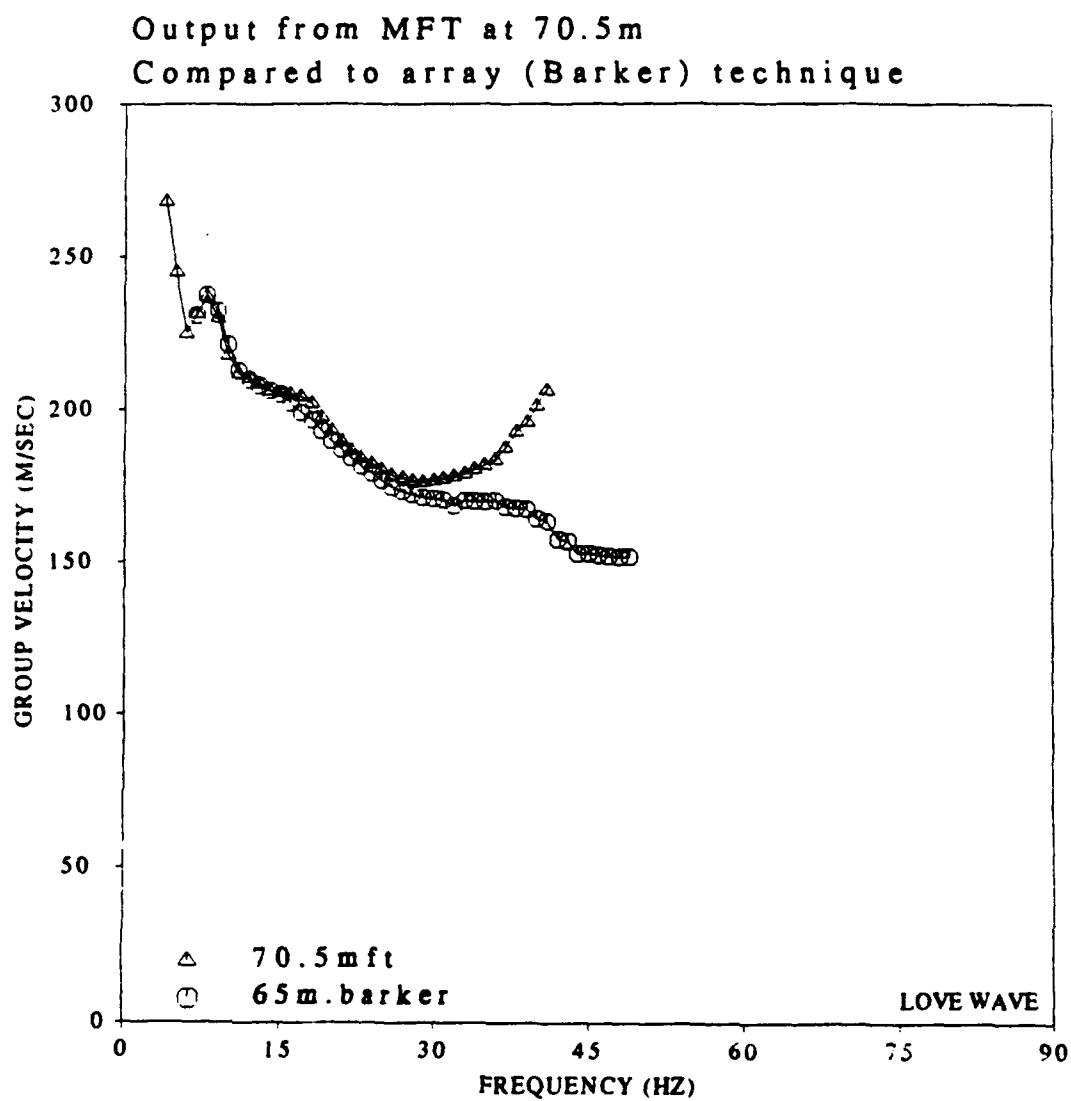


Figure 54. Single station processing at 70.5 m (triangles) versus array processing using Barker technique (circles) of 65 meter SWIG data

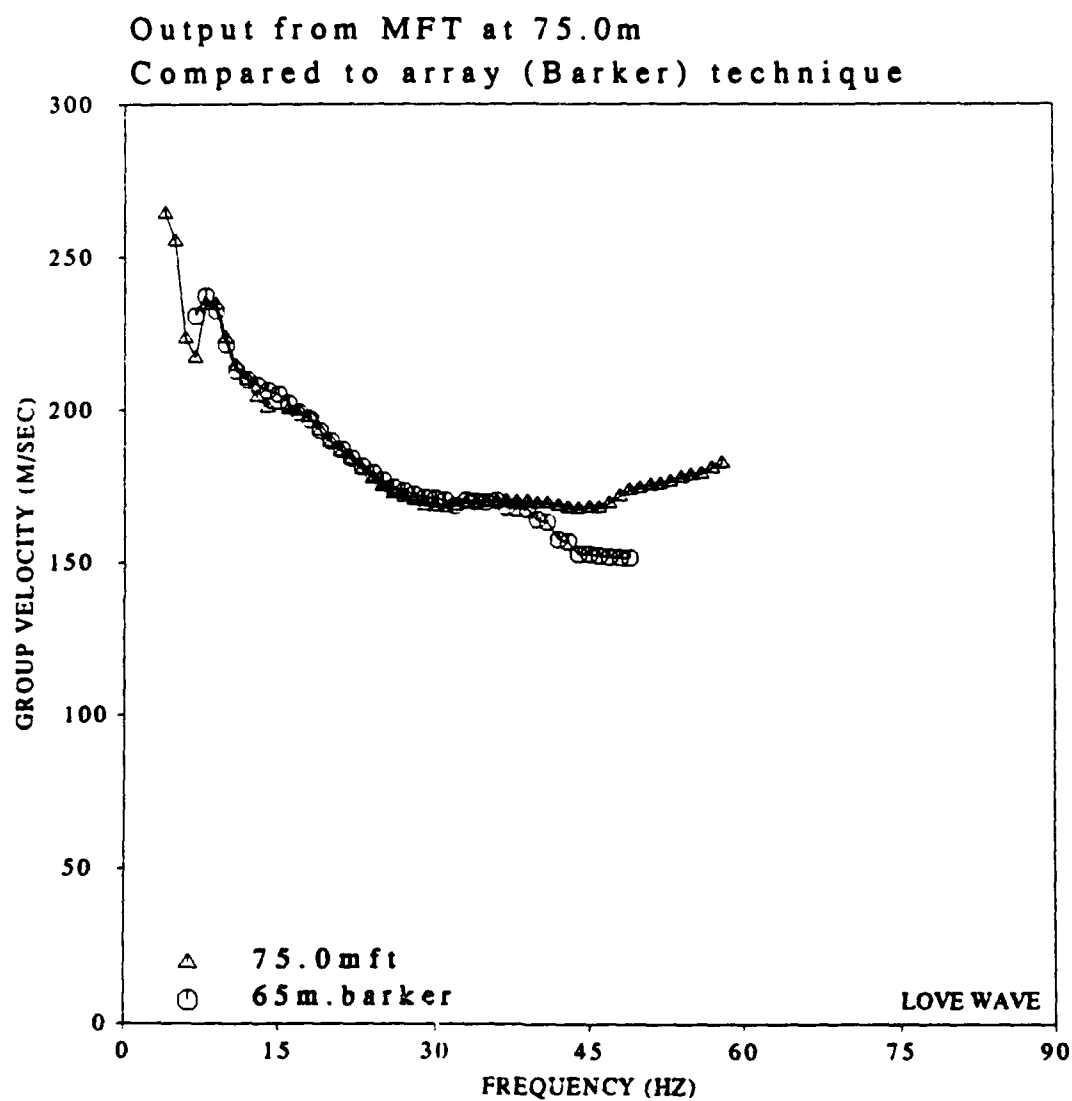


Figure 55. Single station processing at 75.0 m (triangles) versus array processing using Barker technique(circles) of 65 meter SWIG data

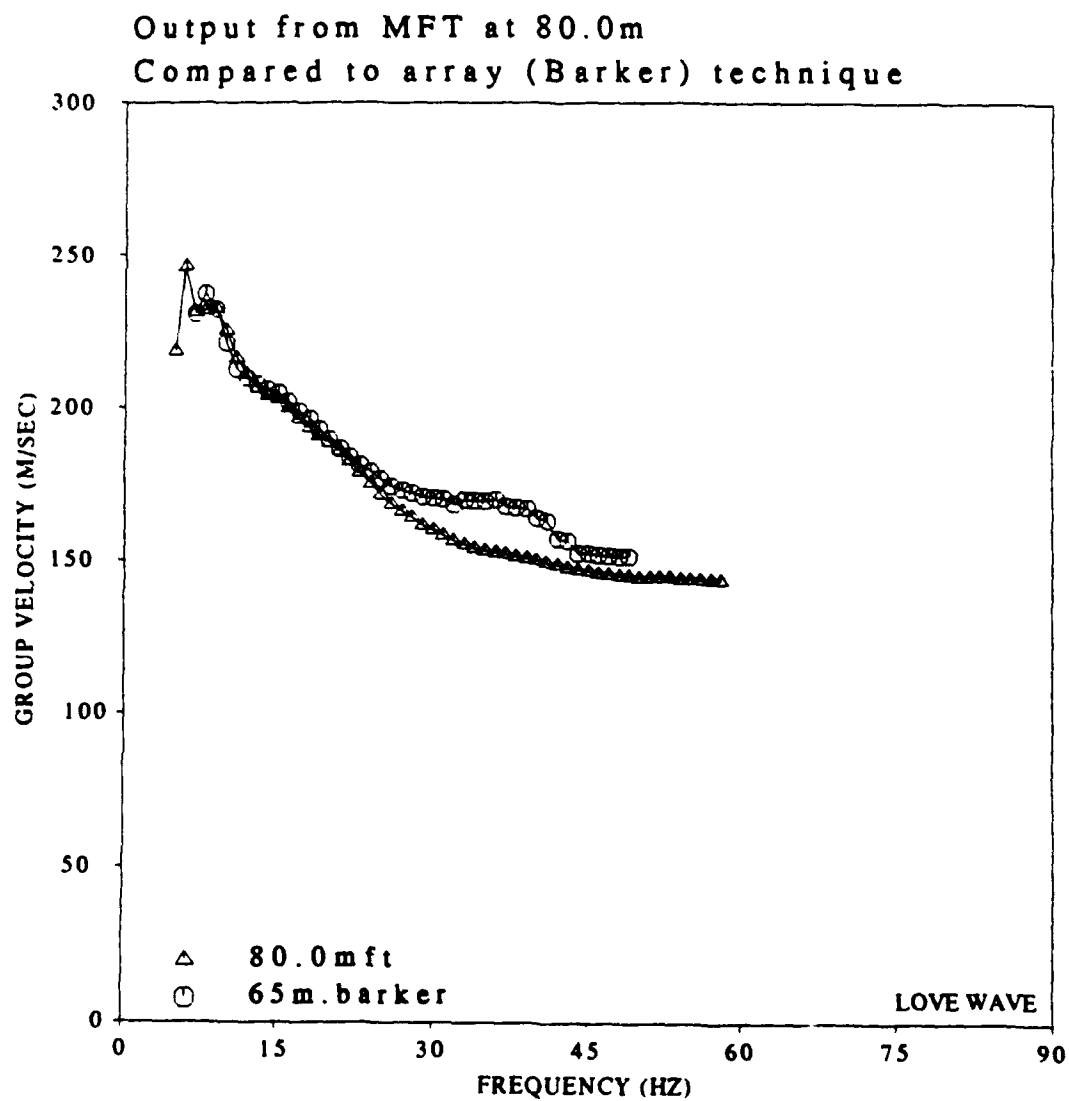


Figure 56. Single station processing at 80.0 m (triangles) versus array processing using Barker technique (circles) of 65 meter SWIG data

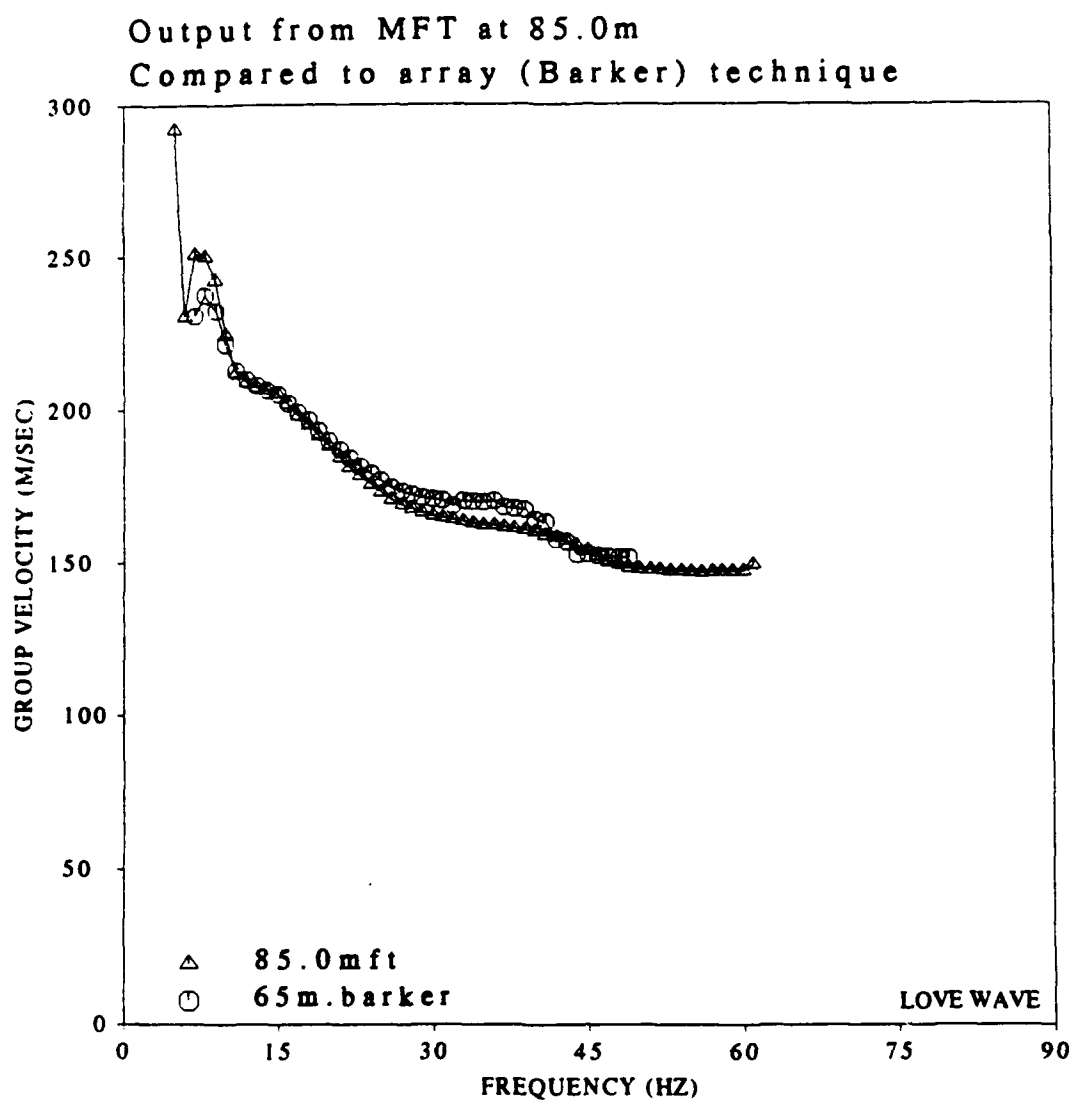


Figure 57. Single station processing at 85.0 m (triangles) versus array processing using Barker technique(circles) of 65 meter SWIG data

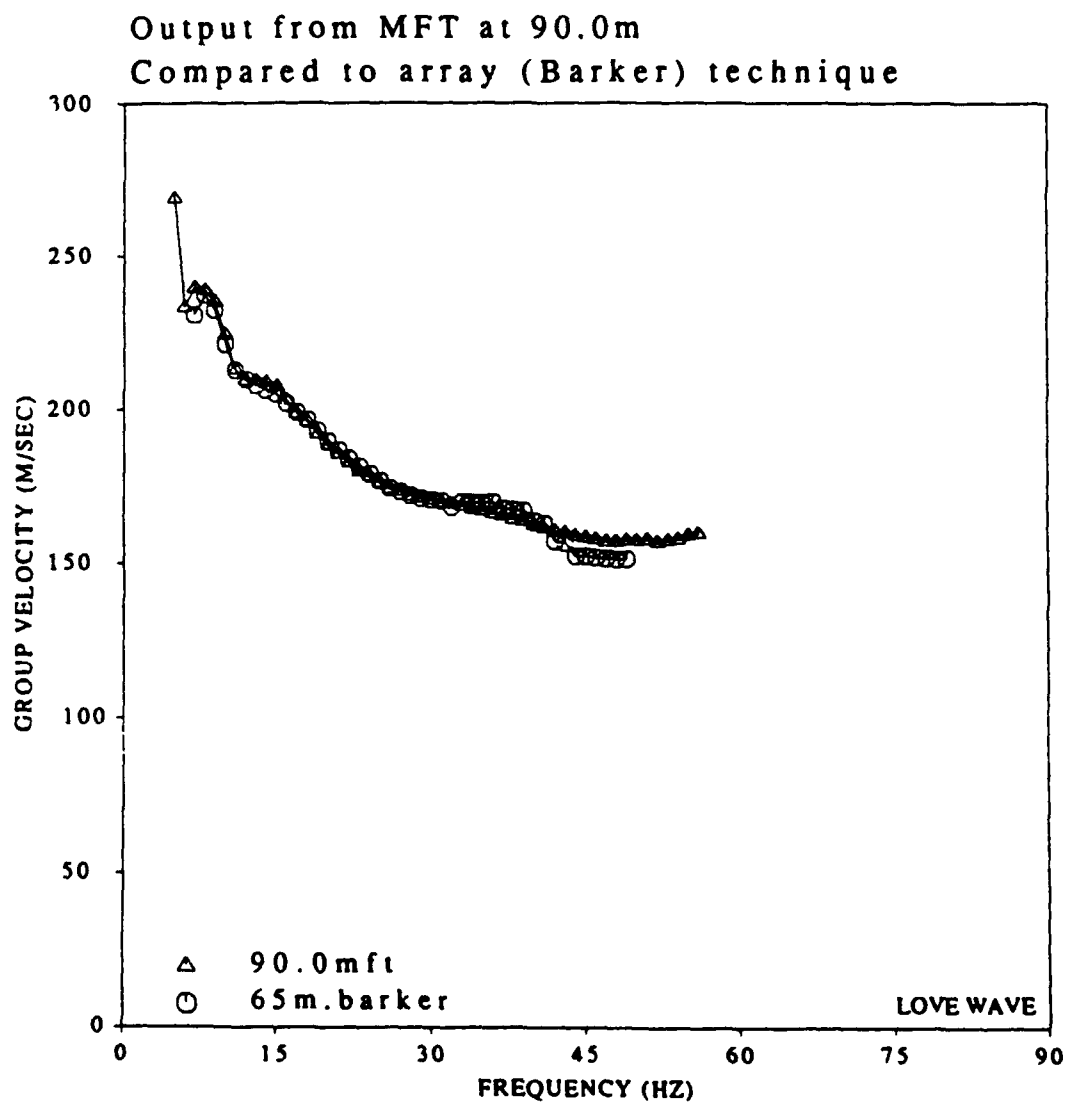


Figure 58. Single station processing at 90.0 m (triangles) versus array processing using Barker technique(circles) of 65 meter SWIG data

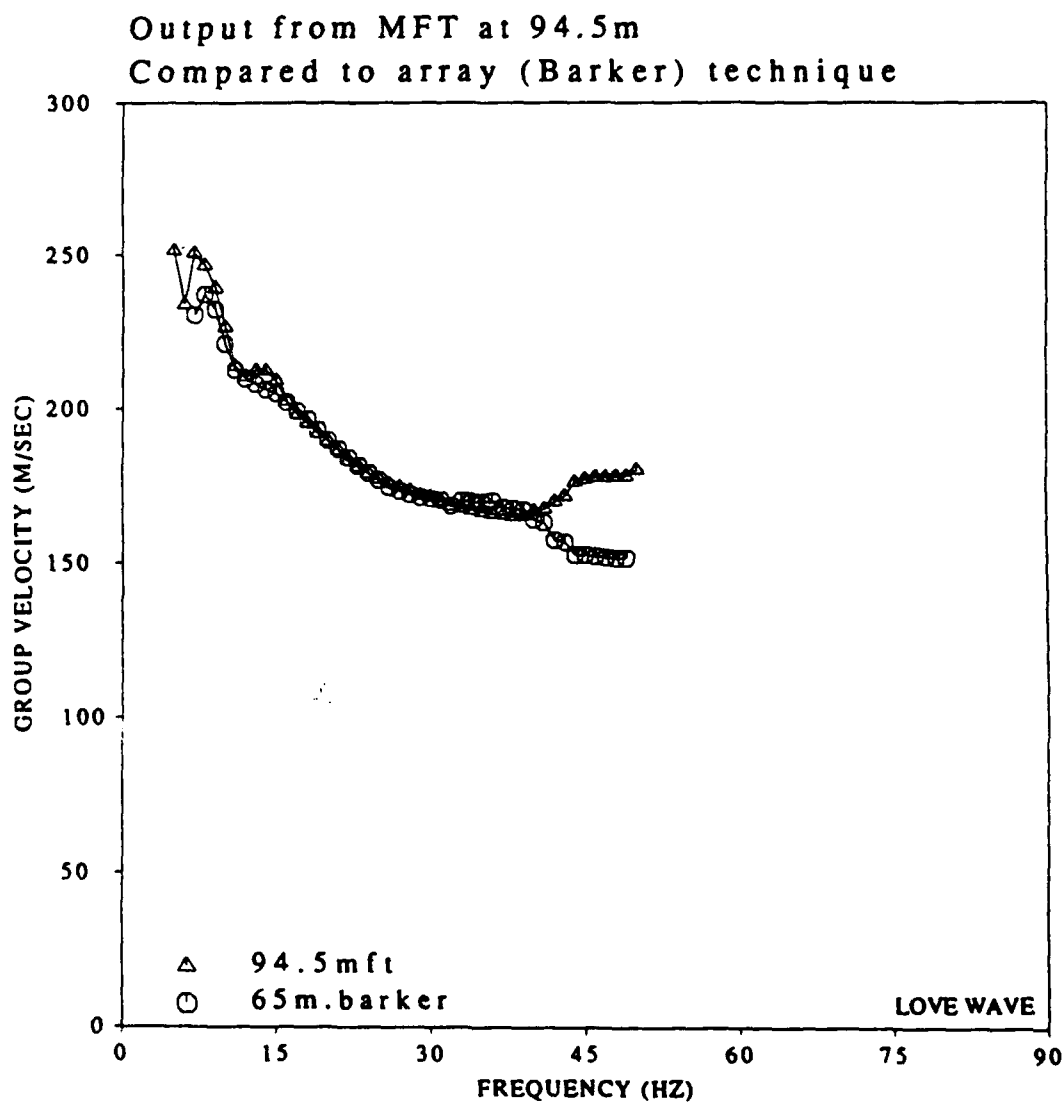


Figure 59. Single station processing at 94.5 m (triangles) versus array processing using Barker technique(circles) of 65 meter SWIG data

very consistent up to 29 Hz. The results above 29 Hz show an increased amount of scatter.

Examination of the endpoints of the data where the sources were moved illustrate some significant aspects of the structure. Figure 60 shows the single station analysis of group velocity at 34.5 and 35.0 m. The single station results are also contrasted to the corresponding array velocities at 5 to 34.5 m and 35 to 64.5 m. Although there is only 0.5 meter difference in range between the two single station measurements, there is a substantial difference in the group velocity curves. The two velocities are almost the same from 6 to 12 Hz and differ by about 10 percent above 20 Hz. The acquisition involved leaving the geophones stationary and moving the sources to increase the range. The group velocity is the result of the average velocity structure between the source and receiver. In this case, although there is only one half meter change in range, there is only 5.0 m overlap in the interval covered. This leads to the conclusion that the difference between the two group velocities is due to lateral changes in the velocity field. The fact that these velocities are different at higher frequencies and the same at low frequencies indicates that the velocity structure is different for the shallower layers, but the same for the deeper structure.

These conclusions can be checked by comparing the results at 64.5 m and 65.0 m in Figure 61. Once again, the two ranges are 0.5 m apart, but the covered interval differs by 30 m. The two dispersion results are similar at low frequencies, but differ by 25 percent at frequencies from 20 to 40 Hz. The other interesting result is that both of these single station estimates are comparable to the corresponding array results. The single station dispersion results at 64.5 m is only slightly higher than the array or average results from 35 to 64.5 m. The

single station group velocity at 65 m matches almost perfectly the array average over the interval 65 to 94.5 m.

As noted earlier, the array processing provides the opportunity to estimate attenuation coefficients. These estimates increase with frequency (Figure 62) although there is some variability in the curves. The three data sets show similar attenuation at the lower frequencies, between 8 and 20 Hz. As with all the data, there is greater scatter at frequencies above 30 Hz.

The variability of the velocity and attenuation estimates at high frequencies is a process that needs to be understood if one is to fully utilize the results. One probable explanation for this variation is that the assumption of horizontally stratified layers is being violated in the shallowest part of the subsurface. At a frequency of 30 Hz, with the shallowest layer shear velocity of 150 m/s, one wavelength is about 5 m. If the shallowest layer was varying smoothly from 1.5 to 4 m in thickness, the dispersion results for the higher frequencies could show substantial variance. Bogaards (1989) indicated that the high frequency variations could be the result of scattering off of caliche lenses.

The high frequency variability indicates more geologic complexity in the shallowest environments than was expected at the start of this study. The consistencies at lower frequencies, or longer wavelengths, indicates that the deeper horizons are more geologically uniform than the shallowest environment.

The body wave portion of the wavefield in the array processing shows some variance in velocity versus frequency, but is centered around 200 m/s for the nearest data set. The body wave velocity increases with offset. This result is consistent with a normal refraction survey with an increase in velocity with depth for various layers.

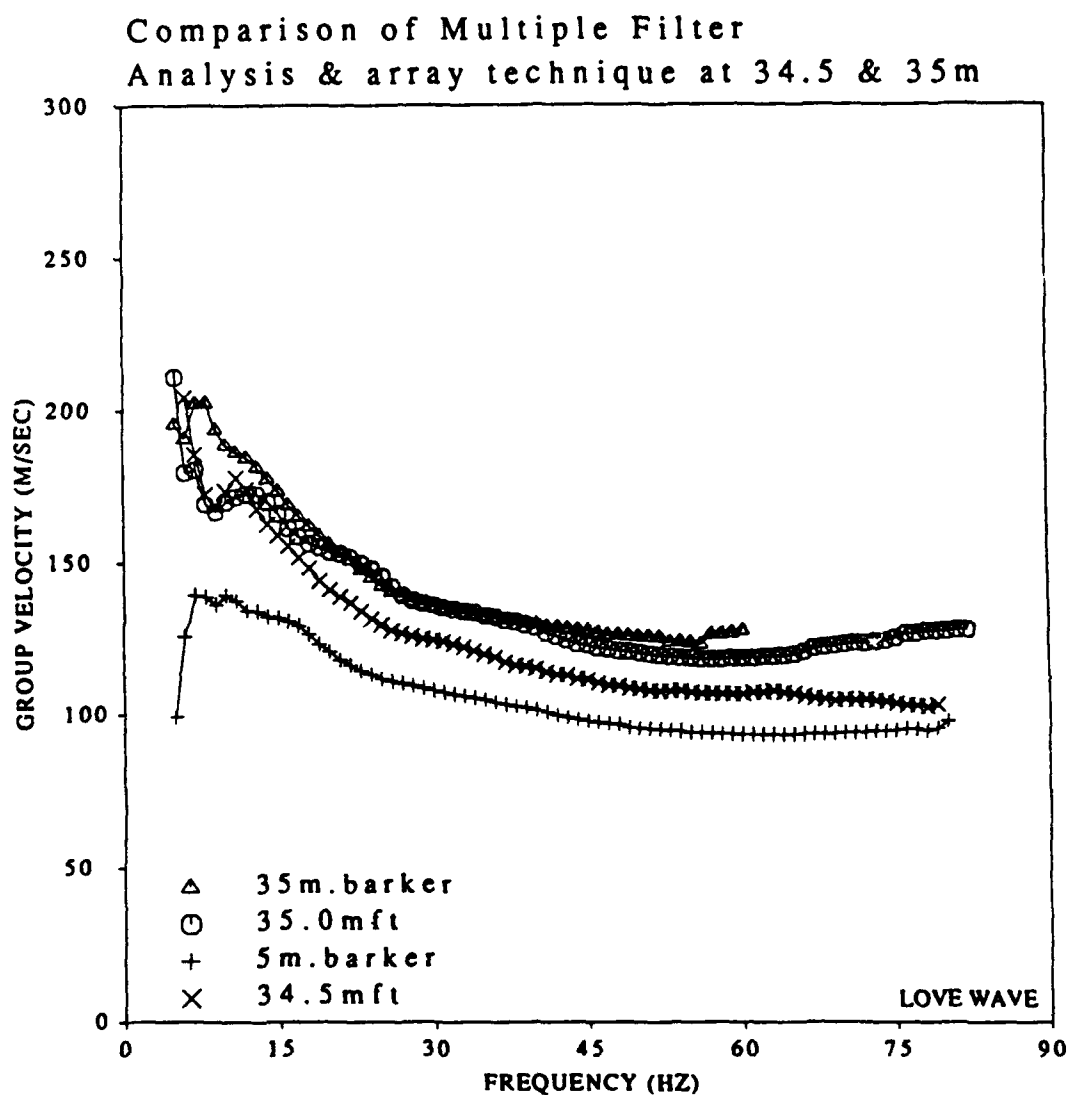


Figure 60. Comparison of Multiple filter analysis and array techniques at 34.5 m and 35.0 m. 34.5 m single station processing represented by X; 35.0 m single station by circle, 5 to 34.5 m array by +, and 35 to 64.5 m array analysis by circles.

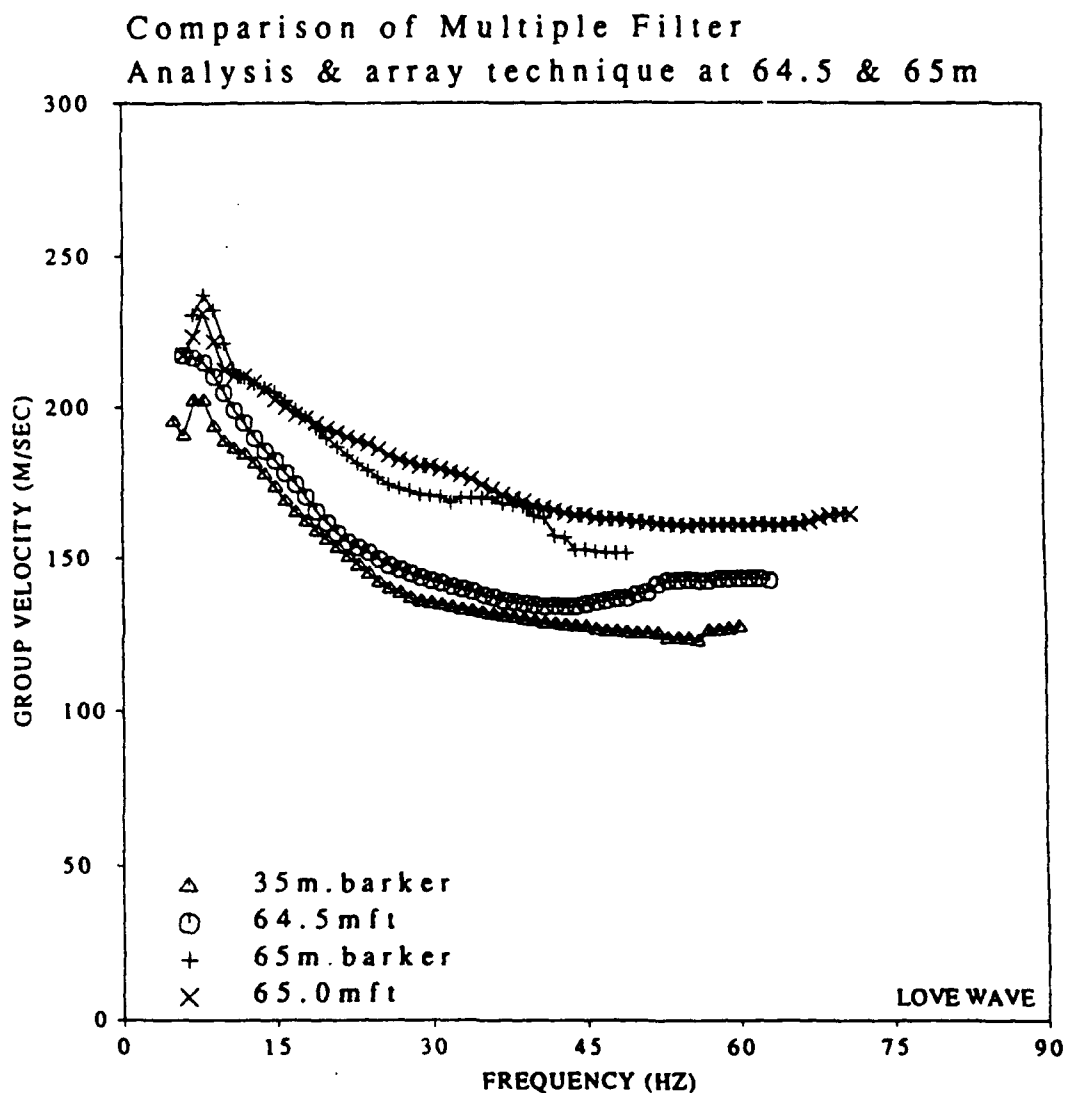


Figure 61. Comparison of Multiple filter analysis and array techniques at 64.5 m and 65.0 m. 64.5 m single station processing represented by circles; 65.0 m single station by X, 35 to 64.5 m array by triangles, and 65 to 94.5 m array analysis by +.

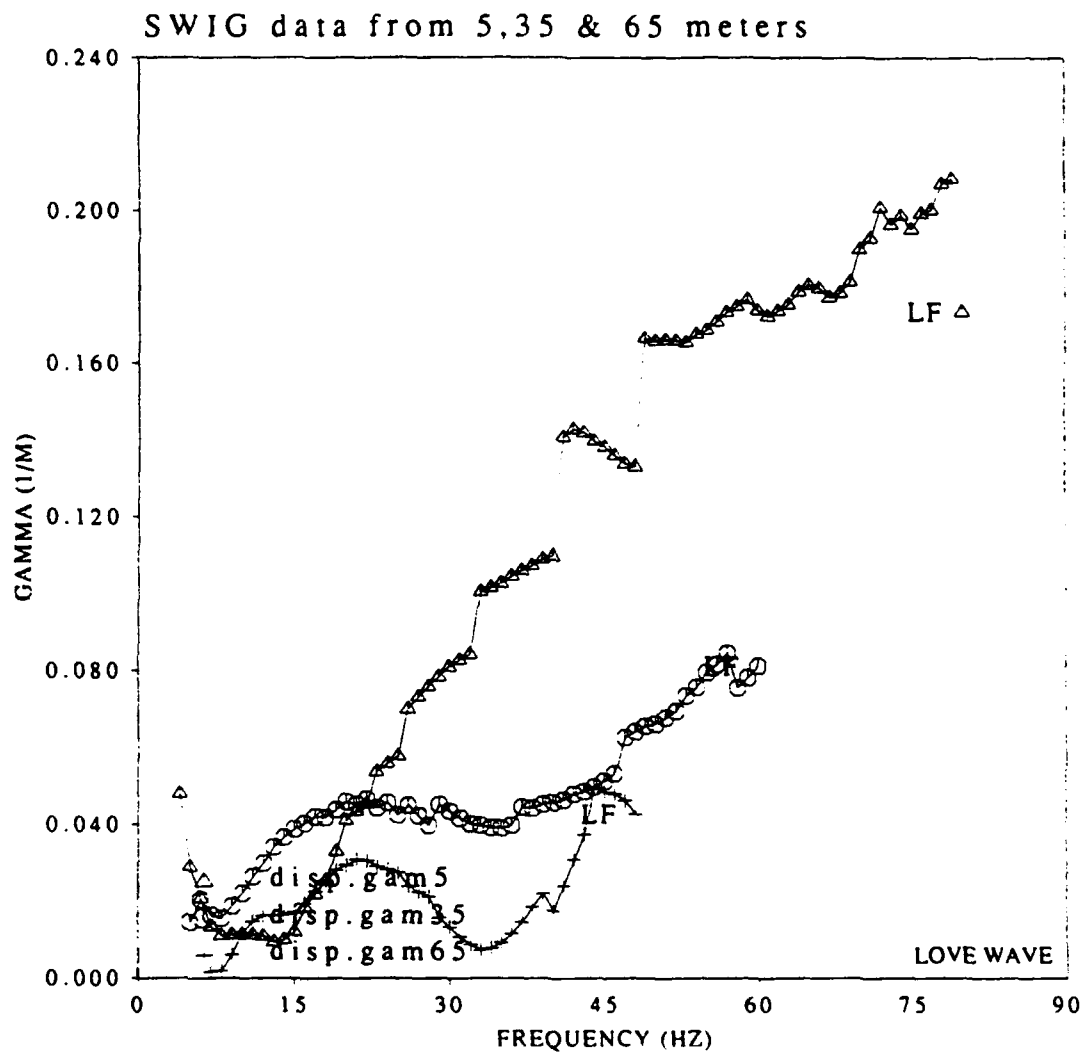


Figure 62. Attenuation coefficients from array processing(Barker Technique) of all three SWIG source positions.

The Betsy source data set is more complicated, but the basic results are similar. The Rayleigh data includes a fundamental mode and one higher mode. Both modes show more clearly defined dispersion and higher group velocities as the source is moved further away. This relationship is consistent with the earlier observation that some time or distance had to elapse before the surface waves are fully developed. The 65 meter data set has a further complication in that the air blast at 300 m/s couples to the higher mode data at high frequencies.

Figures 63 to 65 show the Barker technique results for 5, 35 and 65 meter Betsy data sets. The energy for all of these data sets fall into two distinct bands. The faster, higher frequency band is the first higher mode Rayleigh wave. There also tends to be a less dispersive portion at 300 m/s. This energy is generated by the air blast from the source. The interpreted results of the three fundamental mode data sets are shown in Figure 66. The 35 meter data set breaks up at about 25 Hz and shows some sort of Airy phase at about 18 Hz. This analysis is consistent with the results from Simila (1982). Figure 67 contains the first higher mode dispersion curves for all 3 data sets. The 65 meter data set appears to be strongly biased by the air blast above 45 Hz, and possibly may at lower frequencies as well. The attenuation coefficients for the fundamental modes (Figure 68) are fairly consistent at all distances. The higher mode attenuation coefficients (figure 69) show negative attenuation or an increase in amplitude with distance for the 65 meter data set. This physically impossible result appears to be due to the coupling of the air blast energy back into the wavefield. The 5 and 35 meter array data sets have more normal appearing attenuation.

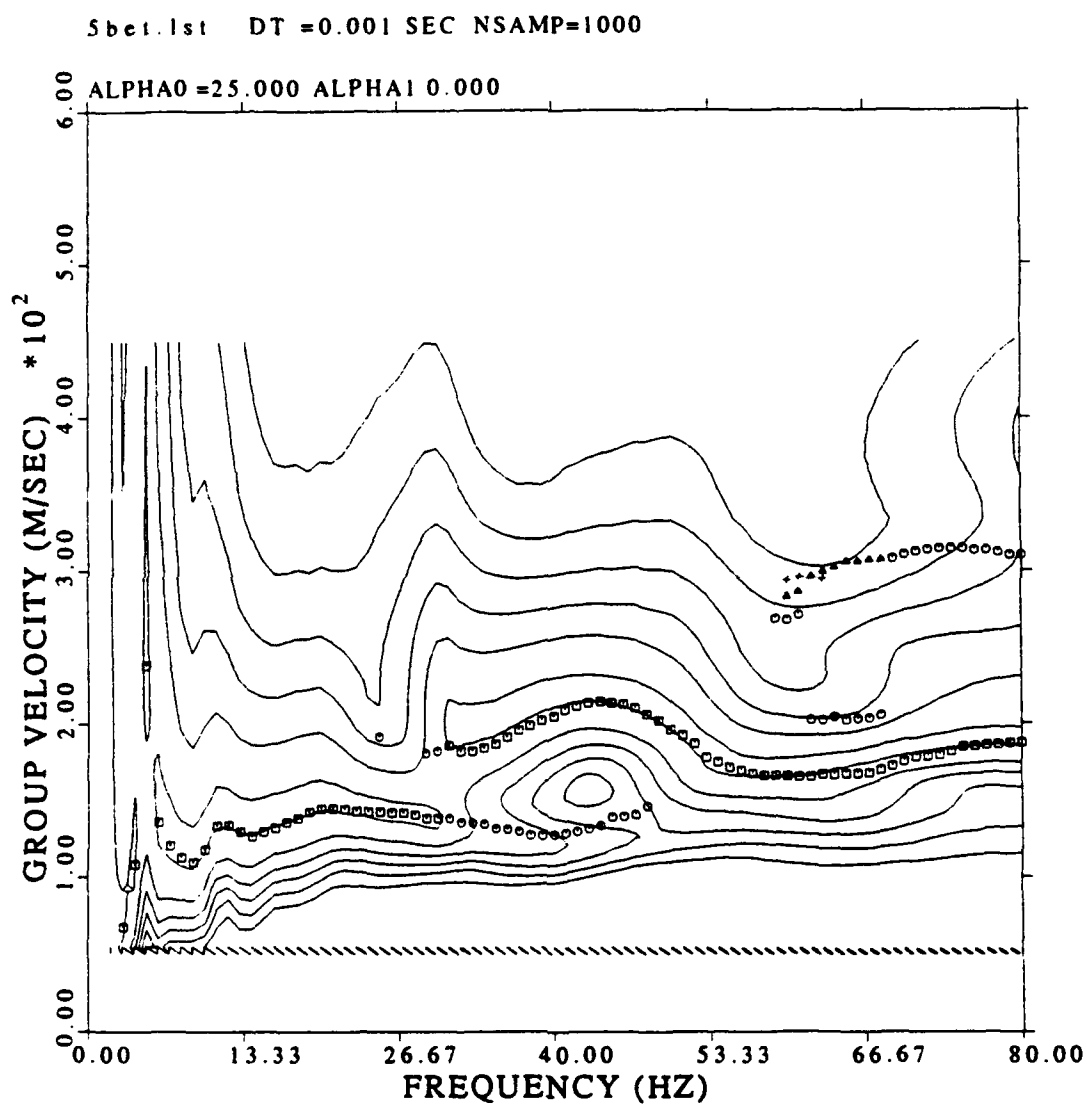


Figure 63. Array processing for group velocity of Betsy data set at 5 m. Highest energy corresponds to squares, second highest circles, third highest triangles, and fourth highest plus signs.

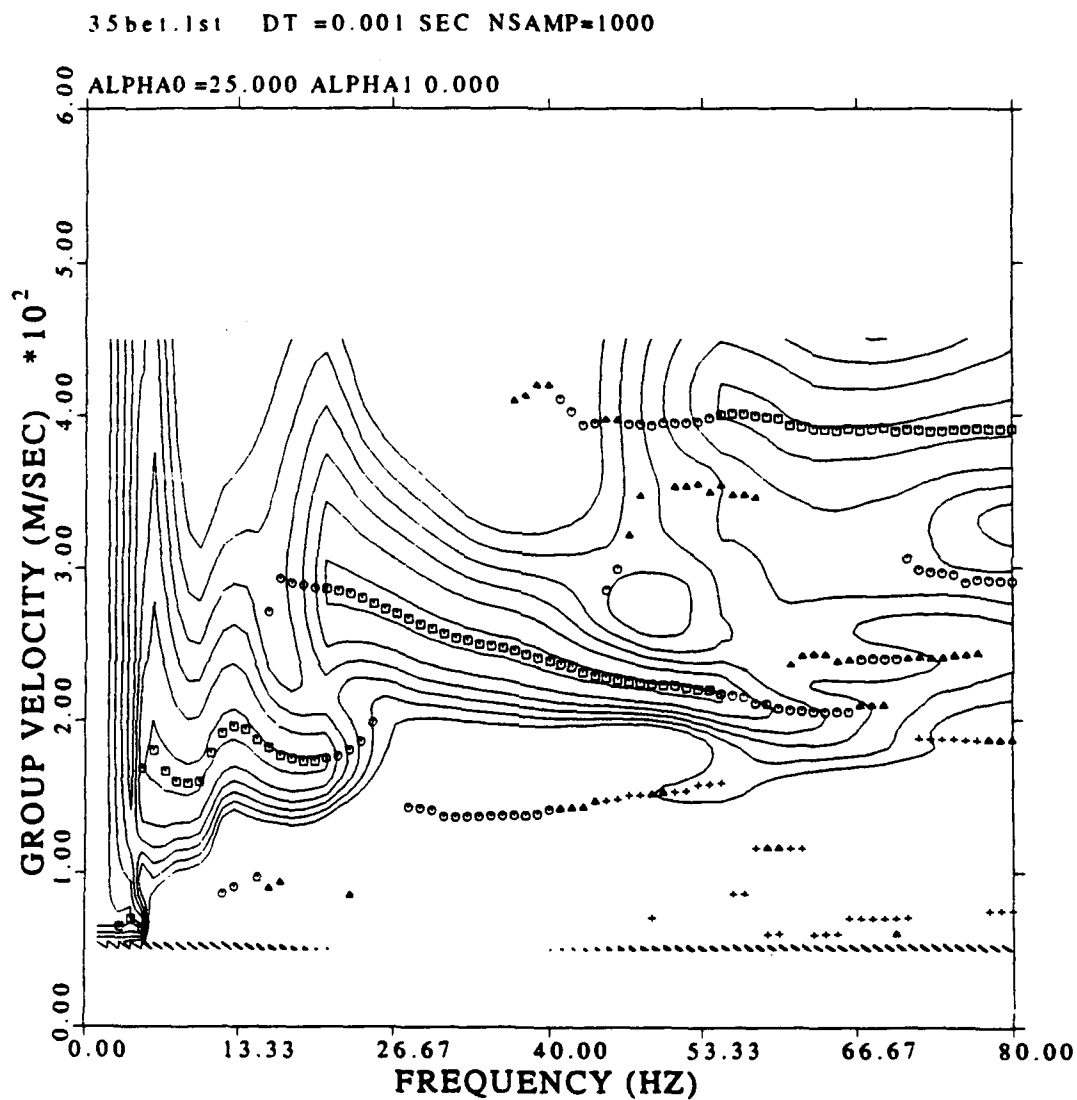


Figure 64. Array processing for group velocity of Betsy data set at 35 m. Highest energy corresponds to squares, second highest circles, third highest triangles, and fourth highest plus signs.

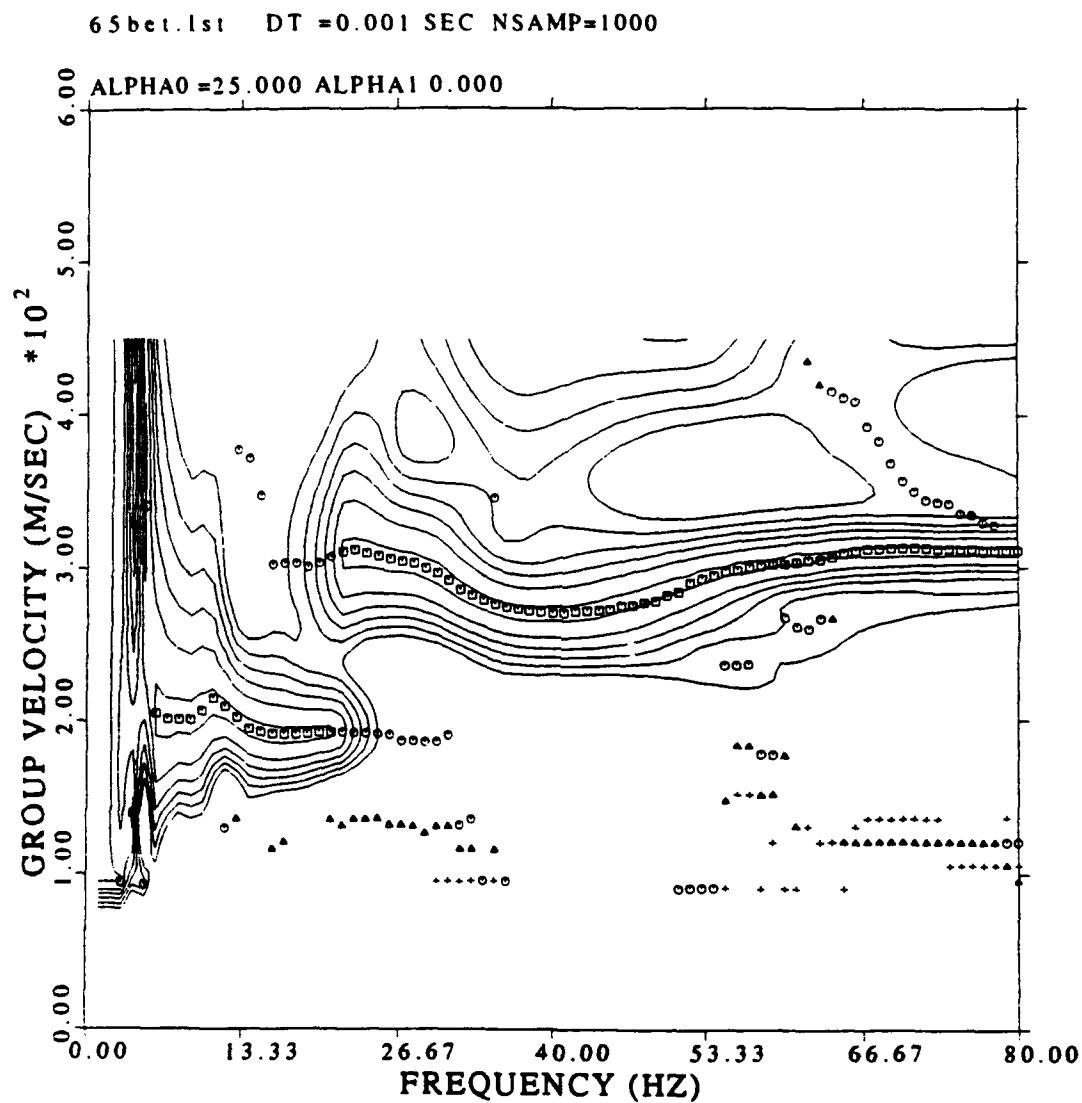


Figure 65. Array processing for group velocity of Betsy data set at 65 m. Highest energy corresponds to squares, second highest circles, third highest triangles, and fourth highest plus signs.

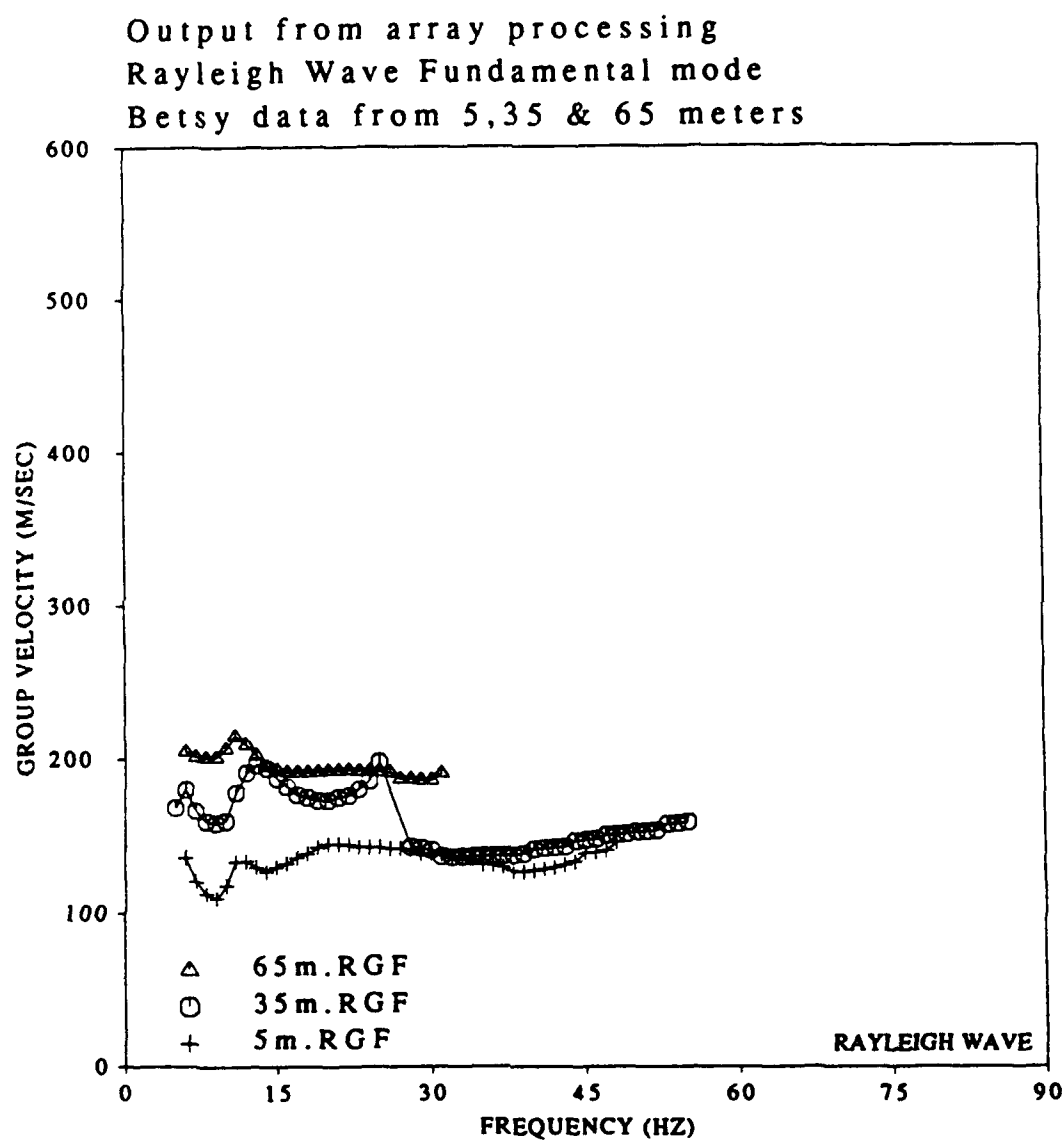


Figure 66. Overlay of the interpreted group velocity of Rayleigh wave fundamental mode from 5,35 and 65 meter Betsy data sets

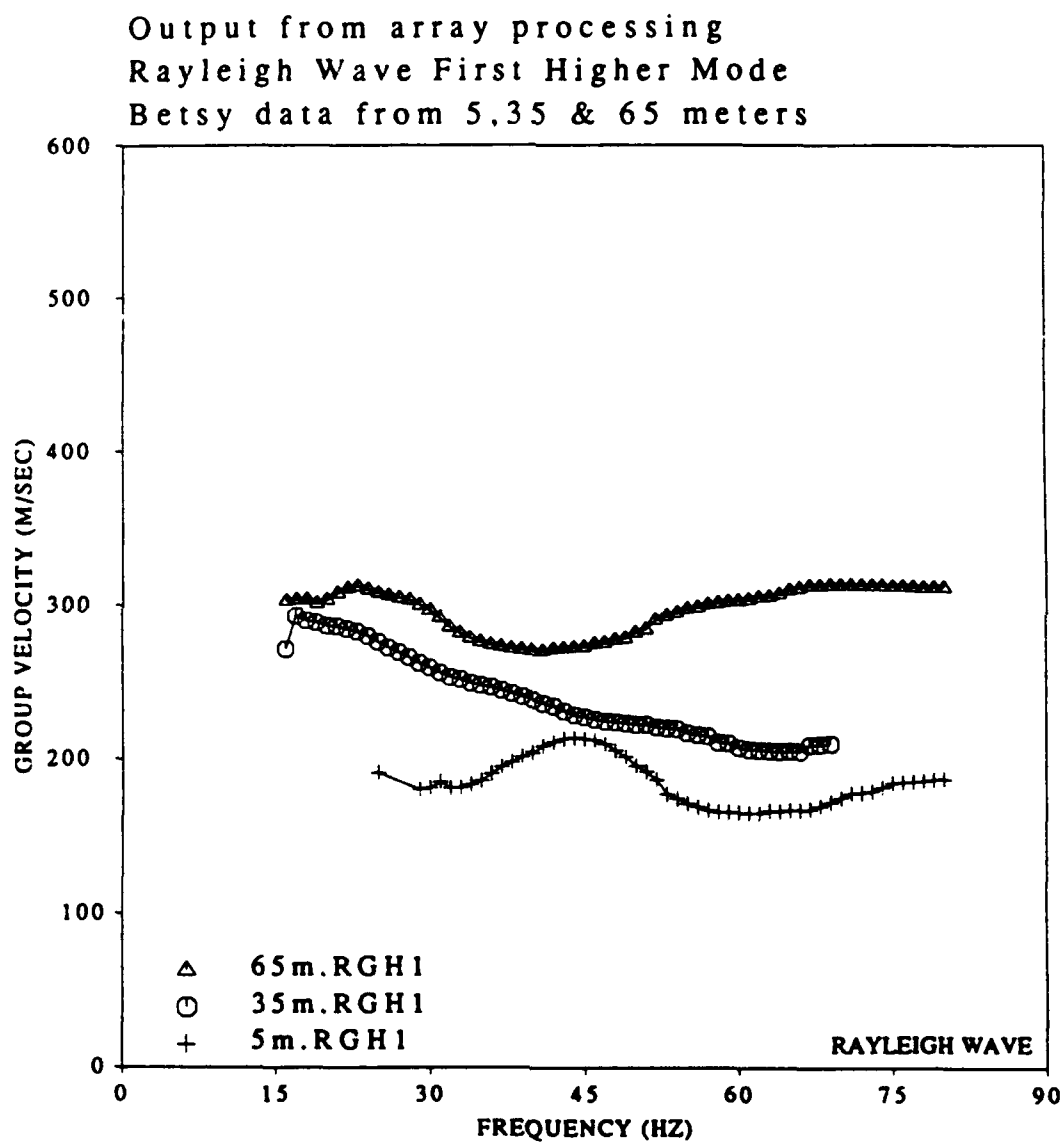


Figure 67. Overlay of the interpreted group velocity of Rayleigh wave first higher mode from 5,35 and 65 meter Betsy data sets

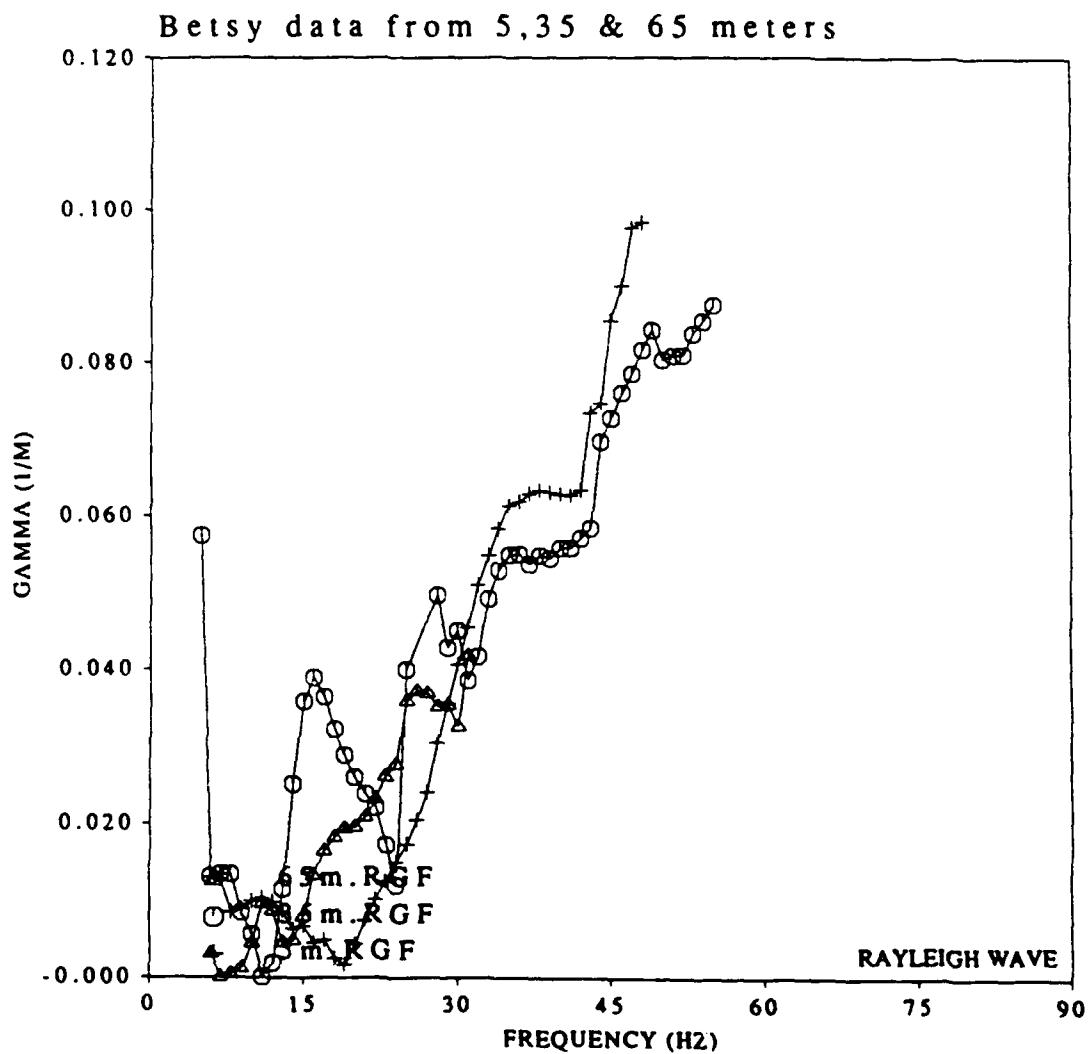


Figure 68. Overlay of the interpreted attenuation coefficients of Rayleigh wave fundamental mode from 5,35 and 65 meter Betsy data sets

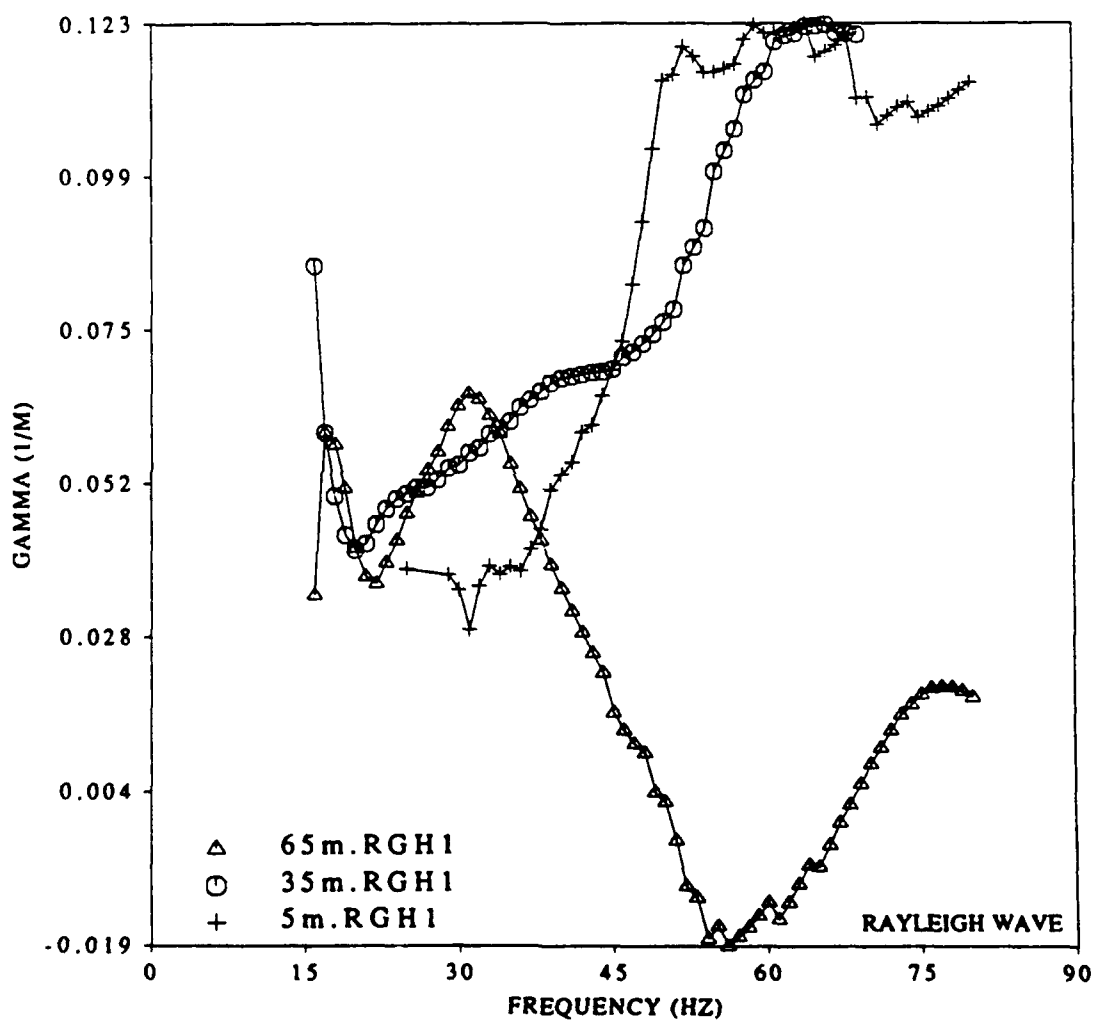


Figure 69. Overlay of the interpreted attenuation coefficients of Rayleigh wave first higher mode from 5,35 and 65 meter Betsy data sets

D. Phase Matched Filter

1. Experimental Technique

A complementary technique for calculating velocity dispersion is phase-matched filtering or PMF as documented by Herrin and Goforth (1977) and Goforth and Herrin (1979). The PMF procedure starts with an initial estimate of dispersion, generally from the multiple filter technique. An iterative technique is used to find and apply a filter that is phase-matched for extracting a particular mode or arrival of a surface wave. This phase-matched filter is then used to calculate the final dispersion curve.

Cross-correlation of a signal, $s(t)$, with a filter, $f(t)$, can be represented in the frequency domain as:

$$(3.5) \quad s(t) \otimes f(t) = |S(\omega)||F(\omega)| \exp i[\sigma(\omega) - \phi(\omega)],$$

where $\delta(\omega)$ and $\phi(\omega)$ are the phase spectrums of $s(t)$ and $f(t)$, respectively. If $f(t)$ is chosen such that the Fourier phase is the same as that of $s(t)$, then $f(t)$ is a phase-matched filter with respect to $s(t)$. The output of the cross-correlation is then $|S(\omega)||F(\omega)|$ and will be an even function in the time domain as is the autocorrelation function. This output is called the pseudo-autocorrelation function or PAF. The PAF depends only upon the selection of the amplitude spectrum of the phase matched filter if the phase of the filter and signal match. $|F(\omega)|$ is selected to be equal to 1, which means that the PAF will tend to have a minimum width spike centered around the time of the event. This event can be windowed in the lag domain or correlation domain and an FFT applied. This process separates out the portion of the data that is of interest and a more accurate phase

matched filter can be calculated. The process is repeated until the solution converges and the phase of the required mode is determined. The final output is the group velocity as a function of period computed from the phase. The group velocity is calculated from the group delay $T_g(\omega)$ which is related to the Fourier phase by:

$$(3.6) \quad T_g(\omega) = \frac{d\phi(\omega)}{d\omega},$$

where $\phi(\omega)$ is the matched phase output from the PMF program. The advantage of using the PMF is that the final results are less contaminated by higher modes or multi-pathed arrivals.

2. Experimental Results

The phase matched filter technique is applied to a single source receiver pair at a time. Like any model based technique, phase matched filtering results are dependent on the quality of the input, which is a group velocity dispersion curve. The most consistent dispersion curve inputs for the SWIG data set are those developed using the Barker technique on the 65 meter data set. The computed group and phase velocities from the phase matched filter contrasted to the array technique results are shown in Figure 70 to 76 at approximately 5 meter increments.

The PMF results are consistent with the multiple filter results. The single phone group velocity deviates from the array averages above 25 Hz. Below 25 Hz the results of all three techniques are comparable. The PMF technique tended to be unstable at the higher frequencies. This instability may be a result

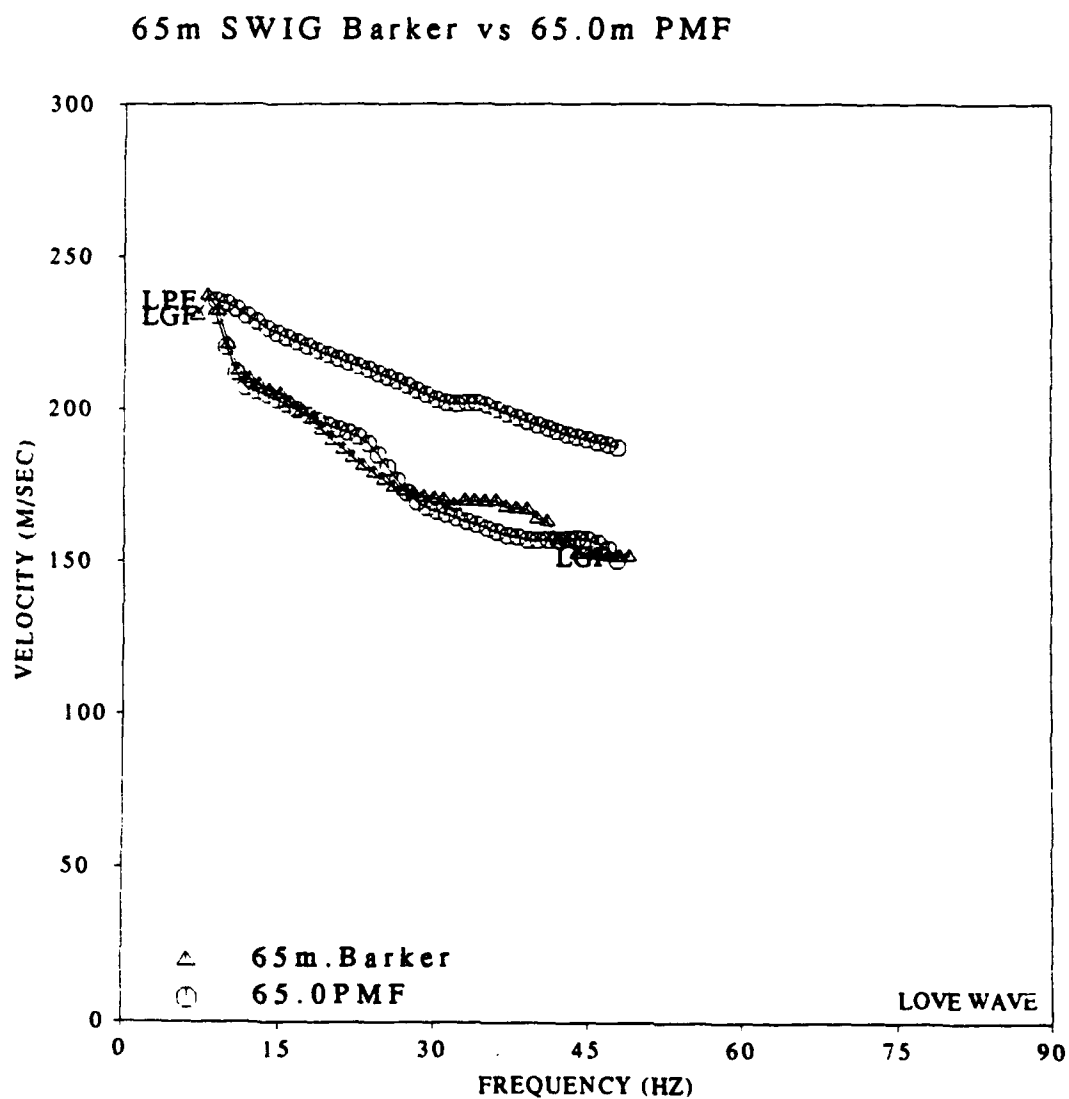


Figure 70. Comparison of array derived group velocity with PMF results at 65 m. PMF results are indicated by circles. The top curve is phase velocity. Barker technique results are represented by triangles.

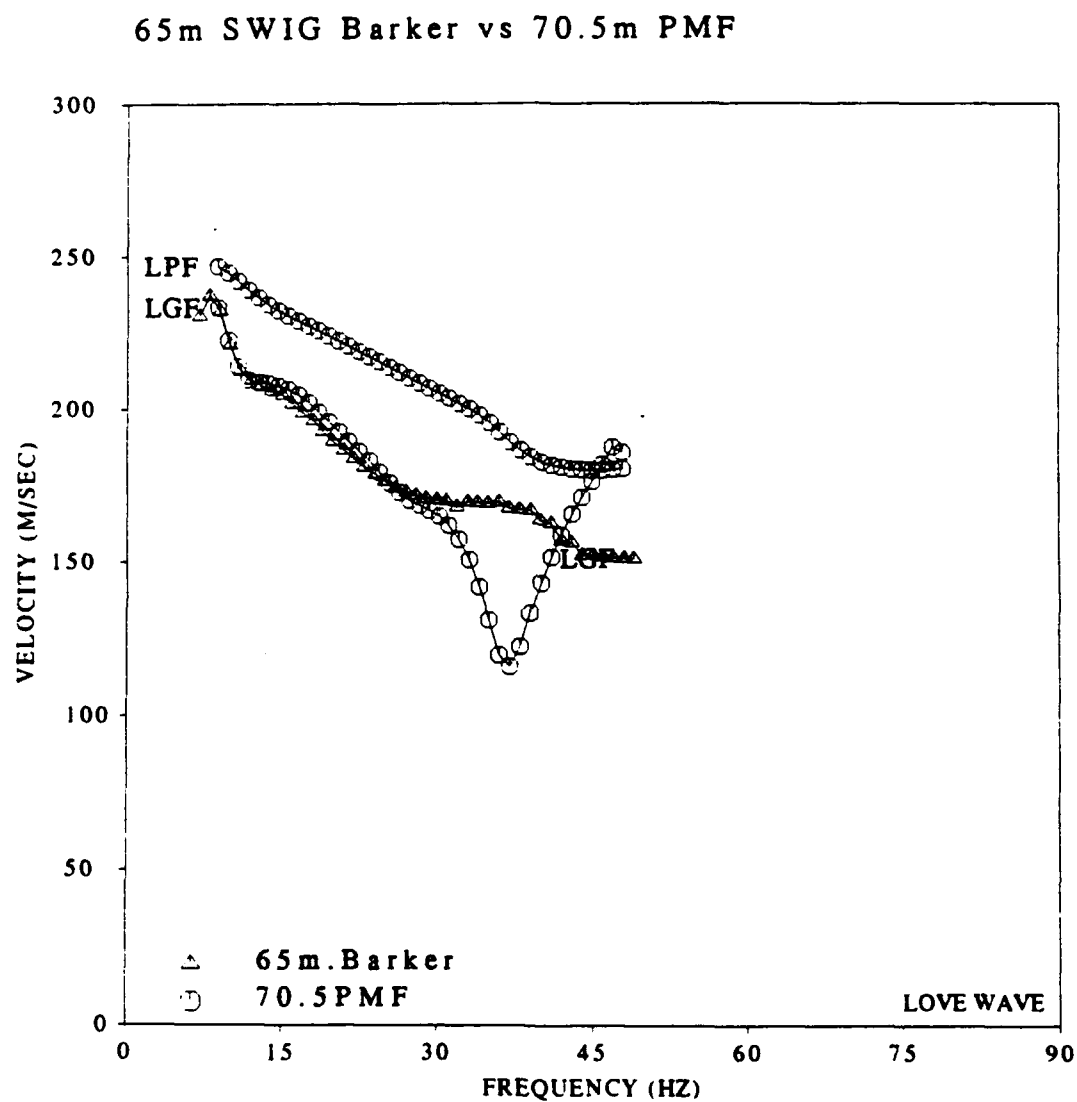


Figure 71. Comparison of array derived group velocity with PMF results at 70.5 m. PMF results are indicated by circles. The top curve is phase velocity. Barker technique results are represented by triangles.

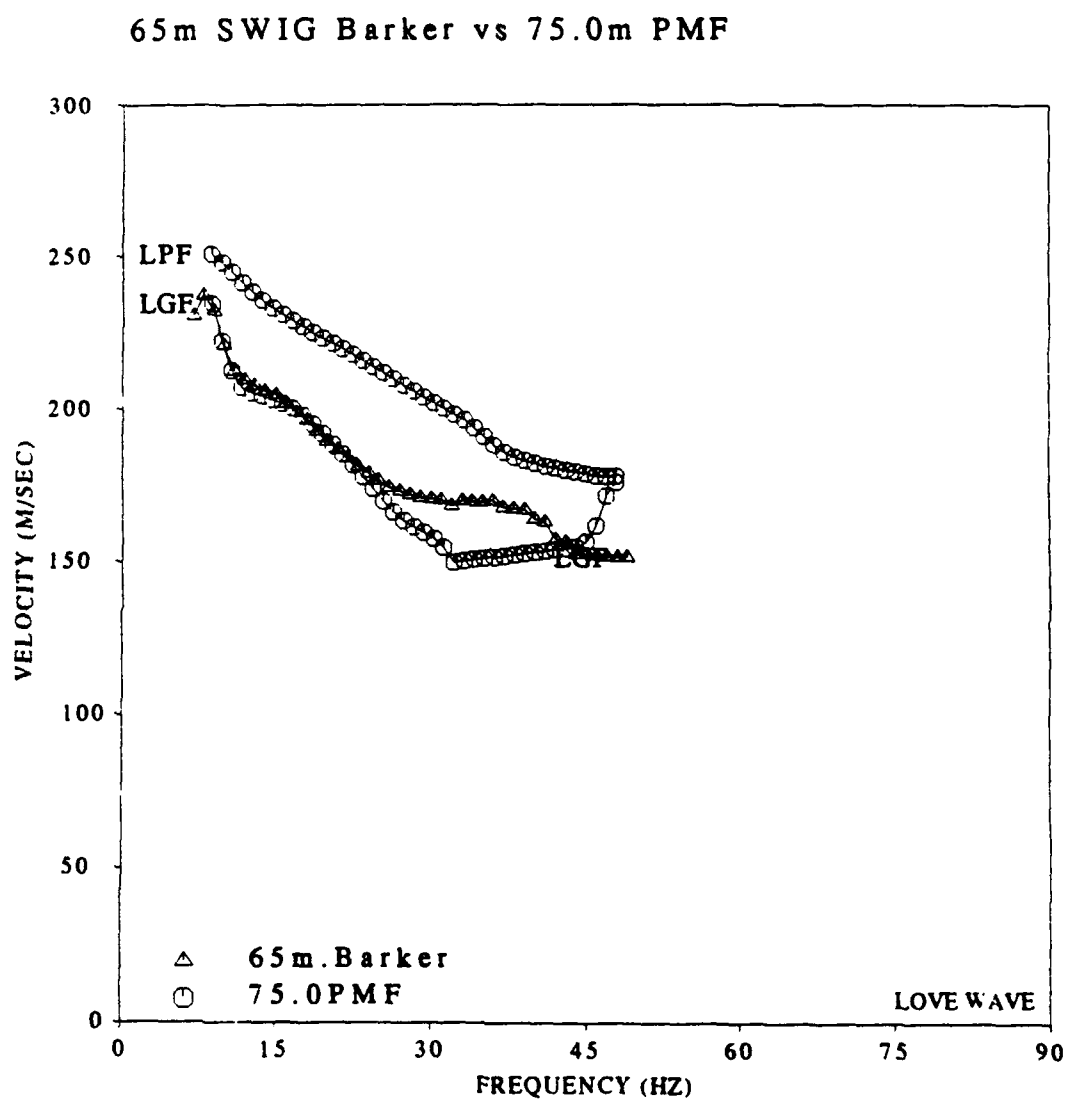


Figure 72. Comparison of array derived group velocity with PMF results at 75 m. PMF results are indicated by circles. The top curve is phase velocity. Barker technique results are represented by triangles.

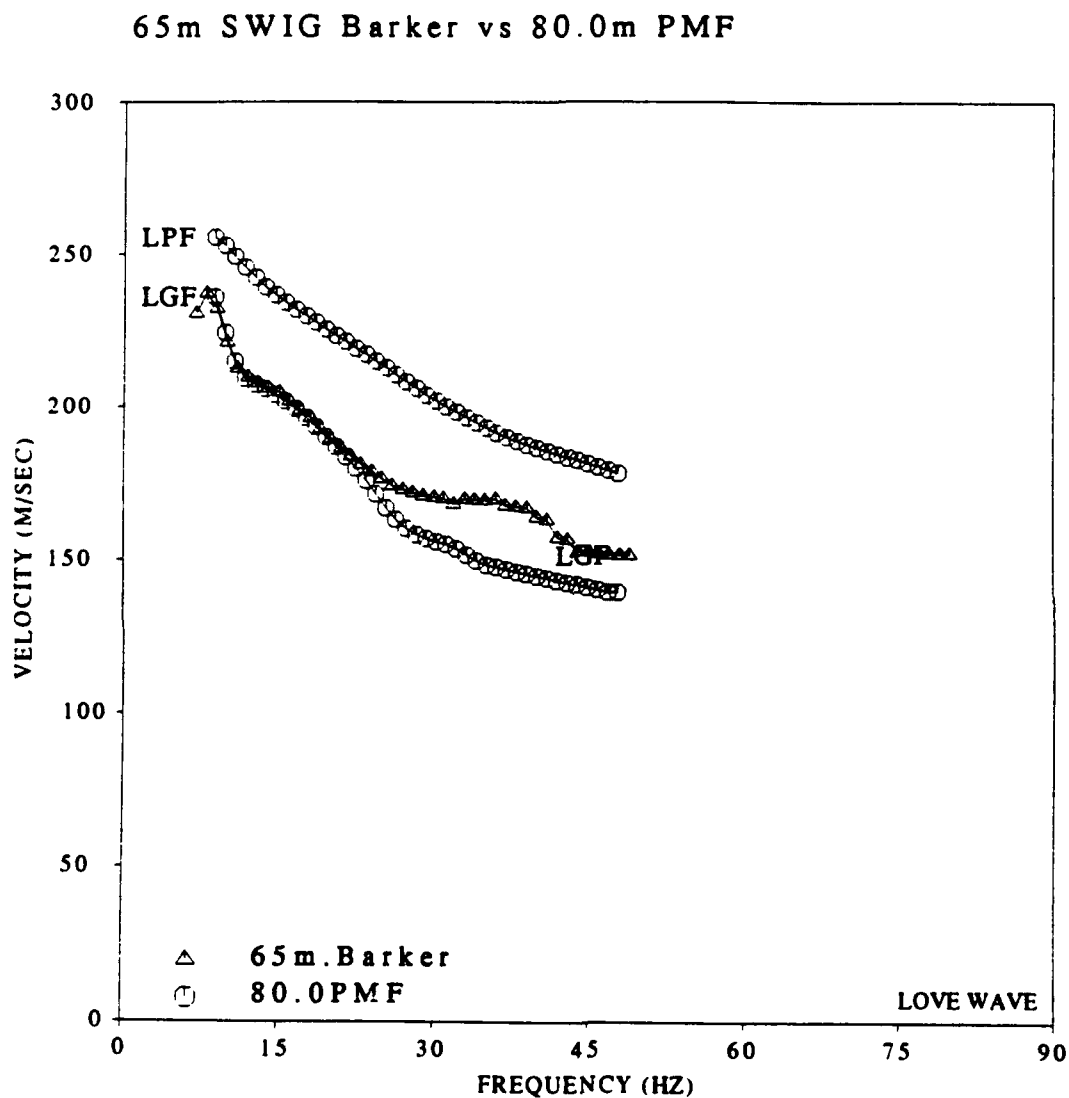


Figure 73. Comparison of array derived group velocity with PMF results at 80 m. PMF results are indicated by circles. The top curve is phase velocity. Barker technique results are represented by triangles.

65m SWIG Barker vs 85.0m PMF

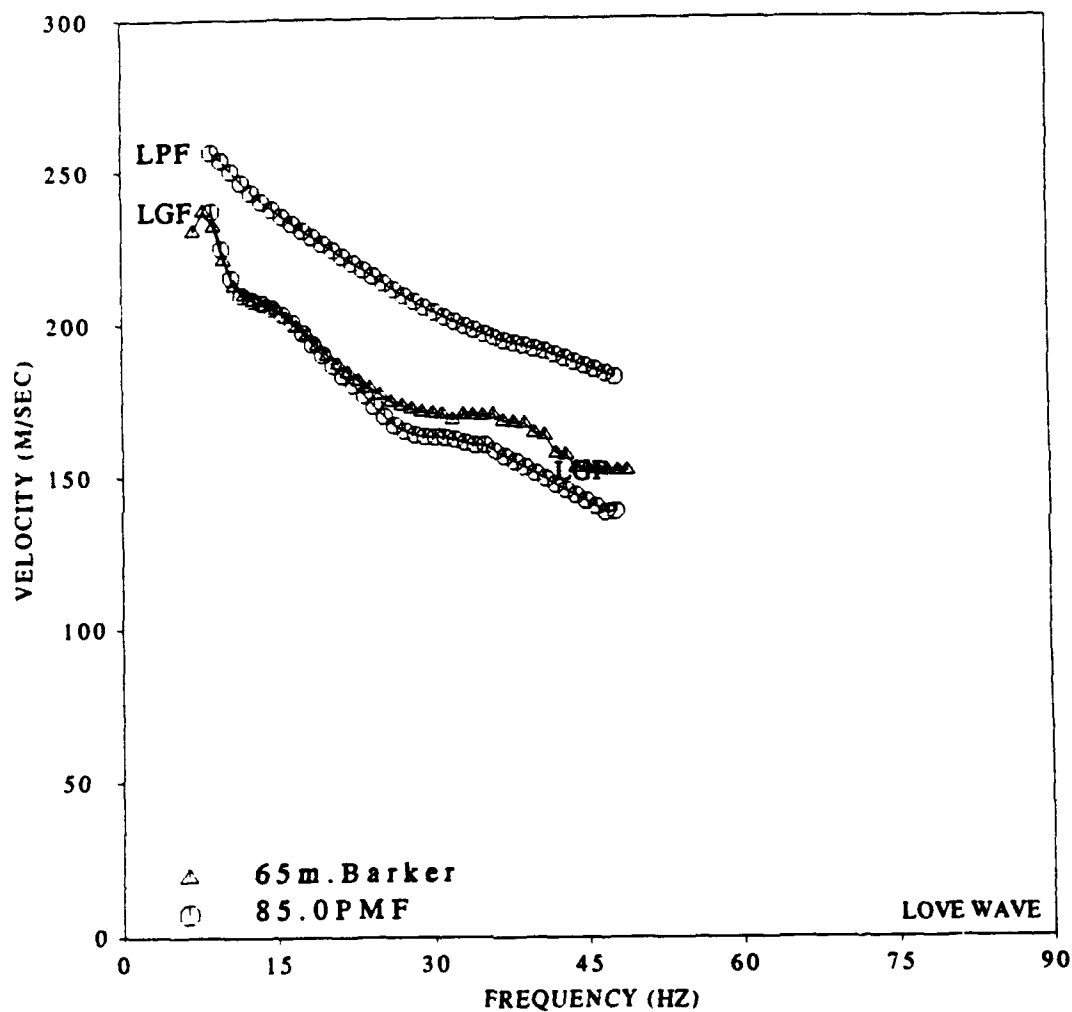


Figure 74. Comparison of array derived group velocity with PMF results at 85 m. PMF results are indicated by circles. The top curve is phase velocity. Barker technique results are represented by triangles.

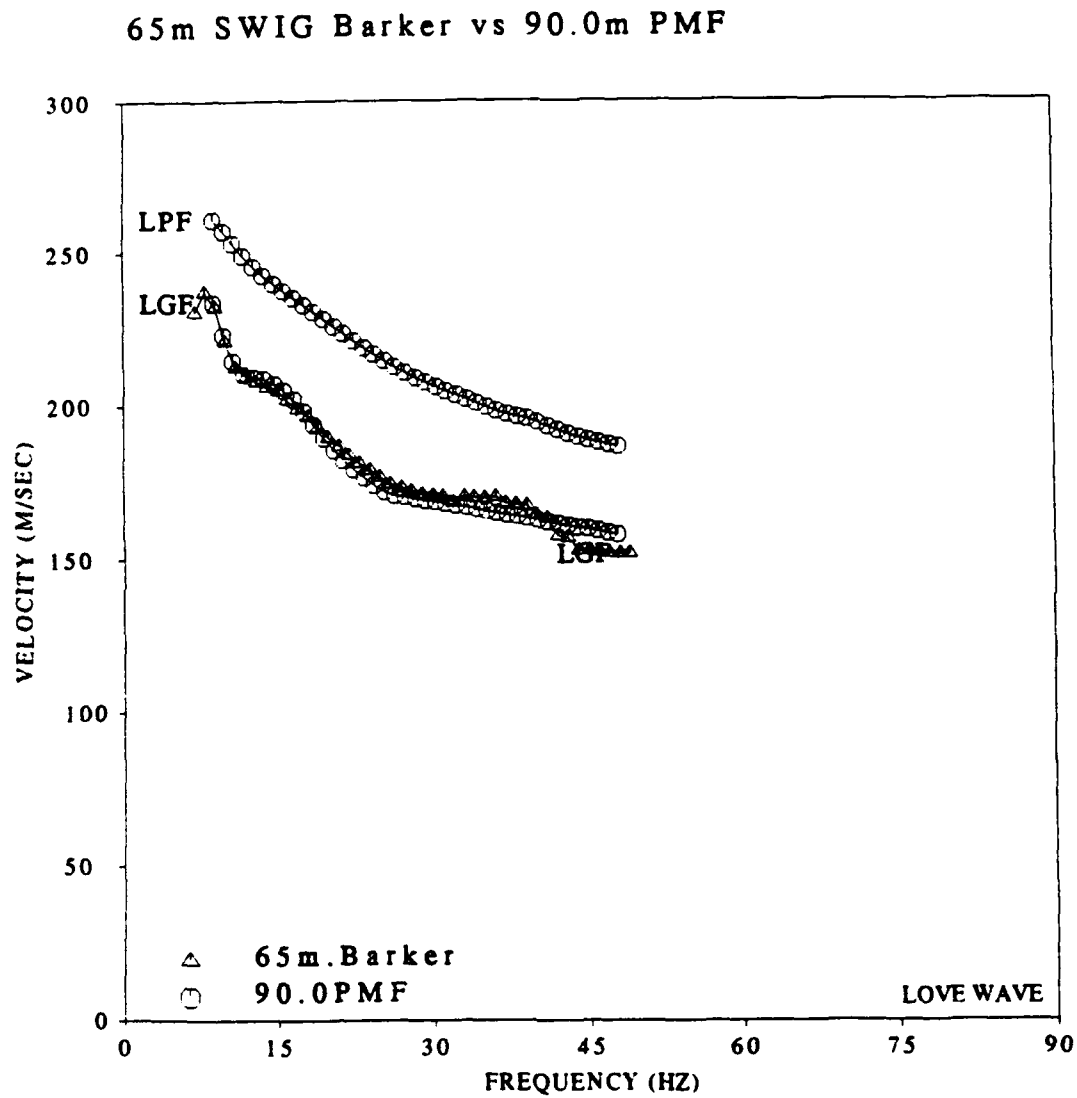


Figure 75. Comparison of array derived group velocity with PMF results at 90 m. PMF results are indicated by circles. The top curve is phase velocity. Barker technique results are represented by triangles.

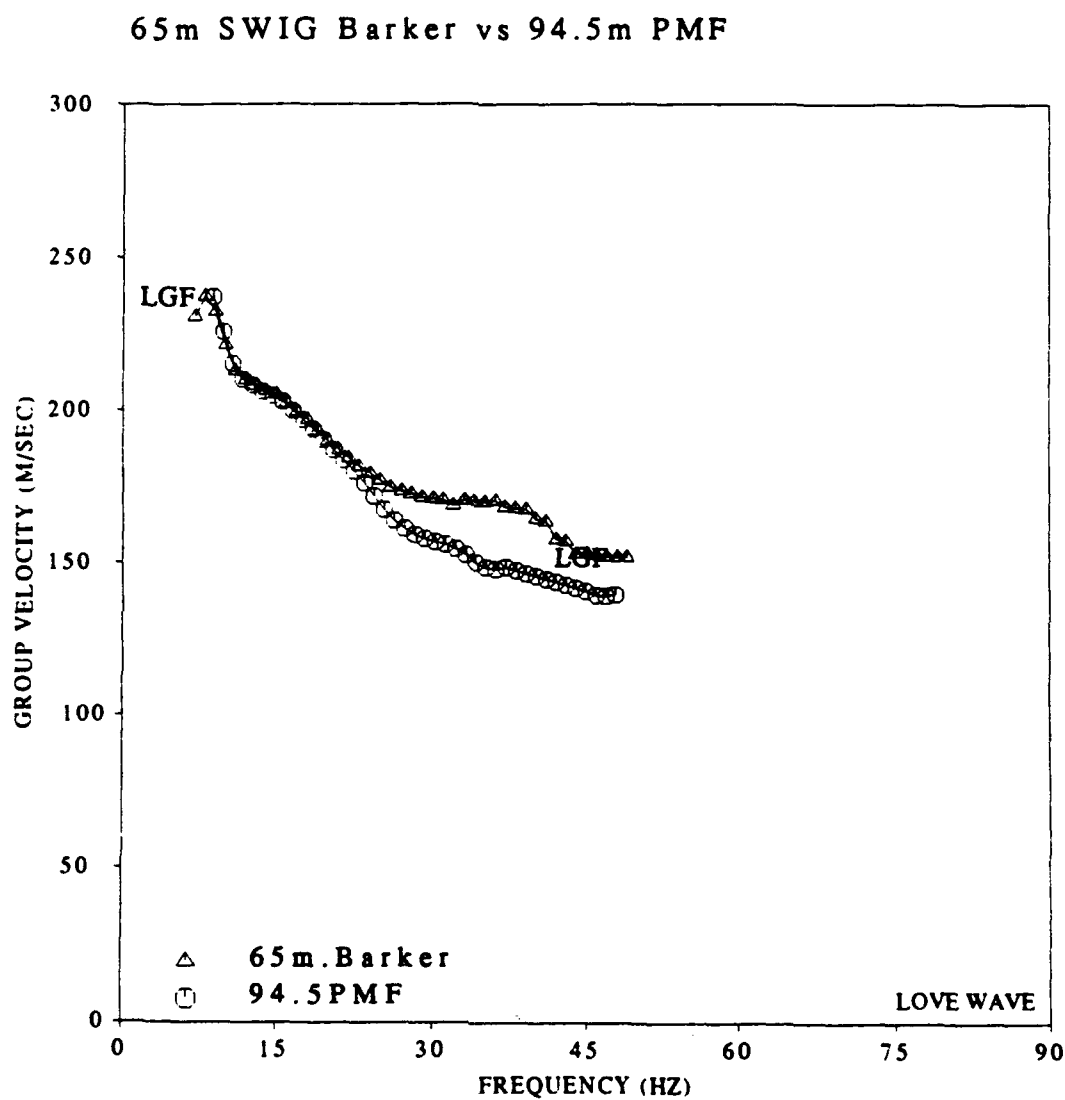


Figure 76. Comparison of array derived group velocity with PMF results at 94.5 m. PMF results are indicated by circles. The top curve is phase velocity. Barker technique results are represented by triangles.

of other, interfering events. The MFA plots (Figures 34 to 40) also indicate that there is a large amplitude interference in the frequency domain above 25 Hz with the main body wave or direct and refracted shear arrivals. The velocities of the body waves are substantially faster than the velocities of the Love waves, 180 versus 320 m/s, but the time separation of these two events is only about 100 msec. The general trend of the PMF results was to give slightly lower velocity estimates than the array technique. This result is probably due to the fact that the PMF technique is less biased by the faster body waves than the other techniques used in this thesis.

The PMF technique generates a phase matched spectrum from which it is possible to create a waveform containing only the surface wave being analyzed. Figure 77 contains a plot of the extracted Love waves using this technique. The traces all have the classic dispersed appearance, with a low frequency at the smallest times and high frequencies arriving later. This technique was used to effectively subtract the body waves. These traces could easily be subtracted from the original traces to generate a body wave trace without interfering surface waves.

The traces after PMF with only the Love waves remaining were processed through the multiple filter technique. The results (Figures 78 to 84) show that the amplitudes of all other events have been dropped by an order of magnitude. The maximum frequency for the input dispersion curve to PMF was limited to 55 Hz. No interpretations or inferences should be made for the resulting data above this frequency. The results look quite coherent above this frequency, but the low amplitudes preclude any interpretation.

Some attempts were made at analyzing the 65 meter Rayleigh wave data set using the PMF technique. These attempts yielded inconsistent results. One problem with this analysis is that the data set tended to be more complex, in part because of the existence of a fundamental and one higher mode. The body wave portion of the data set appeared to contain more relative energy and arrivals than the same portion of the SWIG data set. The higher velocities mean that the events being separated were closer together in time, thus potentially being past the resolving power of the PMF technique. The other problem is that the non-dispersive air blast coupled back into the Rayleigh wave, and thereby distorted the dispersion of surface wave energy.

E. Array Processing For Phase Velocity

1. Experimental Technique

The phase velocity determinations using the array data are based on an algorithm suggested by McMechan and Yedlin (1981) and implemented by Herrmann (1987). This technique relies on two steps starting with a slant stack or transform into the τ - p domain. This step is followed by a 1d transform or FFT along lines of constant slowness, converting the intercept dimension to frequency. Since slowness(p) is the inverse of velocity, this effectively results in a direct representation of amplitude on a phase velocity versus frequency(ω) representation, and is therefore called the p - ω technique. The maximum amplitudes correspond to dispersion of various modes.

Mokhtar et al (1988) describe an alternate method of mapping into the p - ω domain without doing a slant stack. The procedure is described in detail in Herrmann (1988) program documentation for the p ω stack procedure. The

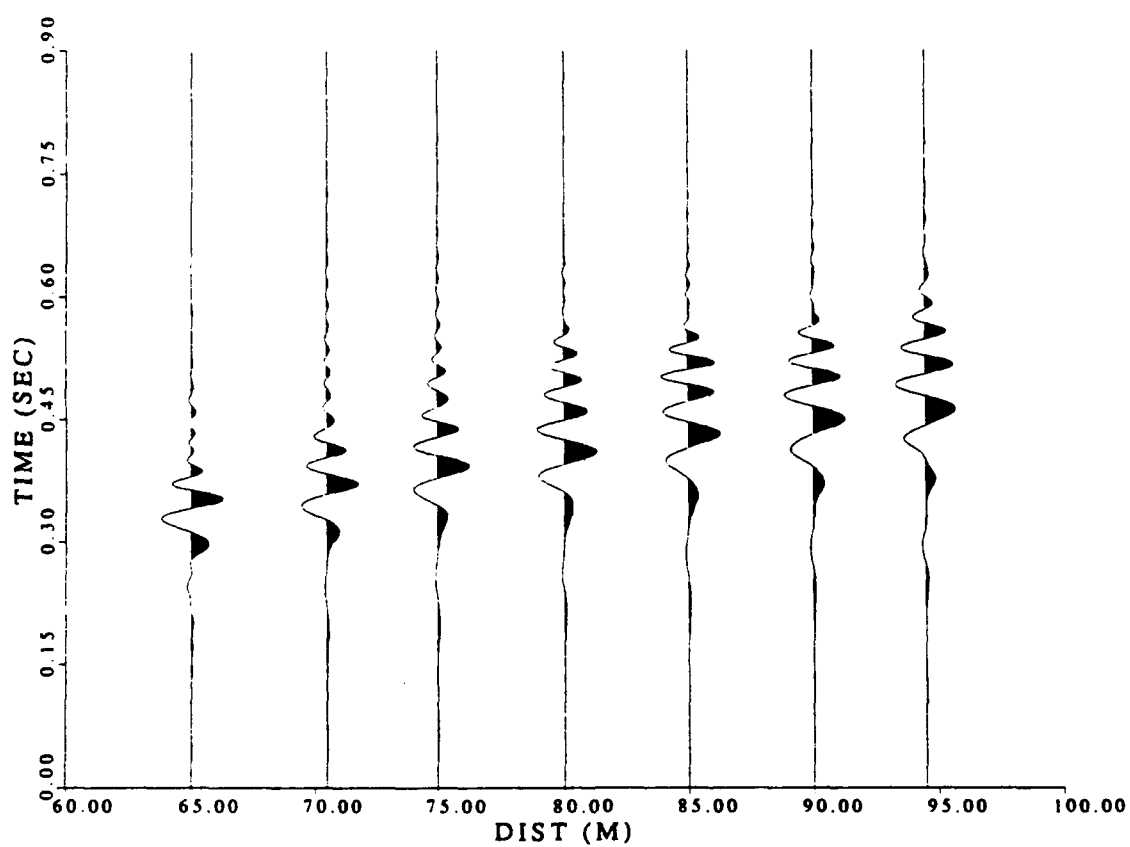


Figure 77. PMF extracted Love waves from 65m SWIG data

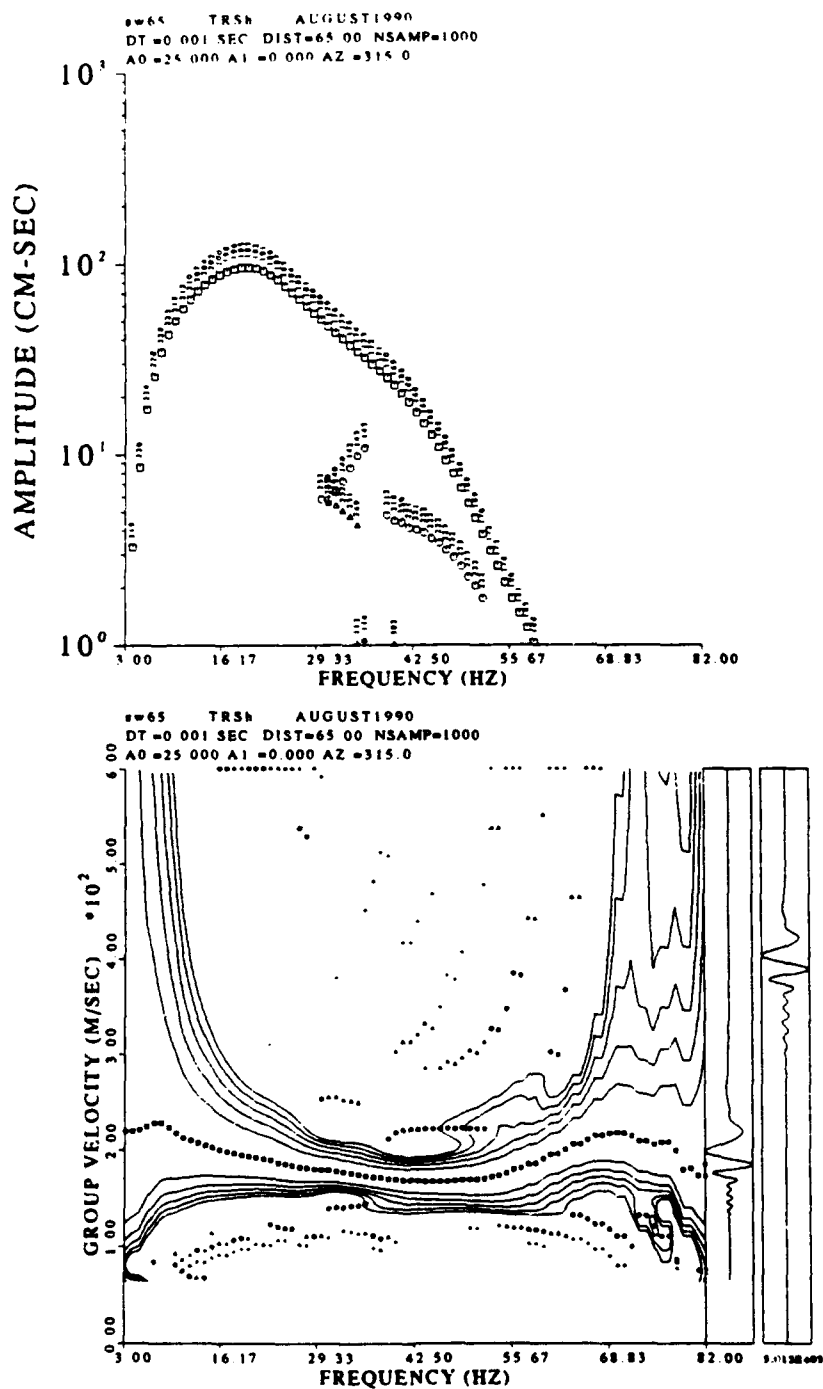


Figure 78. MFT processing of PMF stripped Love waves at 65 m. Upper plot is amplitude spectrums corresponding to lower plot group velocity dispersion. Largest amplitudes are squares, second are circles, third are triangles and fourth amplitude at a frequency is indicated by a plus sign.

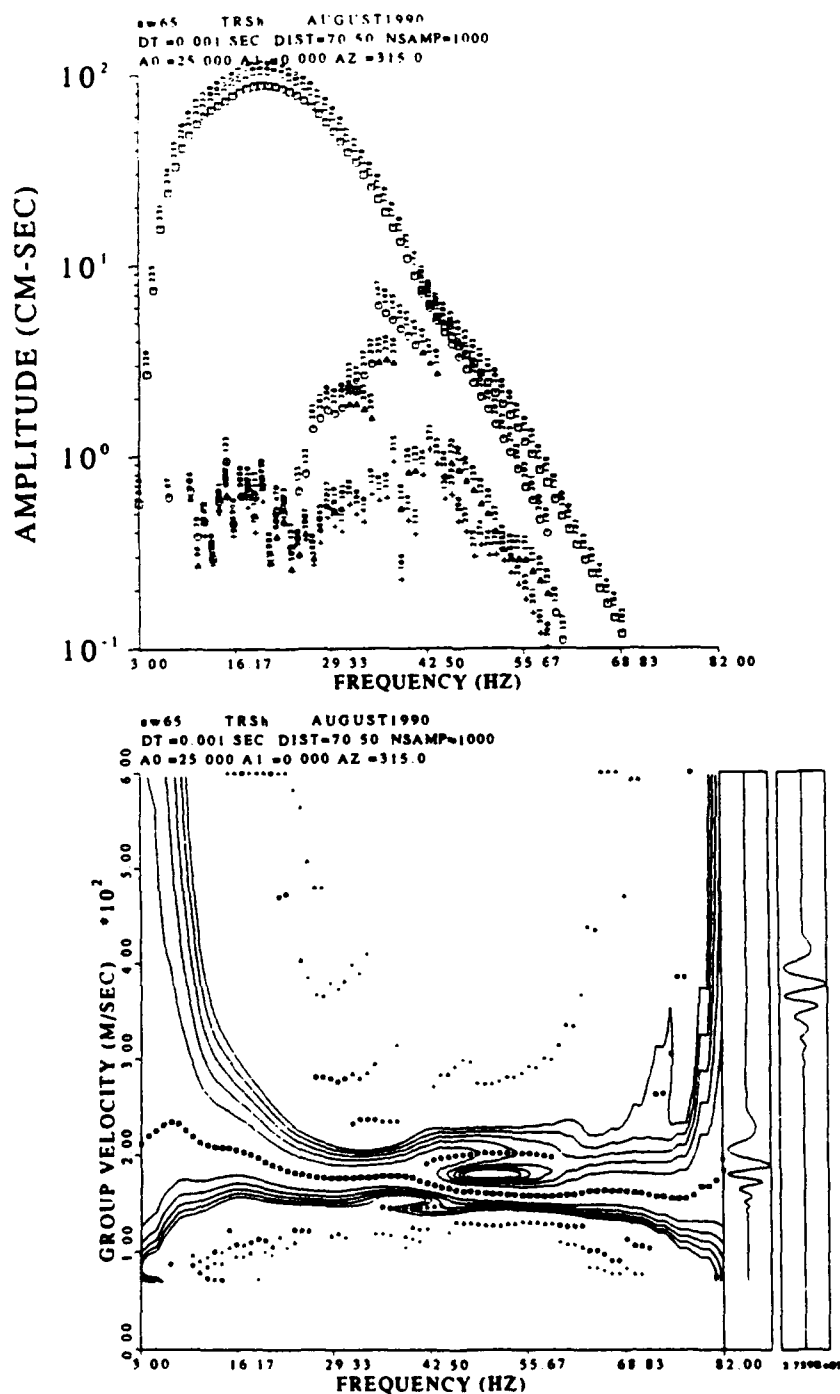


Figure 79. MFT processing of PMF stripped Love waves at 70.5 m. Upper plot is amplitude spectrums corresponding to lower plot group velocity dispersion. Largest amplitudes are squares, second are circles, third are triangles and fourth amplitude at a frequency is indicated by a plus sign.

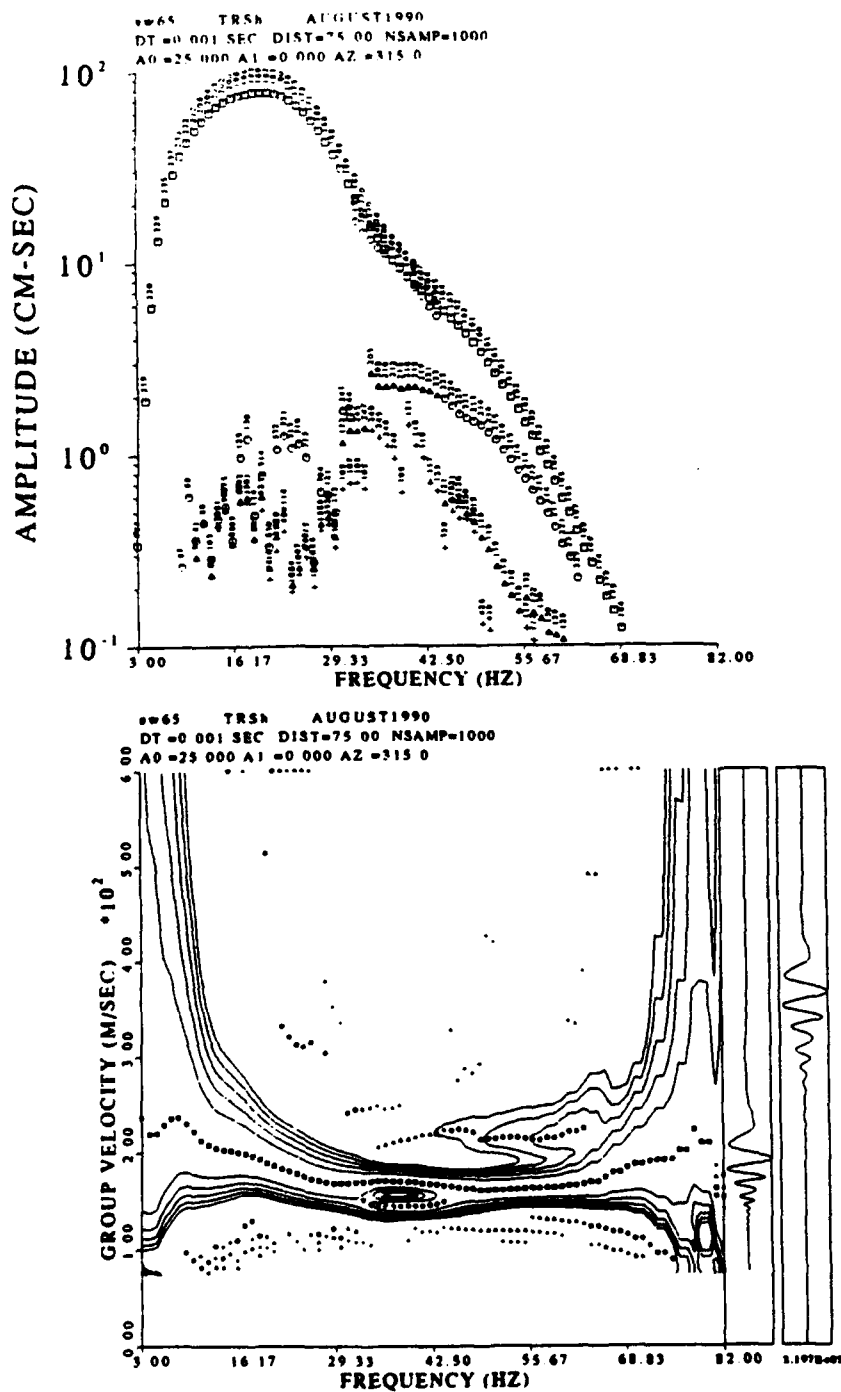


Figure 80. MFT processing of PMF stripped Love waves at 75 m. Upper plot is amplitude spectrums corresponding to lower plot group velocity dispersion. Largest amplitudes are squares, second are circles, third are triangles and fourth amplitude at a frequency is indicated by a plus sign.

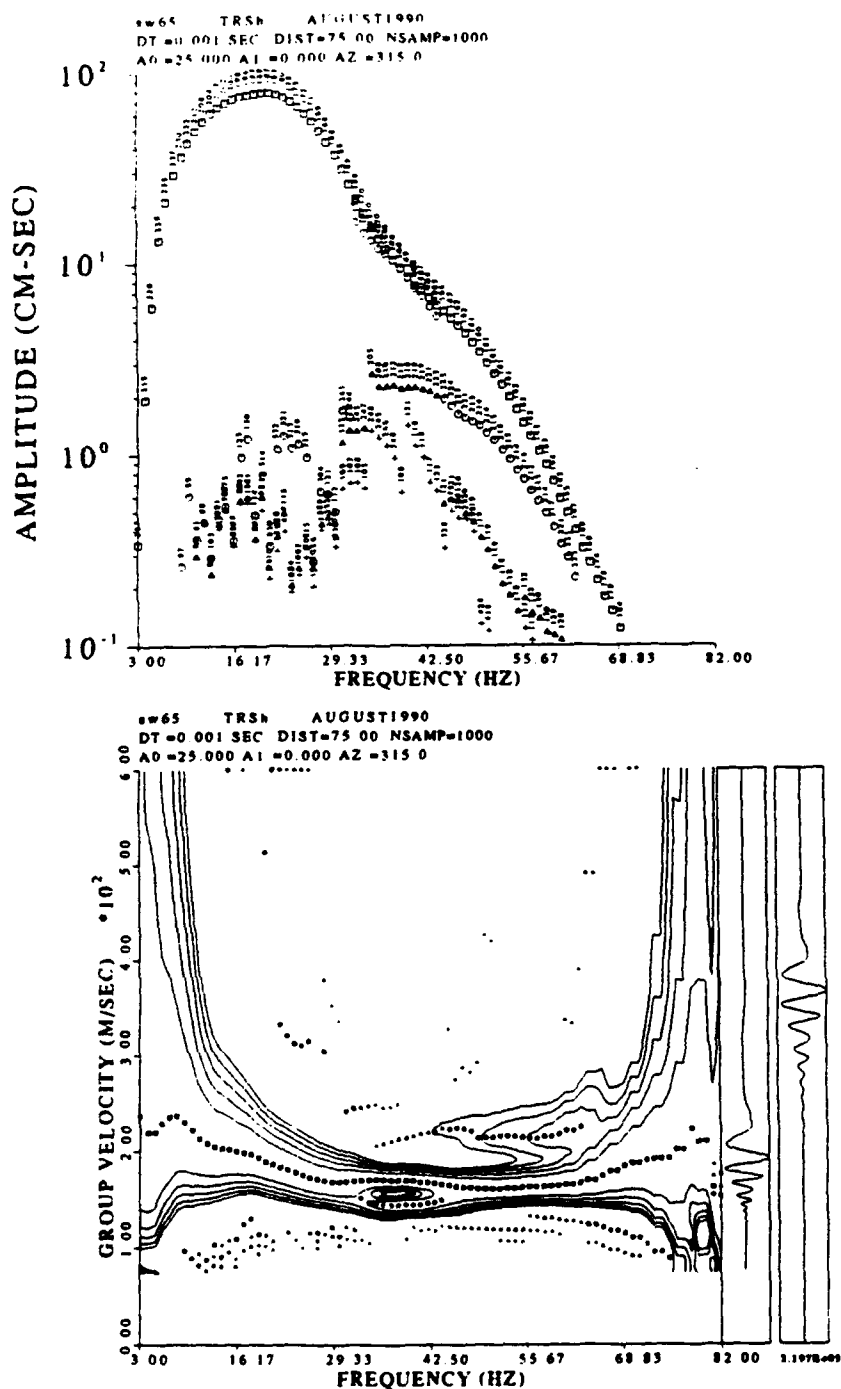


Figure 80. MFT processing of PMF stripped Love waves at 75 m. Upper plot is amplitude spectrums corresponding to lower plot group velocity dispersion. Largest amplitudes are squares, second are circles, third are triangles and fourth amplitude at a frequency is indicated by a plus sign.

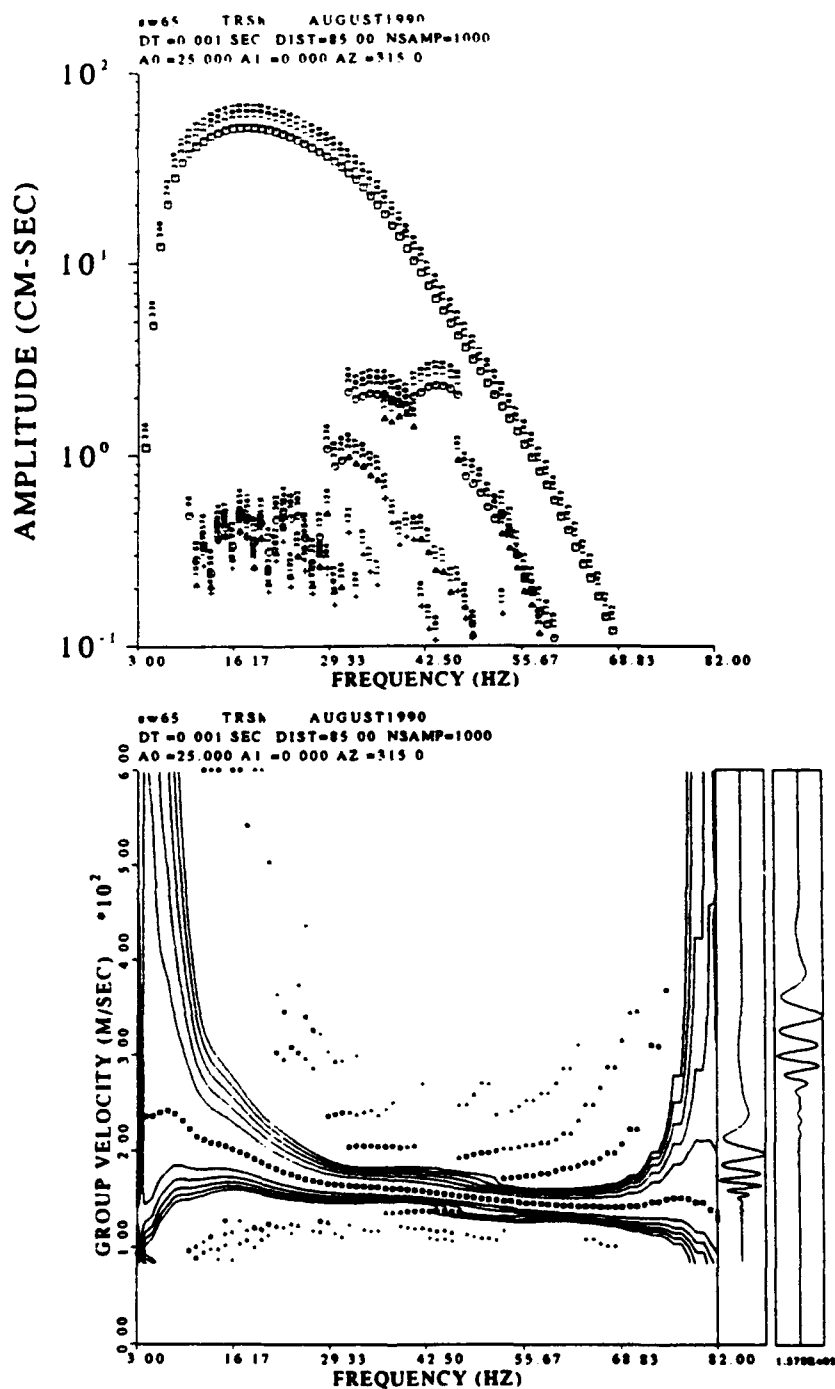


Figure 82. MFT processing of PMF stripped Love waves at 85 m. Upper plot is amplitude spectrums corresponding to lower plot group velocity dispersion. Largest amplitudes are squares, second are circles, third are triangles and fourth amplitude at a frequency is indicated by a plus sign.

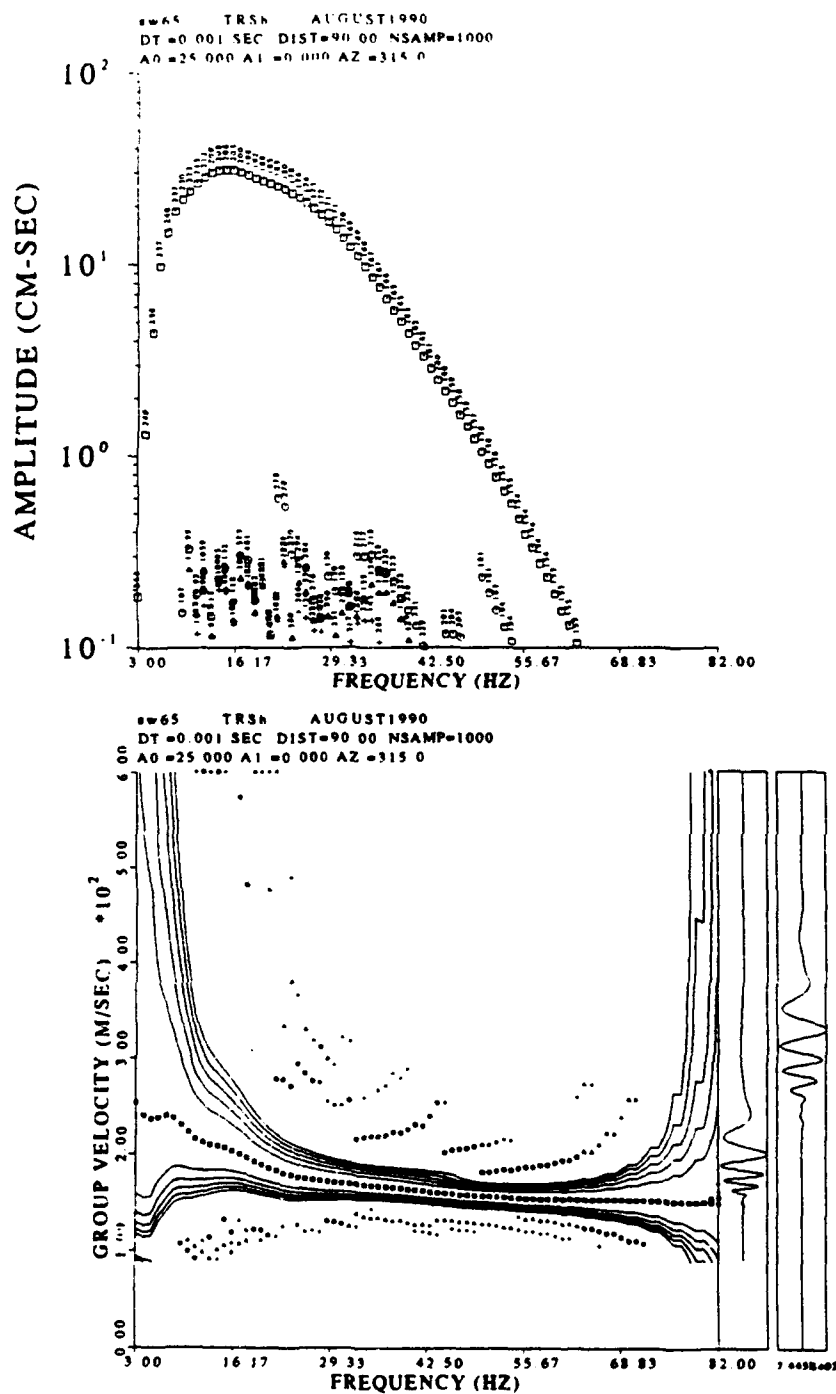


Figure 83. MFT processing of PMF stripped Love waves at 90 m. Upper plot is amplitude spectrums corresponding to lower plot group velocity dispersion. Largest amplitudes are squares, second are circles, third are triangles and fourth amplitude at a frequency is indicated by a plus sign.

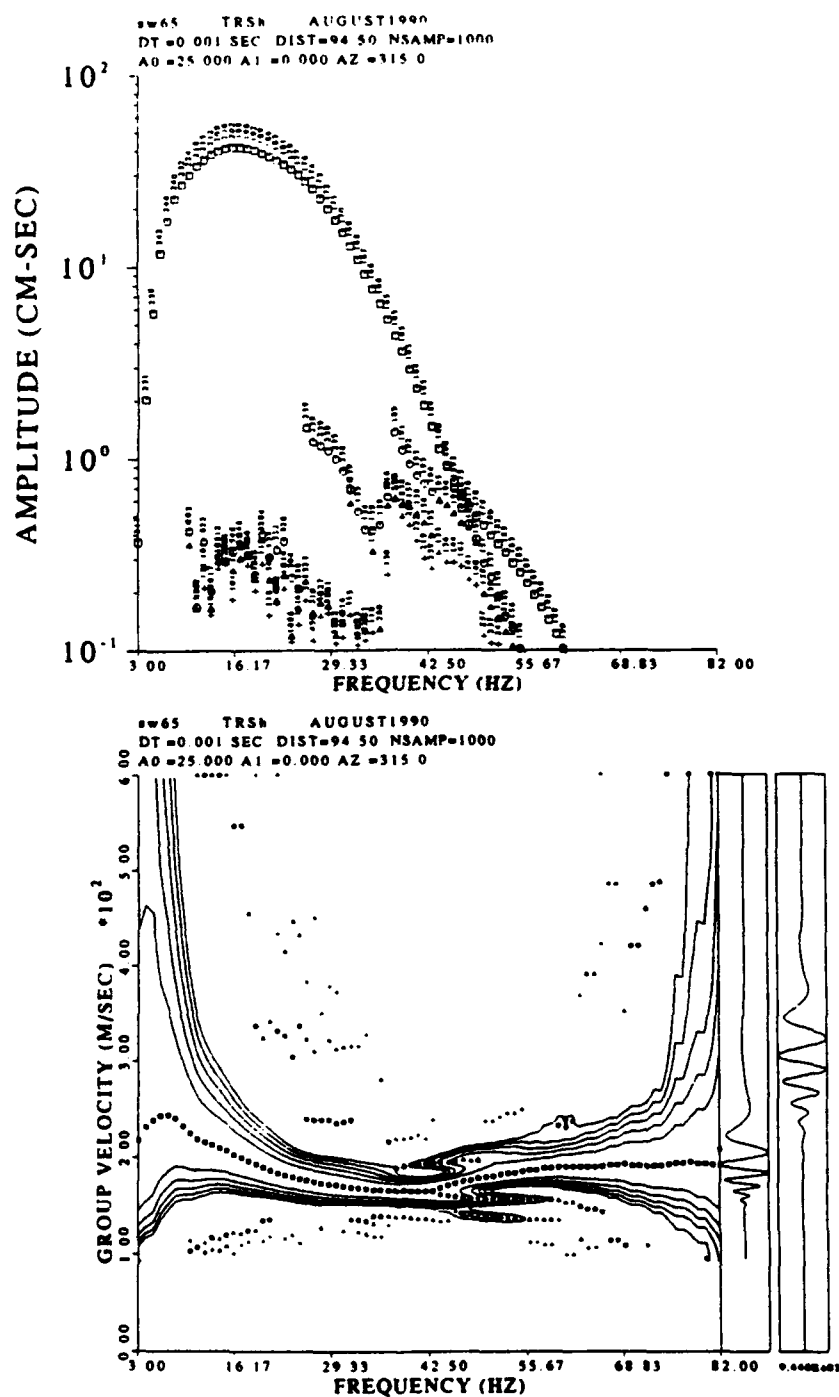


Figure 84. MFT processing of PMF stripped Love waves at 94.5 m. Upper plot is amplitude spectrums corresponding to lower plot group velocity dispersion. Largest amplitudes are squares, second are circles, third are triangles and fourth amplitude at a frequency is indicated by a plus sign.

seismic trace from each offset, r_i , is represented in the Fourier domain by $A(\omega, r_i) \exp j\phi_i(\omega)$. The p - ω stack is defined by the relation:

$$(3.7) \quad U(p, \omega) = \sum_{i=1}^N C(\omega)^{-1} A(\omega, r_i) \exp(j\phi_i) \exp(j\omega p r_i),$$

where $C(\omega) = A(\omega, r_1) \exp(j\phi_1)$. Division by $C(\omega)$ normalizes the spectrum and removes the source phase if the input trace is a single mode. The actual spectrum is assumed to be a sum of multiple (M) modes of surface waves:

$$(3.8) \quad A(\omega, r_i) \exp(j\phi_i) = \sum_{k=1}^M S_k(\omega, r_i) \exp j[\phi_{0k}(\omega) - \omega p_{0k}(\omega) r_i],$$

where $S_k(\omega, r_i)$ is the amplitude of the k 'th mode and the phase is separated into distance-independent $\phi_{0k}(\omega)$, and distance dependent $\omega p_{0k}(\omega) r_i$ components. p_{0k} is the inverse of the phase velocity of the k 'th mode for frequency ω . If the input consists of a single noise-free surface wave mode, then the quantity $U(p, \omega)$ will be a maximum at $p = p_{0k}$.

2. Experimental Results

The software implementation of this technique determines a maxima for $U(p, \omega)$. A stack is created over a user specified number of phase velocities. Up to four frequencies for which the amplitude is maximum are then computed for each velocity. One difficulty that occurred was that if the number of stacking velocities was too large, there would be too many phase velocities for each frequency. Figure 85 is the result of p ω processing of the SWIG data at 65 m stacking over 100 velocities. Figure 86 is the same data set using only 40

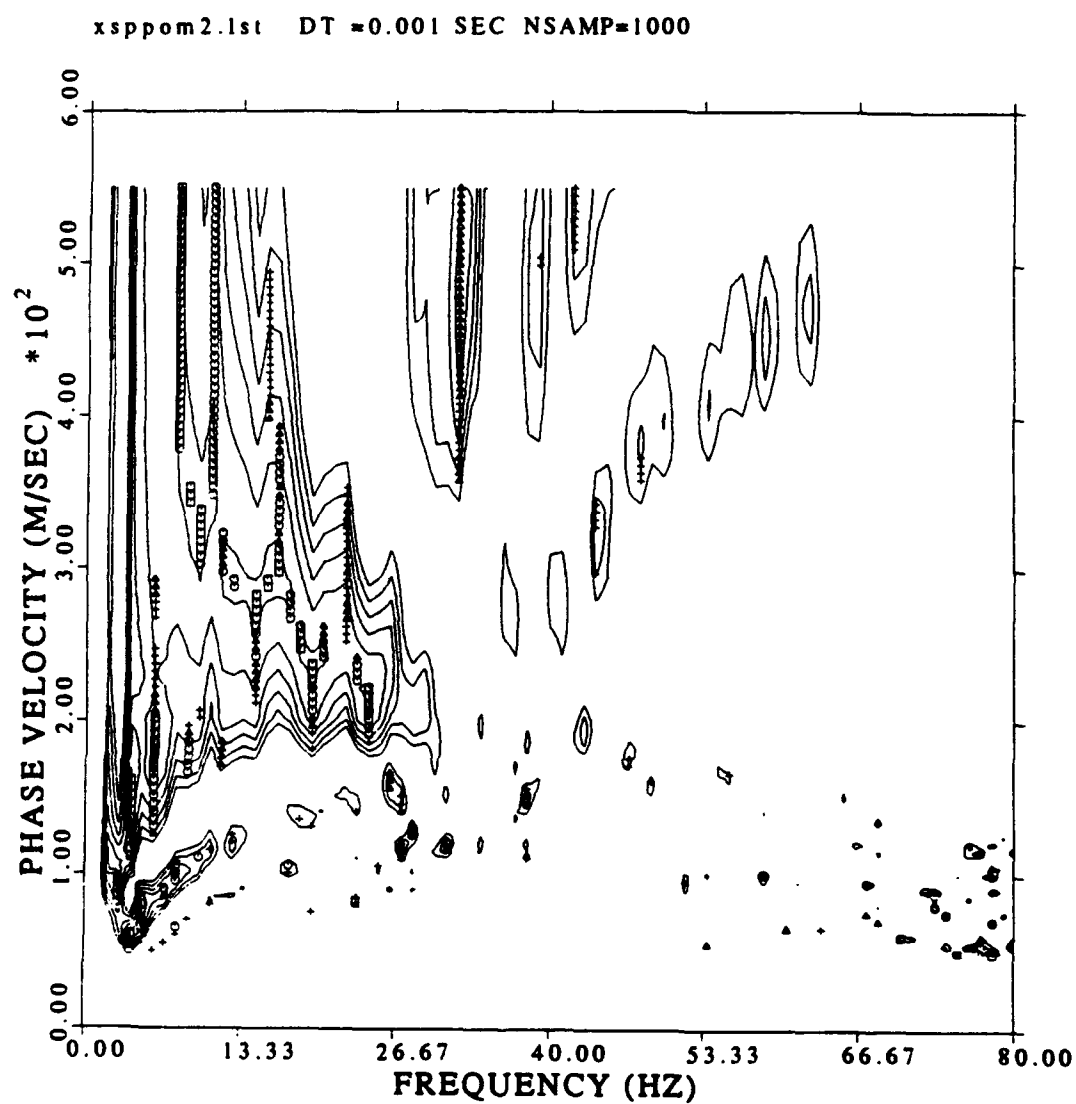


Figure 85. P-omega stacking of 65 meter SWIG data. Nray or the number of velocities computed is set to 100.

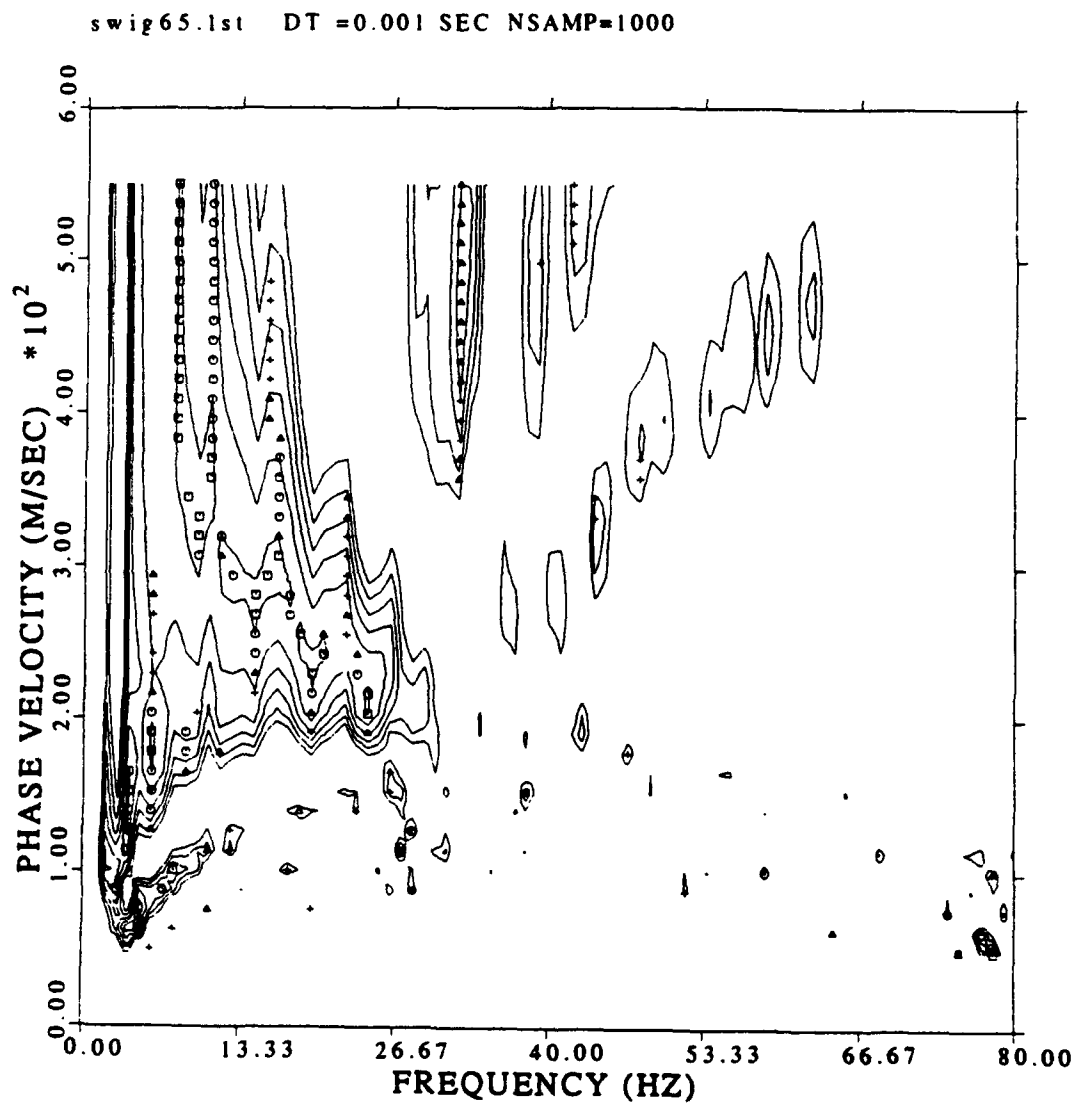


Figure 86. P-omega stacking of 65 meter SWIG data. Nray or the number of velocities computed is set to 40.

velocities. Note that the energy appears to die out or become incoherent beyond 25 Hz. Both velocity stacks resulted in similar amplitude contours in the 5 to 25 Hz range. The 40 velocity results were easier to interpret. Trace number twelve was bad in each data set and so the first twelve traces were excluded from the p-omega processing. The remaining 48 traces appeared to yield stable results.

Figures 87 and 88 illustrate the 40 velocity processing of the SWIG data at 5 and 35 m. Both of these data sets contain information at higher frequencies than the 65 meter data set. The interpreted phase velocity dispersion curves are overlain for comparison in Figure 89. The most notable result is that the phase velocities are consistent over the entire range of the experiment.

The p-omega processing was also applied to the Betsy data. The last eighteen traces were not used because of the bad trace. The results of processing the 5 meter data set is presented in Figure 90. As with the array processing for group velocity, the contours represent 99 percent, 90 percent, 80 percent, 70 percent, 60 percent and 50 percent of the maximum amplitude. Two bands of data appear on the processing. The fundamental mode Rayleigh wave is exhibited by one low frequency, low velocity zone. The first higher Rayleigh mode is exhibited with a second region of higher frequency, higher velocity. Figure 91 is the phase velocity processing of the 35 meter Betsy data set. The results are very complex. This complexity continues with the data from the 65 meter offset (Figure 92). The air blast cuts through the data, and couples with the higher mode making the higher mode Rayleigh waves difficult to interpret. The fundamental mode Rayleigh wave is clear at the 5 meter offset. The fundamental mode has a limited frequency content (to 25 Hz) matching the results of the

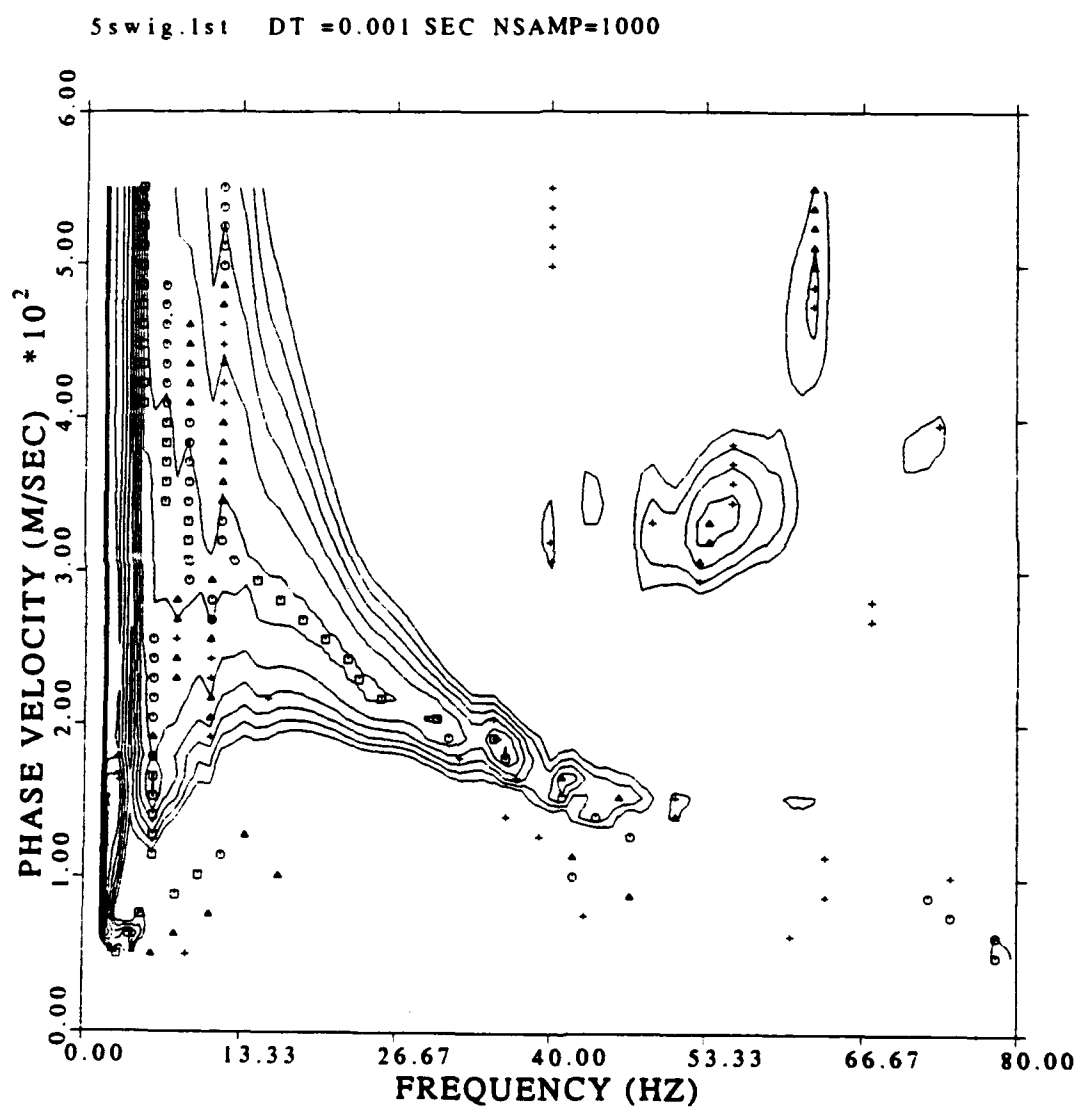


Figure 87. P-omega stacking of 5 meter SWIG data. Nray or the number of velocities computed is set to 40.

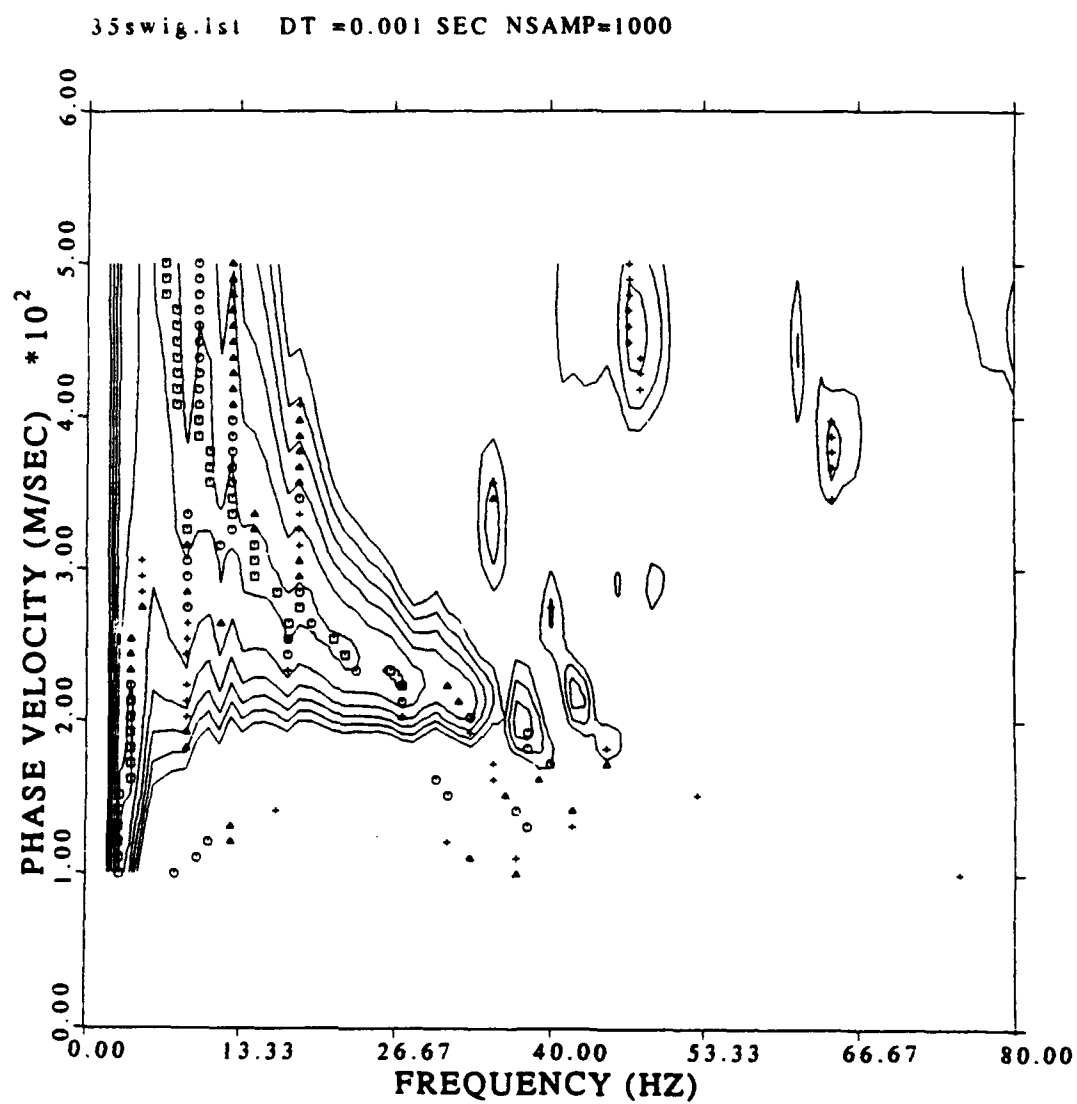


Figure 88. P-omega stacking of 35 meter SWIG data. Nray or the number of velocities computed is set to 40.

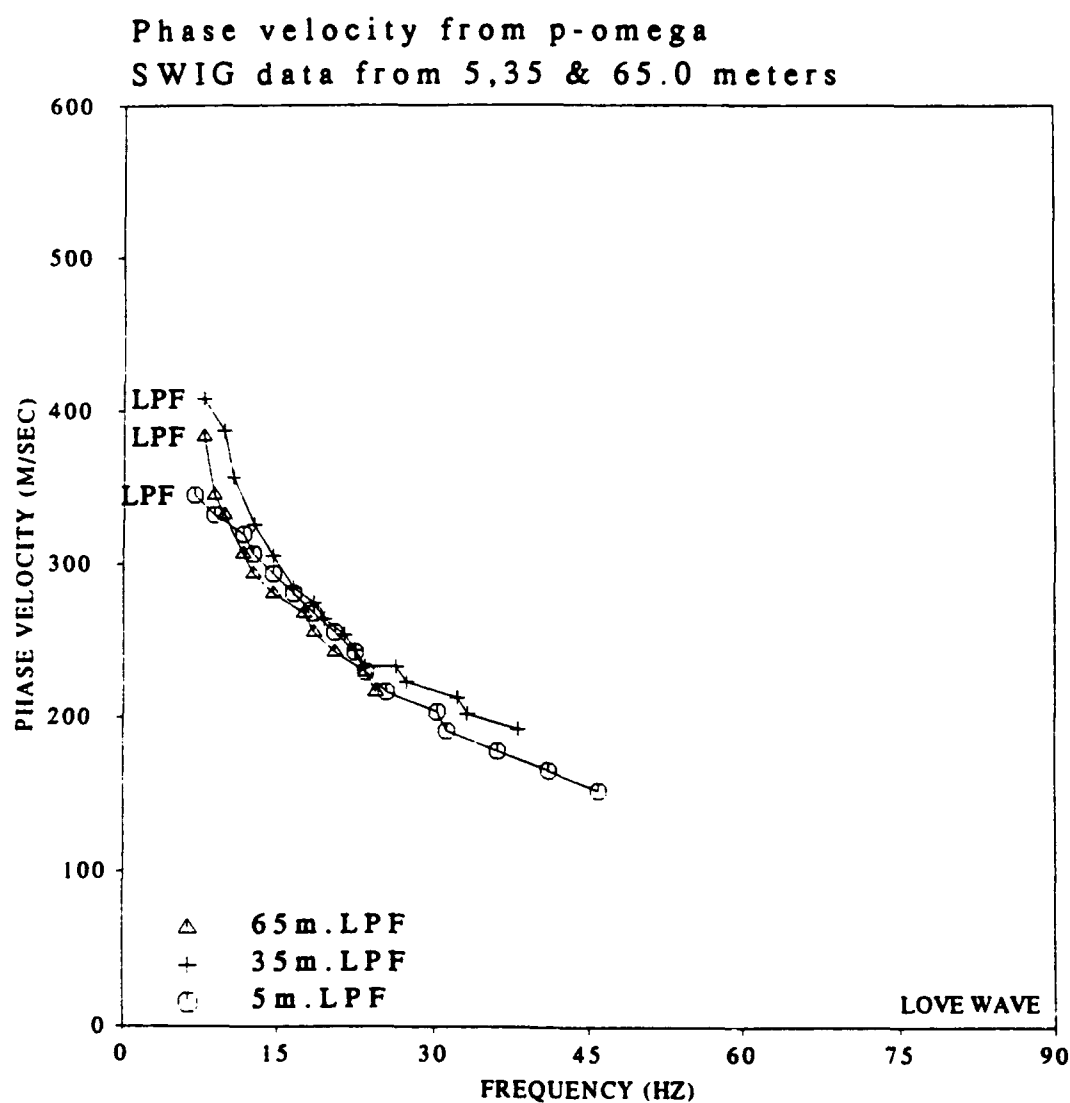


Figure 89. Interpreted Love wave phase velocity dispersion at 5, 35 and 65 m. 5 meter data is represented by circles, 35 meter by plus, and 65 meter by triangles.

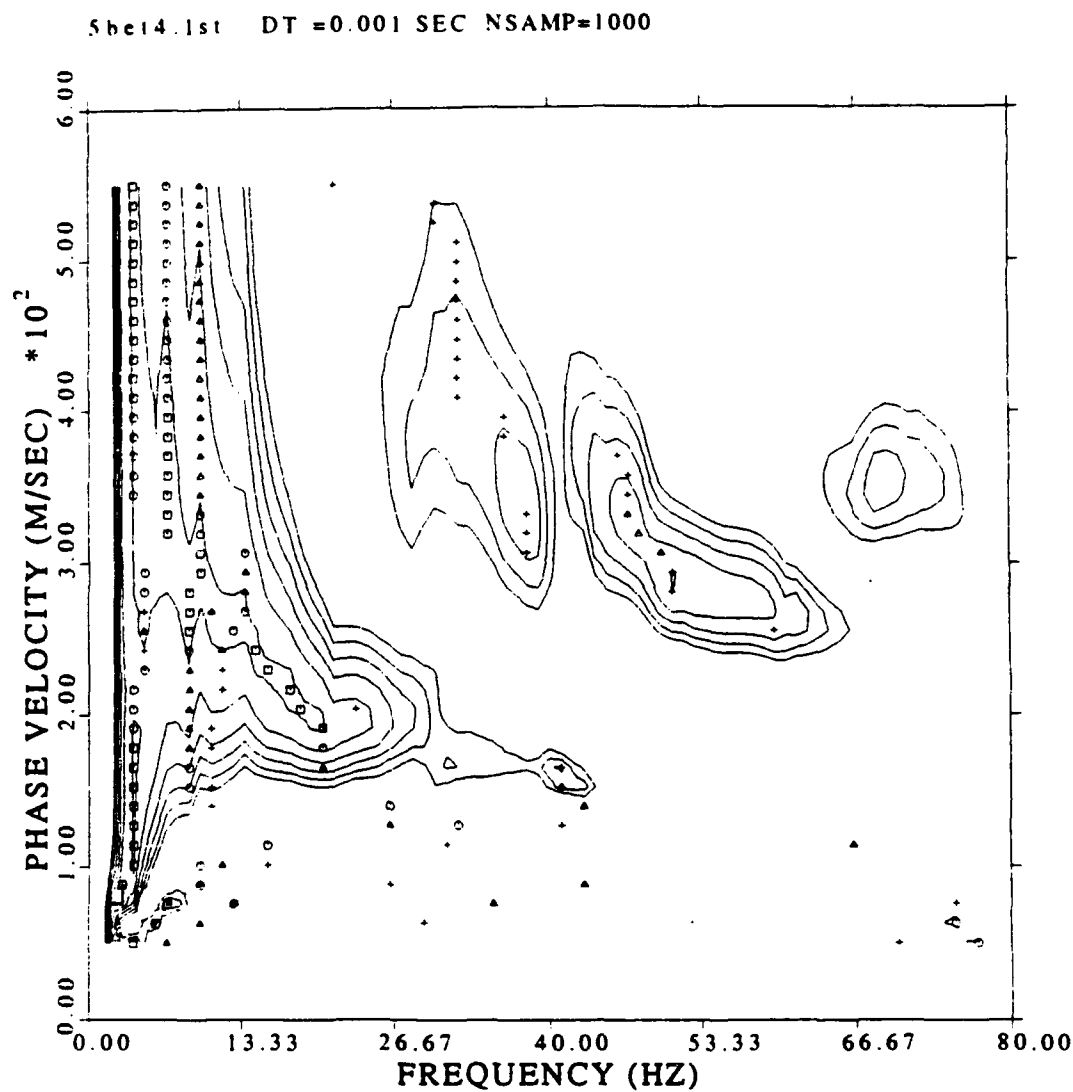


Figure 90. P-omega array processing for phase velocity of 5 meter Betsy data. Largest amplitude for each velocity is represented by squares, second largest by circles, third largest by triangles, and fourth largest by plus signs.

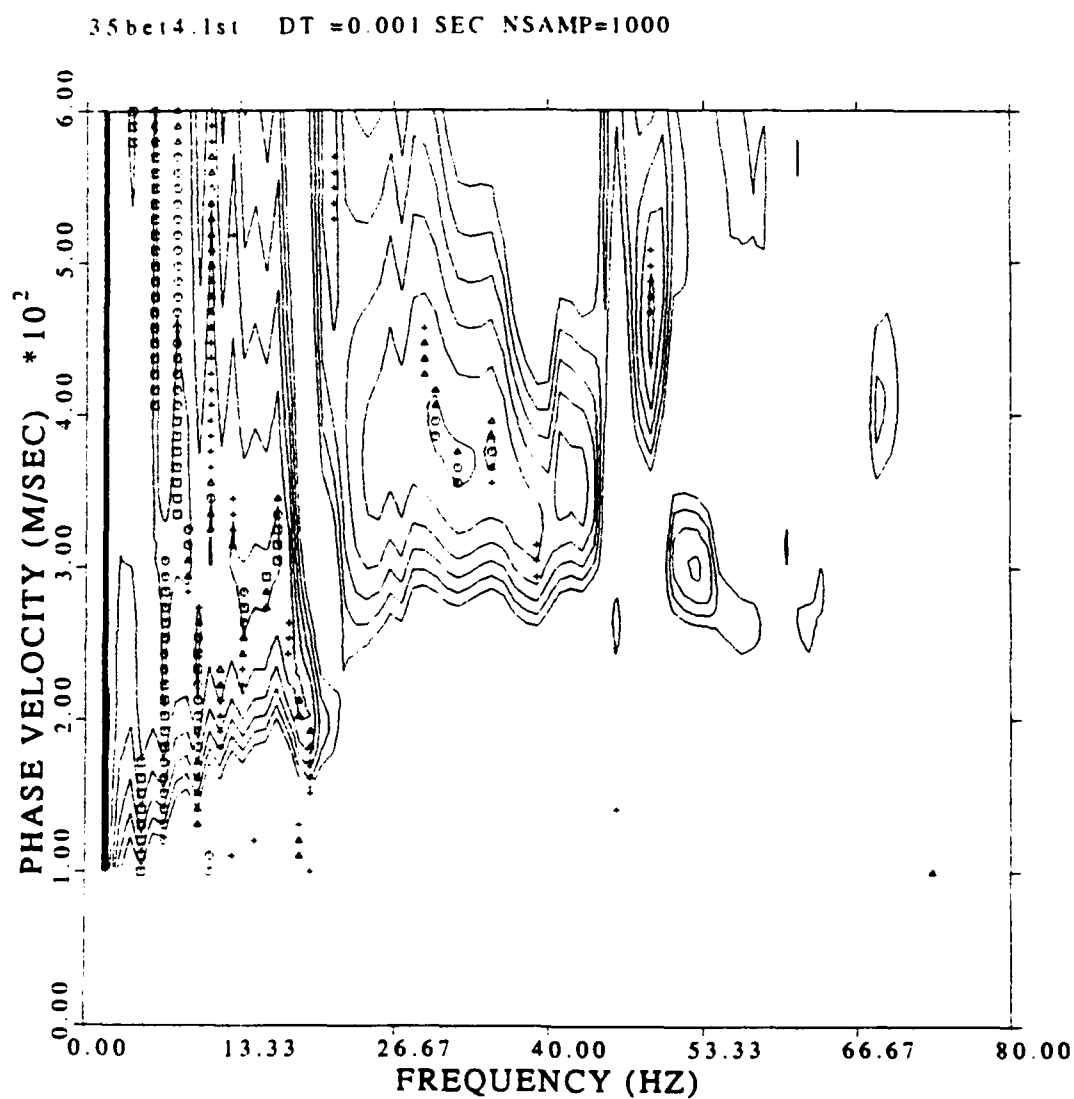


Figure 91. P-omega array processing for phase velocity of 35 meter Betsy data. Largest amplitude for each velocity is represented by squares, second largest by circles, third largest by triangles, and fourth largest by plus signs.

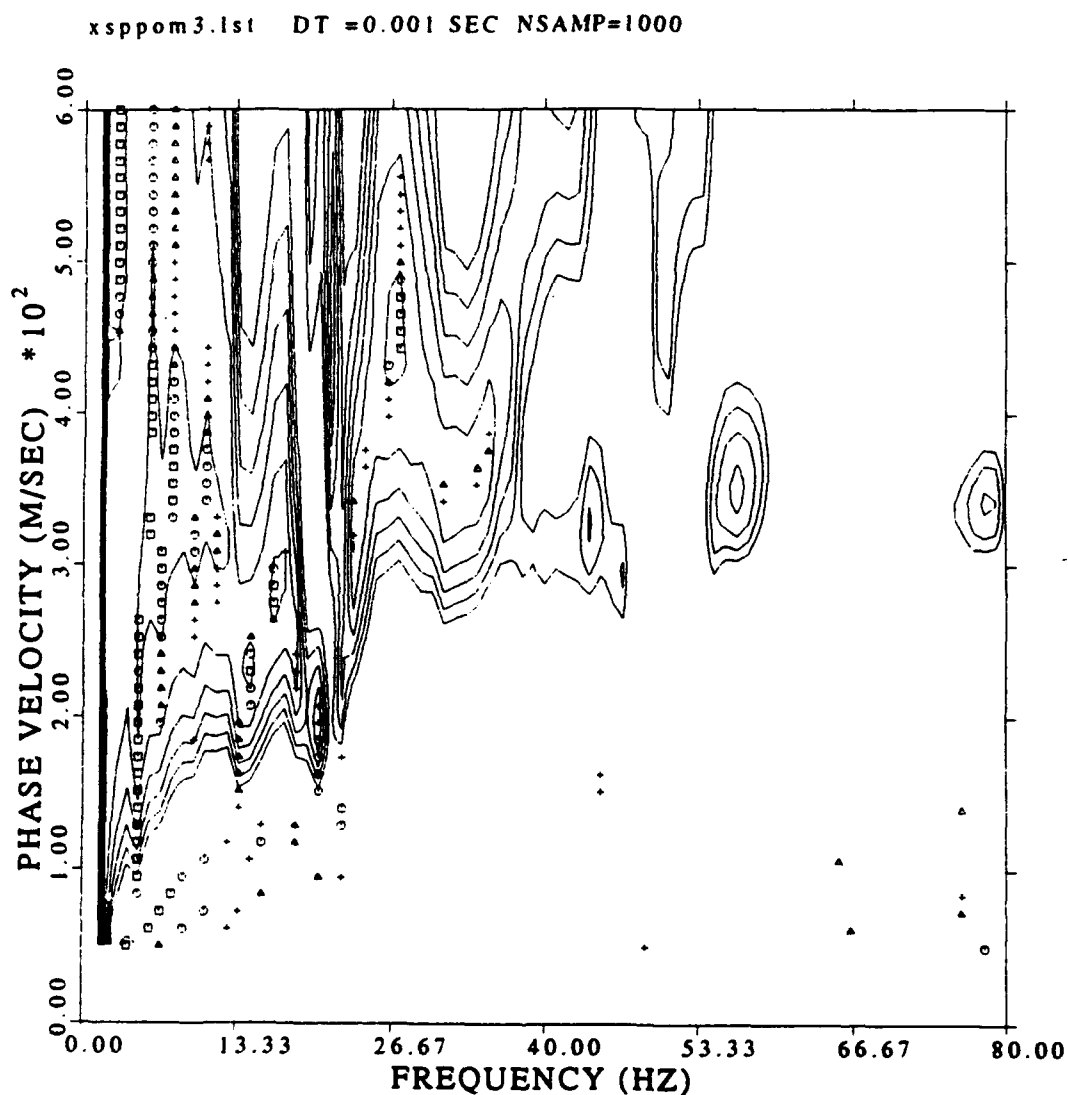


Figure 92. P-omega array processing for phase velocity of 65 meter Betsy data. Largest amplitude for each velocity is represented by squares, second largest by circles, third largest by triangles, and fourth largest by plus signs.

group velocity processing. The energy above this frequency is transferred into the first higher mode.

The interpretation of the processed results was more difficult than for the Love wave data. The fundamental and first higher modes for all 3 offsets are given in Figure 93 and appear consistent with one another. As noted for the Love wave, this is a function of the fact that the phase velocity for all three data sets imaged the same interval. The number of frequency points in the first higher mode data set was so small as to limit the value of this portion of the data set for inversion purposes.

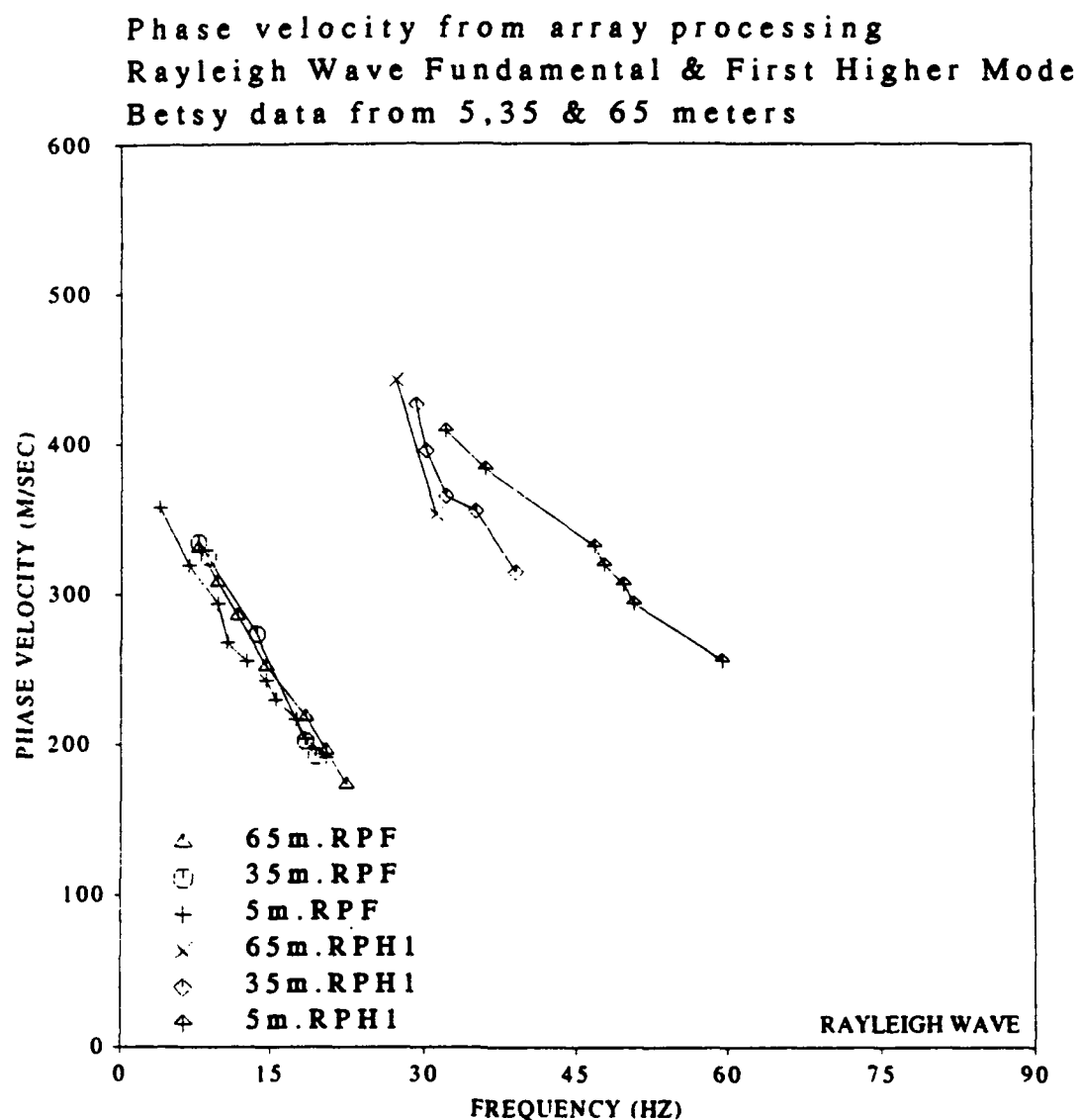


Figure 93. Interpreted phase velocity dispersion results for the Betsy data set at 5, 35 and 65 meter offset. Fundamental mode at 5 meter represented by plus, at 35 meter by circle, and at 65 meter by triangle. First higher mode phase velocity at 5 meter represented by triangle hat, at 35 meter by diamond and at 65 m by X.

CHAPTER 4

INVERSION FOR VELOCITY STRUCTURE

Much effort has been devoted to deriving accurate dispersion curves for the surface waves. The techniques and results are summarized in Chapter 3. These dispersion results can be inverted to derive a velocity and Q model. As with any non-linear inversion technique, a starting model was necessary. In the case of this study a simple refraction analysis of body wave arrival times (both P and SH) was used to build the starting model.

A. Refraction Technique

1. Experimental Technique

The direct travel path time to any receiver can be computed from the source-receiver spacing and the surface layer velocity:

$$(4.1) \quad T = \frac{x_i}{V_1},$$

where T is the total travel time, x_i is the i'th source receiver offset and V_1 is the velocity in layer 1 or the surface layer. If the next deeper layer has a velocity V_2 that is greater than V_1 , at some receiver offset the first arrival or fastest travel time will be from the deeper layer. The travel time for any source receiver pair can be calculated for a simple layered model case. Following Telford et al.

(1976) the travel times for a 2 layer model can be determined from the three segments of the travel path (Figure 94):

$$(4.2) \quad t = \frac{OM}{V_1} + \frac{MP}{V_2} + \frac{PR}{V_1}.$$

Using the relationship $\frac{\sin \theta_1}{V_1} = \frac{\sin \theta_2}{V_2}$ or $\sin \theta_c = \frac{V_1}{V_2}$ and some trigonometric relationships, equation 4.2 can be reduced to:

$$(4.3) \quad t = \frac{x}{V_2} + \frac{2Z \cos \theta}{V_1} = \frac{x}{V_2} + t_1.$$

This equation demonstrates that the velocities can be determined from the slope of the first arrivals on the refraction data. The intercept time, t_1 , or time for $x=0$, can be used to determine the layer thickness Z from:

$$(4.4) \quad Z = \frac{1}{2} V_1 t_1 / \cos \theta.$$

This analysis can be extended to a multiple layer model (Figure 95) assuming that $V_1 < V_2 < V_3$. The refraction path OM'M''P''P'R' is fixed according to Snell's law:

$$(4.4) \quad \frac{\sin \theta_1}{V_1} = \frac{\sin \theta_2}{V_2} = \frac{\sin \theta_3}{V_3} = \frac{1}{V_3},$$

where θ_2 is the critical angle for the second layer while θ_1 is less than the critical angle for the upper layer. As before, the travel times can be represented as:

$$(4.5) \quad t = \frac{OM' + R'P'}{V_1} + \frac{M'M'' + P'P''}{V_2} + \frac{M''P''}{V_3}.$$

As with the two layer model, using some trigonometric relationships equation 4.5 can be rearranged into:

$$(4.6) \quad t = \frac{x}{V_3} + \frac{2Z_2}{V_2} \cos \theta_2 + \frac{2Z_1}{V_1} \cos \theta_1 = \frac{x}{V_3} + t_2.$$

This equation demonstrates that the time-distance curve for the third layer has a slope inversely proportional to the velocity of the third layer with a zero intercept dependent on the thickness of the two upper layers. This conclusion can be generalized to any number of layers n , such that:

$$(4.7) \quad t = \frac{x}{V_n} + \sum_i \frac{2Z_i}{V_i} \cos \theta_i,$$

where $\theta_i = \sin^{-1}(\frac{V_i}{V_n})$. This equation can be used for any number of layers providing that the velocities are increasing with depth and that each layer is thick enough to permit correct analysis from the time-depth relationship. The individual velocities and the subsequent critical angles can be computed from the slope

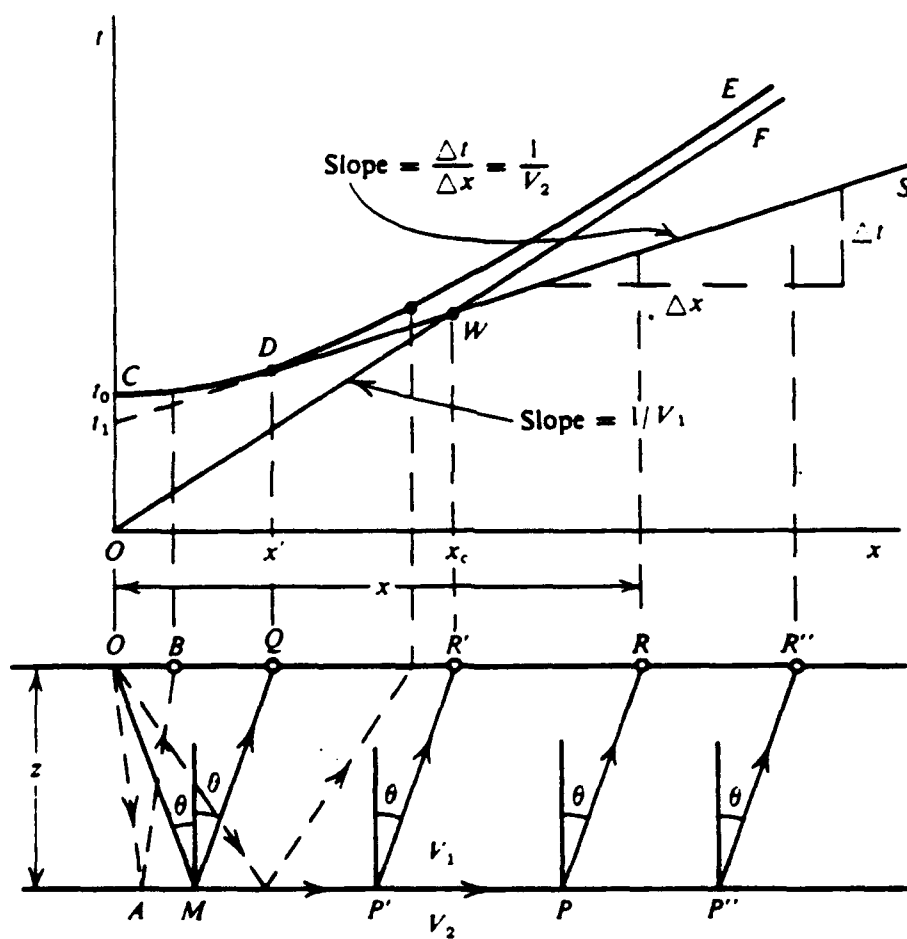


Figure 94. Raypaths for 2 layer model with time distance curves (from Telford et al., 1976)

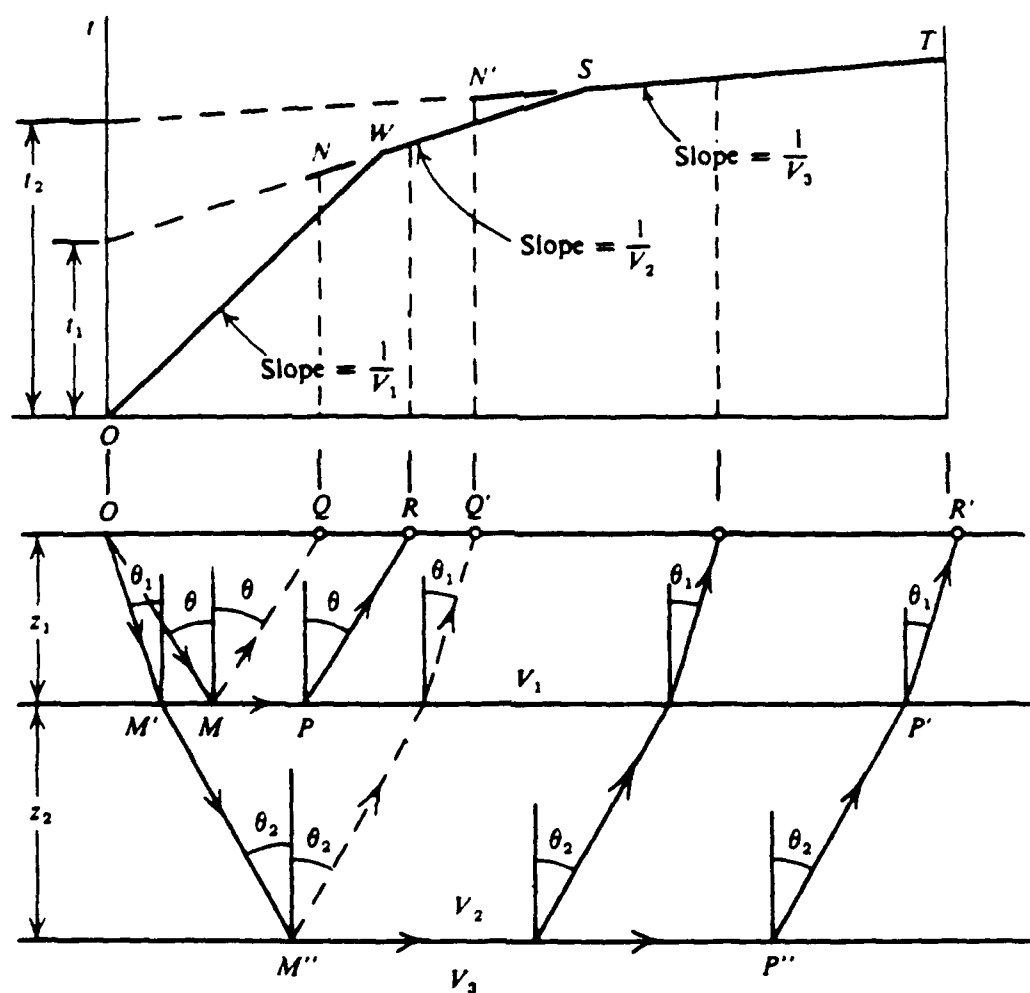


Figure 95. Raypaths for 3 layer model with time distance curves (from Telford et al., 1976)

of the time-distance curve. The layer thicknesses can then be derived from the projected intercepts of the time-distance curves.

2. Experimental Results

The data sets for this study were acquired from 5 to 94.5 meters at half meter spacings. All data sets were interpreted using the Intercept Time Method (ITM) as documented in Telford et al (1976). The basic analysis is performed using equation 4.7. This technique assumes non-dipping, planar layers with velocity increasing with depth. The interpreted first break picks and slopes for all six data sets are plotted in Figures 96 to 101. The data is plotted on an expanded scale, both in time and distance. The data is summarized in tabular form in Tables 4 and 5. Both Betsy and SWIG data indicate 4 layers with similar thicknesses for the corresponding layers. The thicknesses for the Betsy data set or compressional analysis were used for input into the inversions. The primary reason for using the compressional layer thicknesses was that the inversion process assumed a fixed compressional starting model.

B. Inversion of Dispersion Data

1. Experimental Technique

Detailed explanations of the inversion algorithms and techniques are presented in Herrmann (1987). Some of the concepts necessary to interpret the results of this thesis are presented in this section. Several material properties influence surface wave dispersion, including shear and compressional wave velocity, thicknesses of the layers, as well as the bulk density of the layers. The inversion of all of these parameters over a multilayer model is a nonlinear process.

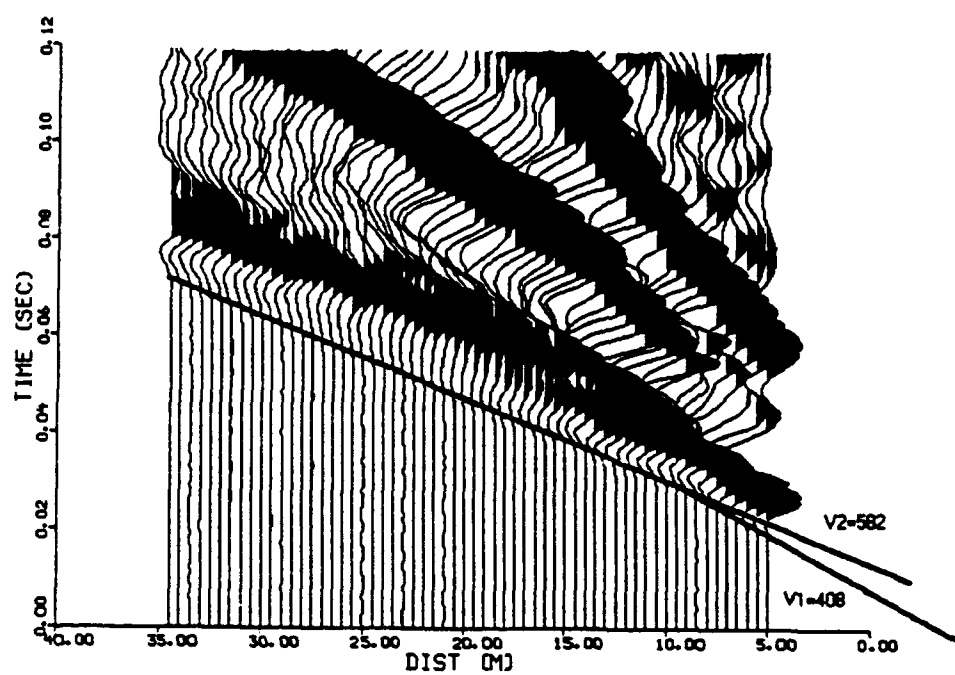


Figure 96. Instrument corrected Betsy data at 5 m with refraction analysis marked

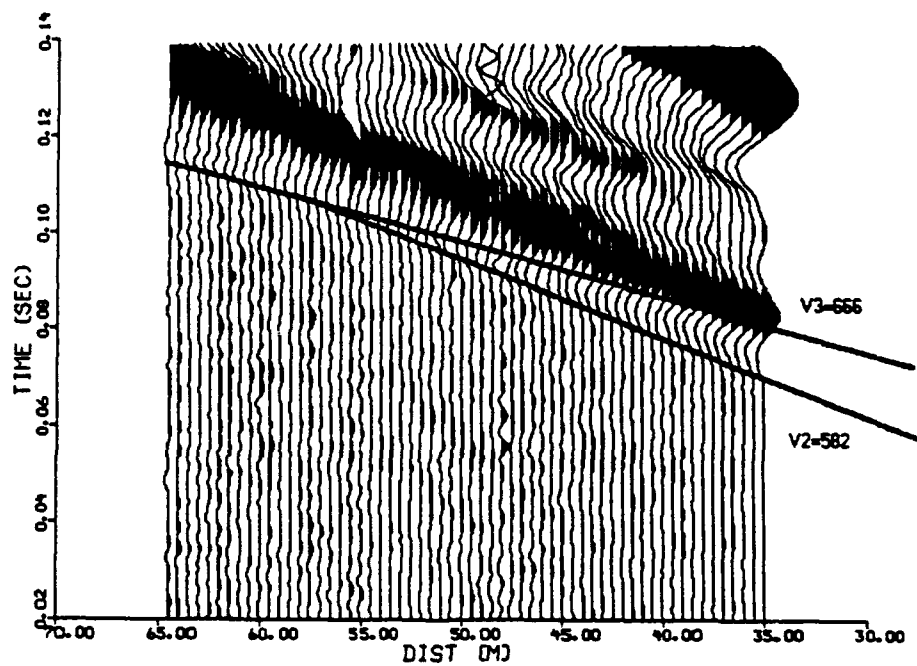


Figure 97. Instrument corrected Betsy data at 35 m with refraction analysis marked

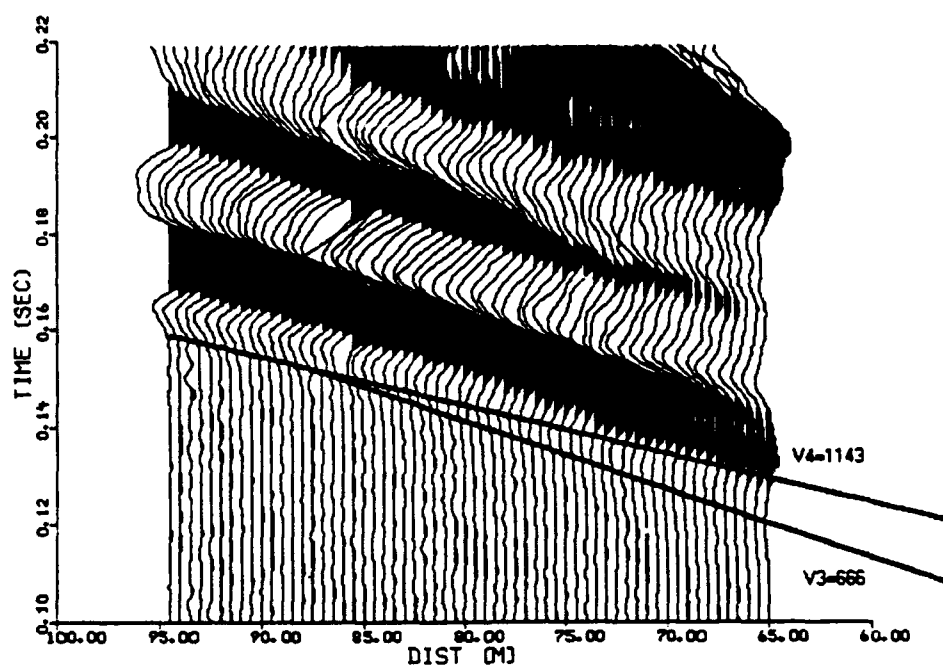


Figure 98. Instrument corrected Betsy data at 65 m with refraction analysis marked

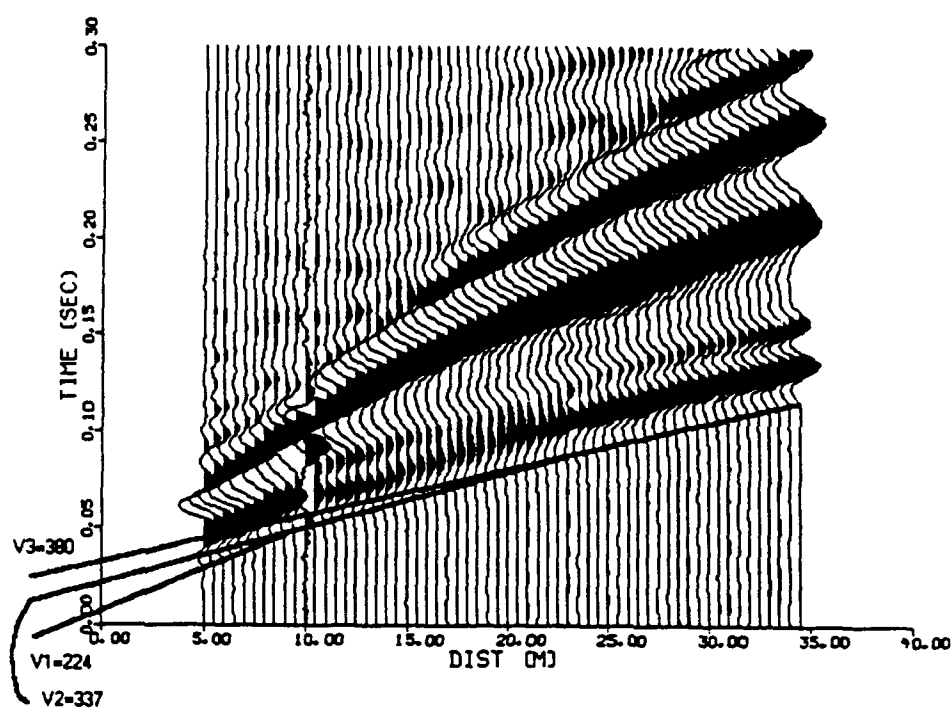


Figure 99. Instrument corrected SWIG data at 5 m with refraction analysis marked

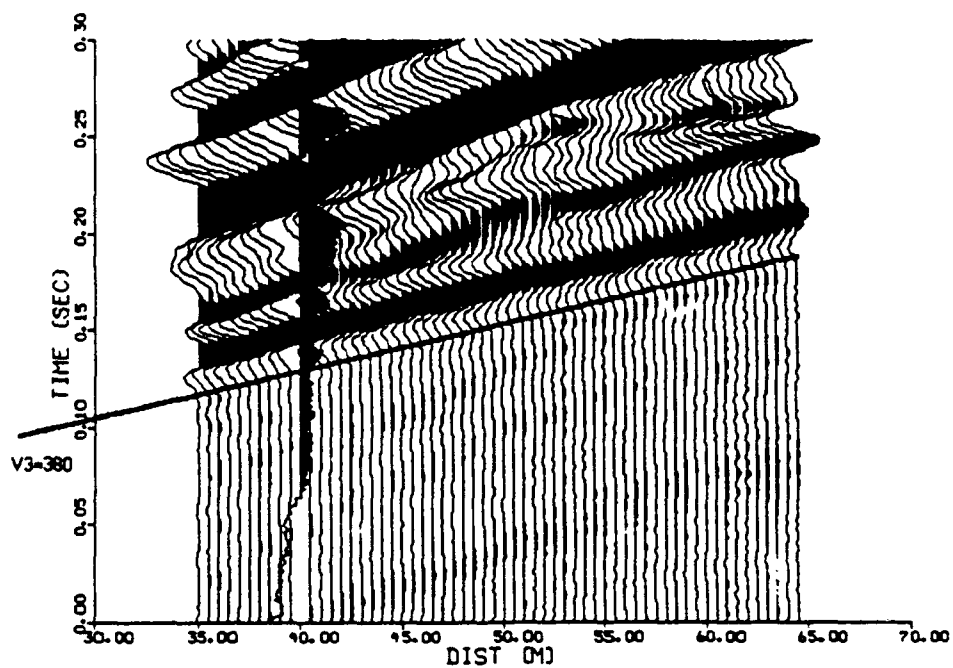


Figure 100. Instrument corrected SWIG data at 35 m with refraction analysis marked

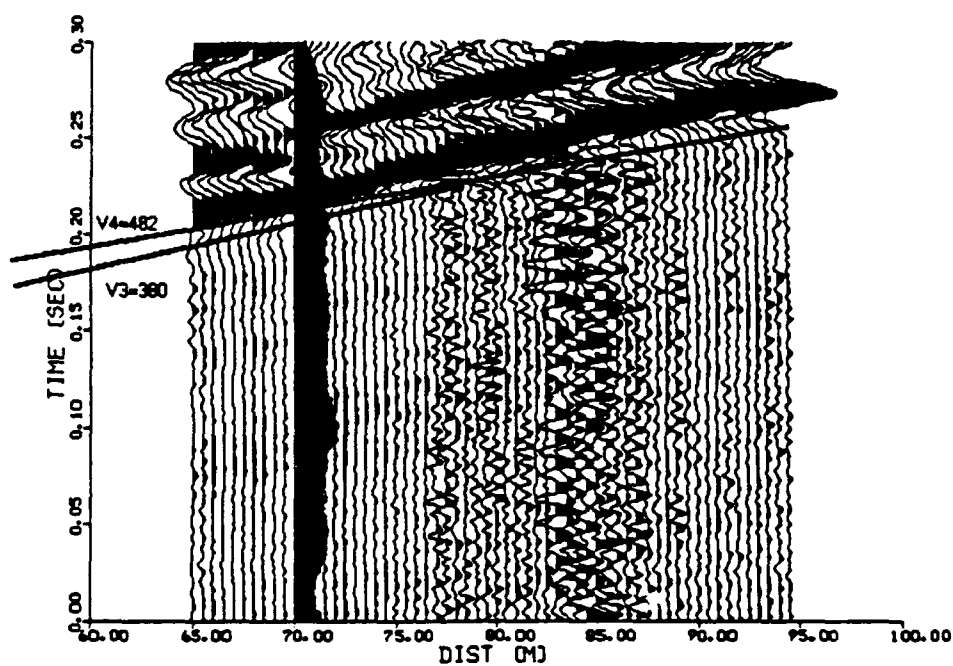


Figure 101. Instrument corrected SWIG data at 65 m with refraction analysis marked

Table 4
BETSY DATA REFRACTION ANALYSIS

Layer Number	1	2	3	4
P Velocity (m/sec)	408	582	666	1143
Intercept (msec)	7.0	12.5	23.0	57.5
Crossover (meters)	9.5	57.0	87.5	NA
Thickness (meters)	1.6	5.9	10.6	Halfspace

Table 5
SWIG DATA REFRACTION ANALYSIS

Layer Number	1	2	3	4
SH Velocity (m/sec)	224	337	380	482
Intercept (msec)	5.0	19.0	26.5	65.7
Crossover (meters)	9.0	23.0	78.5	NA
Thickness (meters)	2.1	2.3	10.6	Halfspace

The inversion of this data is therefore handled in an iterative fashion, using a damping factor to limit how far the parameters are allowed to change at one time.

One additional parameter that influences the velocity dispersion is the attenuation or Q factor of any layer or material relative to compressional or shear wave propagation. The attenuation of the surface wave due to Q must be taken into account in order to keep the results causal. The first step in the inversion processing was to do a non-causal inversion, or an inversion that neglected the effects of Q . The primary reason for doing a non-causal inversion was that the attenuation appeared to be poorly measured, and therefore it seemed appropriate to obtain a starting result that was not contaminated by the uncertainty in measuring attenuation due to Q . Once a non-causal result was obtained, a causal inversion, or inversion in which Q influenced dispersion velocity could be performed.

Because there are so many parameters influencing the dispersion, certain assumptions about the material properties were made to constrain the final results. One assumption that was input into the inversion was that the shear Q or Q_β was related to the compressional Q or Q_α by a constant, in this case 2.25. For this study it was also assumed that the number of layers, layer thicknesses and compressional velocities were all known from the refraction analysis. This leaves velocity dispersion and surface wave attenuation as the observations to invert to change the shear velocity and shear Q for the various layers. These data can be inverted simultaneously with non-zero partial derivatives for attenuation versus β and dispersion velocity versus Q_β . This type of inversion is

known as a coupled inversion. A decoupled inversion is where either Q_β or β are assumed constant and the other parameter is determined by inversion.

In the processing of this data, decoupled inversions were used to obtain estimates of the parameter values before performing a final coupled inversion. Equation 1.10 demonstrates that the phase velocity and group velocity of a surface wave in a plane layered medium are directly related to one another. Since one velocity can be computed from the other, the two data sets should be equivalent for inversion purposes. The inversions that were performed included using the group and phase velocities separately as well as together to solve for the Q_β and β .

2. Experimental Results

The inversion software as implemented by Herrmann (1987), includes the capability to invert for Q structure as well as velocity structures. Inputs can be any combination of Love group velocity, phase velocity, and gamma or attenuation coefficients as well as the corresponding Rayleigh characteristics. The Rayleigh and Love wave information were inverted as separate problems in this study. The two data sets may be imaging different information, such as SV and SH. Additionally, the Rayleigh information was more complex and warranted separate treatment.

The inversion techniques can, in principle, invert multiple modes of velocity information. One limitation is that these different modes must encompass the same frequency band. The energy in the frequency band below 25 Hz was primarily in the fundamental mode while energy from the frequencies above 25 Hz were in the first higher mode. This result is similar to the Simila (1982) and

Bogaards (1989) study. Since these two modes did not overlap in frequency, they could not be inverted together. Additionally, the algorithms for different modes would not allow for the inversion of a higher mode by itself. Consequently, inversion of the Rayleigh wave data was limited to the fundamental mode information.

One Rayleigh wave inversion was performed for this thesis, utilizing the maximum amount of available data. The phase velocity from the p-omega array technique was combined with the group velocity and attenuation coefficients from the Barker array dispersion analysis. The starting model included compressional and shear velocities from the refraction analysis and Q values from the Grant (1988) model (Table 3). The inversion was run as a causal inversion, where Q and velocity structure both affect the surface wave dispersion. The results of the velocity inversion are displayed in Figure 102 with velocity versus depth along with the resolution kernels. The normalized amplitude of the resolution kernels for each layer are presented with depth to the center of the layer across the top versus the depth for each value of the kernels. The results demonstrate that the kernels have maximum amplitudes for the appropriate layers. The unnormalized kernels indicate that the amplitudes for these kernels decrease with depth. The corresponding final decoupled inversion for Q with resolution kernels is displayed in Figure 103. The third model in Figures 102 and 103 is the coupled, composite inversion of the velocity information with the Q or attenuation information. In the composite inversions the velocity and attenuation information are normalized since the amplitudes may be of entirely different orders of magnitude. This allows the inversion to not be overly weighted or biased by either the Q or the velocity information. Figure 104 shows the fit

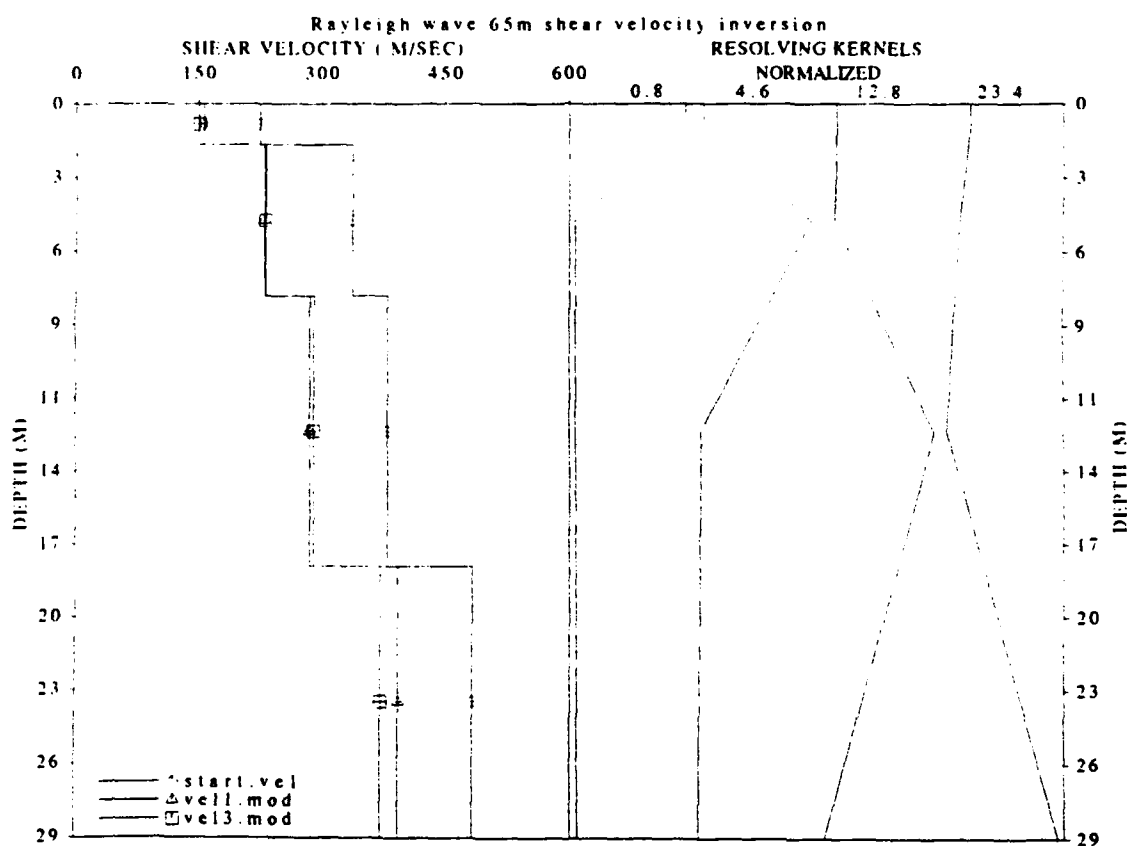


Figure 102. 65m Betsy inversion for shear velocity structure. Diamonds represent the start or input model; triangles are the decoupled causal inversion; squares are the final coupled, causal inversion results. Horizontal bars are standard deviation.

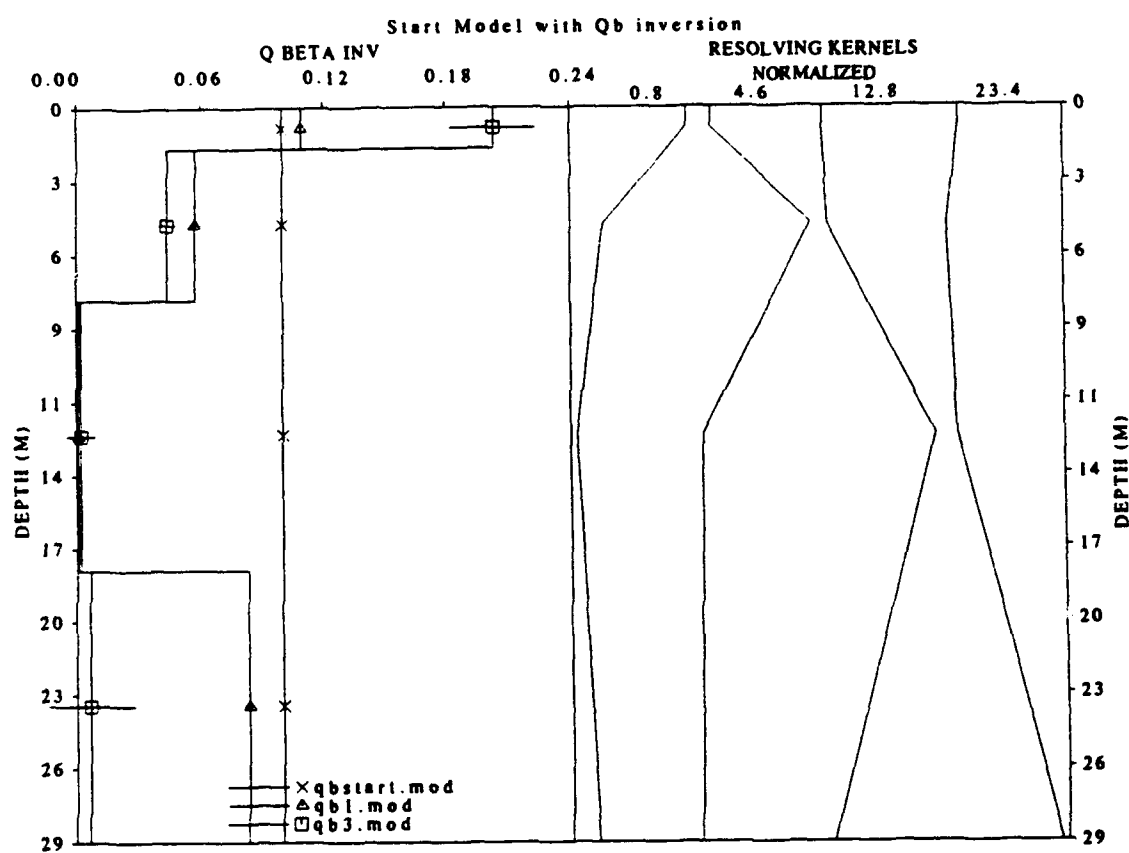


Figure 103. 65m Betsy inversion for shear Q inverse structure. X,s represent the start or input model; triangles are the decoupled causal inversion; squares are the final coupled, causal inversion results. Horizontal bars are standard deviation.

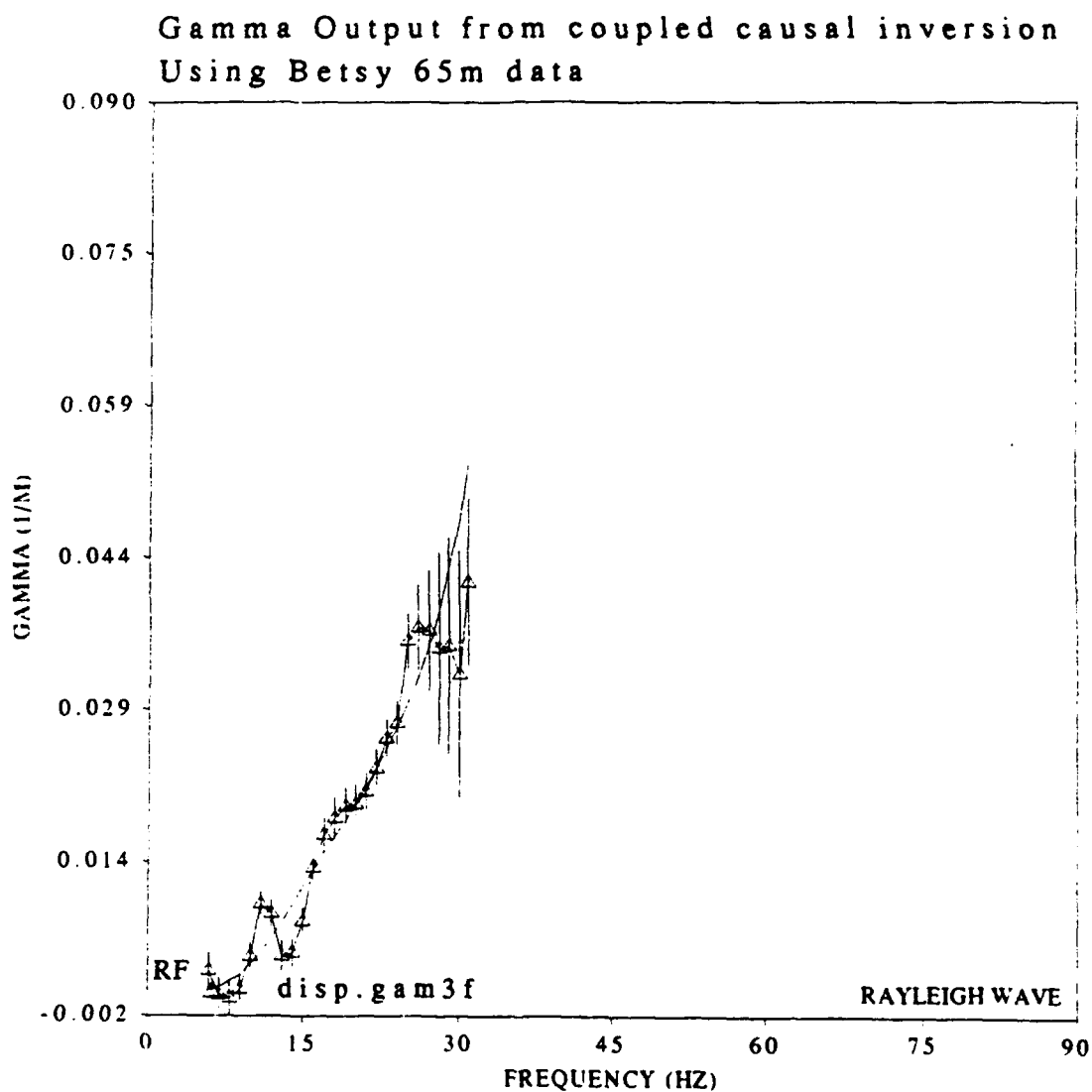


Figure 104. Comparison of observed to predicted gamma for 65m Betsy inversion. Triangles represent observed data with vertical bars representing one standard deviation. The solid curve is the predicted results.

between the observed attenuation coefficients and the predicted attenuation coefficients from the final inverted velocity and Q models. Figure 105 shows the fit between the observed and predicted group and phase velocities. The fit is much better for the group velocities than the phase velocities since the group velocity has many more points in the data set and the inversion is trying to minimize the least squares error between the predicted and observed data sets. The inconsistency in the results between the group and phase velocities may reflect the fact that the phase velocities and group velocities were imaging different lateral extents of the velocity structures.

The inversion process was applied to the Love waves utilizing three different portions of the data set. The phase velocity and gamma or attenuation coefficient data were inverted first. The group velocity and gamma were inverted second. The final inversion included the group velocity, the phase velocity and the gamma data. Each of these inversions followed the same three stages. The first was to invert for a non-causal velocity field, or an inversion for shear velocity structure that ignored the effects of Q. The second inversion included a decoupled, causal inversion for shear velocity structure. In this instance the Q structure was held constant while allowing the shear velocity to vary. The third inversion was a coupled, causal inversion which allowed both the shear velocity structure to vary based on the dispersion inputs, and the Q structure to vary based on the gamma inputs.

Figure 106 summarizes the results of the Love wave phase velocity inversion for shear velocity. The shear velocities in the shallowest two layers calculated from the refraction analysis appear to be too high. There are several possible explanations for this result. One is that there could be some

experimental error since there are only a few time depth pairs used in the shallowest layers. A more reasonable explanation would be that the dispersion results are averaged over a longer spatial interval, on the order of 30 meters for the phase velocity and at least 65 meters for the group velocity. The refraction analysis for the shallowest layer covered only 9 meters laterally. The two deepest layers appear to be fairly stable over all four sets of inversions (three Love and one Rayleigh wave). The maximum of the resolution kernels for both of the deepest layers is about 10^{-2} which indicates that the longest wavelengths are not contributing much to the model. Dispersion data below the 6 Hz cutoff in this data set would help resolve these layers.

Figure 107 illustrates the Q structure from the phase velocity inversion. The results show significant scatter for the different inversions, and probably can only yield a rough estimate of Q. The primary input into this inversion is a comparison of the spectral amplitudes with range for the Love wave portion of the data set. The assumption implicit in this technique is that spreading loss and Q are the only parameters influencing relative amplitude of the Love waves. Some spectral notching due to geology was noted during the section on MFT. This could very easily contaminate the gamma data and bias the Q inversion results.

The predicted phase velocity dispersion from the final inverted velocity model is given in Figure 108. The visual fit is very good, in spite of the fact that the input data have fairly large error bars, especially at the low frequencies. The fit of the predicted to observed gamma data is shown in Figure 109. The fit is fair with most of the divergence at the low end.

A similar comparison of the group velocity results is shown in Figures 110 to 114. The anomalous thing about these results is that after the Q inversion,

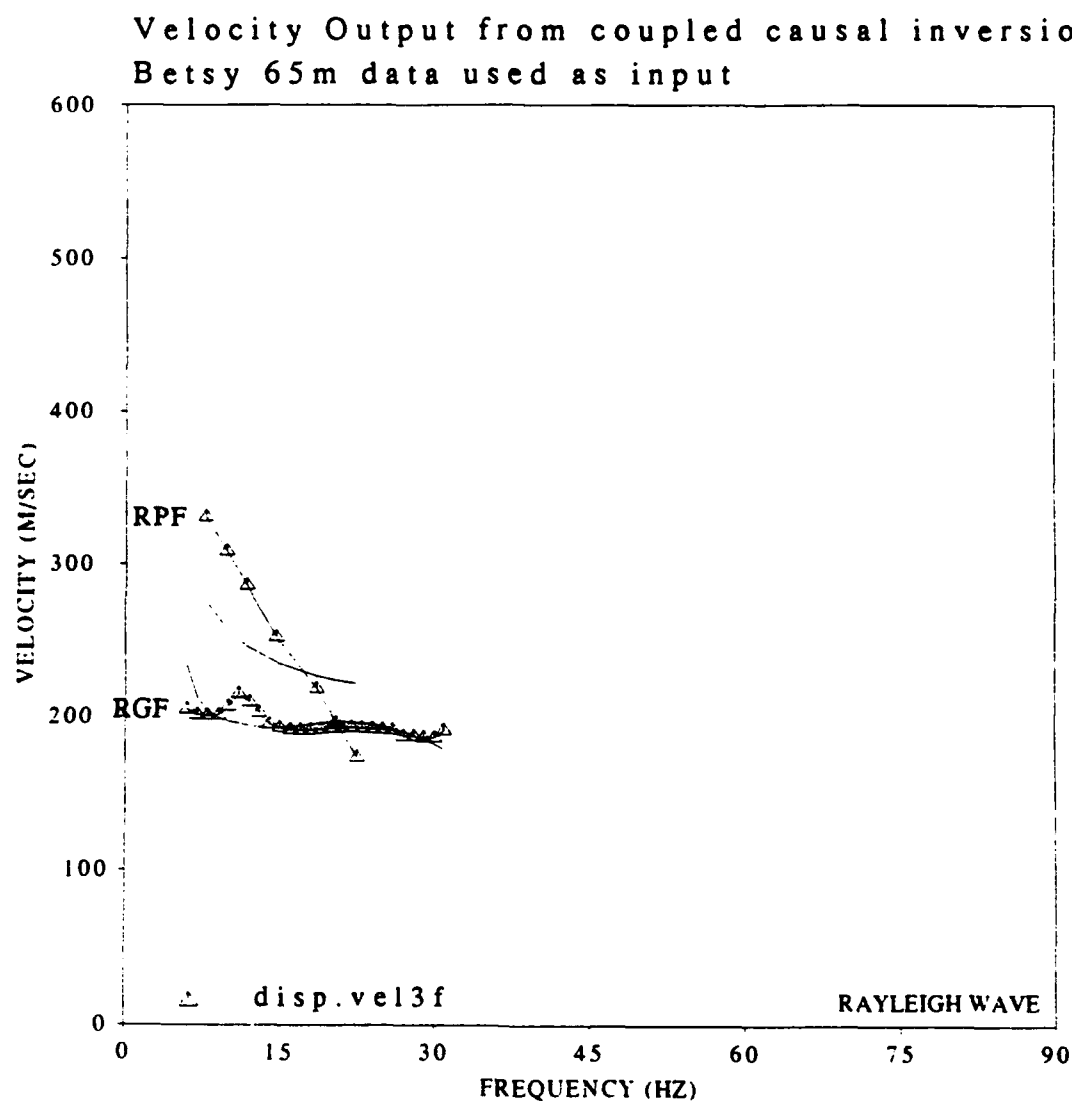


Figure 105. Comparison of observed to predicted group and phase velocities for 65m Betsy inversion(Rayleigh surface wave). The RPF triangles represent observed phase velocity data and the RGF triangles represent the group velocity. The solid curve in both cases is the predicted result.

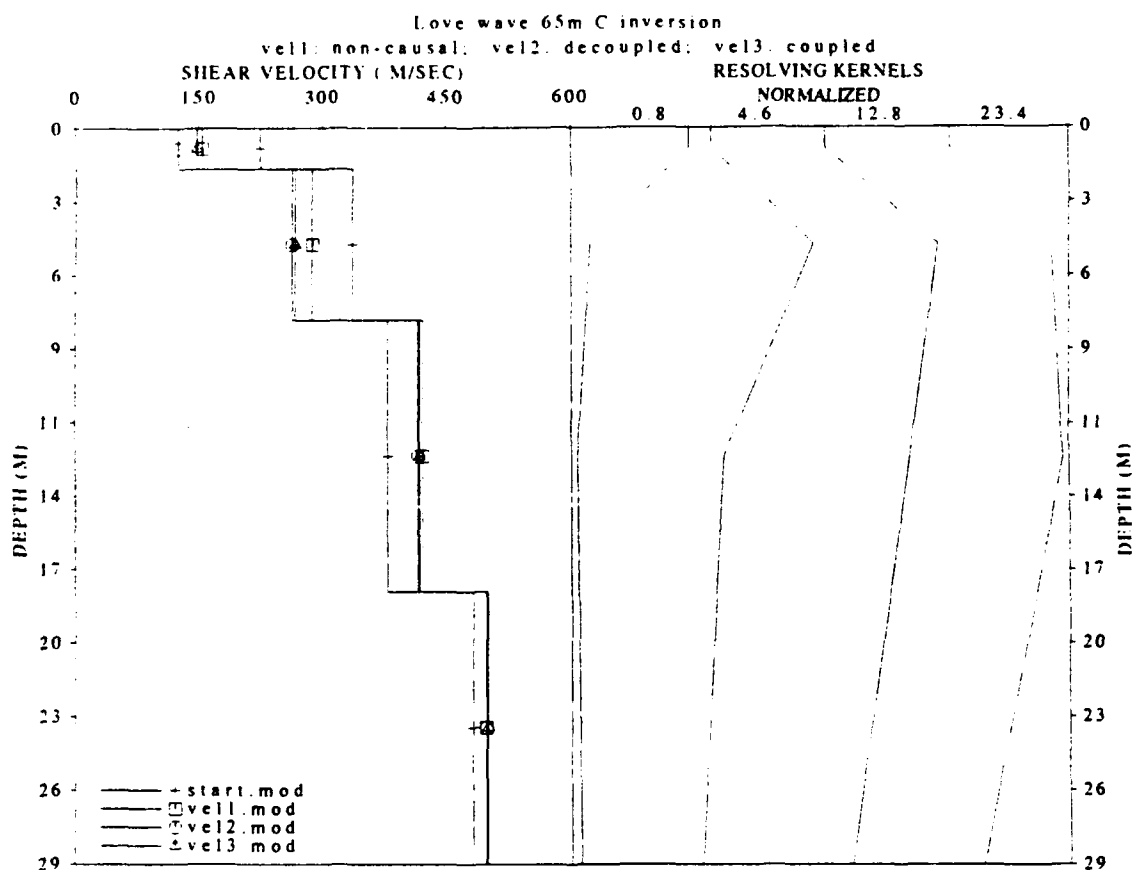


Figure 106. 65 meter SWIG data phase velocity/gamma inversion for shear velocity structure. Plus is input start model, squares is non-causal inversion, circles is decoupled, causal inversion with fixed Q model, triangles is final model from coupled causal inversion.

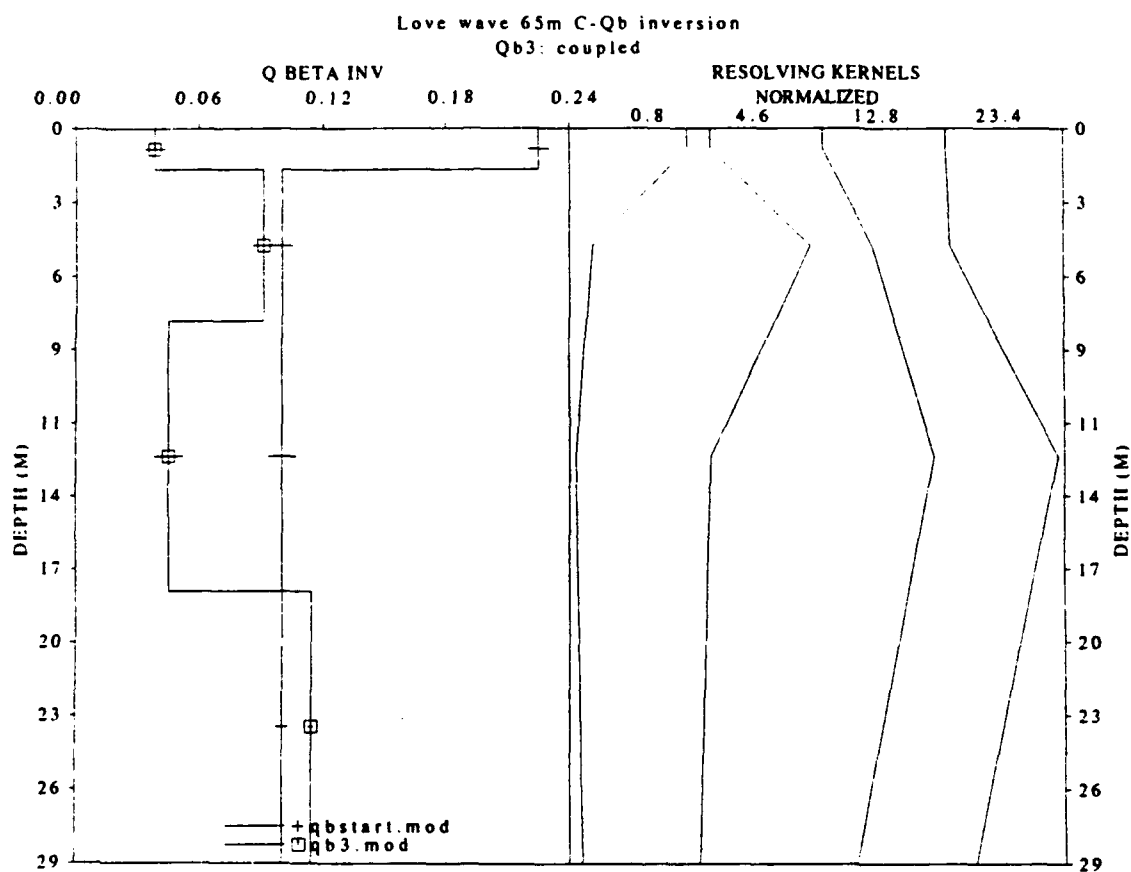


Figure 107. 65 meter SWIG data phase velocity/gamma inversion for Q structure. Plus is input start model, squares is final model from coupled causal inversion.

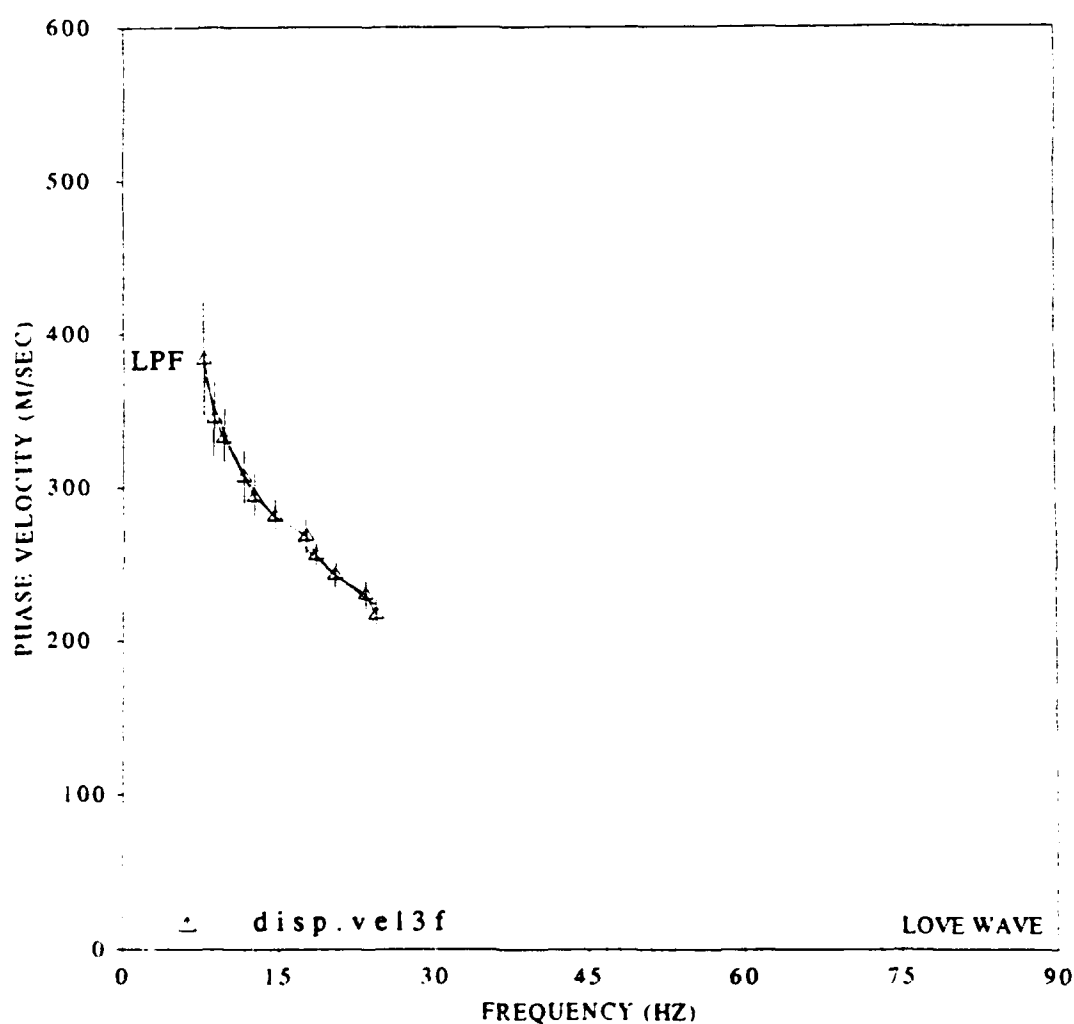


Figure 108. 65 meter SWIG data observed versus predicted phase velocity after final inversion. Triangles are observed data with vertical bars being standard deviation from array processing analysis. Solid line is predicted data set.

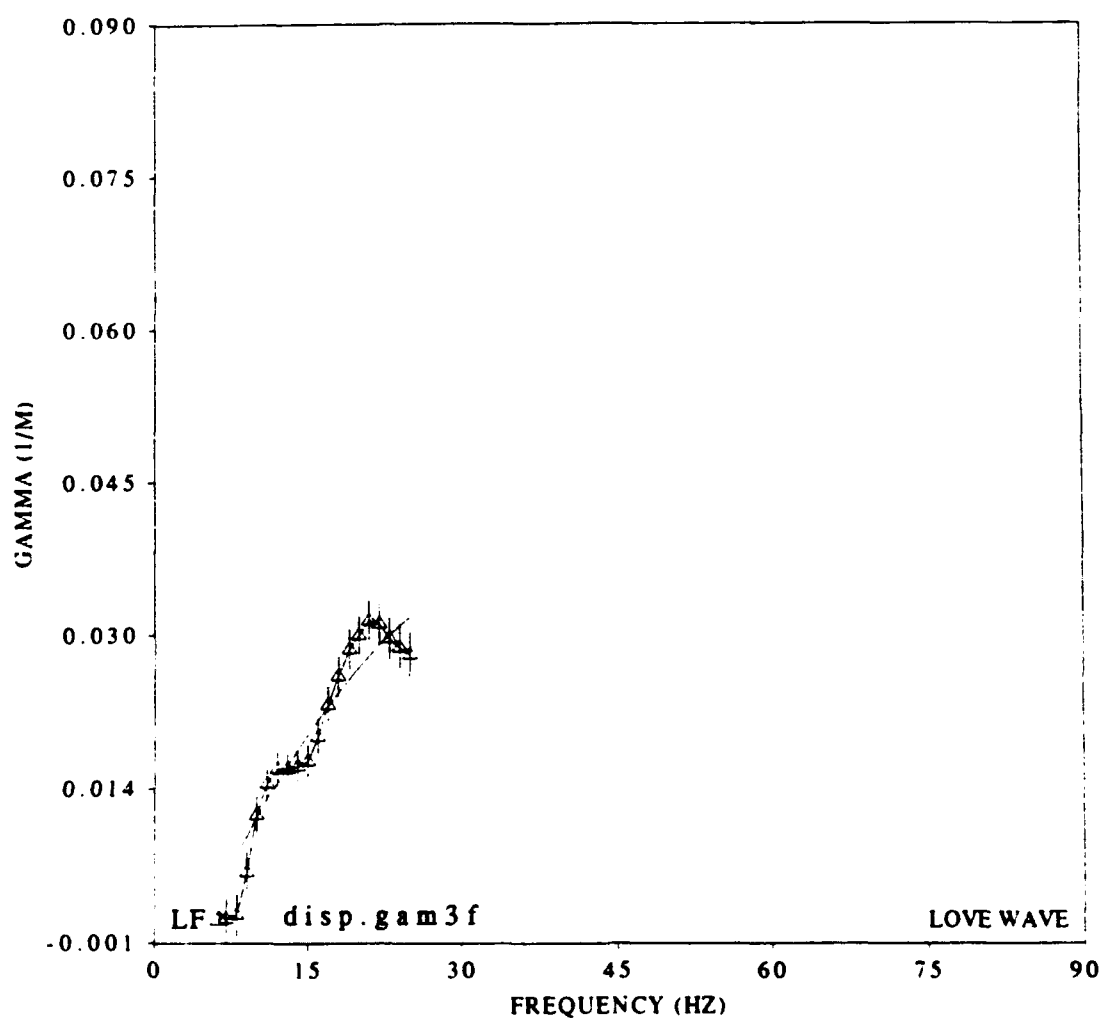


Figure 109. 65 meter SWIG data observed versus predicted attenuation coefficients after final inversion. Triangles are observed data with vertical bars being standard deviation from array processing analysis. Solid line is predicted data set.

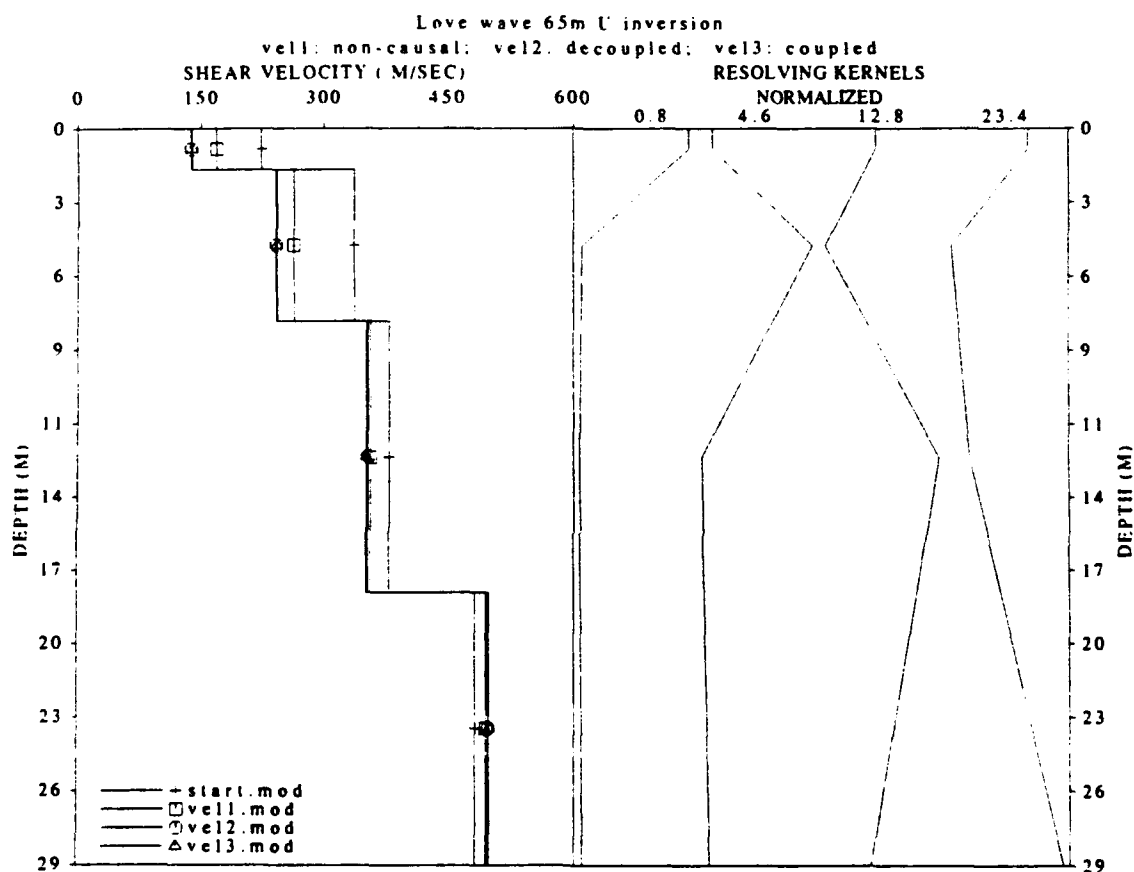


Figure 110. 65 meter SWIG data group velocity/gamma inversion for shear velocity structure. Plus is input start model, squares is non-causal inversion, circles is decoupled, causal inversion with fixed Q model, triangles is final model from coupled causal inversion.

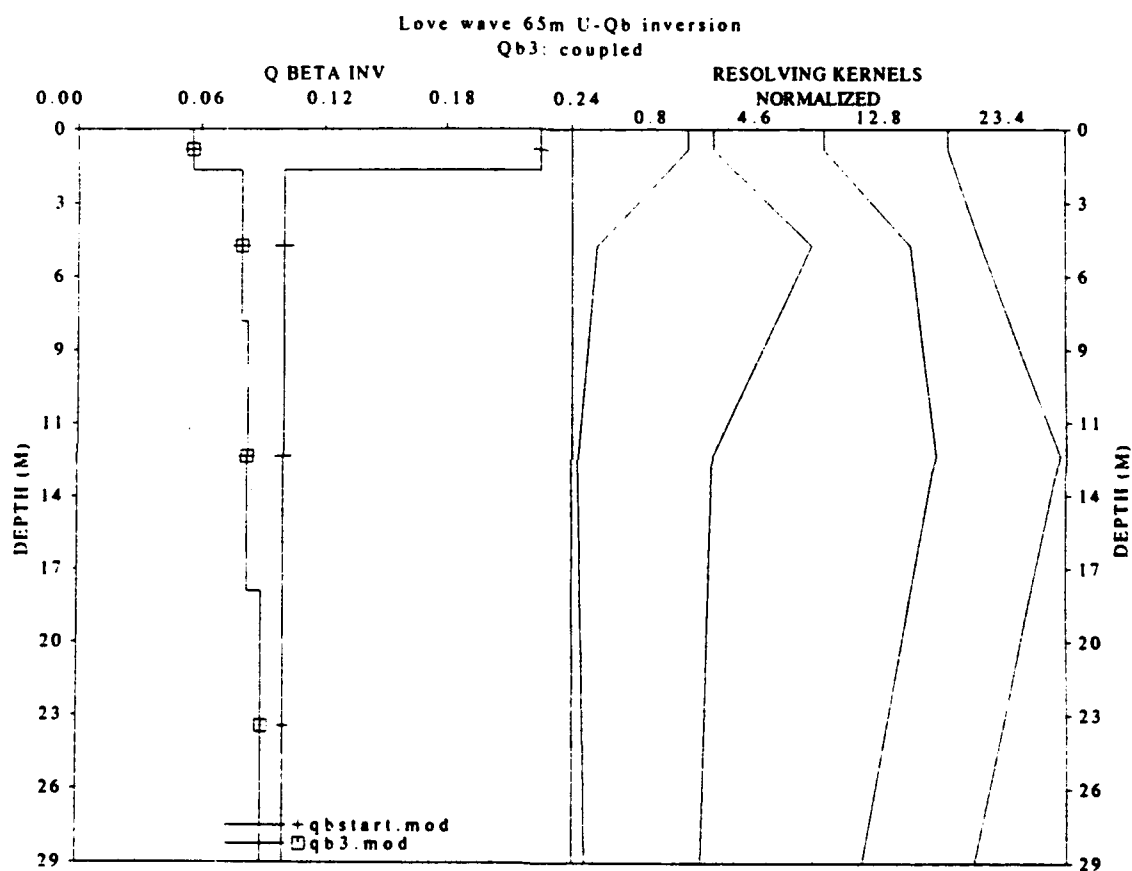


Figure 111. 65 meter SWIG data group velocity/gamma inversion for Q structure. Plus is input start model, squares is final model from coupled causal inversion.

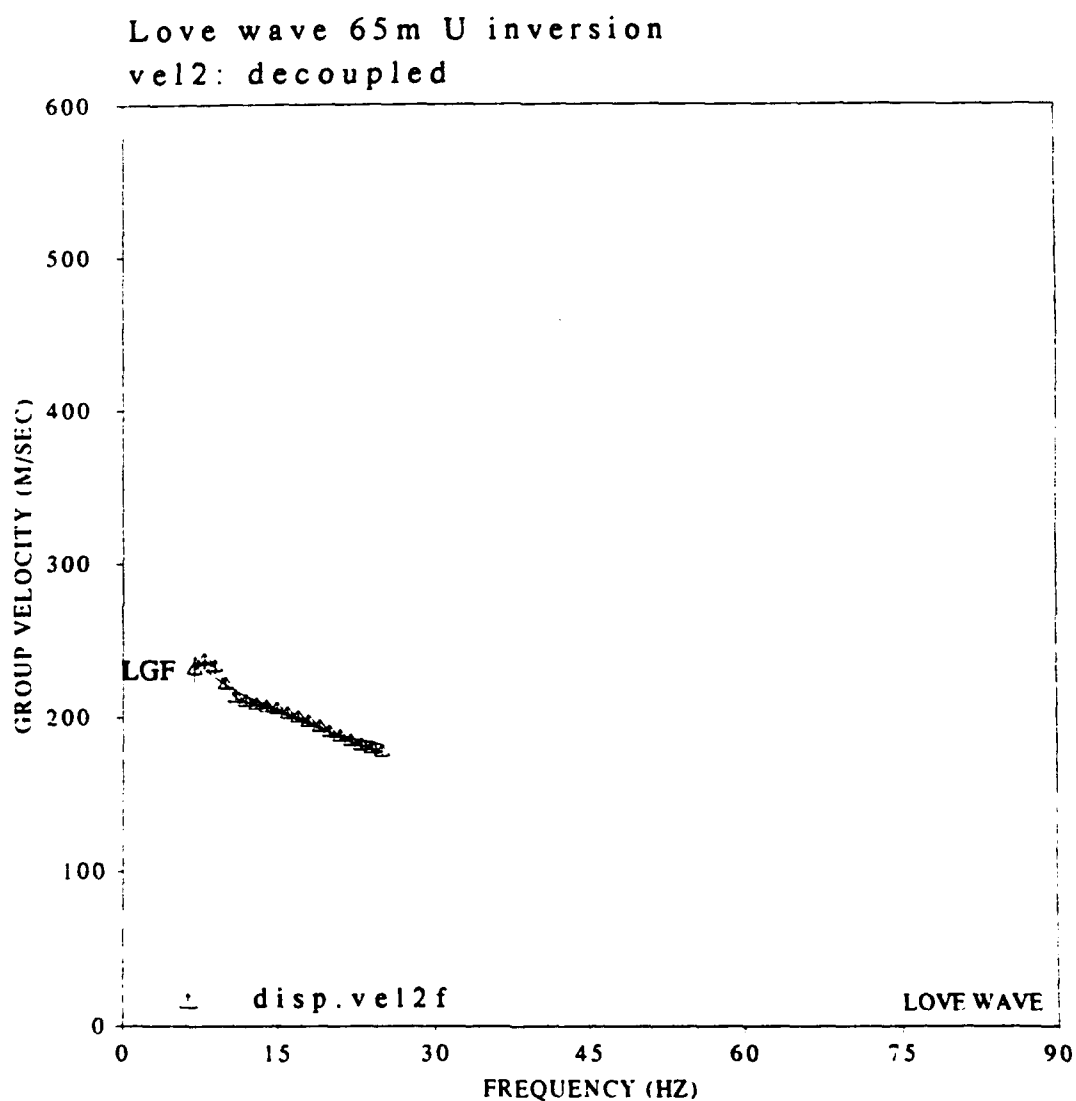


Figure 112. 65 meter SWIG data observed versus predicted group velocity after second inversion. Triangles are observed data with vertical bars being standard deviation from array processing analysis. Solid line is predicted data set.

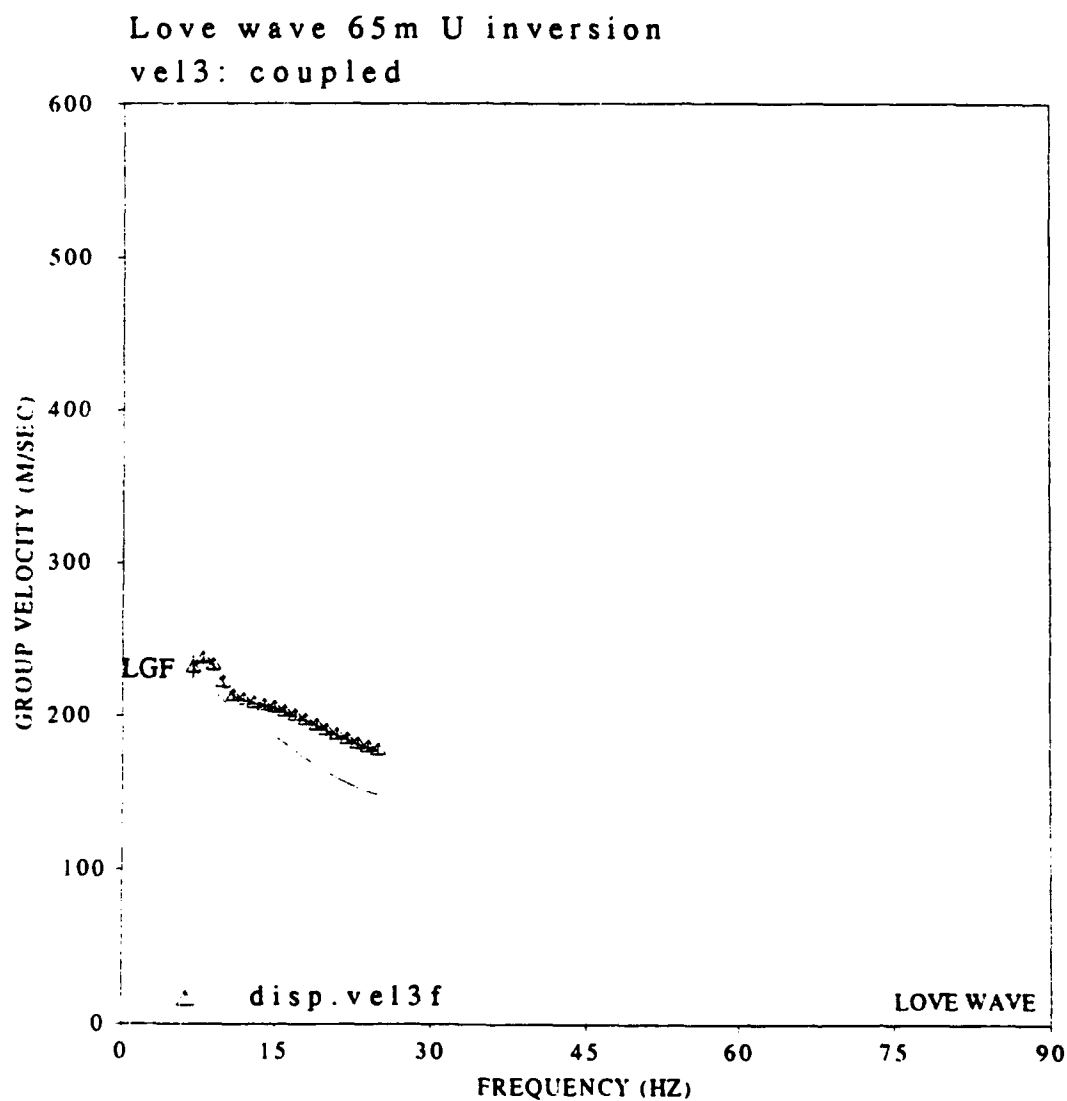


Figure 113. 65 meter SWIG data observed versus predicted group velocity after third and final inversion. Triangles are observed data with vertical bars being standard deviation from array processing analysis. Solid line is predicted data set.

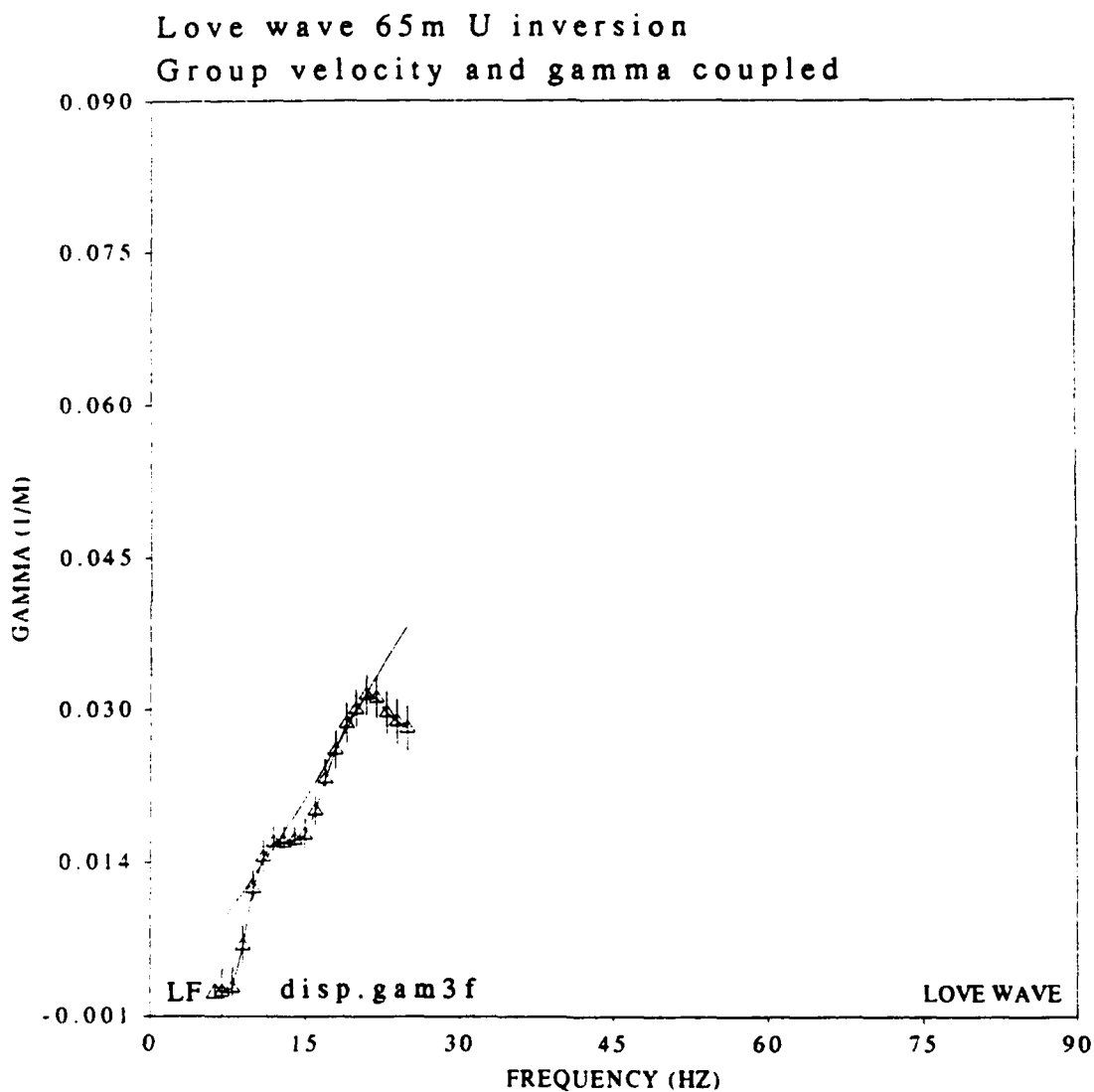


Figure 114. 65 meter SWIG data observed versus predicted attenuation coefficients after final inversion. Triangles are observed data with vertical bars being standard deviation from array processing analysis. Solid line is predicted data set.

the fit to the group velocity curve is degraded. The excellent comparison of the predicted and observed group velocity after inversion with the Q held constant is shown in Figure 112. Allowing the Q to vary in the coupled causal inversion again resulted in poorer fits to both group velocity (Figure 113) and gamma (Figure 114). The degradation of results implies some inconsistency between the different portions of data. The most probable difficulty is that the attenuation coefficients are not strictly a function of Q .

The final set of inversions incorporates all three sets of data, group velocity, phase velocity and gamma. The inverted results are included in Figures 115 to 118. This analysis includes the maximum amount of input data and should therefore provide the best results. Figure 117 demonstrates that the final model is consistent with both the input group and phase velocity, although (Figure 118) the final model did not produce a physical (greater than zero) Q_β structure that was consistent with the measured attenuation coefficients. The variability of inverted Q_β and discrepancies with predicted attenuation coefficients indicates that this technique will only yield a rough estimate of Q . Additionally, it indicates that the attenuation with frequency is influenced by more factors than the two assumed in this study, simple spreading loss and loss due to formation Q .

C. Forward Modeling

Previous dispersion analysis including Simila (1982) have used forward modeling techniques to match a velocity structure to measured velocity dispersion. In general, an attempt was made to match observed to predicted dispersion. In this study, an attempt will be made to match the entire synthetic waveform to the measured waveforms. Because there can be more than one model

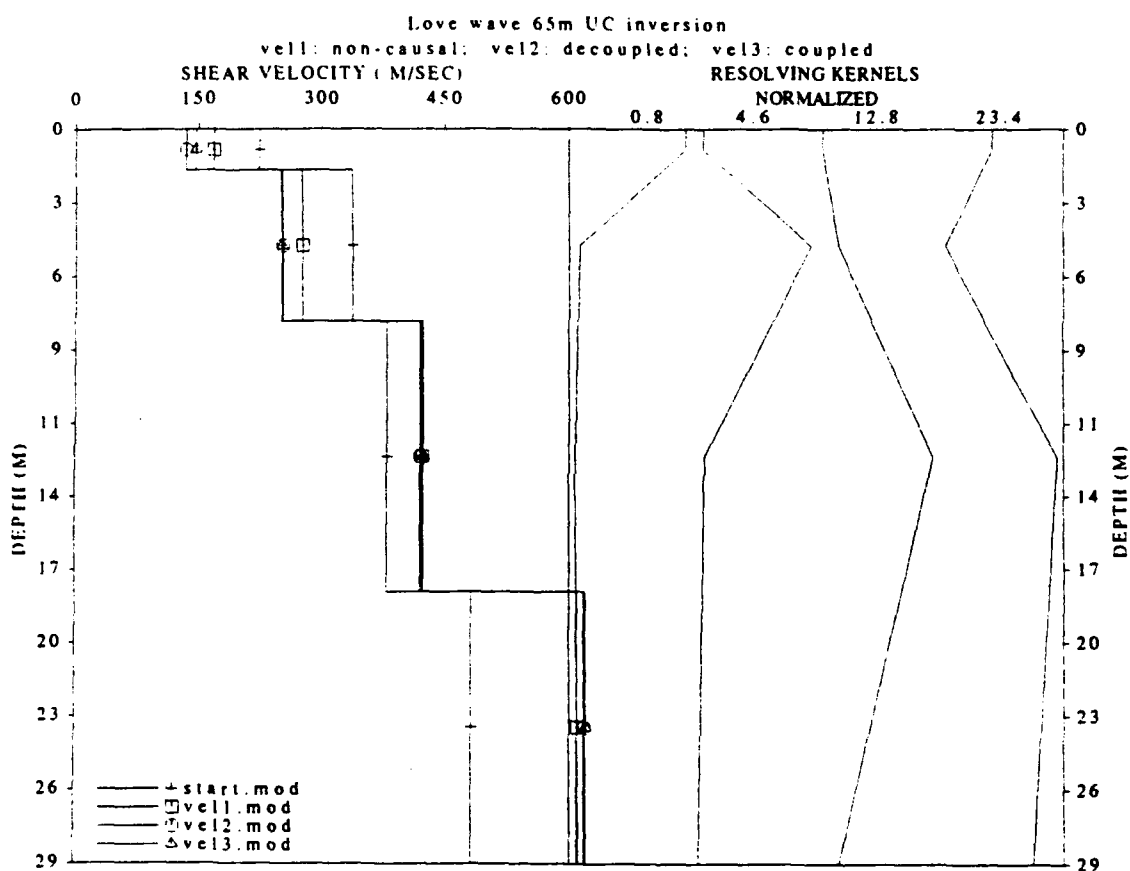


Figure 115. 65 meter SWIG data combined group and phase velocity/gamma inversion for shear velocity structure. Plus is input start model, squares is non-causal inversion, circles is decoupled, causal inversion with fixed Q model, triangles is final model from coupled causal inversion.

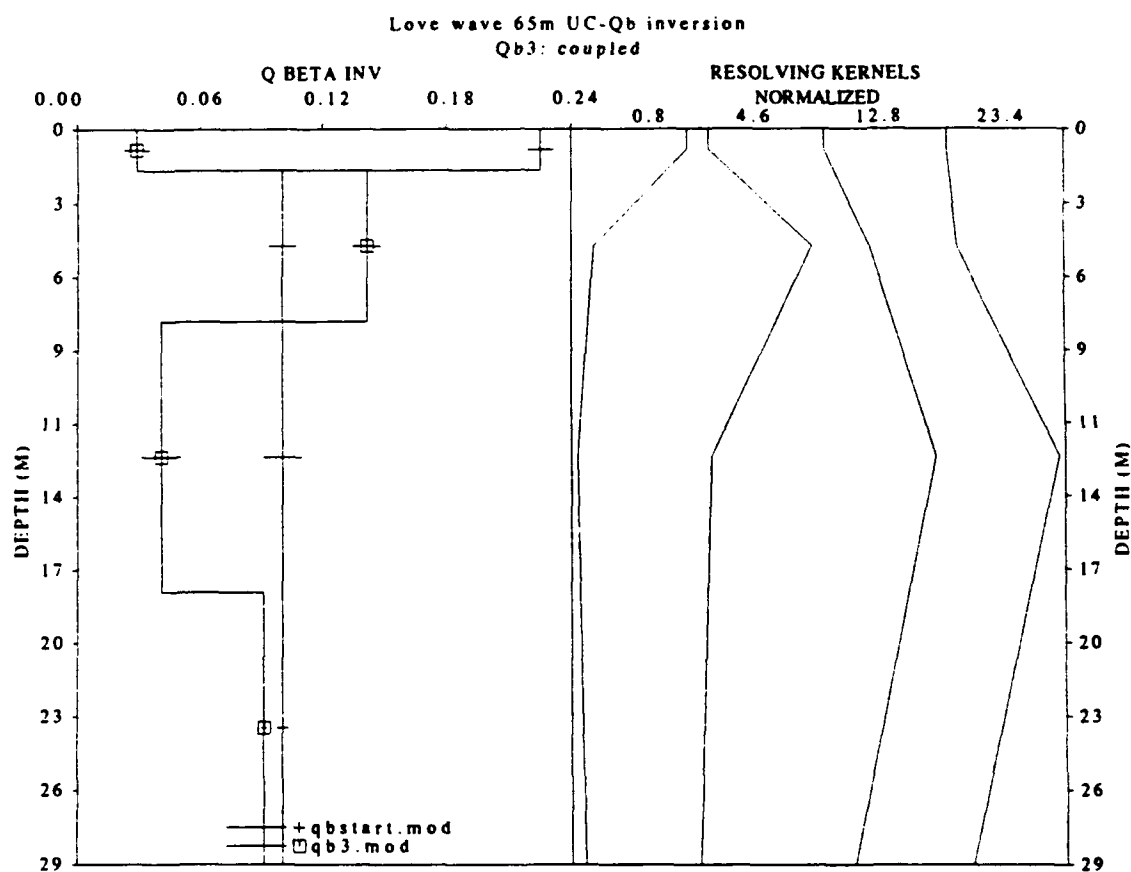


Figure 116. 65 meter SWIG data combined group and phase velocity/gamma inversion for Q structure. Plus is input start model, squares is final model from coupled causal inversion.

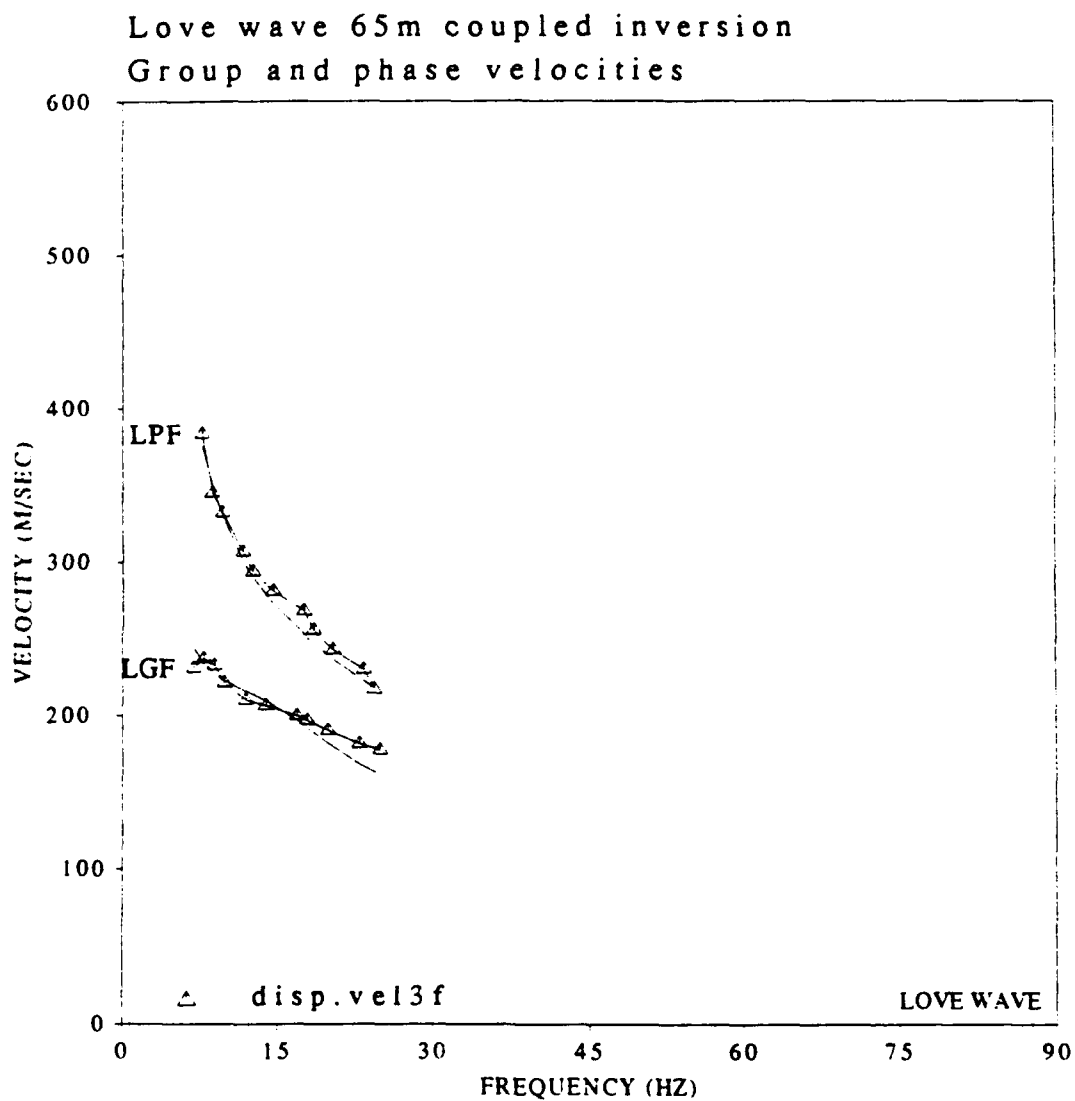


Figure 117. 65 meter SWIG data observed versus predicted group and phase velocity after final inversion. Triangles are observed data with vertical bars being standard deviation from array processing analysis. Solid line is predicted data set.

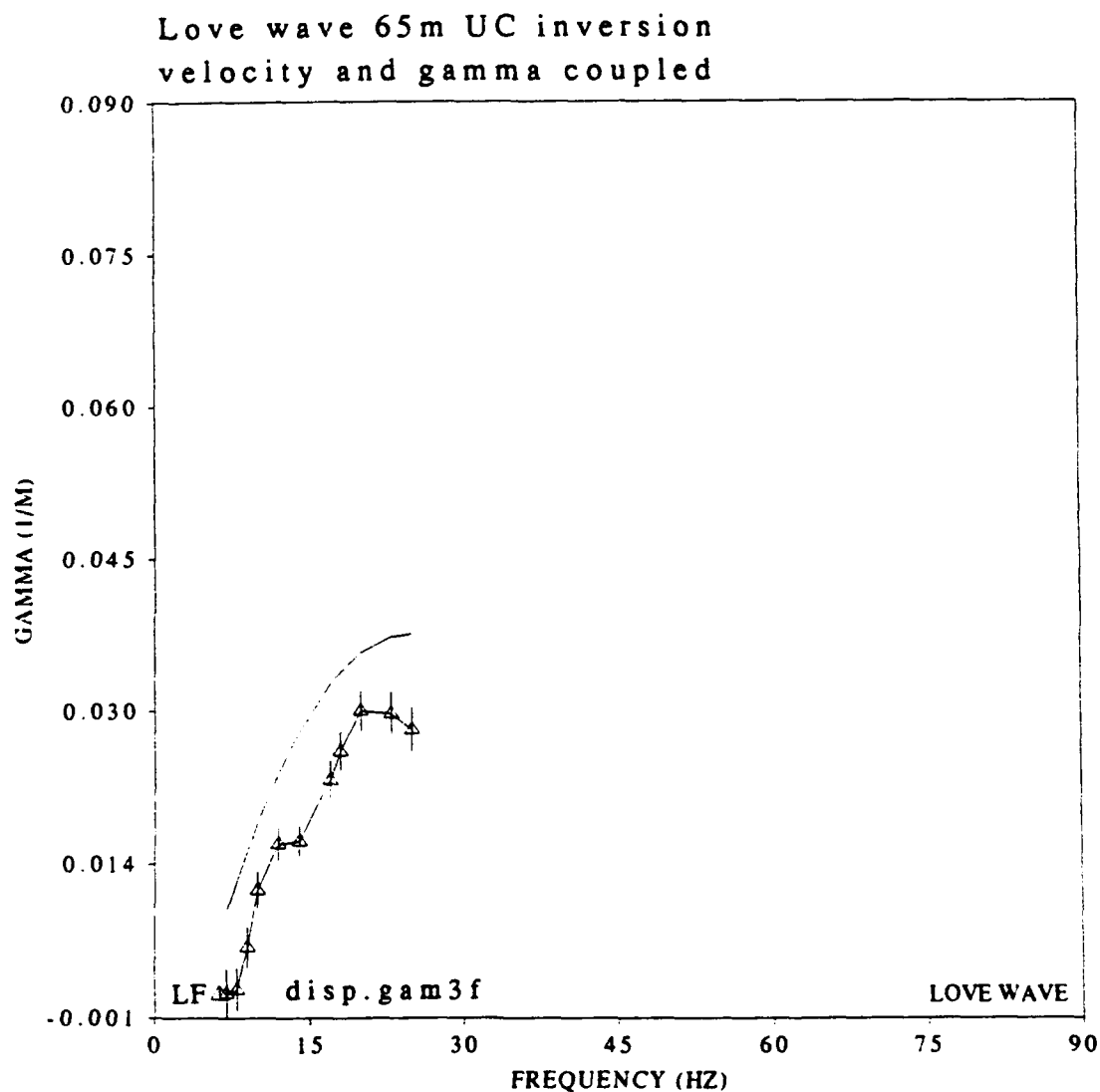


Figure 118. 65 meter SWIG data observed versus predicted attenuation coefficients after final inversion of group velocity, phase velocity and gamma. Triangles are observed data with vertical bars being standard deviation from array processing analysis. Solid line is predicted data set.

Table 6
INPUT PARAMETERS FOR SYNTHETIC SURFACE
WAVE COMPUTATIONS

Parameter	Layer 1	Layer 2	Layer 3	Layer 4
Layer Thickness	1.6	5.9	10.6	Halfspace
Q_α	9.9	22.5	22.5	22.5
Q_β	4.4	10	10	10
α	408	582	666	1143
β	146.7	250.7	424.1	619.8
ρ	1.8	1.9	1.9	2.0

that matches a given dispersion data set, a good visual match of synthetic data would add confidence to the calculated velocity model.

A synthetic Love wave was calculated for the model in Table 6, which was the velocity results from the final Love wave inversion combined with Q values from the Grant (1988) study which appeared more physically reasonable than the ones computed for this study. The algorithms for computing synthetic surface waves are fully documented in Herrmann (1985). The results are compared to the Love wave stripped from the data set using phase matched filtering in Chapter 3 and displayed in Figure 77. The first difficulty encountered was that the synthetic data sets did not match the acquired data set in frequency content. The spectral content of the synthetics was flat below the center frequency (about 10 Hz) and dropped off sharply above the center frequency. A triangular source function with a 40 msec width was finally used as a best match. The synthetics appeared to have the opposite polarity to the real data, so all results have been flipped for a better match. The unfiltered output is presented in Figure 119 on a scale comparable to the PMF output in Figure 77. The synthetic Love wave does not match as well as would be desired, with the largest difference being apparent in the number of lobes and apparent frequency content. The low end of the spectrum predominates in this data set relative to the sharp rolloff in the high frequency end. A high pass filter at 10 Hz was applied to the data set and is displayed as Figure 120. A better fit was obtained by filtering at 20 Hz and is presented in Figure 121. The PMF results have a high frequency ripple at the end corresponding to slower velocities. It appears that these high frequency results from the PMF may not be real, in that the input constraints to the PMF were

limited to 50 Hz. Data outside this frequency limit would not have been eliminated with a boxcar type filter due to the problem with Gibb's phenomena.

Several attempts were made to boost the frequency content of the synthetic with little success. When the triangular source function was cut back from 40 msec, the data exhibited a high frequency ripple on the early arrival part of the wave train. An example of this is Figure 122, where the data has had a triangular function of 8 msec with a low cut filter of 20 Hz applied. It seems surprising that the high frequency portion of this data set arrives earlier or faster in the data set, since the dispersion analysis demonstrates that the highest frequencies should come in latest.

Several Rayleigh wave synthetics were also generated. Because there were two modes, the synthetics were computed three ways. The first synthetic in Figure 123 contains the fundamental mode only. Figure 124 contains the first higher mode and Figure 125 is the results of a synthetic containing both the fundamental as well as the first higher mode Rayleigh wave. Some of the more important features of the real data are not replicated in the synthetic. The two Rayleigh modes in the data are composed of non-overlapping frequencies. It did not appear possible to generate such a bimodal synthetic, matching the appropriate spectral contents.

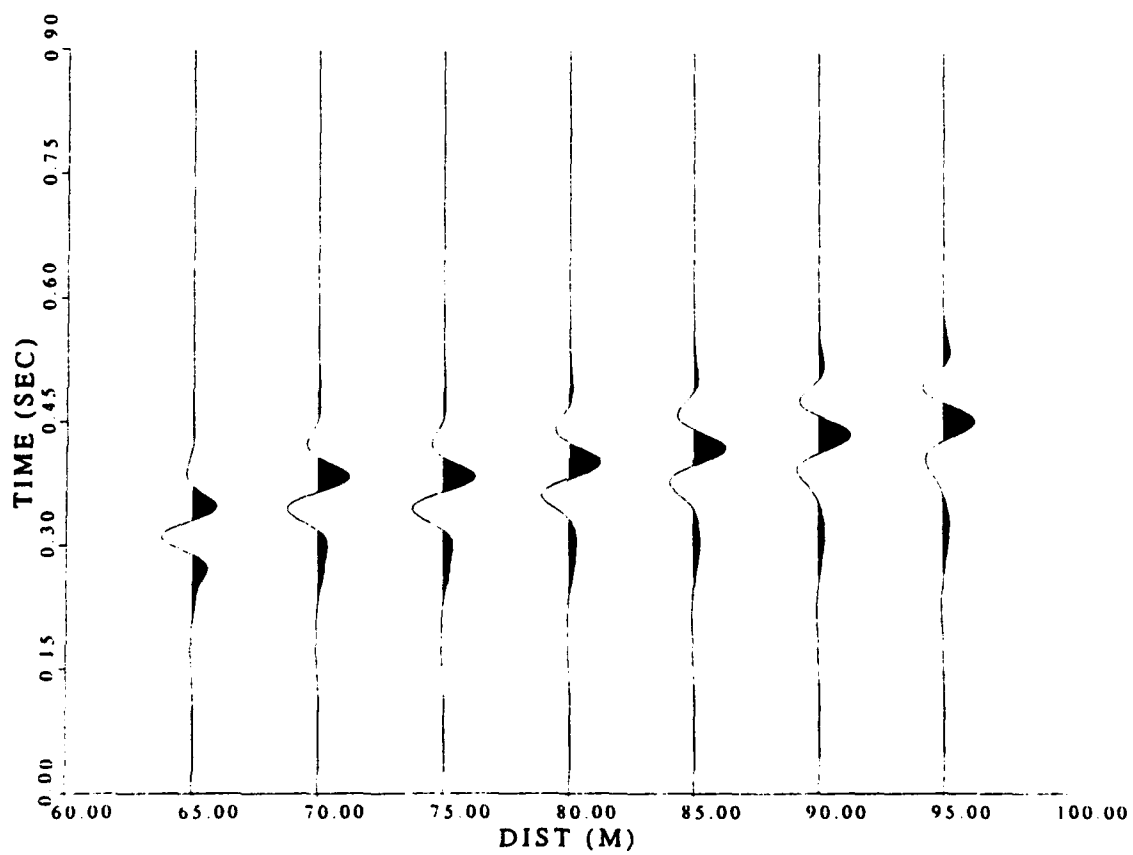


Figure 119. Unfiltered Love wave synthetic. Triangular source width 40 msec.

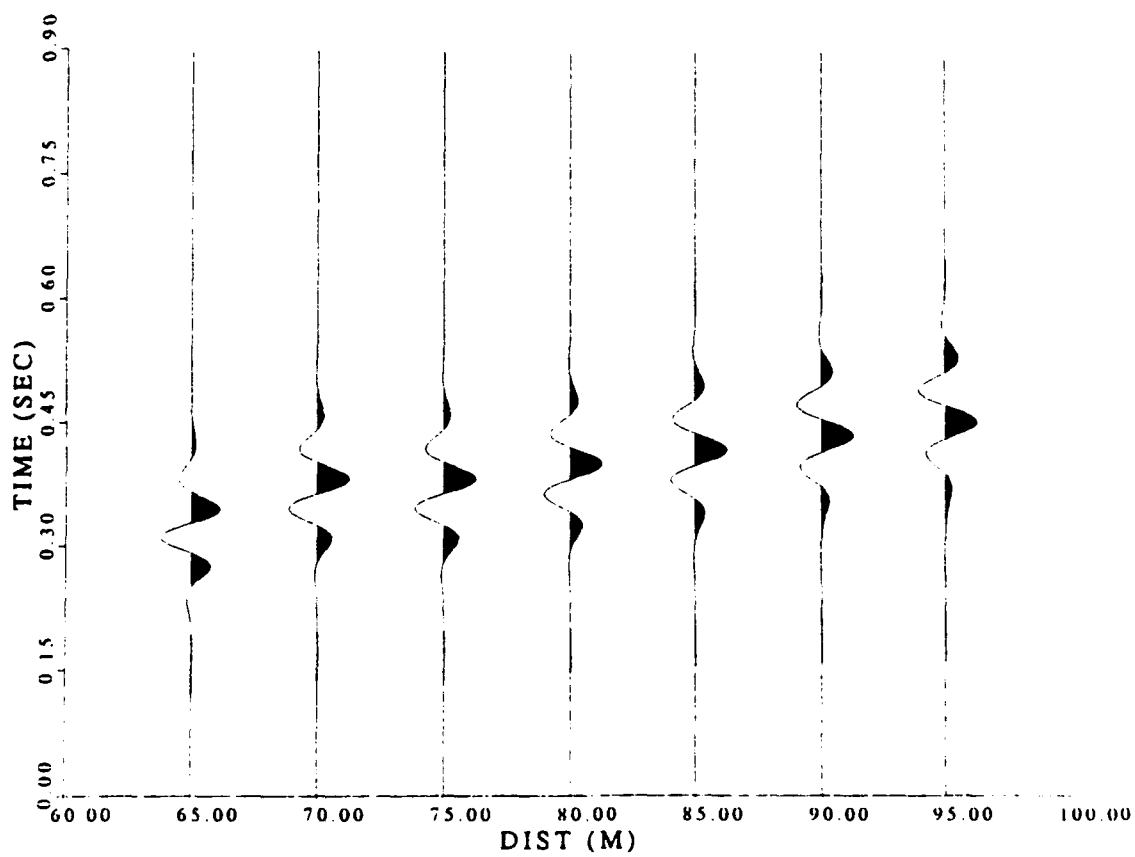


Figure 120. Love wave synthetic with low cut filter at 10 Hz.
Triangular source width 40 msec.

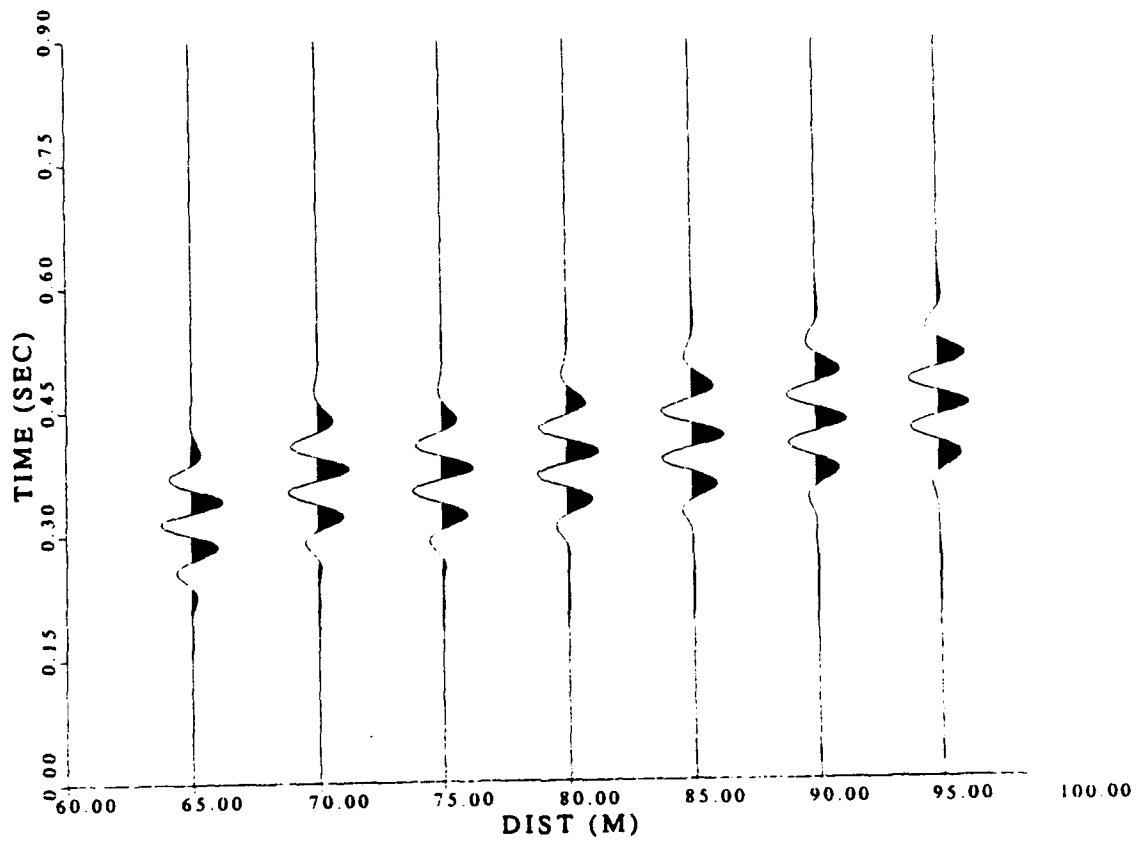


Figure 121. Love wave synthetic with low cut filter at 20 Hz.
Triangular source width 40 msec.

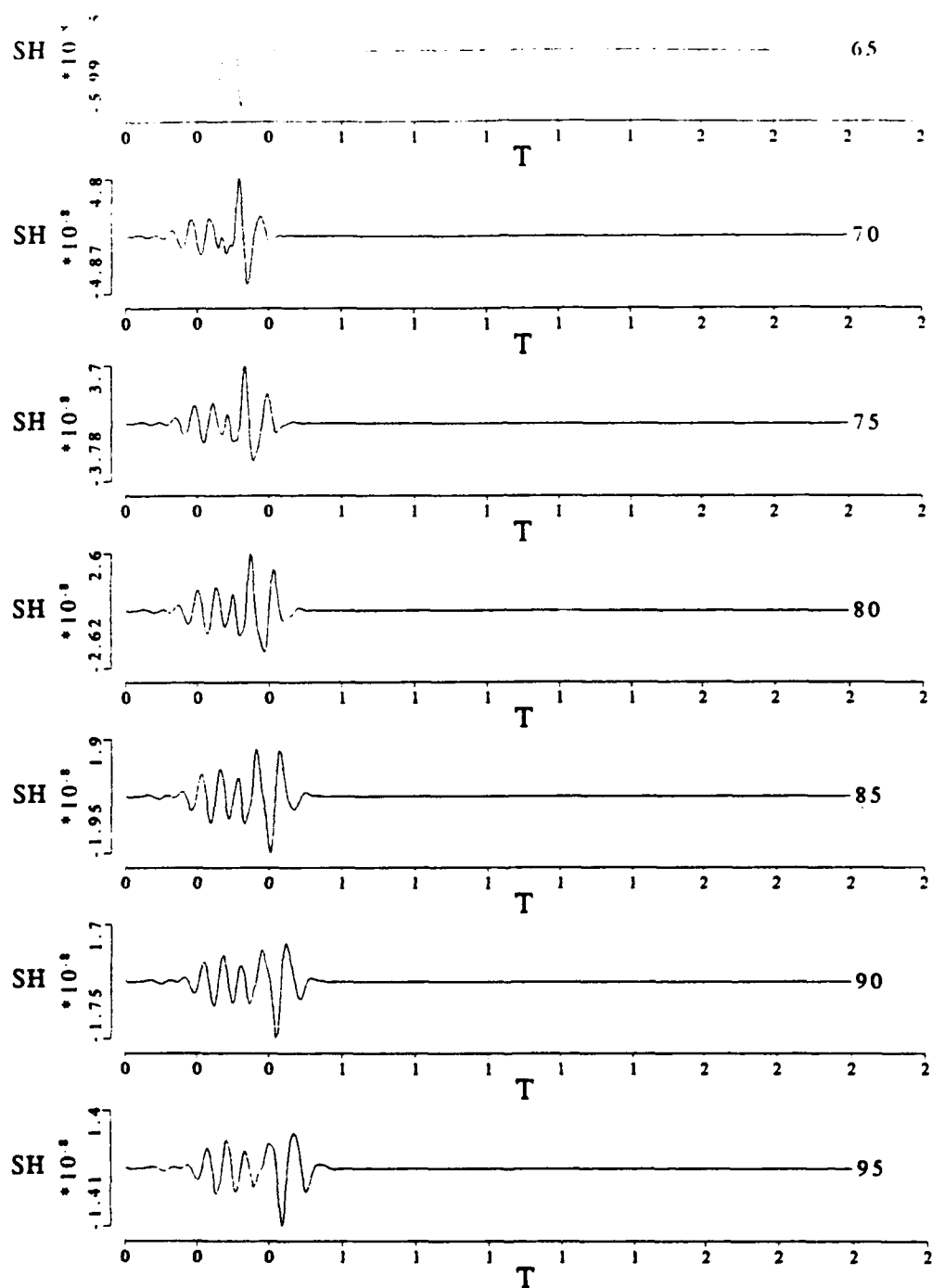


Figure 122. Love wave synthetic with low cut filter at 20 Hz.
Triangular source width 8 msec.

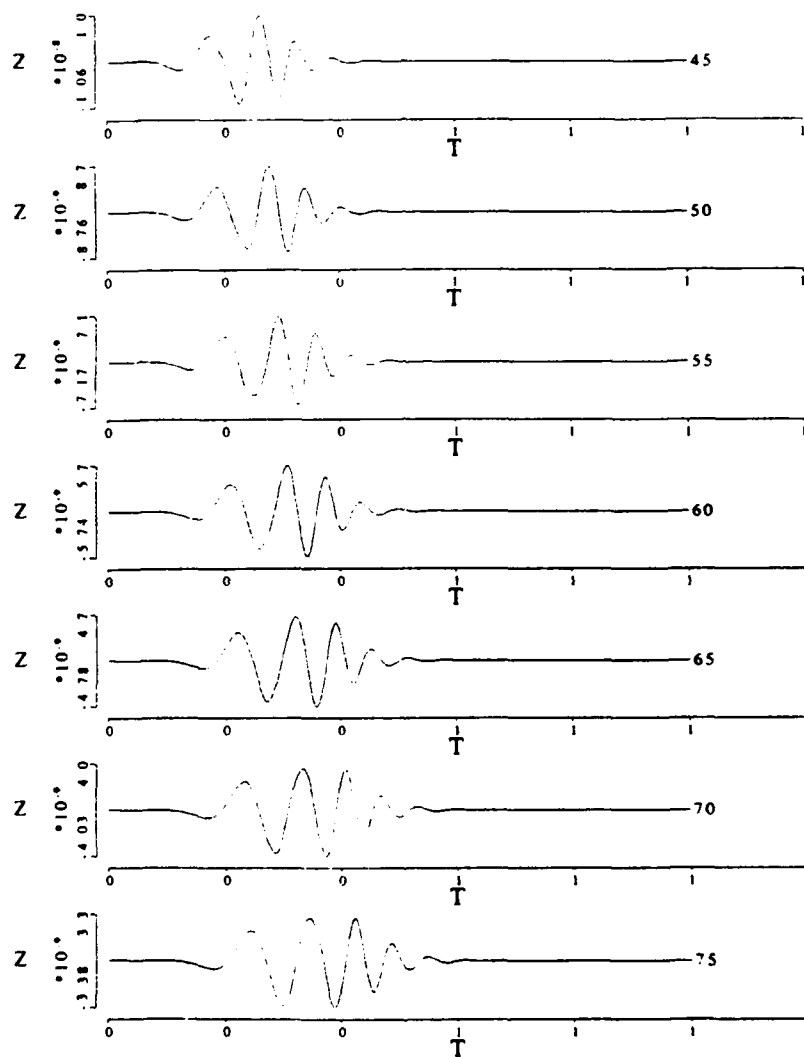


Figure 123. Rayleigh wave synthetic of fundamental mode only

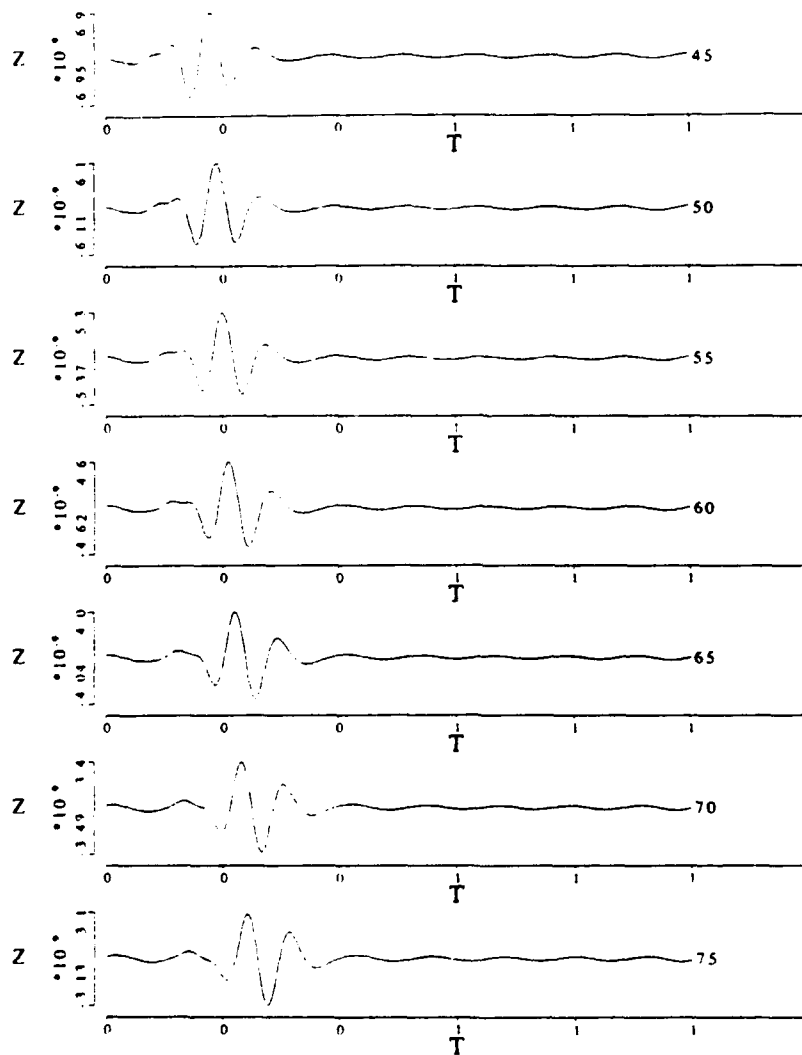


Figure 124. Rayleigh wave synthetic of first higher mode only

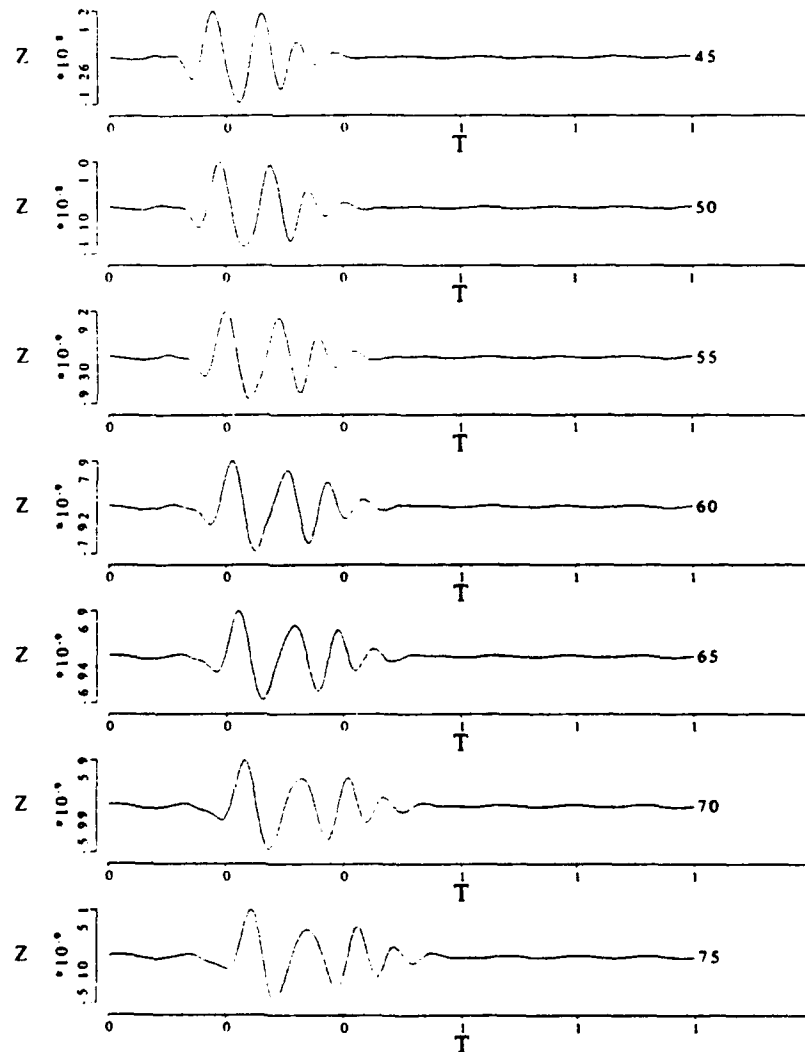


Figure 125. Rayleigh wave synthetic of combined fundamental and first higher mode

CHAPTER 5

CONCLUSIONS

The objective of this study was the determination of the shear velocity structure in a shallow alluvial environment. This thesis utilized several techniques that had been used individually in previous work applied to different scale problems. The project was composed of three major segments. The first segment was the acquisition of the field data. Second, the field data were processed to determine dispersion curves. The third segment was calculating a velocity model by inverting the dispersion information. This final section will try to bring together the different techniques and propose how they can be used in future work.

A. Acquisition Techniques

The field data were acquired with an array of 60 receivers spaced at 0.5 meter increments. The sources were set at 3 ranges from the end of the receiver array, at 5.0 meters, at 35.0 meters and at 65.0 meters. Two sources were used in this study, the Betsy and the SWIG. The Betsy source generated P wave data as well as a Rayleigh surface waves. The SWIG source provided SH energy and therefore Love waves. The results for the SWIG were always the most easily interpreted. The Betsy data set was more difficult to interpret for three reasons: first, the Betsy data contained two modes of Rayleigh waves and the SWIG data set only contained one surface wave mode; second, the Betsy

data set contained an airblast arrival which actively coupled with the first higher mode Rayleigh; and finally, the time separation between the body waves and the surface waves was greater for the SWIG data set.

The airblast biased the first higher mode, making it useless for inversion purposes. The fundamental Rayleigh mode had a bandwidth of approximately 6 to 26 Hz. Almost all of the energy above 26 Hz appeared in the first higher mode Rayleigh. In theory, having two modes of a surface wave should help constrain the inversion, yielding a final answer that is less ambiguous. This extra data could not be used in this study since the inversion technique used would only incorporate different data types over the same frequency interval. An additional limitation was that the higher mode data could not be used by itself. The Simila(1982) data acquired with a different source, high explosives, at McCormick ranch showed a similar frequency content for the two Rayleigh wave modes. This demonstrates that a different source would not alleviate these problems in this alluvial environment.

The SWIG data remained simple and easily interpretable through the entire range of 5 to 94.5 meters used in this study. The data contained a large amplitude direct and refracted first arrival. These events were followed by a visibly dispersive, single mode of Love wave. The time separation between these two portions of the data set was larger for the SWIG data than for the Betsy data, which made the dispersion analysis easier to perform.

B. Dispersion Analysis

Dispersion analysis of the field data yielded group velocity, phase velocity and attenuation information. The group velocity effectively images or illuminates

the average structure of the entire interval between the source and the receiver. The phase velocity is a function of the average structure between the receivers used in the determination of the phase velocity. The attenuation coefficients were based on evaluation of changes in spectral amplitude with range after correction for spreading loss. The assumption used in this study was that any amplitude losses were due to the attenuation or the average Q of the formations between the source and the receiver. Inconsistency in Q estimates indicates that the simple spreading corrections may be inappropriate.

The most basic dispersion analysis technique used was the multiple filter analysis (MFA) which determines the group velocity from a single source receiver pair. The MFA computes the peaks of the envelope function after multiple narrow band Gaussian filters have been applied to the single trace. These peaks are then related to velocity and the center frequency of the filters to derive a dispersion curve. This technique is computationally less intense than the other techniques used in this study. The composite display output from this analysis includes a plot of the single trace versus time as well as versus velocity (see Figures 35 to 45 and Appendix A). This information along with the spectral amplitude plots greatly aids the interpreter in determining what is going on in the data set. This analysis can enable the interpreter to determine where the surface waves are, and what modes are present. One very important use of the MFA in this study was to observe changes in group velocity with range. These observations can be useful in determining at what range the surface waves have stabilized, and additionally, to determine if there are some lateral velocity or structural changes over the range of the data set such as was shown in Figure 46.

The array or Barker technique essentially averages the group velocities from multiple source-receiver pairs. Additionally, this technique yielded the attenuation values subsequently used in the inversion process. One useful feature of this array technique is that it is not sensitive to the spatial sampling interval. In this study, one bad trace in the data set could be thrown out prior to the processing. This technique yielded very consistent results for both the Love and Rayleigh wave data sets.

The phase matched filter (PMF) technique was the only other single station technique utilized in this study. It can be used to fine tune a single station answer derived from some other technique, which for this study was the MFA. The technique yielded a visually better answer in most cases, but was very sensitive to interfering events closely spaced in time. One additional difficulty with this procedure was that it was interactive and very sensitive to user inputs. The final group velocities were very similar to the results from the array or Barker technique. Since the Barker technique was designed for batch processing and is relatively insensitive to user inputs, the PMF technique would be a secondary choice for dispersion analysis if array data was available. One use for the PMF would be as a filter. Figure 77 shows the result of stripping out a data set containing only the fundamental mode Love wave. Alternatively, this technique could be used to remove the surface wave for more detailed analysis of the remaining body waves.

The phase velocity was obtained from the p - ω technique which is based on a concept provided by McMechan and Yedlin (1981). A τ - p transform followed by a 1-d FFT yielded data in the form of slowness (p) versus frequency (ω). Since slowness is the inverse of velocity, the results can be plotted as

phase velocity versus frequency for fairly straightforward interpretation. The composite results for all three SWIG or Love wave data sets are shown in Figure 89. The phase velocities for all 3 sets are extremely consistent. The Rayleigh data sets show the same consistency of phase velocity for different ranges (Figure 93). This result is in marked contrast to the group velocity results where velocity increases substantially with range (see Figures 52, 66 and 67 for group velocity results).

Equation 1.10 demonstrates that in a plane layered medium it is possible to calculate the phase velocity from the group velocity or the group velocity from the phase velocity. The phase velocity remained consistent with range. All three SWIG data sets had almost identical phase velocities, however the group velocity varied with range, which is inconsistent with equation 1.10. The geometry of the experiment (as demonstrated in Figure 9) indicates that the group velocity would be a function of the material properties of a larger region as the source offset increases. The phase velocity is a function of the material properties between the receivers in the array. Since the receivers did not move in this study, the phase velocity imaged the same material for all 3 source positions. The apparent lateral variation in material properties violates the plane layered assumption for the inversion techniques that were used in this study. The interval interrogated by the surface waves allowed for the determination of the average material properties.

C. Inversion Technique

The inversion portion of the study consisted of three discrete phases. The first phase involved normal refraction analysis of both P and SH data. Next, the

refraction model was used as the start model for a non-linear inversion of the dispersion analysis. Finally, synthetics were generated from the inverted model structure for comparison to the original field data.

The refraction analysis was performed on a single linear array assuming horizontal layers. The technique used is documented in Telford et al. (1976) and the results are presented in Tables 4 and 5. The SWIG data set provided an uncontaminated SH wavefield for direct and refracted arrivals. The SH results appeared consistent with the compressional refraction analysis except for some differences in the layer thicknesses. The refraction results were used as a starting model for the surface wave inversions that followed.

The Love wave inversions yielded shear velocities that were similar to the refraction analysis results for the two deepest layers. The inversions indicated the shallowest two layers were slower than the refraction survey results. The shallow layer discrepancies are probably a result of the fact that the surface waves imaged a much longer interval than the refraction survey for the first two layers. The resolution kernels were very small for the deepest two layers, which indicates that the wavelengths were not long enough to image at these depths. It seems obvious that data at a lower frequency than the 6 Hz used in this study would have been beneficial. The other significant result was that the Q inversion appeared fairly unstable, frequently trying to yield negative Q values, even when the models were heavily damped. This instability is less due to technique than the fact that the input attenuation coefficients are assumed to only be a function of Q and spreading loss. There appear to be more factors, including scattering, that are adding to the complexity of the attenuation with frequency.

The final step of this project was to generate synthetic surface waves to match the original field data from the final model. This synthetic was at least partially successful for the Love waves. The final synthetic wavefield (Figure 121) has a frequency content and character similar to the PMF extracted Love waves in Figure 77. The complexity of the Rayleigh wave data set appeared to be beyond the capability of the techniques used in this project. The biggest difficulty was in duplicating the behavior of the splitting of the energy spectrum between the fundamental and first higher mode.

The final velocity model determined for the McCormick Ranch area is the model that was input into the synthetics and documented in Table 6. The layer thickness for the shallowest layer is given as 1.6 meters in this study, but based on other studies in the area, can vary substantially. The compressional and shear velocities are consistent across several different inversions. The Q values are from previous studies, and are not necessarily consistent with the attenuation coefficients determined from the data in this study.

D. Recommendations for Future Work

A variety of previously introduced techniques which primarily depend on surface wave dispersion to constrain shallow shear structure have been applied to the problem of site characterization. These techniques have been applied in conjunction with standard refraction analysis. Since the spatial sampling and frequency content of the data analyzed were new and unique, a number of suggested experimental revisions have been identified.

The first change to be made in any continuation of this work would be acquisition to enhance the low frequency portion of this data set. Data acquisition

with 2 Hz geophones would enable accurate inversions to a deeper depth than was possible in this study. Several additional changes in acquisition would be necessitated by the use of lower frequency phones. Table 3 indicates that the lower the frequency, the poorer or wider the temporal resolution would become. As a result, the events would need to be spaced further apart in time, which would require greater source-receiver spacings than used in this study. This would add more complexity to the study due to increased scattering and lateral velocity variations. The SWIG provided excellent data for this study, but was starting to degrade due to lack of energy at the farthest offsets. This situation could be improved at larger distances by stacking multiple shots.

One difficulty with the Betsy data was the existence of an airblast, which contaminated the first higher mode. The airblast could perhaps be reduced by berming the side of the source closest to the receivers. Alternatively, bermed explosive sources as used by Simila (1982) could be used, especially if an attempt was to be made to increase the source-receiver spacing. In this study area, it is not clear that improving the higher mode Rayleigh data would contribute much, since the different frequency range precluded using the higher mode in the inversion process. The fundamental mode dispersion analysis would be made easier if the events were more widely spaced in time due to a greater source offset. Additionally, if the source offset was increased, a longer time interval would need to be recorded. The sample rate could be decreased in this case, because it is unlikely that any usable data would be available beyond 50 Hz.

One difficulty with the analysis of the data in this study was that there appeared to be some lateral variations in velocity structure. One method for deal-

ing with this would be to shoot the refraction data from both ends of the linear array and process for dip. Two previous studies in the area, Bogaards (1989) and Grant (1988) looked at this problem and found no evidence of dip. Bogaards (1989), however did find some evidence of azimuthal variation of velocity structure. Additionally, different studies have determined a different thickness for the shallowest layer. It seems likely that the shallowest layer varies gradually in thickness throughout the area. Any precise spatial technique, such as a refraction survey, would yield a velocity structure in a small area that might be substantially different from the average structure. A surface wave technique would tend to yield an average structure, and in fact should provide a better estimate of the average as the source-receiver spacing increases.

The final area of concern would be the determination of Q . Q appeared to be poorly resolved in the inversion process. This poor resolution could be dealt with in two ways. The first way would be to determine Q from some other outside method, such as was used by Grant (1988). Alternatively, some effort could be put into determining the other factors influencing the attenuation (such as scattering) with frequency and correcting for those.

The dispersion analysis techniques used in this study appeared fairly robust. It was easiest to determine dispersion with an array of data. The combination of MFA and PMF would make it possible to determine group velocity with single phone measurements if necessary.

APPENDIX

MULTIPLE FILTER ANALYSIS OF BETSY DATA

The multiple filter analysis (MFA) is a single source-receiver pair analysis technique that was applied to both the Betsy and the SWIG data. The SWIG data results were presented in Chapter 3, section B. The Betsy results are presented in this appendix. Each of the plots contains up to four peak amplitude points of the envelope or instantaneous amplitude for very narrow band Gaussian filters. The peak amplitudes from largest to smallest are represented by squares, circles, triangles and plus signs. The corresponding spectral amplitudes are represented by the same symbols in the top portion of the plot. The trace to the far right is the input seismic trace scaled in linear time. The second trace from the right is the input trace scaled in linear velocity corresponding to the group velocity scale at the far left.

The data is presented in approximately 5 meter increments. The primary features that can be distinguished are the fundamental and first higher mode Rayleigh waves. The higher mode Rayleigh wave blends into the airblast at 300 m/s for the high frequencies.

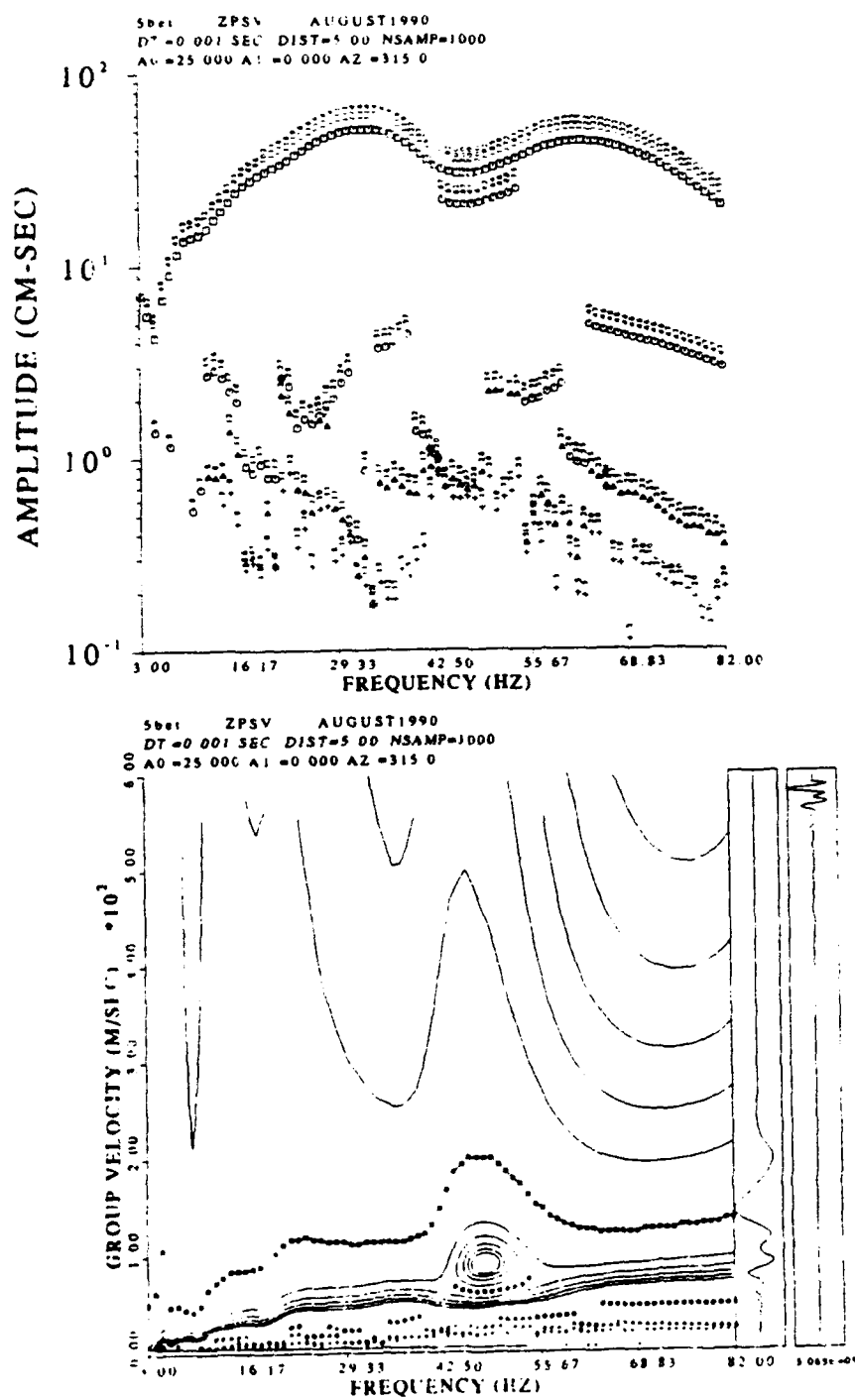


Figure 126. MFT analysis at 5.0 meters for Betsy data

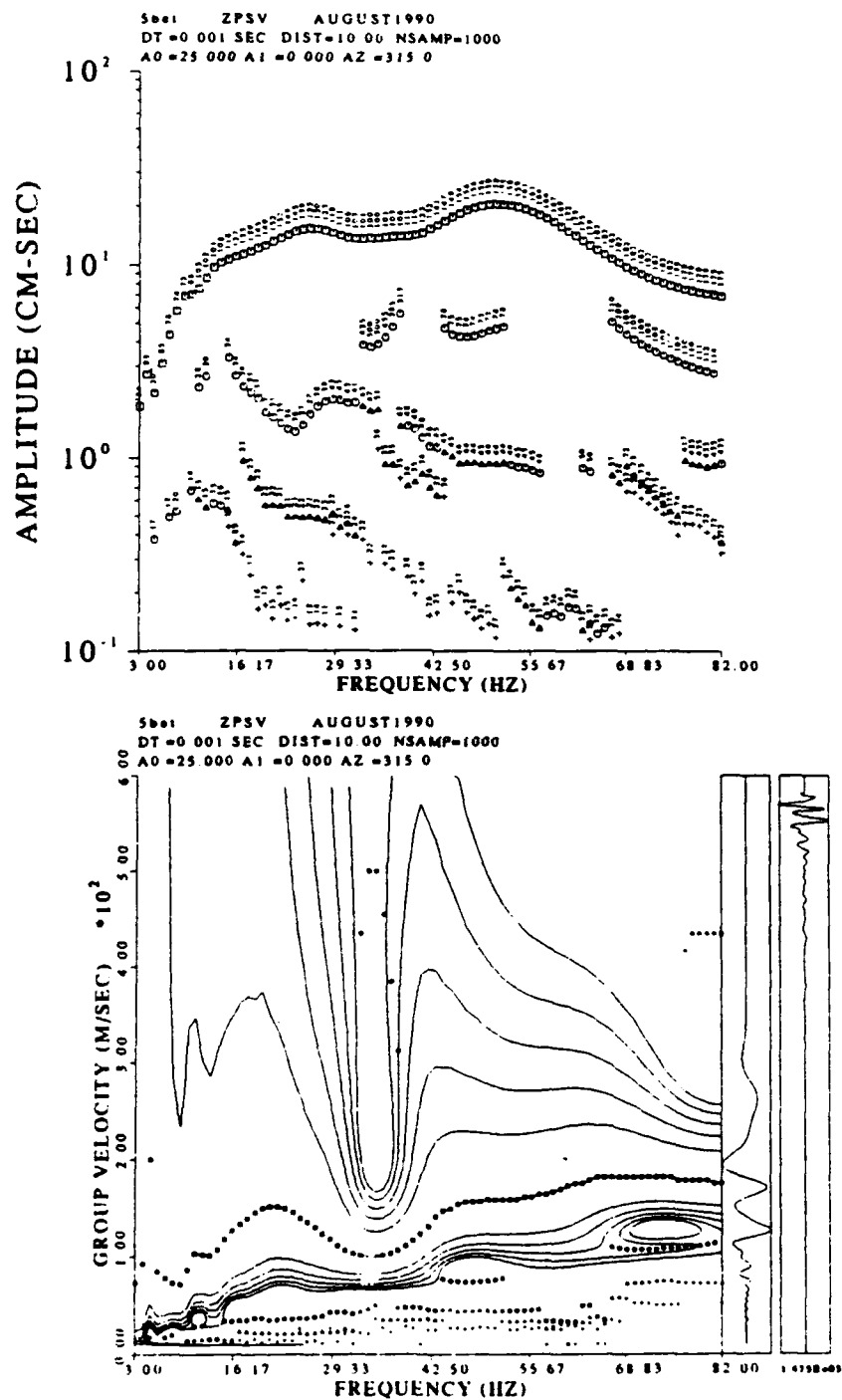


Figure 127. MFT analysis at 10.0 meters for Betsy data

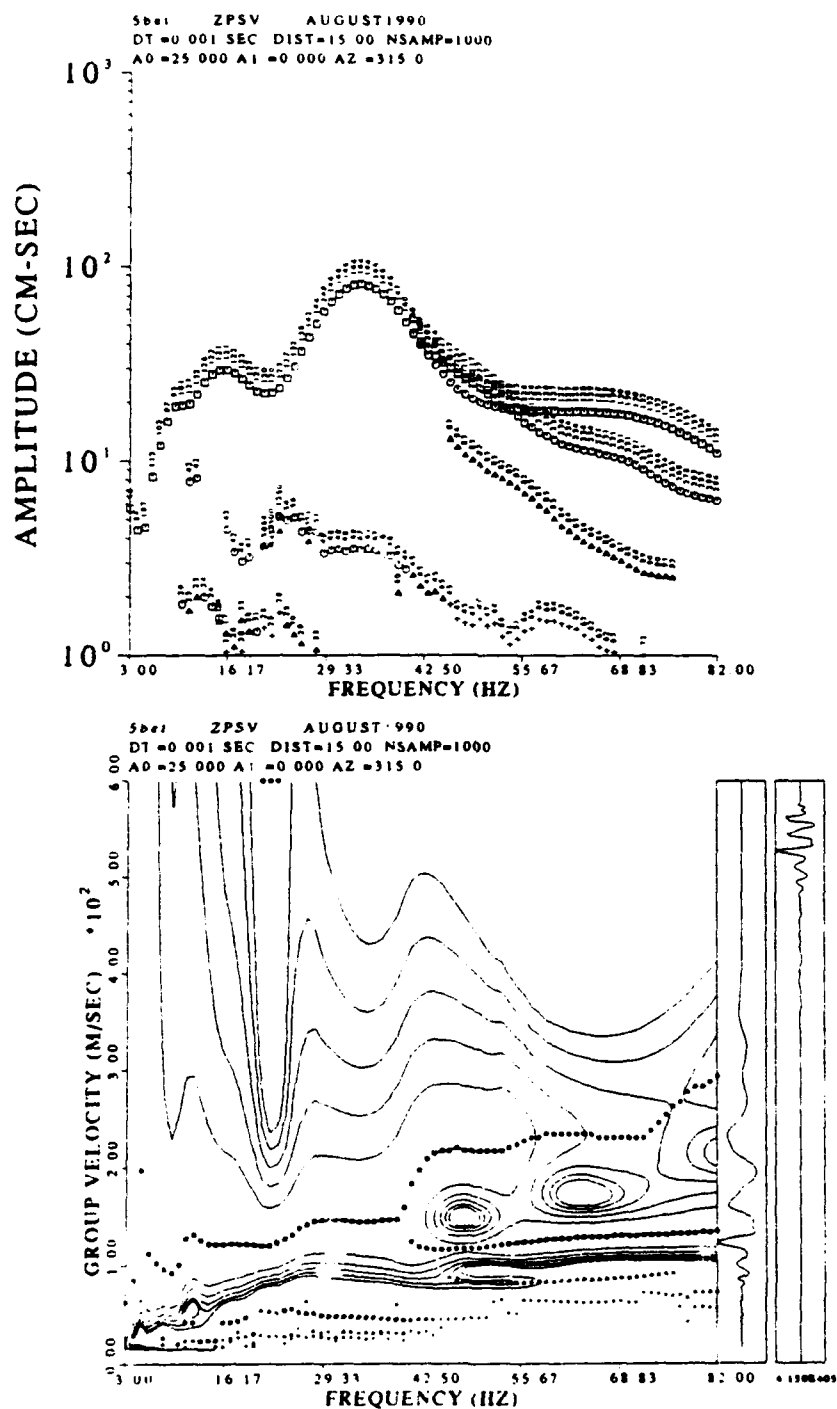


Figure 128. MFT analysis at 15.0 meters for Betsy data

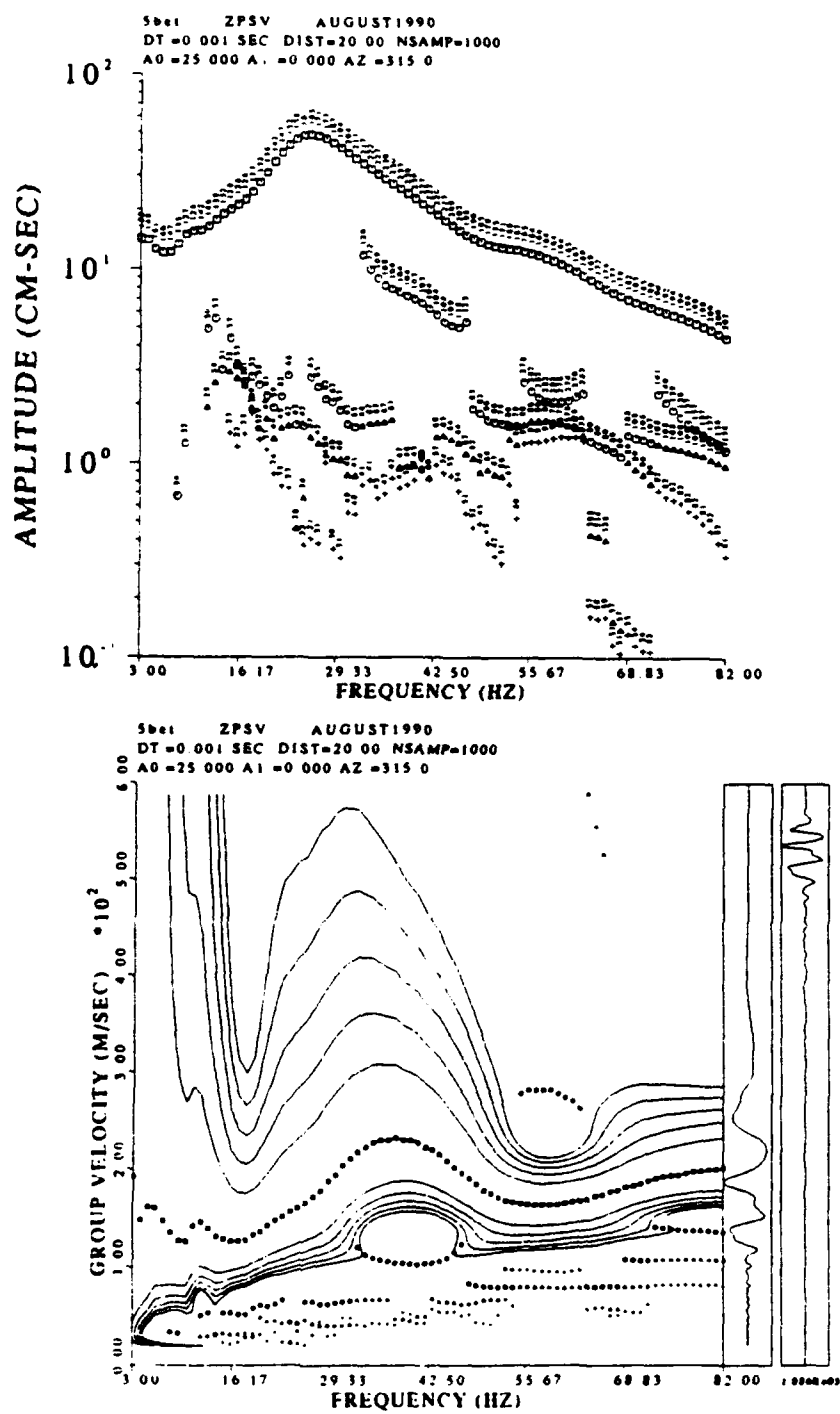


Figure 129. MFT analysis at 20.0 meters for Betsy data

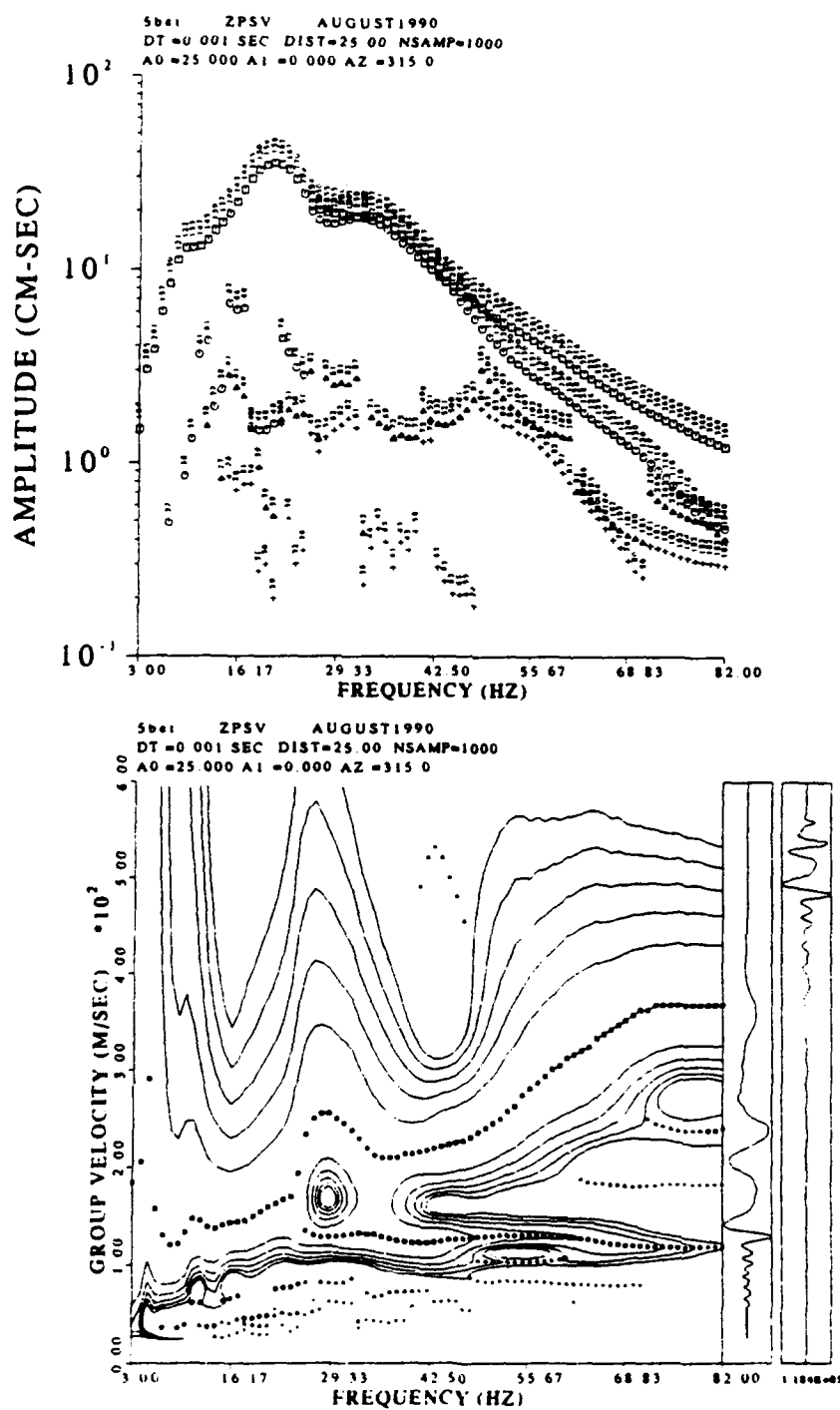


Figure 130. MFT analysis at 25.0 meters for Betsy data

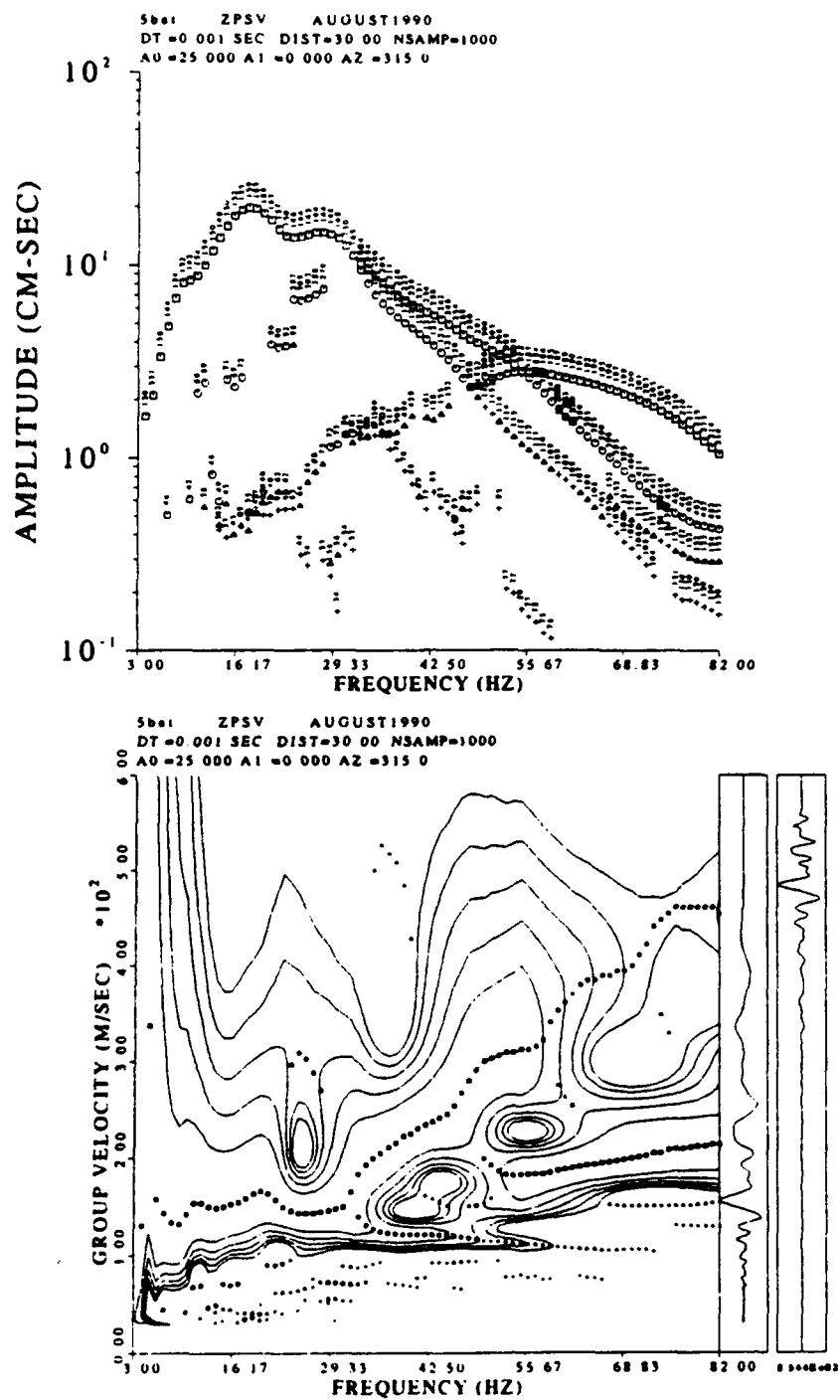


Figure 131. MFT analysis at 30.0 meters for Betsy data

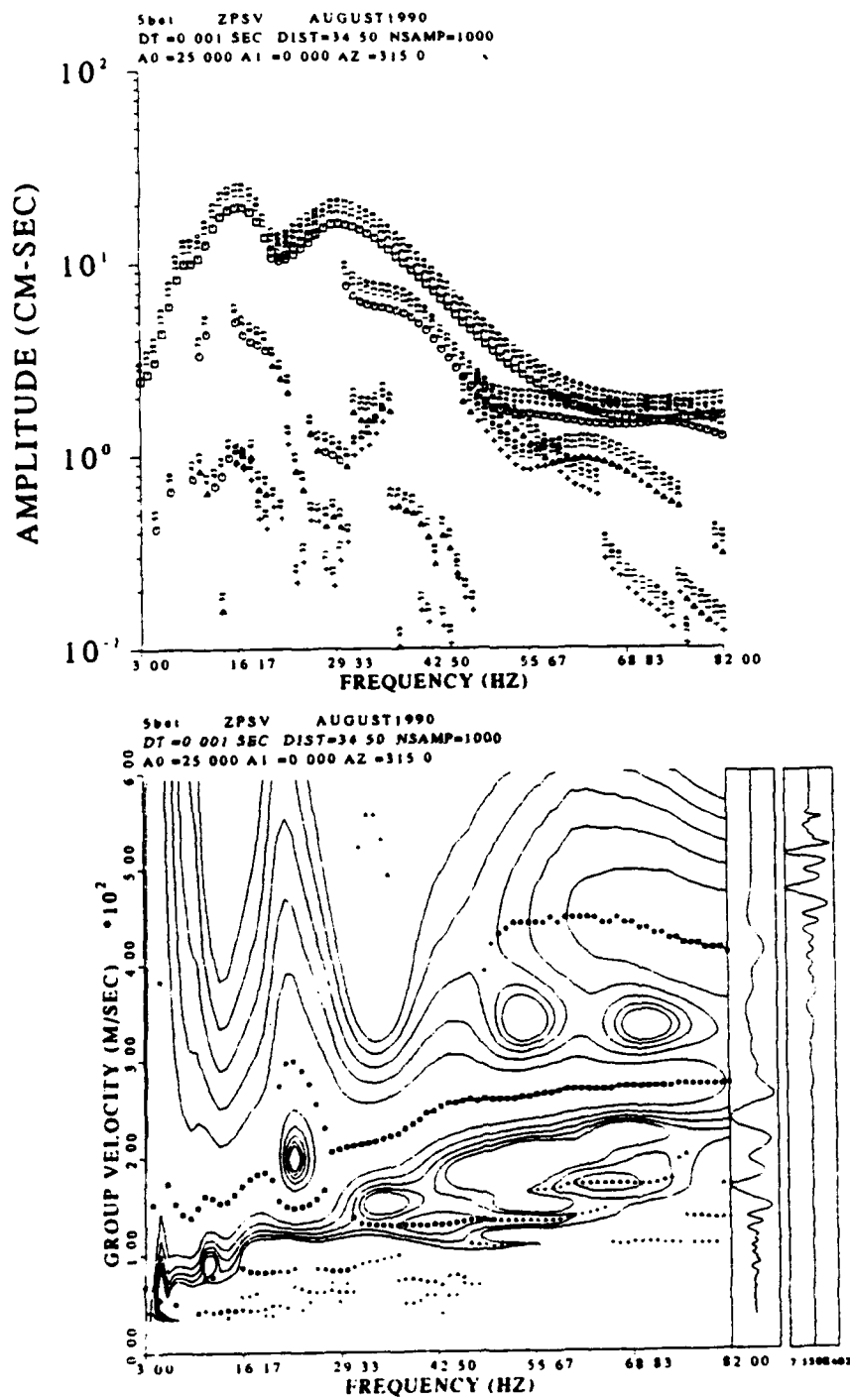


Figure 132. MFT analysis at 34.5 meters for Betsy data

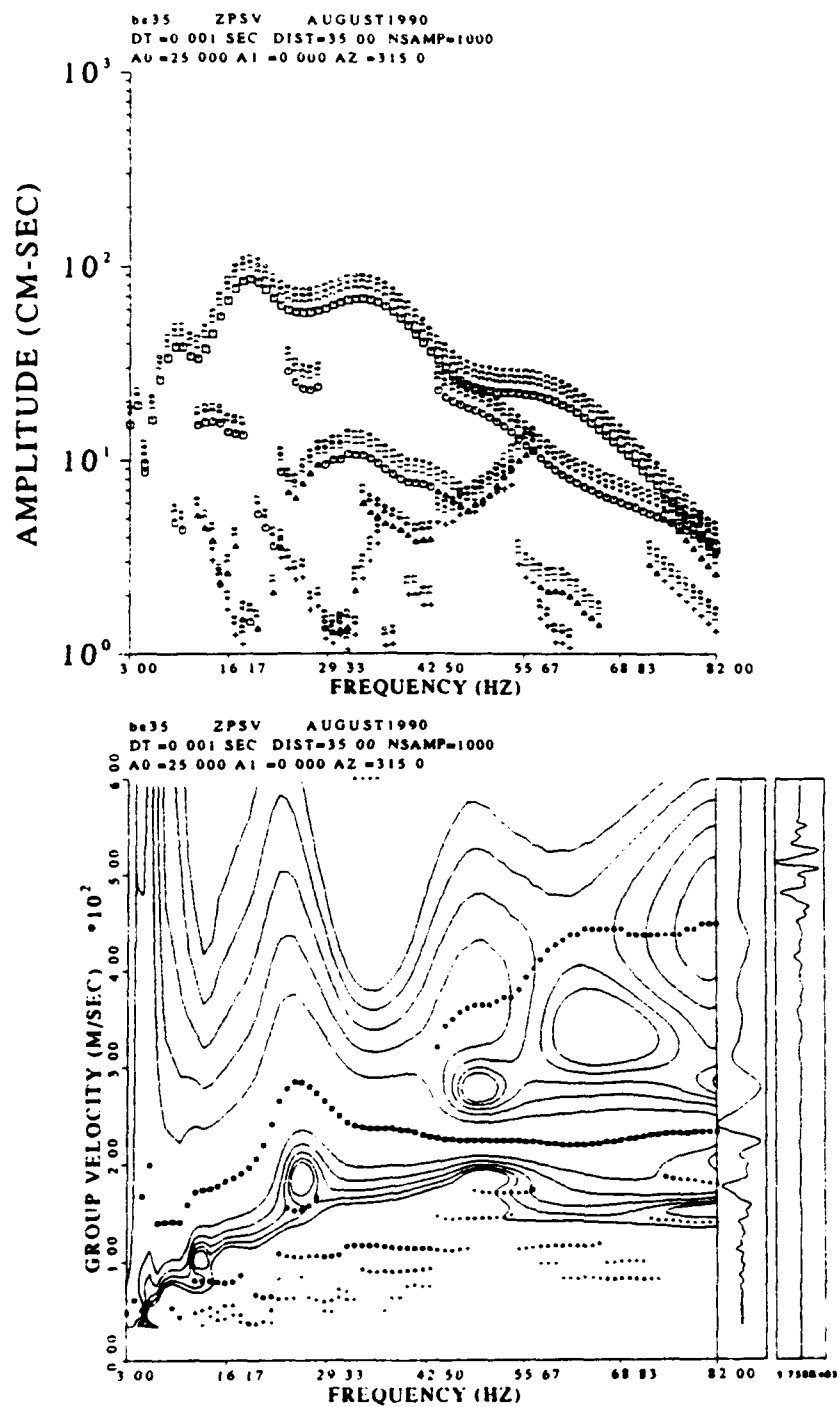


Figure 133. MFT analysis at 35.0 meters for Betsy data

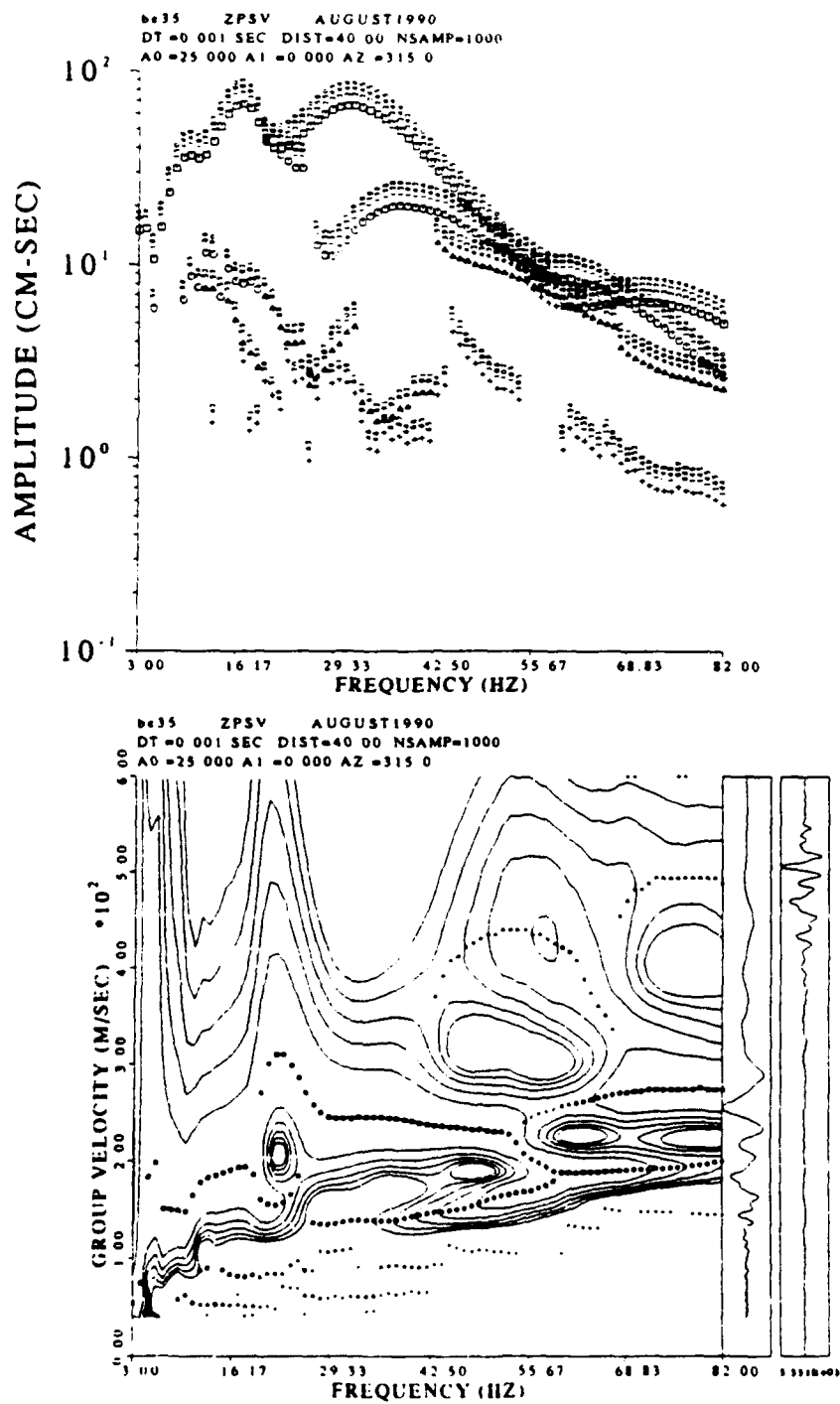


Figure 134. MFT analysis at 40.0 meters for Betsy data

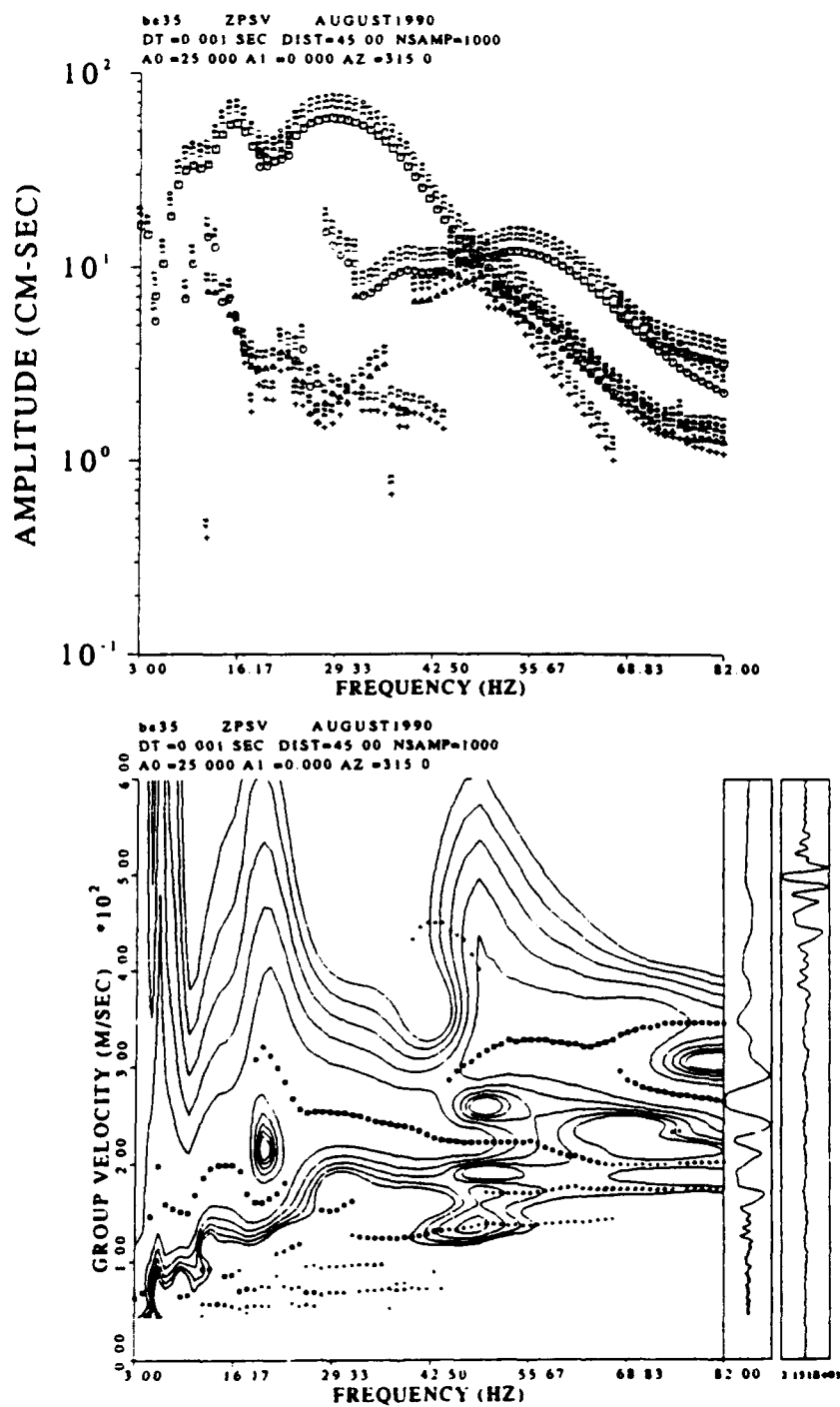


Figure 135. MFT analysis at 45.0 meters for Betsy data

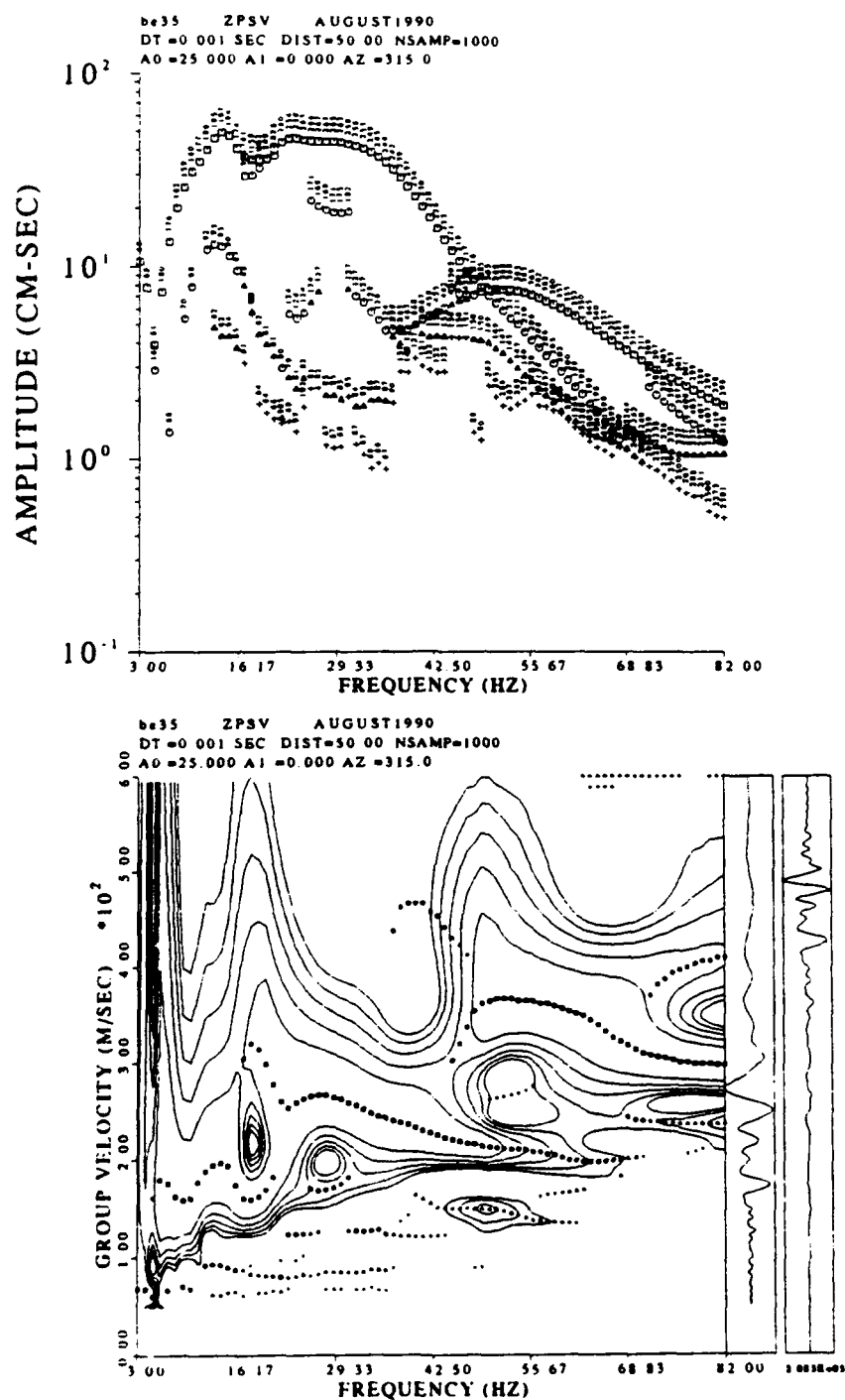


Figure 136. MFT analysis at 50.0 meters for Betsy data

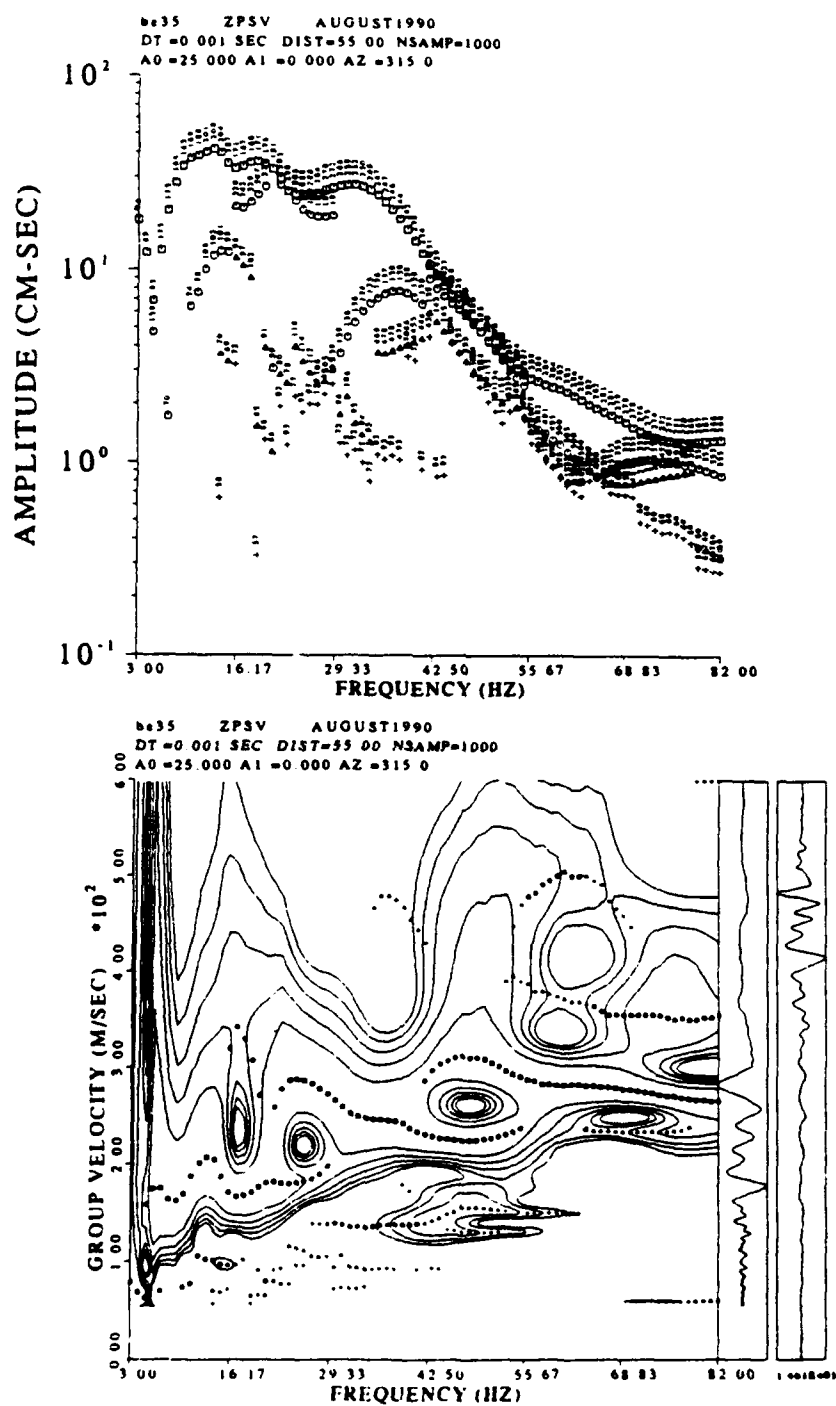


Figure 137. MFT analysis at 55.0 meters for Betsy data

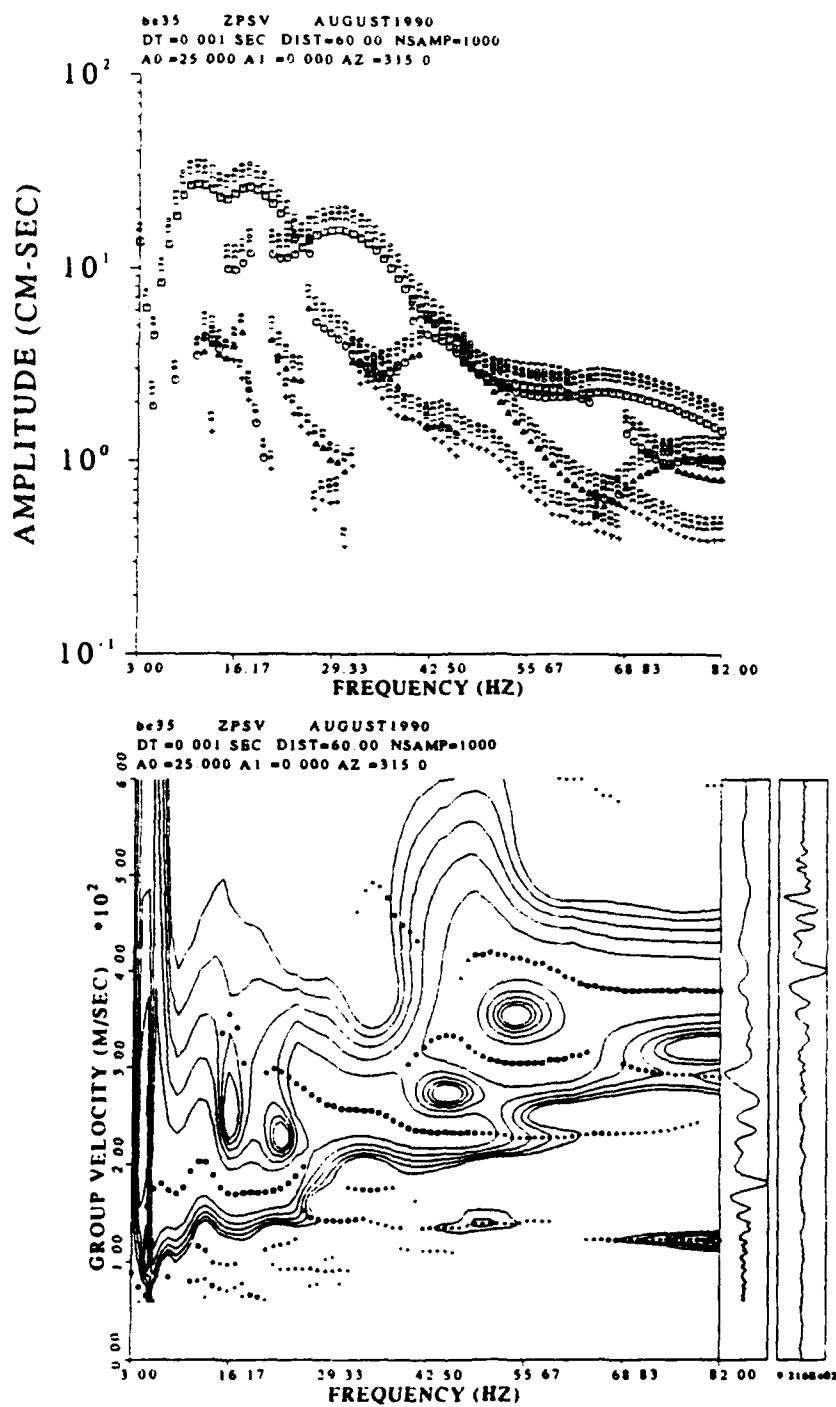


Figure 138. MFT analysis at 60.0 meters for Betsy data

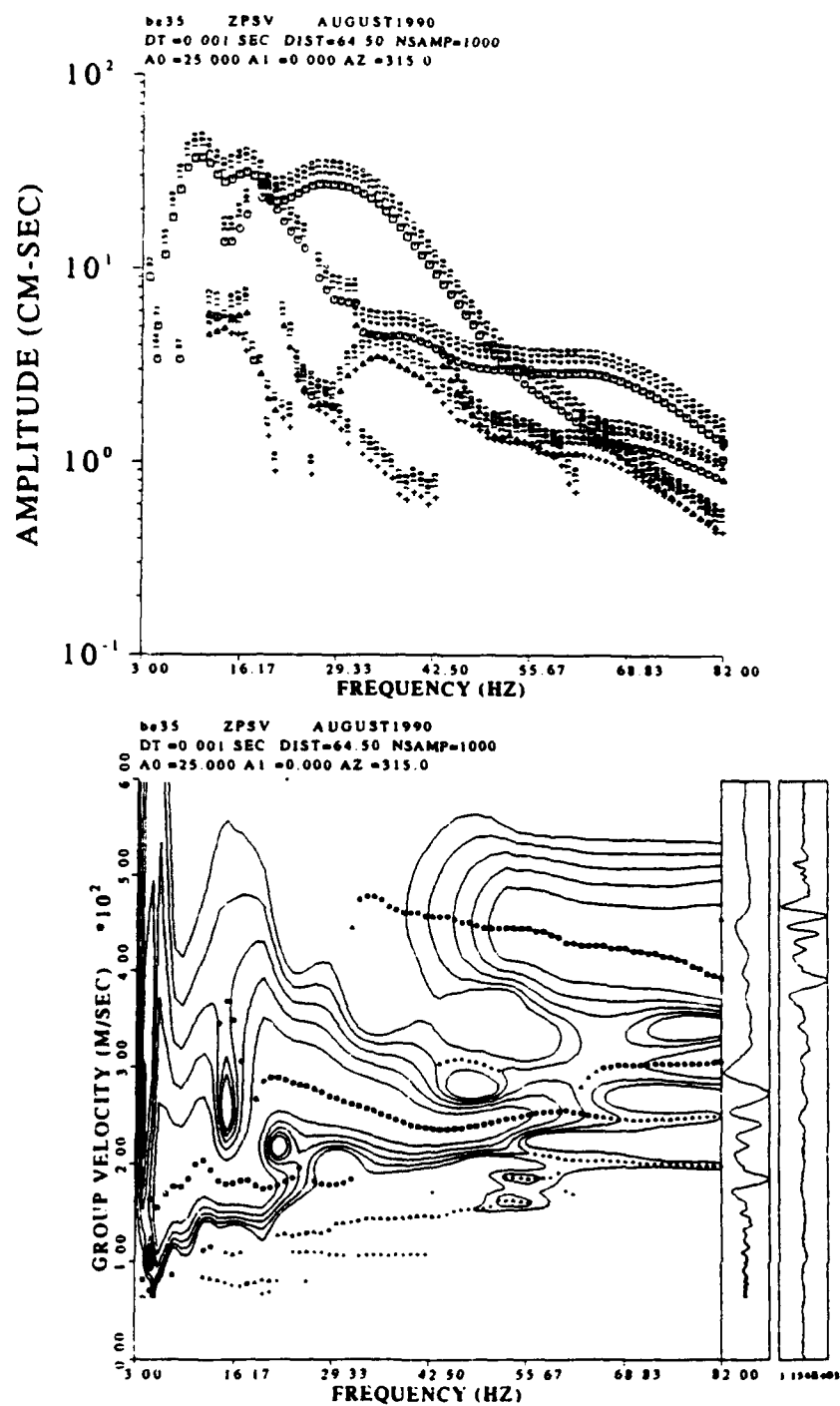


Figure 139. MFT analysis at 64.5 meters for Betsy data

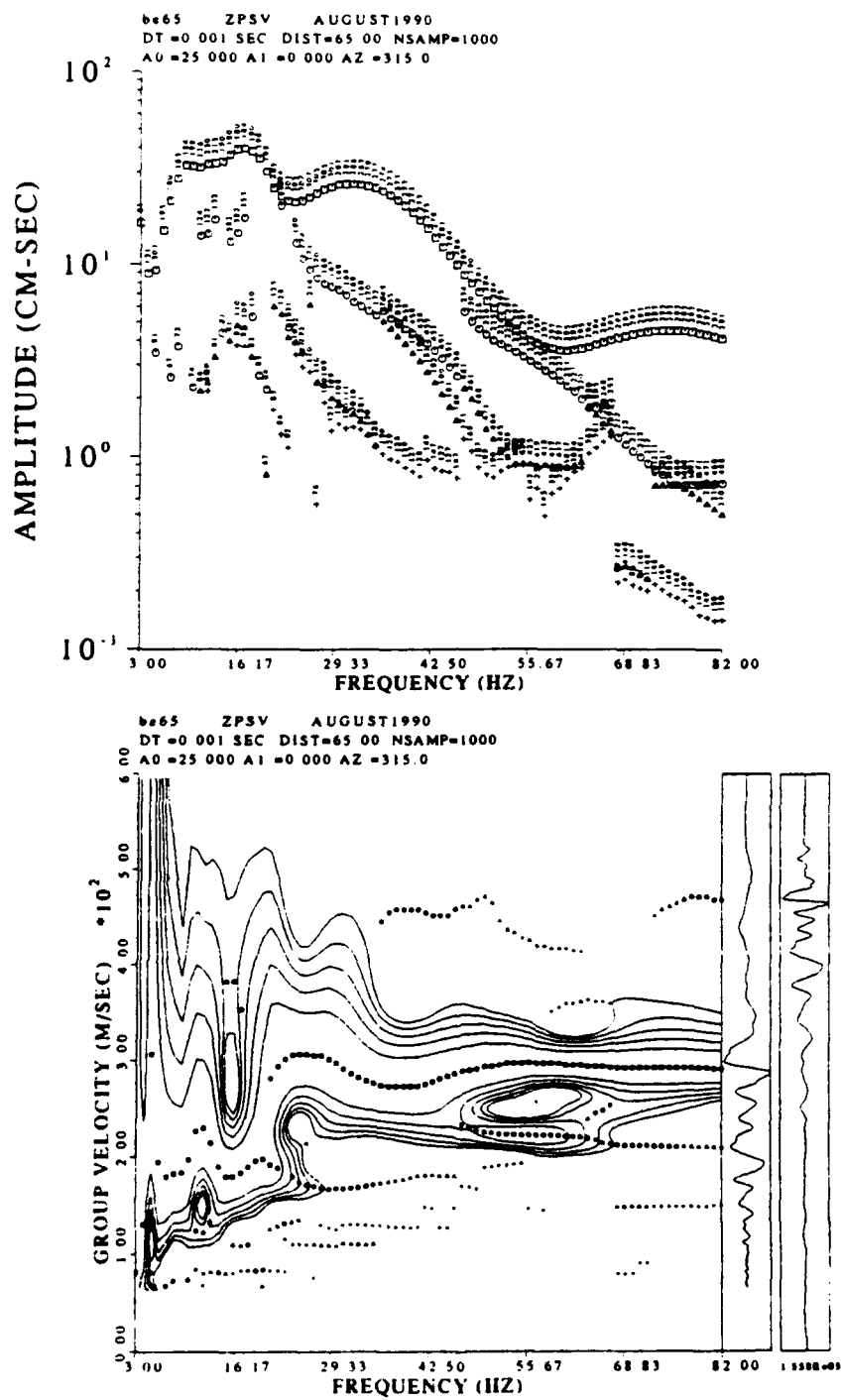


Figure 140. MFT analysis at 65.0 meters for Betsy data

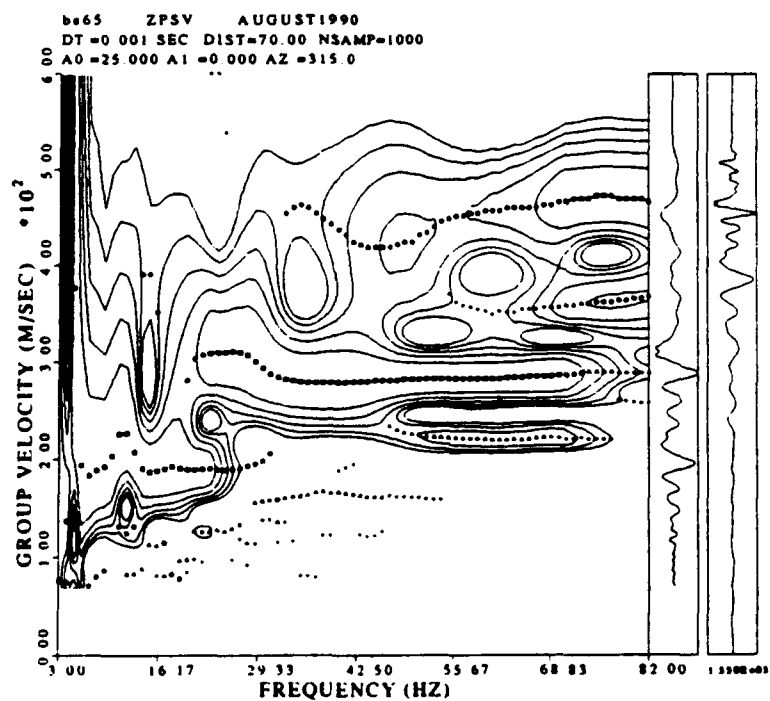
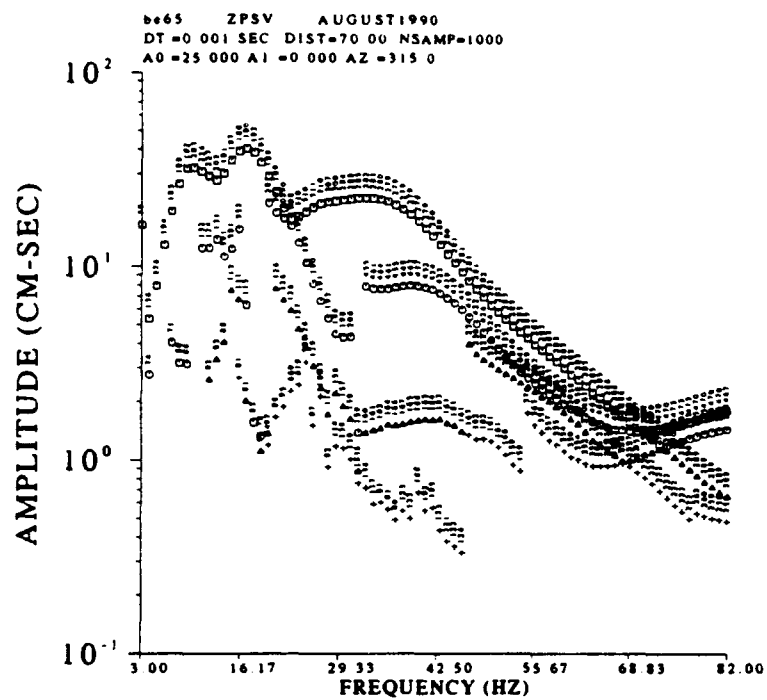


Figure 141. MFT analysis at 70.0 meters for Betsy data

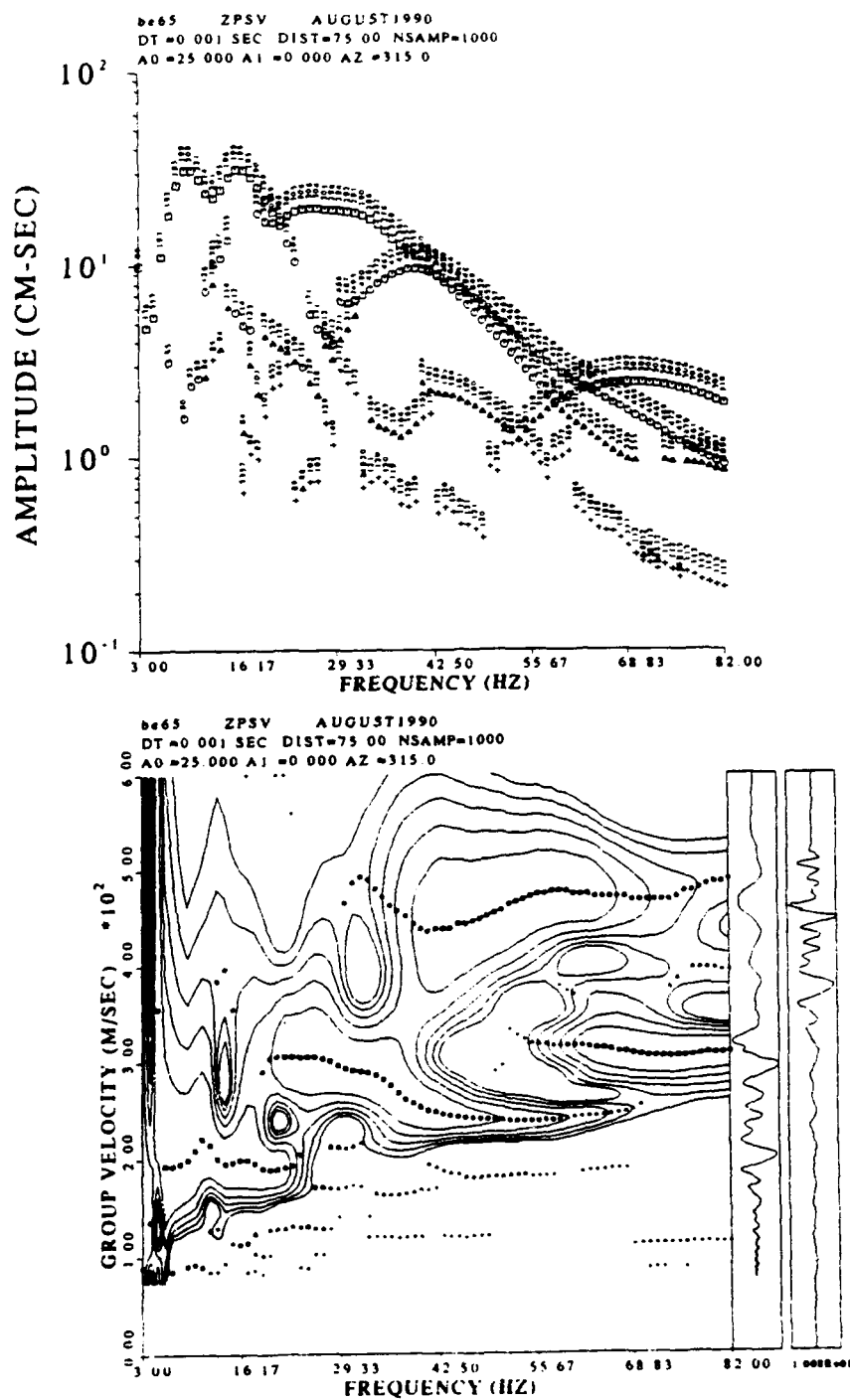


Figure 142. MFT analysis at 75.0 meters for Betsy data

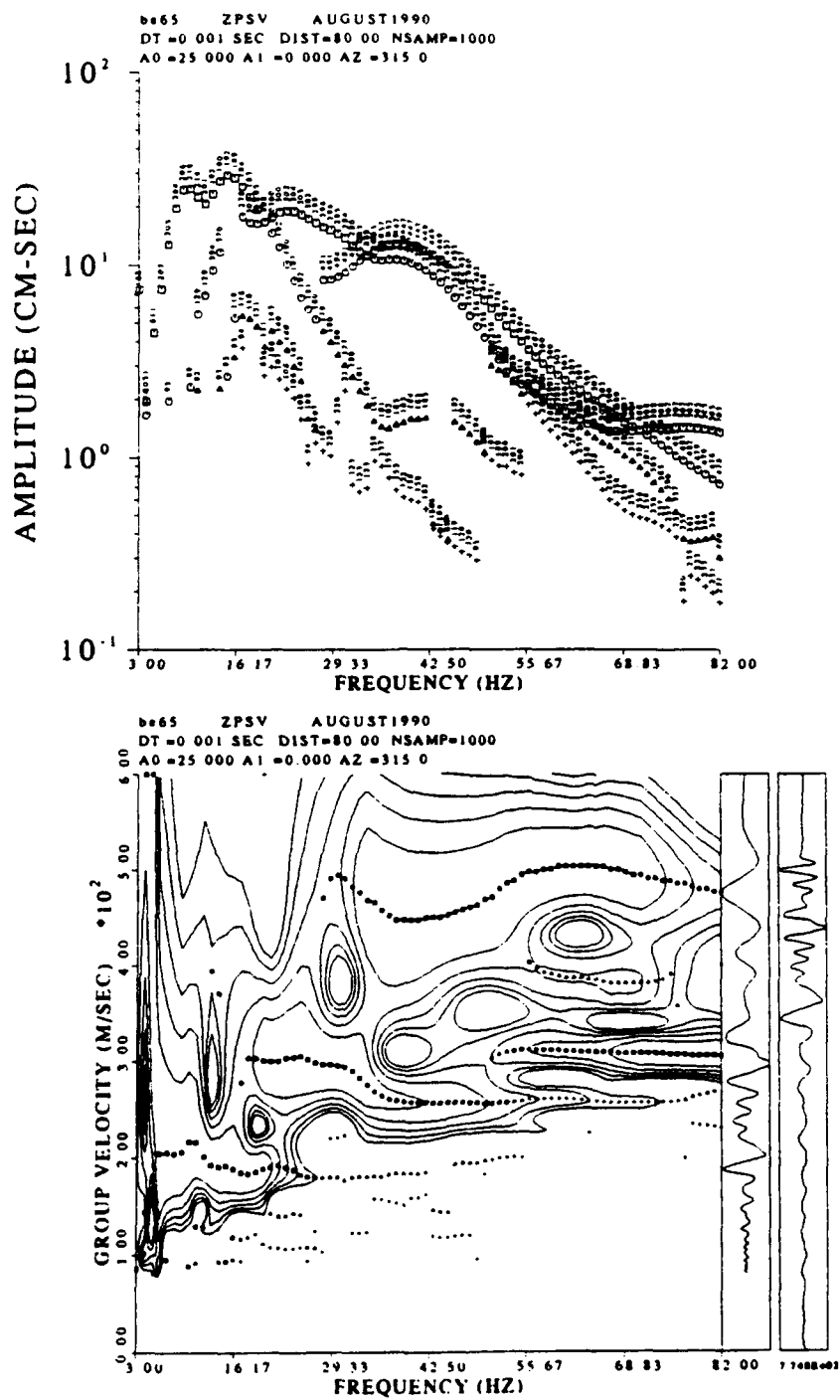


Figure 143. MFT analysis at 80.0 meters for Betsy data

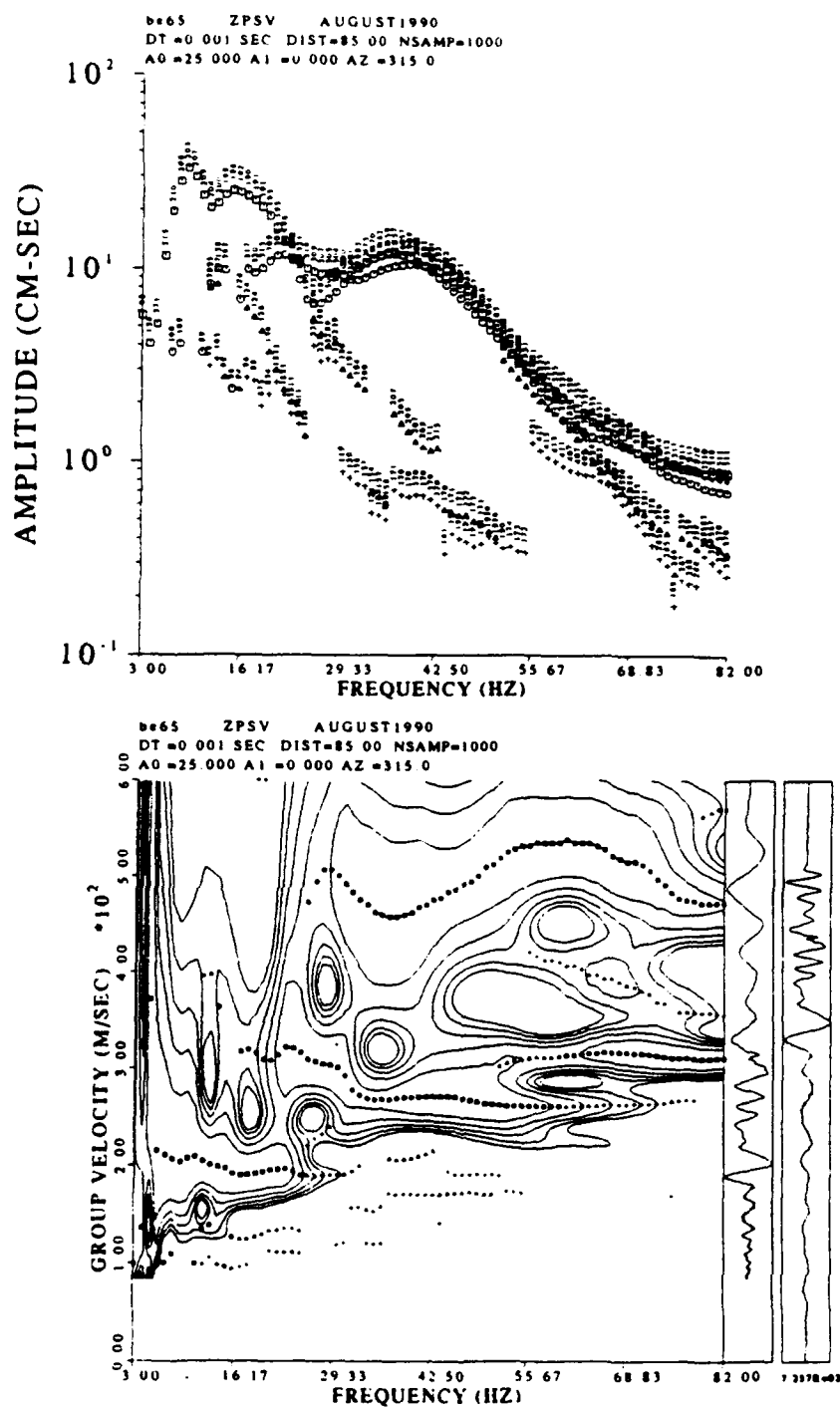


Figure 144. MFT analysis at 85.0 meters for Betsy data

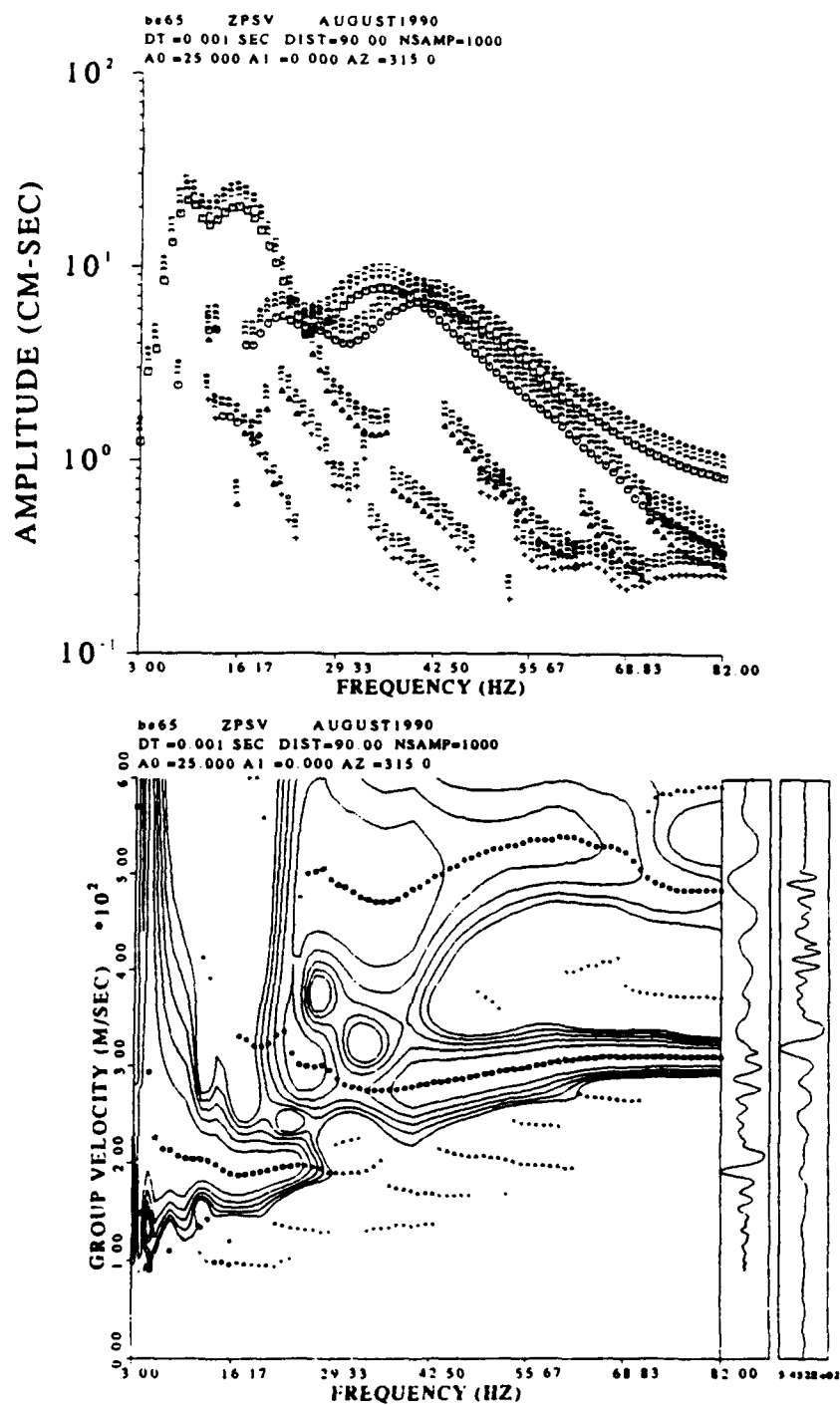


Figure 145. MFT analysis at 90.0 meters for Betsy data

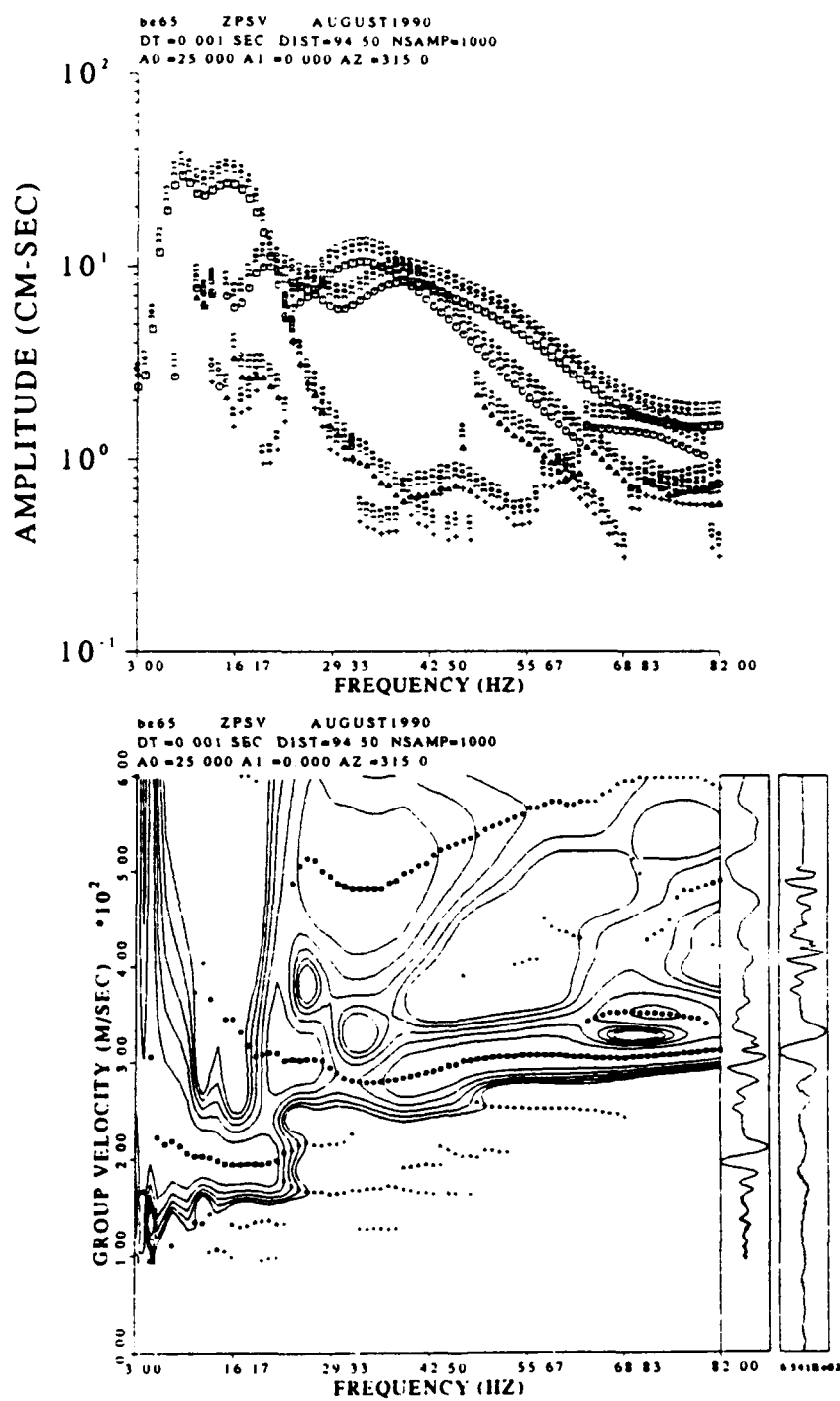


Figure 146. MFT analysis at 94.5 meters for Betsy data

BIBLIOGRAPHY

- Barker, T. G. 1988. "Array processing of Rayleigh waves for shallow shear wave velocity structure", abstract in Seismological Research Letters. Vol. 59, no. 1, January-March, 12.
- Bogaards, M. A. 1989. Characterization of Whole Wave Seismograms in the Shallow Weathered Zone, M.S. thesis, Southern Methodist University.
- Cherry, J. T., W. E. Farrell, W. L. Rodi, H. J. Swanger and B. Shkoller. 1979. "Shear wave velocities in MX valleys estimated from an inversion of Rayleigh wave group velocities", Systems, Science and Software report SSS-R-80-4232. December.
- Dobrin, M. B., and C. H. Savit. 1988. Introduction to Geophysical Prospecting. Fourth edition, McGraw-Hill Book Company.
- Dziewonski, A., S. Bloch, and M. Landisman. 1969. "A technique for the analysis of transient seismic signals", Bull. Seism. Soc. Am. Vol. 59, 427-444.
- Edelmann, H. A. K. 1985. Shear Wave Energy Sources: Seismic Shear Waves. Part B: Applications, Geophysical Press, p. 134-178.
- Farrell, W. E., R. C. Goff, and J. Wang. 1980. "Shear Waves in MX valleys: Rayleigh wave and Love wave excitation by vertical and horizontal weight drop sources", Systems, Science and Software Report SSS-R-80-4363. February.
- Goforth, T. T., and E. Herrin. 1979. "Phase-matched filters: application to the study of Love waves", Bulletin of the Seismological Society of America. Vol. 69, no. 1, 27-44.
- Golden, P. W. 1986. Acoustic Properties of Thin Plastic Plates with Application to Two Dimensional Seismic Modeling, M.S. thesis, Southern Methodist University.

- Grant, L. T. 1988. Experimental Determination of Seismic Source Characteristics for Small Chemical Explosions, M.S. thesis, Southern Methodist University.
- Graff, K. F. 1975. Wave Motion in Elastic Solids. Ohio State University Press.
- Haskell, N. A. 1953. "The dispersion of surface waves on multilayered media", Bulletin of the Seismological Society of America. Vol. 43, no. 1, 17-34.
- Herrin, E. and T. T. Goforth. 1977. "Phase-matched filters: application to the study of Rayleigh waves", Bulletin of the Seismological Society of America. Vol. 67, 1259-1275.
- Herrmann, R. B. 1973. "Some aspects of band-pass filtering of surface waves", Bulletin of the Seismological Society of America. Vol. 63, No.2, 663-671.
- _____. 1985. Computer Programs in Seismology, Vol III, "Surface Waves in Plane Layers".
- _____. 1987. Computer Programs in Seismology, Vol IV, "Surface Wave Inversion".
- _____. 1988. Computer Programs in Seismology, Vol II, "General Purpose Programs".
- Herrmann, R. B., and C. Y. Wang. 1985. "A comparison of synthetic seismograms", Bulletin of the Seismological Society of America. Vol. 75, no. 1, 41-56.
- Jackson, D.D. 1972. "Interpretation of inaccurate, insufficient and inconsistent data", Geophysical Journal of the Royal Astr. Soc. Vol. 28, 97-109.
- Jin, D. J., and Herrin, E. 1980. "Surface wave studies of the Bering Sea and Alaska area", Bulletin of the Seismological Society of America. Vol. 70, no. 6, 2117-2144.
- Kitsunczaki, C. 1980. "A new method for shear-wave logging", Geophysics. Vol. 45, no. 10, 1489-1506.
- Landisman, M., A. M. Dziewonski, and Y. Sato. 1969. "Recent improvements in the analysis of surface wave observations", Geophysical Journal of the Royal Astronomical Society. Vol. 17, 369-403.

- Lankston, R. W. 1989. "The seismic refraction method: A viable tool for mapping shallow targets into the 1990s", Geophysics. Vol. 54, no. 12, 1535-1542.
- Liu, Hsi-Ping, R.E. Warrick, R.E. Westerlund, J.B. Fletcher, and G.L. Maxwell. 1988. "An air-powered impulsive shear wave source with repeatable signals", Bulletin Seism. Soc. America. Vol. 78, 355-369.
- Mari, J. L. 1984. "Estimation of static corrections for shear-wave profiling using the dispersion properties of Love waves", Geophysics. Vol. 49, no. 8, 1169-1179.
- McMechan, G.A. and M. J. Yedlin. 1981. "Analysis of dispersive waves by wave field transformation", Geophysics. Vol. 46, no. 6, 869-874.
- Menke, W. 1989. Geophysical Data Analysis: Discrete Inverse Theory. Academic Press.
- Mokhtar, T. A., R.B. Herrmann and D.R. Russell. 1988. "Seismic velocity and Q model for the shallow structure of the Arabian shield from short-period Rayleigh waves", Geophysics. Vol. 53, no. 11, 1379-1387.
- Mooney, H. M. and B. A. Bolt. 1966. "Dispersive characteristics of the first three Rayleigh modes for a single surface layer", Bulletin of the Seismological Society of America. Vol 56, no. 1, 43-67.
- Press, F. 1956. "Determination of crustal structure from phase velocity of Rayleigh waves", Bulletin of the Geological Society of America. Vol. 67, 1647-1658.
- Reinke, R. E. 1986. "A computational study of thin layer effects in shallow seismic refraction surveys", Report for Air Force Weapons Laboratory, AFWL-TR-85-81.
- Reinke, R. E. and B. W. Stump. 1988. "Stochastic geologic effects on near-field ground motions in alluvium", Bulletin of the Seismological Society of America. Vol. 78, 1037-1058.
- Simila, G. W. 1982. "Shear wave velocity from Rayleigh wave dispersion analysis", Report AFWL-TR-82-08. September, pp. 34.
- Stokoe, K. H. and S. Nazarian. 1984. "Seismic testing of two apron sections at Tyndall AFB using crosshole and surface wave methods", Geotechnical Engineering Report GR84-3, pp. 157.

- Stump, B. W., D. C. Pearson, and K. D. Thomason. 1991. SMU Portable Seismic Instrumentation Development.
- Stump, B. W., and R. E. Reinke. 1982. "Spall-Like Waveforms Observed in High Explosive Testing in Alluvium", AFWL-TR-82-15. Air Force Weapons Laboratory, Kirtland AFB, New Mexico, pp. 122.
- Telford, W. M., L. P. Geldart, R. E. Sheriff, and D. A. Keys. 1976. Applied Geophysics, Cambridge University Press, pp. 860.
- Wang, C. Y., and R. B. Herrmann. 1980. "A numerical study of P-, SV-, and SH- wave generation in a plane layered medium", Bulletin of the Seismological Society of America. Vol. 70, no. 4, 1015-1036.
- Waters, K. H. 1981. Reflection Seismology, J. Wiley & Sons, pp. 453.
- Wiggins, R.A. 1972. "The general linear inverse problem: Implication of surface waves and free oscillations for earth structure", Reviews of Geophysics and Space Physics. Vol 10, No. 1, 251-285.
- Won, I. J., and Clough, J. W. 1981. "A new torsional shear-wave generator", Geophysics. Vol. 46, no. 11, 1607-1608.